

The Telecommunications and Data Acquisition Progress Report 42-118

April-June 1994

Joseph H. Yuen
Editor

(NASA-CR-196409) THE
TELECOMMUNICATIONS AND DATA
ACQUISITION REPORT Progress Report,
Apr. - Jun. 1994 (JPL) 185 p

N95-14620
--THRU--
N95-14632
Unclas

G3/32 0019778

August 15, 1994



National Aeronautics and
Space Administration

Jet Propulsion Laboratory
California Institute of Technology
Pasadena, California

8p

The Telecommunications and Data Acquisition Progress Report 42-118

April-June 1994

Joseph H. Yuen
Editor

August 15, 1994

NASA

National Aeronautics and
Space Administration

Jet Propulsion Laboratory
California Institute of Technology
Pasadena, California

Note From the Editor

The format of the current issue is different from past issues. This is a step toward the goal of publishing *The Telecommunications and Data Acquisition Progress Report* electronically. The *TDA Progress Report* will be available both in print and in electronic form for a period of time. Ultimately, it will only be available electronically through the Internet. It is time to get on the information superhighway.

PREVIOUS PAGE BLANK NOT FILMED

PAGE 11 INTENTIONALLY BLANK

Preface

This quarterly publication provides archival reports on developments in programs managed by JPL's Telecommunications and Mission Operations Directorate (TMOD), which now includes the former Telecommunications and Data Acquisition (TDA) Office. In space communications, radio navigation, radio science, and ground-based radio and radar astronomy, it reports on activities of the Deep Space Network (DSN) in planning, supporting research and technology, implementation, and operations. Also included are standards activity at JPL for space data and information systems and reimbursable DSN work performed for other space agencies through NASA. The preceding work is all performed for NASA's Office of Space Communications (OSC).

The TMOD also performs work funded by other NASA program offices through and with the cooperation of OSC. The first of these is the Orbital Debris Radar Program funded by the Office of Space Systems Development. It exists at Goldstone only and makes use of the planetary radar capability when the antennas are configured as science instruments making direct observations of the planets, their satellites, and asteroids of our solar system. The Office of Space Sciences funds the data reduction and science analyses of data obtained by the Goldstone Solar System Radar. The antennas at all three complexes are also configured for radio astronomy research and, as such, conduct experiments funded by the National Science Foundation in the U.S. and other agencies at the overseas complexes. These experiments are either in microwave spectroscopy or very long baseline interferometry.

Finally, tasks funded under the JPL Director's Discretionary Fund and the Caltech President's Fund that involve the TMOD are included.

This and each succeeding issue of *The Telecommunications and Data Acquisition Progress Report* will present material in some, but not necessarily all, of the aforementioned programs.

PRECEDING PAGE BLANK NOT FILMED

PAGE 10 INTENTIONALLY BLANK

Contents

OSC TASKS DSN Advanced Systems

TRACKING AND GROUND-BASED NAVIGATION

The Long-Term Forecast of Station View Periods.....	1
M. W. Lo	
NASA Code 310-10-63-50-00	

COMMUNICATIONS, SPACECRAFT-GROUND

The Stark Anomalous Dispersion Optical Filter: The Theory.....	14
B. Yin and T. M. Shay	
NASA Code 310-20-67-92-02	
Convolutional Encoding of Self-Dual Block Codes (II).....	22
G. Solomon and Y. Jin	
NASA Code 310-30-71-83-02	
Spin Glasses and Error-Correcting Codes	26
M. L. Belongie	
NASA Code 315-91-40-20-36	

STATION CONTROL AND SYSTEM TECHNOLOGY

Linear Quadratic Gaussian and Feedforward Controllers for the DSS-13 Antenna.....	37
W. K. Gawronski, C. S. Racho, and J. A. Mellstrom	
NASA Code 310-20-65-92-02	
A Radio Telescope for the Calibration of Radio Sources at 32 Gigahertz.....	56
M. S. Gatti, S. R. Stewart, J. G. Bowen, and E. B. Paulsen	
NASA Code 310-30-69-91-01	

DSN Systems Implementation CAPABILITIES FOR EXISTING PROJECTS

The Block V Receiver Fast Acquisition Algorithm for the Galileo S-Band Mission	83
M. Aung, W. J. Hurd, C. M. Buu, J. B. Berner, S. A. Stephens, and J. M. Gevorgiz	
NASA Code 314-30-63-01-01	

CAPABILITIES FOR NEW PROJECTS

Research and Development Optical Deep Space Antenna Sizing Study	115
D. Wonica	
NASA Code 310-20-67-92-02	

NETWORK UPGRADE AND SUSTAINING

Pilot Retrofit Test of Refrigerant R-134a for GDSCC	125
J. Albus, B. Brown, M. Dungao, and G. Spencer	
NASA Code 314-40-32-10-23	
A Trajectory Preprocessor for Antenna Pointing.....	139
S. R. Tyler	
NASA Code 314-40-42-01-03	

**DSN Operations
NETWORK OPERATIONS AND OPERATIONS SUPPORT**

The Network Operations Control Center Upgrade Task: Lessons Learned 160 11
J. S. Sherif, T.-L. Tran, and S. Lee
NASA Code 314-30-43-09-01

LONG-RANGE PROGRAM PLANNING

Low-Earth-Orbiter Resource Allocation and Capacity Planning for the DSN Using LEO4CAST... 169 12
G. Fox and C. Borden
NASA Code 315-90-71-10-08

Referees..... 179

1995109207

324450

N95- 14621

SP-14
19779
8-13

The Long-Term Forecast of Station View Periods

M. W. Lo
Mission Design Section

Using dynamical systems theory, a definite integral is obtained that gives the average view period of a ground station for spacecraft in circular orbits. Minor restrictions exist on the class of circular orbits to which this method can be applied. This method avoids the propagation of the orbit, which requires a lot of resources, and simplifies the algorithm used to compute the mean station view period. The integral is used for long-term station load forecast studies. It also provides a quantitative measure of the effectiveness of a ground station as a function of its latitude.

I. Introduction

Planners for the Deep Space Network frequently need to perform long-term station loading studies to determine resource allocations. Typical questions asked by the planners are as follows:

- (1) Will the current 34-m subnet be adequate for the support of mission set *A* for the next 5 years? The mission set represents a collection of current and planned missions that requires support from the subnet.
- (2) How will either adding or removing a station at location *X* affect the performance of the 26-m subnet for the support of mission set *B*? Will the performance improve if location *Y* is selected instead of *X*?

It is important to make the distinction between short-term planning and long-term planning, because the problems encountered are very different. In this article, problems lasting less than a month are defined as short-term planning problems, or scheduling problems; problems lasting more than a month are defined as long-term planning problems, or forecasting problems. The period of 1 month, while somewhat arbitrarily selected, is a convenient demarcation.

With scheduling problems, the interest is in the actual times of events, such as the start and stop times of the view periods of a particular ground station for a set of spacecraft. Typically, the prediction of orbital ephemeris for scheduling activities must be performed weekly or more often due to the various perturbations that cause the actual orbits to quickly drift away from the predicted orbits. Many of the perturbations have random components, and some of the perturbations are not well understood; these factors make their prediction practically impossible. Thus, scheduling problems are concerned with very short durations not far into the future.

With forecasting problems, the interest is not in the actual times of the events but in their long-term trends and cycles. With such problems, the short-term variations are typically ignored due to

their variability and unpredictability. This is usually achieved by averaging techniques; for example, one finds the mean of a parameter by integration over time. Thus, forecasting problems are concerned with long-term trends and average behavior far into the future.

One way to obtain station loading trends is to compute the station view periods, assuming some perturbation models, and then to compute statistics from this database. This has been the method of choice since it is reasonably straightforward to implement. In order to obtain the station view periods, the satellite ephemeris must be propagated. When the period of analysis is 5 to 10 years for a mission set of dozens of spacecraft, this quickly becomes a data-intensive computational problem. For example, using an analytical orbit generator, to compute the view periods of an Earth-orbiting spacecraft with an altitude around 1000 km for the DSN 26-m subnet for the duration of 1 year requires roughly 20 min on a high-speed workstation. For a more complicated orbit generator, with a larger mission set and a longer duration, say 5 years, the time required to generate the view periods alone would be considerable. Thereafter, the large view-period data set requires additional software for manipulation and computation to produce the desired statistics.

Another way to obtain station loading trends is to consider dynamical systems methods. Dynamical systems is the interdisciplinary field that evolved from the qualitative study of differential equations, first begun by Henri Poincaré at the turn of the century. When one sees the adjective “qualitative,” one usually assumes no quantitative results can be obtained from such methods. Fortunately, this is not always the case. But the quantities estimated by qualitative methods tend to be global in nature. This article presents an integral that gives the average view period of a spacecraft to a ground station and is derived using dynamical systems theory.¹

II. The Long-Term Station View Period Ratio, ρ

An integral was obtained that represents the long-term station view period ratio, ρ , for the class of circular orbits with nonrepeating ground tracks. This ratio provides an estimate of the total time a station is in view of a spacecraft divided by the total elapsed time. More precisely, let

T = total elapsed time

$P(T)$ = total station view period during the elapsed time T

then the long-term station view period ratio is defined by

$$\rho = \lim_{T \rightarrow \infty} \frac{P(T)}{T} \quad (1)$$

Thus, given a time period, T , the total amount of time a station is in view of the satellite is given by the following expression:

$$V(T) = \rho T \quad (2)$$

As the ratio, ρ , is a limit, the larger the value of T , the closer $P(T)$ is to $V(T)$. For example, for a 200-km circular orbit with an inclination of 28.5 deg (Case 1, Table 1), the total view period at a ground station at 0-deg latitude for 1 year as computed by $P(T)$ and $V(T)$ is

$$P(1 \text{ year}) = 0.021014 \text{ year}$$

$$V(1 \text{ year}) = 0.021030 \text{ year}$$

¹ An article describing the full derivation of the integral is under preparation.

Here $P(T)$ is computed by propagating the orbit and finding all of the view periods of the station at latitude 0 deg; $V(T)$ is computed from Eq. (2), where the ratio, ρ , is given by the integral.

Preliminary numerical results indicate excellent agreement between the numerical and the theoretical values for the view period ratio, ρ , for circular orbits. The numerical values are computed typically from 1 year's worth of station view periods. For the circular orbits used in the numerical study, $\Delta\rho$ is less than ± 0.2 percent, where $\Delta\rho$ is the difference between the theoretical and numerical values of ρ . For the elliptic orbits used in the numerical study, at $e = 0.05$, the maximum $\Delta\rho$ for the cases tested exceeds 15 percent. For orbits whose period is commensurate with the Earth's rotational period, the $\Delta\rho$ for the cases tested is within ± 1.5 percent. These results are tabulated in Tables 1 through 3 and discussed in Section V.

III. Heuristics and Theoretical Background

Examine first the geometry of the spacecraft and the ground station. Figure 1 shows the geometry of the station mask, which is determined by the altitude of the spacecraft and has the following interpretation. The station mask is the circle of angular radius, θ_0 , about the ground station. When the spacecraft ground track is within the station mask, the spacecraft is in view of the station. When the ground track is outside of the station mask, the spacecraft is not in view of the station. The angle, ε , is the minimum station elevation angle below which the station cannot view the spacecraft, due to some constraint or obstruction at the horizon. In particular, when the spacecraft-to-station elevation angle is ≤ 0 deg, then the Earth itself is obstructing the spacecraft from the station view. A spherical Earth is assumed here.

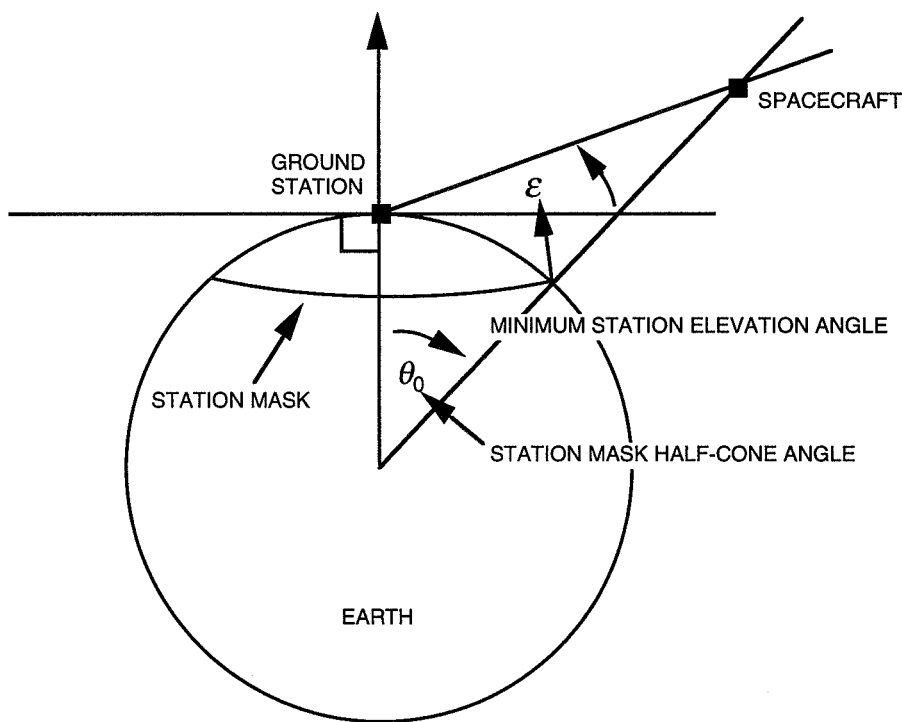


Fig. 1. Geometry of the station mask.

Figure 2 illustrates the ground tracks of a spacecraft in circular orbit at a 7714.14-km radius (this is the radius of the TOPEX/POSEIDON orbit) and a 28.5-deg inclination. The circle centered at the equator with the label "Case 4" is the station mask of a fictitious station on an ocean platform at the equator (latitude = 0 deg) with longitude equal to that of the 26-m station at Goldstone. The station

mask of the Madrid station is labeled "Case 7" and that of the Canberra station is labeled "Case 6." They are only partially in view. Consider a station at the pole; its mask is the cap about the pole. For the spacecraft in Case 4, this cap does not intersect the ground track pattern. This means that the spacecraft would not see the station at the pole. The Madrid station mask (Case 7) intersects the ground tracks in a much smaller area than that of Case 4. Intuitively, one might think that, somehow, the total view period (sum of all the view periods) is proportional to the area of the intersection between the band of the ground track and the station mask. After all, when there is no intersection, there is no view period. When there is a lot of intersection, there is a large view period. But, unfortunately, this is not the whole story. There are other factors.

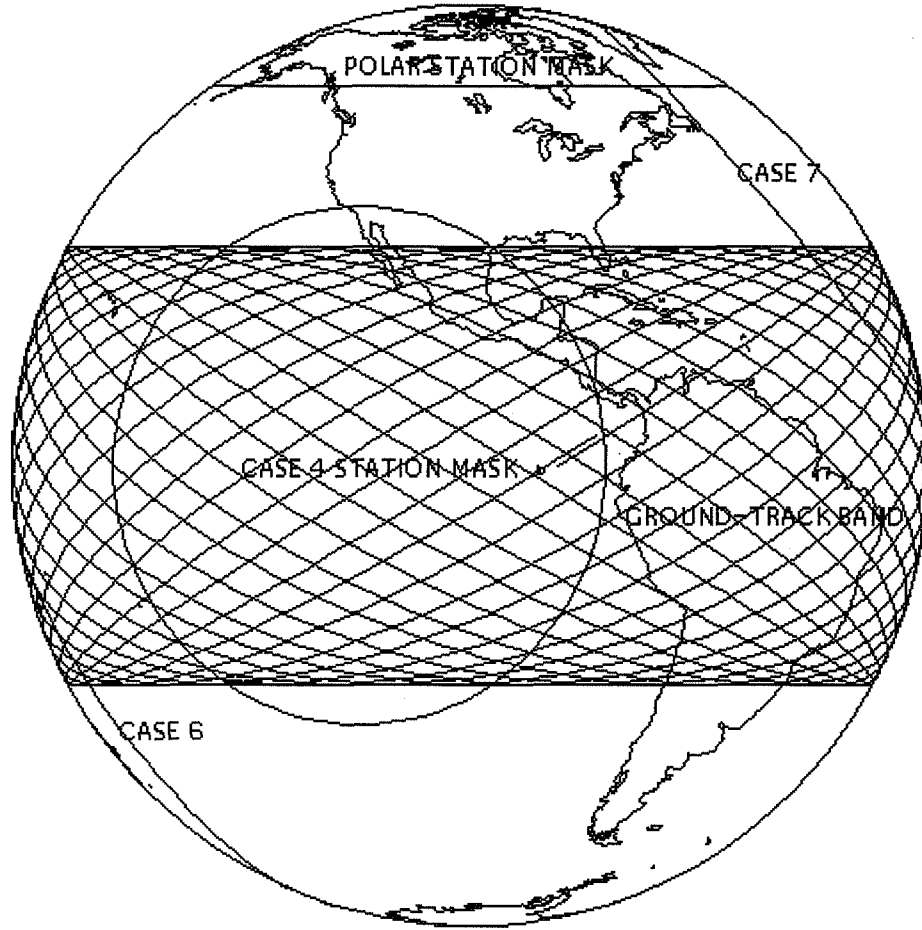


Fig. 2. Station masks and ground tracks for cases 4, 6, and 7 (orthographic projection).

Consider the following example: suppose now that the orbit is of sufficiently high inclination and low altitude that the station mask is a small circle completely within the ground track band, as illustrated in Fig. 3. Calculations quickly show that Station 1 has a much higher total view period than Station 2, even though they have the same mask area and are both enveloped by the spacecraft ground tracks. This agrees with the well-known observation that stations at higher latitudes tend to have more and longer view periods.

This problem is resolved by looking at Fig. 2 more carefully. Notice that the ground tracks are more closely packed near the top than near the equator. Furthermore, the speed of the spacecraft nadir along the ground track is not constant even though that of the circular orbit is constant. This is due to the

rotation of the Earth and the projection of the spacecraft motion onto the sphere. Thus, the time spent near the equator and that near the top and bottom of the ground track band is not the same. However, the station mask is unaffected by the rotation of the Earth, and it has the same size regardless of the location of the station. Hence, going back to Fig. 3, even though the two station masks contain the same amount of ground track area, the actual time spent in each area is not the same. Thus, one has to use a weight factor to compute the area of intersection in order for it to be proportional to the total view period. In mathematical terms, one needs to find an invariant measure for the dynamics. This measure will give the connection between the weighted area of the mask and the time spent in the mask. This has been done for the case of circular orbits with certain mild restrictions and is discussed in the next section.

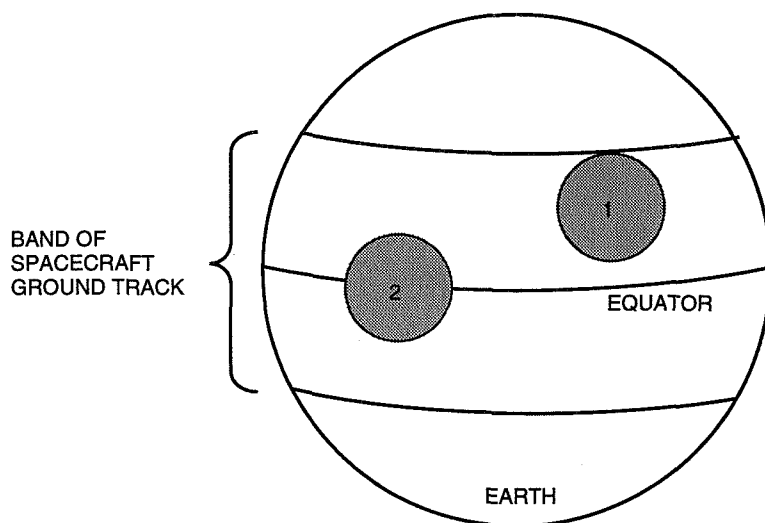


Fig. 3. Station masks at different latitudes.

The system of spacecraft ground tracks belongs to a class of dynamical systems known as “ergodic.” The discussion on ergodic theory below drew on [1–3]. The analysis used many of the ideas described in [4]. The important property about ergodic systems for this discussion is the following.

Let $F(x)$ be a well-behaved function on the space where there is an ergodic system. Then the time mean of F and the space mean of F are equal. The time mean of F is the path integral of $F(x)$ along the trajectory as a function of time. The space mean of F is simply the integral of F over the space. This is known as the Ergodic Theorem.

Now let F be the station view function. This means F is equal to 1 when the spacecraft is in view of the station, and F is equal to 0 otherwise. The time mean of F is just the time average of the total view period. The view periods require a lot of calculations, which one would like to avoid. But the Ergodic Theorem states that one can skip all this computation by simply calculating the space mean of F . This is a great simplification; notice that the space mean of F is just its integral over the sphere, which is easy to compute. One arrives at the following:

$$\lim_{T \rightarrow \infty} \frac{P(T)}{T} = \text{time mean of } F$$

$$\int_{EARTH} F(x) d\mu = \text{space mean of } F$$

$$\rho = \lim_{T \rightarrow \infty} \frac{P(T)}{T} = \int_{EARTH} F(x) d\mu$$

The construction of the weight function, μ , also known as the invariant measure, is geometric in nature. Referring back to Fig. 2, follow a small segment along the ground tracks and see how it gets stretched as time progresses. This stretching factor then enables one to compute μ . It is this weight function that enables one to relate the time with the area. Having done so, it becomes an easy task to perform the integral, F , whereupon, one has computed the long-term view period ratio, ρ . This demonstrates the power of qualitative methods even for engineering applications.

IV. The Integral Representation of ρ

The integral ρ for a spacecraft in circular orbit is subject to the following perturbations and constraints:

- (1) The spacecraft is in circular orbit; the orbit eccentricity is 0.
- (2) The spacecraft is perturbed only by the linear J_2 term of the spherical harmonic expansion of the gravity field of Earth. Thus, the first-order linear perturbations for the node and argument of perigee are:

$$\Omega(T) = \Omega_0 + \frac{d\Omega}{dt} T$$

$$\omega(T) = \omega_0 + \frac{d\omega}{dt} T$$

The derivatives $d\Omega/dt$ and $d\omega/dt$ are constant. The semimajor axis, eccentricity, and inclination are constant. Mean elements are assumed throughout this discussion.

- (3) The orbit inclination is not 0 deg. Circular orbits with a 0-deg inclination have constant view periods that can be easily calculated.²
- (4) The orbit has an orbital period that is incommensurate with the period of the Earth's rotation. Hence, this orbit does not have repeating ground tracks.
- (5) The ground station is not centered at the north or south pole.
- (6) The intersection of the station mask with the ground-track region forms a simply connected domain.

The variables and the integral for ρ are

$$\left. \begin{aligned} \rho &= \text{long-term station view period ratio} \\ \varphi_0 &= \text{station latitude} \neq \pm 90 \text{ deg} \\ \theta_0 &= \text{station mask angular radius} \\ &= \arccos(R_E/R) \text{ for stations with } \varepsilon = 0 \text{ deg} \\ R_E &= \text{Earth radius} \\ R &= \text{spacecraft orbit radius} \\ \varepsilon &= \text{minimum station elevation angle} \end{aligned} \right\} \quad (3a)$$

²M. W. Lo, "The View Period of Circular Equatorial Orbits," JPL Interoffice Memorandum 312/94.7-10 (internal document), Jet Propulsion Laboratory, Pasadena, California, June 3, 1994.

$$\left. \begin{aligned}
& i = \text{spacecraft orbit inclination} > 0 \text{ deg} \\
L_i &= \begin{cases} i & \text{if } i \leq 90 \text{ deg} \\ 180 - i & \text{if } i > 90 \text{ deg} \end{cases} \\
\varphi_1 &= \max \{ \varphi_0 - \theta_0, -L_i \} \\
\varphi_2 &= \min \{ \varphi_0 + \theta_0, L_i \} \\
f(\varphi) &= \frac{\cos \varphi \arccos \left(\frac{\cos \theta_0 - \sin \varphi \sin \varphi_0}{\cos \varphi_0 \cos \varphi} \right)}{\pi^2 \sqrt{(\sin^2 i - \sin^2 \varphi)}} \\
\rho &= \int_{\varphi_1}^{\varphi_2} f(\varphi) d\varphi
\end{aligned} \right\} \quad (3b)$$

V. Numerical Verification

Three sets of tests were performed to verify the algorithm. The first set used circular orbits; the results are shown in Table 1. The second set used elliptic orbits with eccentricity = 0.05; the results are shown in Table 2. The third set used orbits with repeating ground tracks; the results are shown in Table 3. The parameter that measures the accuracy of the model is $\Delta\rho$ (listed in the last column of the tables):

$$\Delta\rho\% = 100 \frac{\rho_{\text{THEORY}} - \rho_{\text{NUMERIC}}}{\rho_{\text{NUMERIC}}}$$

Table 1 lists the 31 cases used in the verification of Eq. (3). The numerical view periods are generated by propagating the orbit using the linear J_2 perturbations. The integral for ρ is evaluated using a mathematical symbolic computation program. The low Earth orbits selected for the verification have various altitudes with inclinations at 28.5, 48, 88.5, 98.5, and 151.5 deg. For those cases with an asterisk in front of the inclination, the orbit propagation begins at the descending node. For all other cases, the orbit propagation begins at the ascending node. The cases in Table 3 use an orbit with repeating ground tracks with a repeat pattern of 20 orbits in 3 days. All other orbits have nonrepeating ground tracks; thus, their periods are incommensurate with that of the period of the Earth's rotation.

The stations at latitudes of 0, 5, and 10 deg have the longitude of the 24-m Goldstone DSN station. The stations at latitudes of -35.4 and 40.4 deg are the 24-m Canberra and Madrid DSN stations, respectively.

The $\Delta\rho$ for the circular orbits of Table 1 are plotted in Fig. 4. It shows the differences between the theoretical and numerical values of ρ for these orbits to be under 0.2 percent, indicating excellent agreement.

Figure 5 plots the $\Delta\rho$ of the circular orbits from Table 1 as a solid curve on top of which the values for the corresponding elliptic orbits from Table 2 have been added. For example, Case E1 and Case 4 in Fig. 5 have the same test parameters except for the orbit eccentricity. By changing the eccentricity of the orbit of Case 4 to 0.05 while keeping all other parameters fixed, $\Delta\rho$ increased from under 0.2 percent to about 1 percent. But for Case 23, the change in eccentricity and the high inclination caused $\Delta\rho$ to exceed 15 percent. This shows that the algorithm does not work as well for elliptic orbits. However, the accuracy may be sufficient for load studies since many of the parameters are even less well known.

Figure 6 plots the $\Delta\rho$ of orbits with repeating ground tracks from Table 3; a single fixed orbit with a repeat pattern of 20 orbits in 3 days is used with different stations for these cases. The difference between the theoretical and numerical values of ρ is still quite good at less than 1.3 percent.

Table 1. Comparison of numerical versus theoretical long-term view period ratio for circular orbits with nonrepeating ground tracks (eccentricity = 0).

Case number ^a	Orbit radius, km	Orbit inclination, deg ^b	Station latitude ^c	Numeric ^d	Theory ^e	Difference ^f	Percentage ^g
1	6578.14	28.5	0.0	0.021014	0.021030	0.000015	0.072847
2	6578.14	28.5	-35.4	0.014719	0.014740	0.000020	0.138198
3	6578.14	28.5	40.4	0.004976	0.004985	0.000009	0.178944
4	7714.14	28.5	0.0	0.154513	0.154505	-0.000008	-0.005178
5	7714.14	28.5	5.0	0.148701	0.148664	-0.000037	-0.024882
6	7714.14	28.5	-35.4	0.085387	0.085383	-0.000004	-0.004685
7	7714.14	28.5	40.4	0.073382	0.073393	0.000011	0.014854
8	7714.14	*28.5	0.0	0.154513	0.154505	-0.000008	-0.005178
9	7714.14	*28.5	-35.4	0.085368	0.085383	0.000015	0.017454
10	7714.14	*151.5	0.0	0.154543	0.154505	-0.000038	-0.024589
11	7714.14	*151.5	-35.4	0.085507	0.085383	-0.000124	-0.145017
12	7714.14	*151.5	40.4	0.073483	0.073393	-0.00009	-0.122614
13	7714.14	151.5	5.0	0.148658	0.148664	0.000006	0.004036
14	7714.14	151.5	-35.4	0.085361	0.085383	0.000022	0.025421
15	7714.14	151.5	40.4	0.073422	0.073393	-0.000029	-0.039498
16	7714.14	48.0	0.0	0.081425	0.081432	0.000007	0.008351
17	7714.14	48.0	5.0	0.082509	0.082453	-0.000056	-0.067993
18	7714.14	48.0	10.0	0.086041	0.086012	-0.000029	-0.033821
19	7714.14	48.0	-35.4	0.100203	0.100189	-0.000014	-0.013972
20	7714.14	48.0	40.4	0.096789	0.0968	0.000011	0.011675
21	7714.14	61.0	0.0	0.067089	0.067078	-0.000011	-0.016424
22	7714.14	61.0	-35.4	0.099756	0.099737	-0.000019	-0.018588
23	7714.14	61.0	40.4	0.102233	0.102237	0.000004	0.003912
24	7714.14	88.5	0.0	0.057763	0.057726	-0.000037	-0.064401
25	7714.14	88.5	-35.4	0.072831	0.07285	0.000019	0.025538
26	7714.14	88.5	40.4	0.079102	0.079127	0.000025	0.031731
27	7714.14	98.5	0.0	0.05849	0.058413	-0.000077	-0.132331
28	7714.14	98.5	-35.4	0.074554	0.074609	0.000055	0.073638
29	7714.14	98.5	40.4	0.081762	0.081743	-0.000019	-0.02385
30	10,000.14	61.0	0.0	0.15332	0.153309	-0.000011	-0.007175
31	10,000.14	61.0	5.0	0.155375	0.155142	-0.000233	-0.14996

^a Circular orbits. All orbits have nonrepeating ground tracks.

^b The * indicates the orbit propagation started at the descending node. All other cases started at the ascending node.

^c The stations with latitudes at 0, 5, and 10 deg have the longitude of the Goldstone station. The station with latitude at -35.4 deg is the Canberra station. The station with latitude at 40.4 deg is the Madrid station.

^d (Total view periods)/(total time), numerically generated using linear J_2 orbit propagation.

^e Limit (total view periods)/(total time), theoretical value.

^f Theory - numeric.

^g (Difference/numeric) × 100.

Table 2. Comparison of numerical versus theoretical long-term view period ratio for elliptical orbits (eccentricity = 0.05).

Case number ^a	Orbit radius, km	Orbit inclination, ^b deg	Station latitude ^c	Numeric ^d	Theory ^e	Difference ^f	Percentage ^g
E1	7714.14	28.5	0.0	0.152476	0.154505	0.002029	1.33082
E2	7714.14	28.5	-35.4	0.086059	0.085383	-0.000676	-0.785138
E3	7714.14	28.5	40.4	0.072582	0.073393	0.000811	1.11773
E4	7714.14	61.0	0.0	0.067196	0.067078	-0.000117	-0.174601
E5	7714.14	61.0	-35.4	0.112791	0.099737	-0.013054	-11.5733
E6	7714.14	61.0	40.4	0.088053	0.102237	0.014184	16.1085
E7	7714.14	88.5	0.0	0.057875	0.057726	-0.000149	-0.256726
E8	7714.14	88.5	-35.4	0.071308	0.072850	0.001542	2.16308
E9	7714.14	88.5	40.4	0.081627	0.079127	-0.002500	-3.0623
E10	10,000.14	28.5	0.0	0.261715	0.261864	0.000149	0.056955
E11	10,000.14	28.5	-35.4	0.173428	0.173361	-0.000067	-0.038629
E12	10,000.14	28.5	40.4	0.158665	0.158644	-0.000021	-0.012950
E13	10,000.14	61.0	0.0	0.153501	0.153308	-0.000193	-0.125588
E14	10,000.14	61.0	-35.4	0.19271	0.18373	-0.008980	-4.65991
E15	10,000.14	61.0	40.4	0.17489	0.184627	0.009736	5.56719

^a Elliptical orbits. All orbits have nonrepeating ground tracks.

^b All cases started at the ascending node.

^c The stations with latitudes at 0, 5, and 10 deg have the longitude of the Goldstone station. The station with latitude at -35.4 deg is the Canberra station. The station with latitude at 40.4 deg is the Madrid station.

^d (Total view periods)/(total time), numerically generated using linear J_2 orbit propagation.

^e Limit (total view periods)/(total time), theoretical value.

^f Theory - numeric.

^g (Difference/numeric) \times 100.

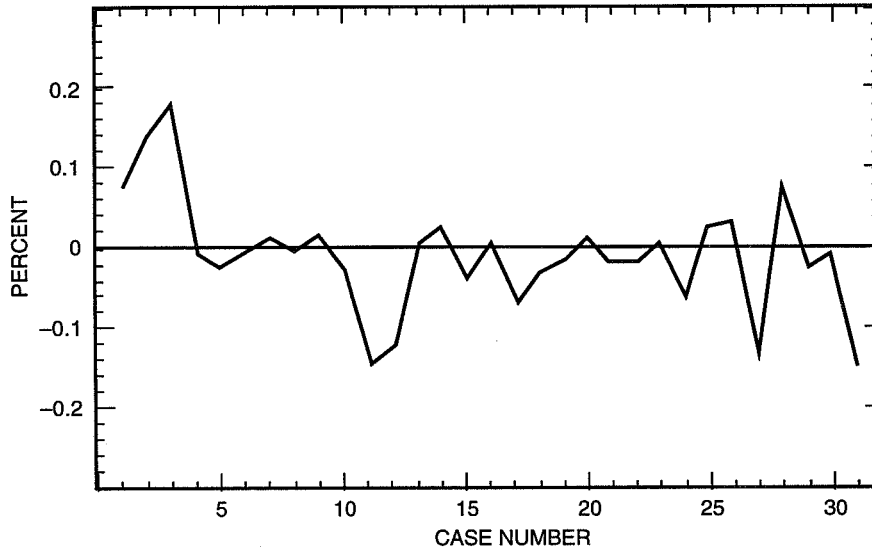


Fig. 4. Difference of theoretical versus numerical long-term view period ratio (all orbits with eccentricity = 0, see Table 1).

Table 3. Comparison of numerical versus theoretical long-term view period ratio for circular orbits with repeating ground tracks (eccentricity = 0).

Case number ^a	Orbit radius, km	Orbit inclination, ^b deg	Station latitude ^c	Numeric ^d	Theory ^e	Difference ^f	Percentage ^g
P1	11889.43	28.5	0.0	0.306147	0.30619	0.000043	0.014046
P2	11889.43	28.5	5.0	0.305175	0.305147	-0.000028	-0.009175
P3	11889.43	28.5	10.0	0.301975	0.301929	-0.000046	-0.015233
P4	11889.43	28.5	28.5	0.258294	0.258513	0.000219	0.084787
P5	11889.43	28.5	-35.4	0.226208	0.224439	-0.001769	-0.782024
P6	11889.43	28.5	-35.4	0.22622	0.224439	-0.001781	-0.787287
P7	11889.43	28.5	40.4	0.204349	0.206974	0.002625	1.284567
P8	11889.43	28.5	40.4	0.204369	0.206974	0.002605	1.274655

^a Circular orbits with a (3/20) repeat pattern (20 orbits in 3 days).

^b All cases started at the ascending node.

^c The stations with latitudes at 0, 5, and 10 deg have the longitude of the Goldstone station. The station with latitude at -35.4 deg is the Canberra station. The station with latitude at 40.4 deg is the Madrid station.

^d (Total view periods)/(total time), numerically generated using linear J_2 orbit propagation.

^e Limit (total view periods)/(total time), theoretical value.

^f Theory - numeric.

^g (Difference/numeric) × 100.

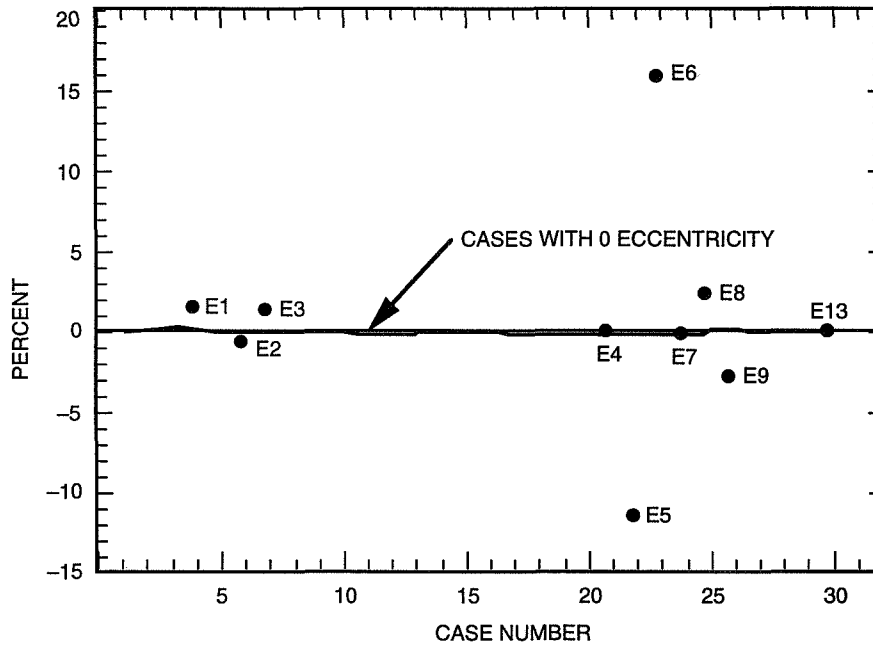


Fig. 5. Comparison of circular and elliptical orbits: difference of theoretical versus numerical long-term view period ratio (see Table 2).

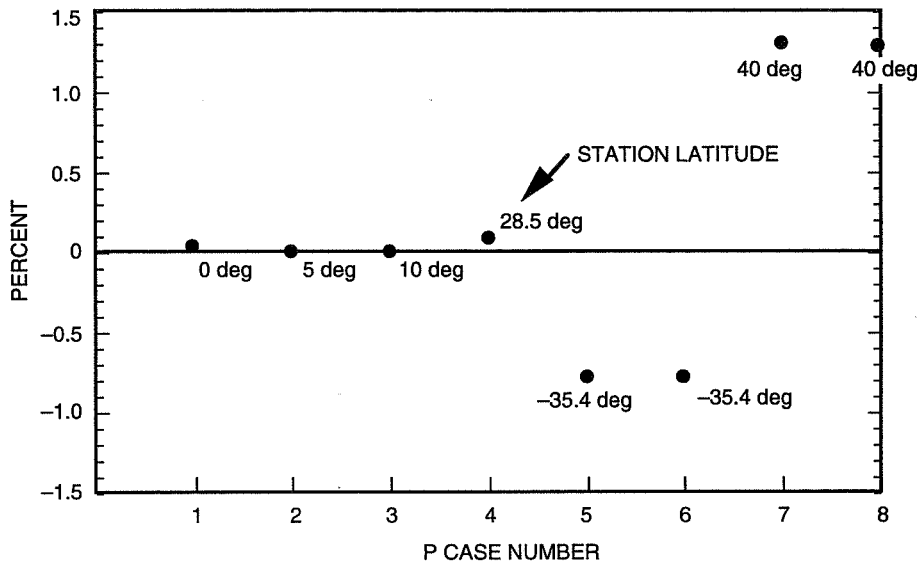


Fig. 6. Difference of theoretical versus numerical long-term view period ratio for orbits with repeating ground tracks (see Table 3).

These results indicate that putting the circular orbit at different inclinations, altitudes, and nodes does not greatly affect the agreement between the numerical and theoretical values for the view period ratio, ρ . The errors are all within 0.15 percent. The error goes up by a factor of 10 when the orbit ground tracks are repeating, but a fairly good agreement is retained.

VI. Applications

The definite integral for ρ is easily integrated using a mathematical symbolic computation program, each case requiring seconds. As mentioned before,

$$\rho T = \text{total view periods during elapsed time } T$$

is a good estimate of the total station view period. Thus,

$$\rho \text{ 24 hr} = \text{average daily total view periods}$$

$$\rho \text{ 7 days} = \text{average weekly total view periods}$$

and so on are some useful numbers that are very easy to compute.

Now consider a more interesting problem. Suppose one has a spacecraft and K ground stations. Compute ρ for each station: $\rho_1, \rho_2, \dots, \rho_K$. Suppose the spacecraft requires τ sec daily for downlink using these stations. The following sum represents the maximum average contact time possible with the K ground stations:

$$C = (\rho_1 + \rho_2 + \dots + \rho_K) \text{ 24 hr}$$

If $\tau > C$, then it means there is not enough contact time on the average for the spacecraft to downlink its data. But if $\tau < C$, one cannot say very much since the overlaps between the ground stations are not known. However, if, for example, $\tau/C < 0.5$, then it seems very likely the ground stations will be able to satisfy the downlink requirement. One can look at the geometry of the overlap of the station masks to further refine this approximation.

This approach gives a very quick way to bound performance. One can consider other scenarios of N spacecraft with K stations and so on. This would be a good capability to place into a spreadsheet program to provide quick estimates for what-if studies. It also has the advantage that the theoretical basis of the method is well understood so that one need not have that uncomfortable feeling that frequently accompanies statistical analyses not as well understood.

Another application is the performance measure for the location of ground stations. The definite integral, ρ , provides a quantitative measure of the well-known observation that ground stations at higher latitudes generally have more and longer view periods.

These applications require further refinement but indicate the type of calculations possible with this approach.

VII. Discussion

The circularity of the orbits is not as severe a restriction in applications since, according to Negron et al. [5], roughly 75 percent of the Earth spacecraft orbits have eccentricity < 0.05 . The sensitivity of the integral in Eq. (3) to eccentricity needs to be determined to see if it can be applied to orbits with lower (but nonzero) eccentricity. With elliptic orbits, the motion of the argument of perigee causes the geometry to change with time, which complicates the situation considerably. The extension of the theory to elliptic orbits is under study. The basic approach may be used, but the problem is more difficult and additional analysis is required to construct the function $F(x)$ and the measure μ .

The period noncommensurability requirement appears to be restrictive, since orbits with repeating ground tracks are very useful and popular. However, as Cases 26 to 33 show, the same integral provides a fairly good estimate of ρ to within 1.3 percent. In fact, for stations at low latitudes, the estimate is good to within 0.015 percent. This seemed surprising at first; but when one considers the fact that any orbit can be approximated by one with repeating ground tracks to an arbitrary degree of precision, it seems less surprising. Also, the number of different view periods of orbits with repeating ground tracks is finite and can easily be determined numerically. Of course, for orbits that are geosynchronous, this integral does not make sense at all. But the view periods for such orbits are trivial. Additional analysis is required to determine the limits of applicability of the integral to orbits with periodic ground tracks.

The integral for ρ , Eq. (3), depends on the following parameters only: $\{R_E, R, i, \phi_0\}$, which are the Earth radius, spacecraft orbit radius and inclination, and the station latitude. The station longitude, the orbit node, and J_2 do not appear in the equation. Since this is an averaging process, the absence of the station longitude and orbit node is reasonable. These two parameters should simply average out in the long term. The absence of J_2 is surprising. But, it is actually hidden in the requirement that the orbit period be incommensurate with that of the rotation period of the Earth. And it is not so surprising in light of the Ergodic Theorem, which states that the details of the dynamics such as rates and the equations of motion that appear on the time-mean side of Eq. (3) can be replaced with an area integral on the space-mean side of Eq. (3). Thus, J_2 and other dynamic quantities appear only in the time mean but not in the space mean.

The tests described in Table 1 and in Section V above indicate an excellent agreement between the numerically computed values for ρ and those computed from Eq. (3). However, additional numerical results are also needed to further substantiate the theoretical results and scope the limits of applicability.

Work continues on this approach to analyze station load forecasts. The extension of the integral to elliptic orbits is highly desirable. Other dynamical systems methods can be used to refine the forecasts, giving statistical data of more resolution than the mean. These are also being explored.

Acknowledgments

The author would like to thank Johnny H. Kwok and Steven Matousek of JPL for bringing this problem to his attention; Lawrence E. Bright, Jeff A. Estefan, David L. Farless, Johnny H. Kwok, and Mark A. Vincent of JPL for the invaluable input and review of this article; and Professors H. B. Keller and S. Wiggins of the California Institute of Technology for several useful discussions. The author would also like to thank Charles D. Edwards and Vincent Pollmeir for their support. In particular, the author would like to thank Warren L. Martin of JPL for his strong support, which made this work possible.

References

- [1] V. I. Arnold, *Ergodic Problems of Classical Mechanics*, New York: Addison-Wesley, 1989.
- [2] I. E. Farquhar, *Ergodic Theory in Statistical Mechanics*, New York: John Wiley & Sons, 1964.
- [3] K. Petersen, *Ergodic Theory*, Cambridge, England: Cambridge University Press, 1983.
- [4] V. I. Arnold, *Geometrical Methods in the Theory of Ordinary Differential Equations*, New York: Springer-Verlag, 1983.
- [5] D. Negron, Jr., S. Alfano, and D. Wright III, "The Method of Ratios," *Journal of the Astronautical Sciences*, vol. 40, no. 2, pp. 297–309, April–June 1992.

1995108208

N95-14622

5-74
19780

TDA Progress Report 42-118

324451

August 15, 1994

281

The Stark Anomalous Dispersion Optical Filter: The Theory

B. Yin and T. M. Shay
New Mexico State University, Las Cruces, New Mexico

The Stark anomalous dispersion optical filter is a wide-frequency-tunable ultra-narrow-bandwidth optical filter. The first theoretical investigation of this filter matched to the wavelength of a doubled Nd:YAG laser is reported. The calculations show that such a filter may provide above 80 percent transmission, and a noise equivalent bandwidth of 3 GHz.

I. Introduction

In a deep space laser communication system, a doubled Q-switched Nd:YAG laser is a potential laser transmitter. At the receiver end, in addition to a very weak signal with a large Doppler frequency shift (up to ± 77 GHz, typical for the Mars orbital missions); a considerable amount of background noise (sun, sunlit Earth, etc.) is expected within the field of view of the receiver. A high-sensitivity and high background-noise-rejection optical filter with wide-frequency tunability around the doubled Nd:YAG laser emission can simultaneously track Doppler frequency shifts and reject intense background radiation. The Stark anomalous dispersion optical filter (SADOF) is designed to provide high background noise rejection and wide frequency tunability and to operate at the wavelength of the doubled Nd lasers [1,2]. The SADOF is similar to our previously reported nontunable Faraday anomalous dispersion optical filter (FADOF) [3-5]. It may be considered as simply an addition of an electric field and optical pumping to the FADOF. In the following sections, the basic design and theoretical calculations are presented, the issues of shifting the SADOF center frequency using the Stark effect are investigated, and the calculation results for the SADOF operating at the doubled Nd:YAG laser line are discussed. These results have been used to direct the thrust of the experimental design.

II. Basic Design

Like the FADOF, the SADOF has a longitudinal magnetic field to induce the polarization rotation due to the resonant Faraday effect. However, in addition, the SADOF has an external electric field to shift the energy levels of the atoms. To use the resonant Faraday effect, an atomic transition that matches the Nd laser lines is required. To have a large energy level shift that results in a filter center frequency shift, a large scalar polarizability for an energy level in the filter transition is desired. Alkali atoms have large scalar polarizabilities, and the candidate transitions appropriate for doubled Nd laser lines are summarized in Table 1. For the transitions in Table 1, the lower states are the first or second excited states of the atoms, and the upper states are higher lying states. Since the lower-level state of the filter transition is not the ground state, optical pumping to populate the lower-level state is required

for filter operation at those transitions. The scalar polarizability is determined by examining the Stark Hamiltonian for the interaction between an atom and an electric field ε , which is

$$H_e = -\varepsilon(\mathbf{p}) \quad (1)$$

where \mathbf{p} is the induced dipole moment. For alkali elements, the perturbation of electrons in the closed shells may be neglected; then \mathbf{p} is given by

$$\mathbf{p} = -e\mathbf{r} \quad (2)$$

where \mathbf{r} is the position vector of the valence electron, and e is the electron charge. The high-lying states have much larger $\langle \mathbf{r} \rangle$, therefore, much stronger Stark interaction, or larger polarizabilities. Because the upper levels of the SADOE transitions in Table 1 are high-lying levels, their polarizabilities are large. For example, the scalar polarizability of the Rb(10S) state is about $280 \text{ MHz}/(\text{kV}/\text{cm})^2$, while the scalar polarizability of the Rb(5P) state is only about $0.2 \text{ MHz}/(\text{kV}/\text{cm})^2$.

Table 1. Potential SADOE lines in alkali vapors.

Transition	Wavelength (in air), nm	Compatible doubled Nd laser	Laser wavelength (air $T = 300 \text{ K}$), nm
Rb $5P_{1/2}-8D_{3/2}$	536.26	YALO	536.45
Rb $5P_{3/2}-9D_{5/2}$	526.00	YLF	526.5
Rb $5P_{1/2}-10S_{1/2}$	532.24	YAG	532.07 ^a
Rb $5P_{3/2}-10S_{1/2}$	539.06	BEL	539.5
		YALO	539 \pm 1
Rb $5P_{3/2}-11S_{1/2}$	523.39	YLF	523.6
K $4P_{3/2}-6D_{5/2}$	535.96	YALO	536.45
K $4P_{1/2}-8S_{1/2}$	532.32	YAG	532.07 ^a
Cs $6P_{3/2}-13D_{5/2}$	535.04	BEL	535.05

^a Nd:YAG laser needs to be heated to about 100–150 deg C for the wavelength to match the filter.

Because the Rb 532-nm transition is the closest transition to the strongest line of doubled Nd:YAG laser, we discuss the Rb 532-nm SADOE Rb ($5P_{1/2}-10S_{1/2}$) in this article. The basic structure for an Rb 532-nm SADOE that operates at the doubled Nd:YAG laser line is shown in Fig. 1. An Rb vapor cell is placed between two crossed polarizers under the external longitudinal magnetic field and transverse electric field. The optical pumping is applied from one end of the cell. The colored-glass filter is used to ensure that the infrared pump radiation does not reach the photodetector.

III. The Energy Hamiltonian in the Presence of Magnetic and Electric Fields

When an electric field is applied to an atom, it shifts the electronic energy levels. This is known as the Stark effect, and the energy level shift is quadratically dependent on the electric field strength. The effective Hamiltonian element for the energy shift can be expressed as

$$\langle IJFM | H_e | IJF'M' \rangle = -\frac{1}{2}(\alpha_0 \delta_{FM, F'M'} + \alpha_2 Q_{FF', MM'}) \varepsilon^2 \quad (3)$$

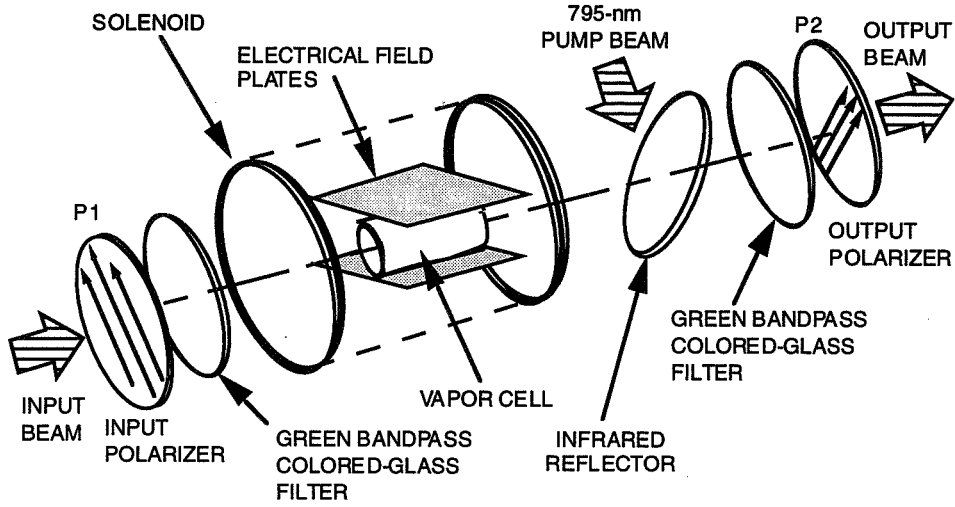


Fig. 1. The basic structure of an Rb 532-nm SADOF.

where $J, I, F = J + I$, and M are the quantum numbers for the total orbital angular momentum, the nuclear spin, the total angular momentum, and the projection of total angular momentum, respectively. The values of α_0 and α_2 are the scalar and tensor polarizabilities, respectively. The delta function $\delta_{FM, F'M'}$ is unity only if $F = F'$ and $M = M'$; otherwise it is zero. The quadrupole matrix element between hyperfine states is $Q_{FF', MM'}$ [6], and its values are dependent on the quantum numbers of the sublevels. The $\delta_{FM, F'M'}$ weighting of α_0 in Eq. (3) shows that the change in energy level associated with the scalar polarizability term is common to all sublevels of a state, whereas the energy change associated with a tensor polarizability term differs for the various sublevels because of the $Q_{FF', MM'}$ factor. Because of the large scalar polarizability of the high-lying Rb $10S_{1/2}$ state, the energy level, i.e., frequency, of the optical transition can be shifted over a very large range using reasonable electric field strengths. The tensor polarizability is zero for all $J = 1/2$ states; hence, α_2 for the $10S_{1/2}$ and $5P_{1/2}$ states is zero.

Like the FADOF theory, the theory for the transmission of the Rb 532-nm SADOF begins by constructing the energy Hamiltonian. Assuming the Stark splitting is small compared with the fine structure, the element of the total energy Hamiltonian in the presence of an external electric field and magnetic field for the Rb 532-nm SADOF is given by

$$\begin{aligned}
 \langle IJFM | H | IJF'M \rangle &= \{hyperfine\ energy\} + \{Stark\ energy\} + \{magnetic\ energy\} \\
 &= \Delta E_F \delta_{F, F'} - \frac{1}{2} \alpha_0 \epsilon^2 \delta_{F, F'} + \left\{ \mu B_z (-1)^{M+J-1+I} g_J \right. \\
 &\quad \left. \times \sqrt{J(J+1)(2J+1)(2F+1)(2F'+1)} \begin{Bmatrix} J & 1 & J \\ F' & 1 & F \end{Bmatrix} \begin{pmatrix} F & 1 & F' \\ -M & 0 & M \end{pmatrix} \right\} \quad (4)
 \end{aligned}$$

where ΔE_F is the hyperfine energy shift caused by nuclear spin and is not influenced by external fields [5], μ is the Bohr magneton, B_z is the external magnetic field, and g_J is the Lande g factor that depends on J . The 6-j symbol (enclosed by the curly brackets) and the 3-j symbol (enclosed by the parentheses) are matrix representations of the spherical coordinate components of the electron wave function for the single atom. The hyperfine energy term and the magnetic energy term are exactly the same as in the FADOF theory. Since the tensor polarizability is zero for $J = 1/2$, the only effect of the electric field in the Rb 532-nm SADOF is to shift the center of gravity of an atomic energy level. Therefore, the atomic

transition intensities and polarization rotation calculations are the same as for the FADOF model, except that the atomic number density of the transition lower energy level will depend on the optical pumping. An energy level diagram depicting the Rb 532-nm SADOFF pumping is shown in Fig. 2.

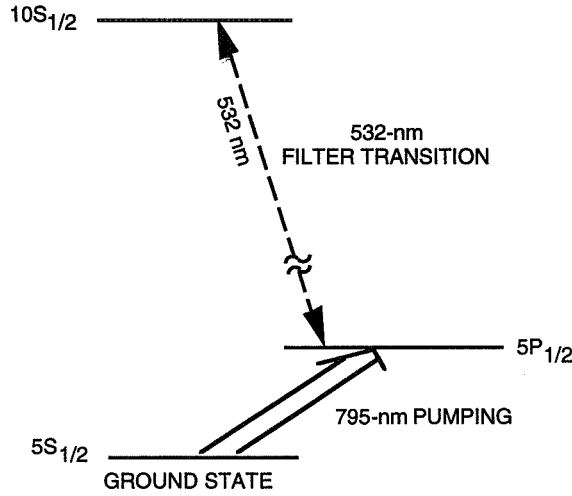


Fig. 2. A simplified Rb 532-nm SADOFF energy-level diagram.

Optical pumping is key to SADOFF operation. Significant transmission of the signal radiation is achieved only if the lower level atomic state $5P_{1/2}$ of the filter transition is sufficiently populated. We have developed a simple model to predict the required optical pumping. In this, our first SADOFF design, we have tailored the filter parameters to achieve operation at reasonable optical pumping powers and operating temperatures. Our analysis predicts that a 10-cm-long cell operating at a temperature of 190 deg C and pumped by 200 mW of optical power can demonstrate filter performance.

IV. SADOFF Transmission

To predict the SADOFF performance, the energy Hamiltonian, the hyperfine transition frequencies and line strengths, and the complex refractive indices need to be determined. The complex refractive indices are used to calculate the optical polarization rotation and absorption, and hence the filter transmission. This has been shown in our previous Rb FADOF articles [3–5]. The following is a brief summary of the equations necessary to predict the filter performance. The polarization rotation angles can be determined from complex refractive indices,

$$\phi(\omega) = \left(\frac{\omega L}{2c}\right) \text{Re}[\tilde{n}_+(\omega) - \tilde{n}_-(\omega)] \quad (5)$$

where \tilde{n}_{\pm} is the complex refractive index for the two circular polarizations, L is the cell length, and c is the speed of light. The absorption coefficient is given by

$$k_{\pm}(\omega) = \left(\frac{2\omega}{c}\right) \text{Im}[\tilde{n}_{\pm}(\omega)] \quad (6)$$

The transmission of the SADOFF filter is

$$T(\omega) = \frac{1}{4} \left\{ \exp[-k_+(\omega)L] + \exp[-k_-(\omega)L] - 2 \cos[2\phi(\omega)] \exp\left[-\frac{k_+(\omega) + k_-(\omega)}{2}L\right] \right\} \quad (7)$$

The equivalent noise bandwidth (ENBW) is expressed as

$$ENBW = \frac{1}{T_{max}} \int_0^{\infty} T(\omega) d\omega \quad (8)$$

where $T(\omega)$ represents the filter transmission spectrum, and T_{max} represents the maximum transmission for the filter. The equivalent noise bandwidth corresponds to the bandwidth of a rectangular notch filter with transmission T_{max} that transmits the same amount of noise as our filter. The equivalent noise bandwidth provides a ready comparison of different filter designs and even different kinds of optical filters.

V. Results and Discussion

A. Rotation and Transmission Spectrum

The SADOFF transmission spectrum was calculated using the equations presented in the previous sections. Figures 3 and 4 show the SADOFF rotation and transmission spectrum for a filter operating at a temperature of 190 deg C with 200 mW optical pumping, and in a magnetic field of 700 G.

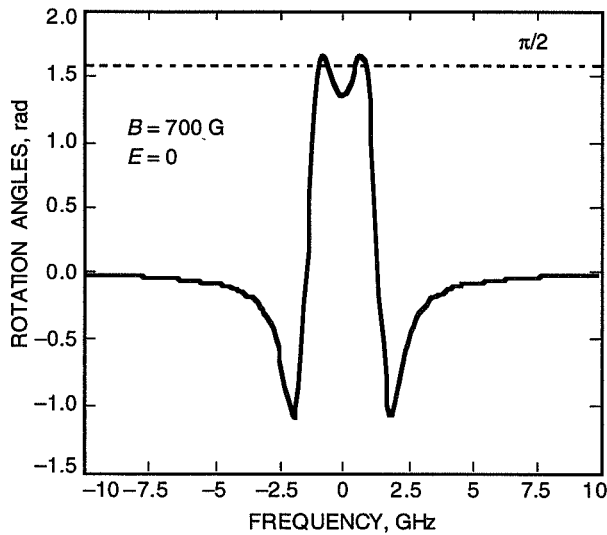


Fig. 3. Rb 532-nm SADOFF rotation angles versus frequency at $T = 190$ deg C and $B = 700$ G, where the horizontal axis is normalized to the frequency shift from the Rb 532-nm transition.

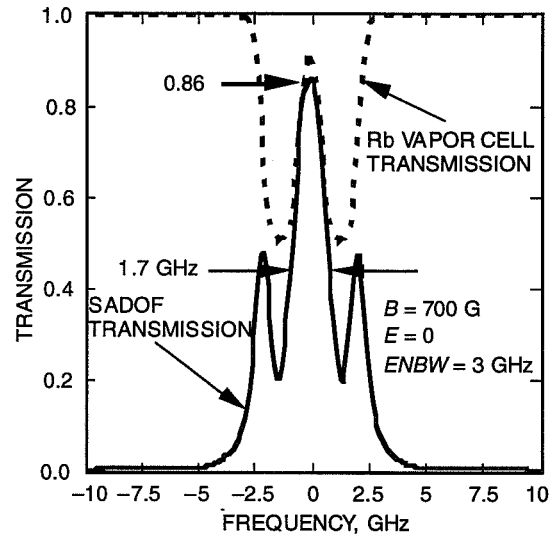


Fig. 4. Rb 523-nm SADOFF transmission spectrum at $T = 190$ deg C, $B = 700$ G, and $E = 0$ kV/cm, where the horizontal axis is normalized to the frequency shift from the 532-nm transition.

As in the FADOFF, the peak transmission occurs just outside the resonance absorption band where the rotation angle is nearly $-\pi/2$. Under these operating conditions, the SADOFF has a peak transmission of about 0.86, a 1.7-GHz bandwidth across the principal transmission peak, and equivalent noise bandwidth of 3.0 GHz.

The SADOFF center frequency is tuned by varying the electric field. Figure 5 shows the predicted E-field frequency shift of the SADOFF transmission spectrum. The filter is in a 20-kV electric field, and the transmission spectrum is red-shifted about 55 GHz without any degradation in filter performance.

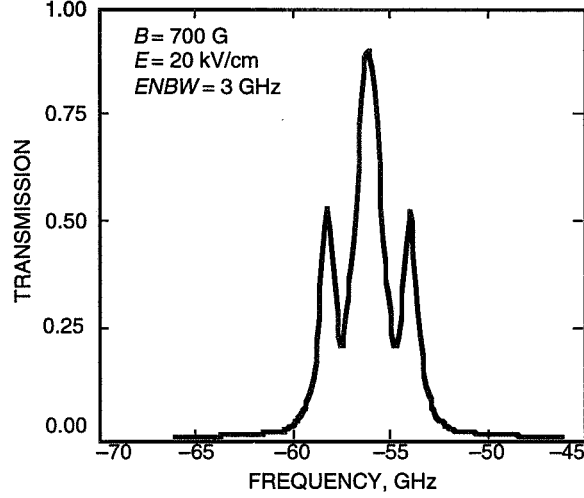


Fig. 5. Rb 532-nm SADOE transmission spectrum at $T = 190$ deg C, $B = 700$ G, and $E = 20$ kV/cm.

B. Frequency Tunability

Because the scalar polarizability in the upper energy level is much larger than the scalar polarizability in the lower level, the upper energy-level shifts determine to a good approximation the Rb 532-nm transition center frequency shift. Therefore, the filter center frequency shift depends quadratically on the electric field,

$$\Delta\nu = -\frac{1}{2}\alpha_0(10S_{1/2})\epsilon^2 - \left[-\frac{1}{2}\alpha_0(5P_{1/2})\epsilon^2 \right] \approx -\frac{1}{2}\alpha_0(10S_{1/2})\epsilon^2 \quad (9)$$

The calculated center frequency shift of the filter passband versus the electric field is plotted in Fig. 6. It shows that the center frequency is shifted by about 250 GHz, or 0.25 nm by a 40-kV/cm field.

C. Optimized Operating Conditions

Figure 7 gives a series of transmission curves with different operating conditions. These curves are for different B-fields and temperatures and can be used to tailor the SADOE performance to the specific application based on the ENBW and peak transmission requirements.

This figure is calculated for a zero electric field since adding the electric field only tunes the center frequency. These curves also demonstrate that the bandwidth of the transmission can be varied by changing the magnetic field and the temperature.

D. Noise Leakage From Adjacent Filter Lines

The nearest green transition for the Rb 532-nm SADOE is the Rb ($5P_{1/2}-8D_{3/2}$) 536.3-nm transition. This transition can contribute a background noise component to the Rb SADOE. However, radiation from this and other Rb green transitions can be suppressed by using a commercial interference filter ($BW \approx 6$ nm) as a prefilter. The transition probability of Rb $5P_{1/2}-8D_{3/2}$ is seven times larger than the Rb $5P_{1/2}-10S_{1/2}$; the equivalent noise bandwidth of the $5P_{1/2}-8D_{3/2}$ transition is much larger than that of the $5P_{1/2}-10S_{1/2}$. The calculated ENBW for the Rb $5P_{1/2}-8D_{3/2}$ transition at a temperature of 190 deg C and a magnetic field of 700 G is 8 GHz. A lower ENBW (~ 3 GHz) can be achieved by using a narrower bandpass prefilter.

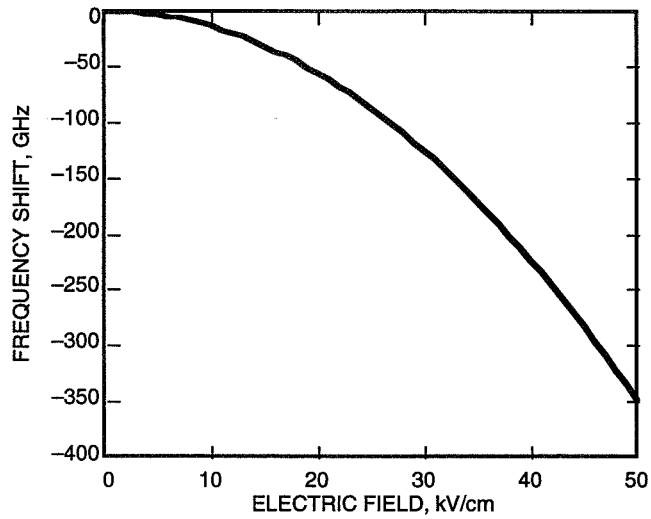


Fig. 6. Rb 532-nm SADOF center frequency versus external electric field.

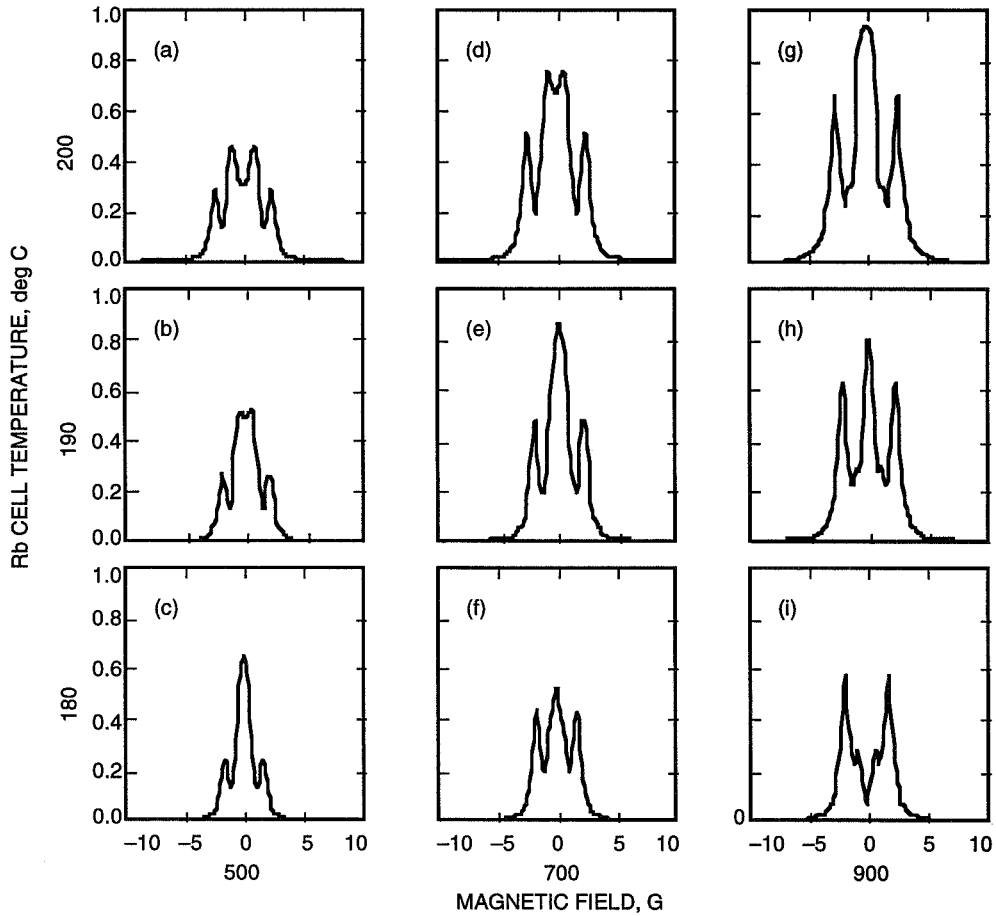


Fig. 7. Rb 532-nm SADOF transmission spectrum at $E = 0$ and at (a) 500 G, 200 deg C, $ENBW = 3.9$ GHz; (b) 500 G, 190 deg C, $ENBW = 3.2$ GHz; (c) 500 G, 180 deg C, $ENBW = 2.0$ GHz; (d) 700 G, 200 deg C, $ENBW = 4.2$ GHz; (e) 700 G, 190 deg C, $ENBW = 3.0$ GHz; (f) 700 G, 180 deg C, $ENBW = 3.2$ GHz; (g) 900 G, 200 deg C, $ENBW = 4.0$ GHz; (h) 900 G, 190 deg C, $ENBW = 3.4$ GHz; and (i) 900 G, 180 deg C, $ENBW = 3.0$ GHz.

VI. Conclusions

The first theoretical model for calculating the performance of the SADOFF is developed. The operating conditions for a 532-nm SADOFF are determined. The filter is compatible with the strongest line of a frequency-doubled Nd:YAG laser. The results show that the SADOFF can provide very narrow bandwidth, high transmission, low equivalent noise bandwidth, and, most of all, can be tuned over a very large frequency range (250 GHz at $E = 40$ kV/cm). The SADOFF is a good candidate for a filter in the deep space laser communications using a doubled Nd:YAG laser as a source.

Acknowledgments

The authors wish to thank Drs. K. Wilson and J. R. Lesh in the JPL Optical Communications Group for reviewing this work.

References

- [1] B. Yin and T. M. Shay, "Theoretical Model for a Stark Anomalous Dispersion Optical Filter," *Proc. Laser '92*, Houston, Texas, pp. 837-843, December 1992.
- [2] B. Yin and T. M. Shay, "A Rb 532 nm Stark Anomalous Dispersion Optical Filter for Doubled Nd:YAG Lasers," *Proc. LEOS '93*, San Jose, California, pp. 359-360, November 1993.
- [3] D. J. Dick and T. M. Shay, "Ultra-High Noise Rejection Optical Filter," *Opt. Lett.*, vol. 16, p. 867, June 1991.
- [4] B. Yin and T. M. Shay, "Theoretical Model of Faraday Anomalous Dispersion Optical Filter," *Opt. Lett.*, vol. 16, pp. 1617-1619, October 1991.
- [5] B. Yin, L. S. Alvarez, and T. M. Shay, "The Rb 780-Nanometer Faraday Anomalous Dispersion Optical Filter: Theory and Experiment," *The Telecommunications and Data Acquisition Progress Report 42-116*, vol. October-December 1993, Jet Propulsion Laboratory, Pasadena, California, pp. 71-85, February 15, 1994.
- [6] H. L. Zhou and B. W. Norcross, "Improved Calculation of the Quadratic Stark Effect in the 6P_{3/2} State of Cs," *Phys. Rev. A*, vol. 40, no. 9, pp. 5048-5051, November 1989.

Convolutional Encoding of Self-Dual Block Codes (II)

G. Solomon¹Y. Jin²

Solomon and van Tilborg [2] have developed convolutional encoding algorithms for quadratic residue (QR) codes of lengths 48 and beyond. For these codes and reasonable constraint lengths, there are sequential decodings for both hard and soft decisions. There are also Viterbi type decodings that may be simple, as in a convolutional encoding/decoding of the extended Golay Code. In addition, the previously found constraint length $K = 9$ for the $(48, 24; 12)$ QR code was lowered to $K = 8$ by Solomon [1]. In our search for the smallest possible constraint lengths K for $(80, 40; 16)$ self-dual quadratic residue and nonquadratic residue codes, we have found the constraint lengths $K = 14$ and $K = 13$, respectively. We have discovered a $K = 21$ convolutional encoding for the $(104, 52; 20)$ QR code; there may be a smaller K for a $(104, 52; 20)$ self-dual code that is not a quadratic residue code. The smaller the K , the less complex the sequential or Viterbi decoder.

I. $(80, 40; 16)$ QR Code

The vector (c_i) is a codeword of the $(79, 40; 15)$ QR code generated by check polynomial $g(x) = x^{40} + x^{39} + x^{37} + x^{35} + x^{32} + x^{29} + x^{28} + x^{24} + x^{22} + x^{18} + x^{17} + x^{16} + x^{15} + x^{13} + x^{12} + x^{11} + x^6 + x^4 + x^3 + 1$, where

$$c_i = 1 \text{ for } i = 0, 1, 14, 15, 24, 30, 34, 35, 37, 39, 41,$$

$$43, 47, 53, 57, 58, 61, 66, 68, 69, 70, 71, 74$$

$$c_i = 0 \text{ otherwise}$$

Let

¹ Independent consultant to the Communications Systems Research Section.

² Student at the California Institute of Technology, Pasadena, California.

$$f_i^{(1)} = c_{1 \times 44^i}$$

$$f_i^{(2)} = c_{3 \times 44^i} \text{ for } i = 0, 1, \dots, 38$$

Then

$$f^{(1)}(x) = 1$$

$$\begin{aligned} f^{(2)}(x) = & x + x^2 + x^3 + x^6 + x^8 + x^{10} + x^{11} + x^{14} \\ & + x^{15} + x^{17} + x^{19} + x^{21} + x^{22} + x^{23} + x^{25} + x^{26} \\ & + x^{27} + x^{28} + x^{30} + x^{32} + x^{33} \end{aligned}$$

Since

$$f^{(2)}(x) = \frac{x^d q(x)}{p(x)} \pmod{x^{39} + 1}$$

where

$$q(x) = 1 + x^2 + x^4 + x^5 + x^{11} + x^{12} + x^{13}$$

$$p(x) = 1 + x + x^2 + x^8 + x^9 + x^{11} + x^{13}$$

$$d = 27$$

$$\gcd(p(x), x^{39} + 1) = 1$$

$$K = 14$$

By previous results in Solomon and van Tilborg [2], we can use $p(x)$ and $q(x)$ as taps in the convolutional encoder with the tail biting sequence of information of length 39. Appending the overall parity checks to the length 39 parity sequences and then adding the 40th information bit to the $p(x)$ sequence gives us the appropriate QR code. We have thus found an encoding with constraint length $K = 14$.

II. (80, 40; 16) Non-QR Code

On the other hand, let us use as the encoding taps the following polynomials in the convolutional encoder:

$$p(x) = 1 + x + x^2 + x^4 + x^5 + x^{10} + x^{12}$$

$$q(x) = 1 + x^2 + x^7 + x^8 + x^{10} + x^{11} + x^{12}$$

$$K = 13$$

Adjoining the parity checks to the parity sequences and then adding the 40th information bit to the $p(x)$ sequence as in Solomon [1], we construct a self-dual (80, 40; 16) block code. The minimum distance is verified by computer simulation. This code may not be the QR code.

III. (104, 52; 20) QR Code

The vector (c_i) is a codeword of the (103, 52; 19) QR code generated by check polynomial $g(x) = x^{52} + x^{51} + x^{50} + x^{48} + x^{45} + x^{42} + x^{38} + x^{37} + x^{36} + x^{35} + x^{33} + x^{28} + x^{27} + x^{26} + x^{21} + x^{17} + x^{16} + x^{12} + x^{10} + x^8 + x^4 + x^3 + x^2 + 1$, where

$$c_i = 1 \text{ for } i = 0, 1, 6, 10, 11, 12, 31, 37, 39, 43, 45, 47, 48, 53, 54, 73, 75, 85, 87, 88, 89, 99, 101$$

$$c_i = 0 \text{ otherwise}$$

Let

$$f_i^{(1)} = c_{1 \times 2^i}$$

$$f_i^{(2)} = c_{3 \times 2^i} \text{ for } i = 0, 1, \dots, 50$$

Then

$$f^{(1)}(x) = 1$$

$$f^{(2)}(x) = x + x^2 + x^4 + x^6 + x^7 + x^8 + x^{10} + x^{12} + x^{19} + x^{21} + x^{26} \\ + x^{29} + x^{30} + x^{31} + x^{36} + x^{38} + x^{43} + x^{44} + x^{46} + x^{48} + x^{50}$$

Since

$$f^{(2)}(x) = \frac{x^d q(x)}{p(x)} \pmod{x^{51} + 1}$$

where

$$q(x) = 1 + x^4 + x^5 + x^9 + x^{10} + x^{12} + x^{15} + x^{16} + x^{17} + x^{19} + x^{20}$$

$$p(x) = 1 + x + x^3 + x^4 + x^5 + x^8 + x^{10} + x^{11} + x^{15} + x^{16} + x^{20}$$

$$d = 30$$

$$\gcd(p(x), x^{51} + 1) = 1$$

$$K = 21$$

By Solomon and van Tilborg [2], we can use $p(x)$ and $q(x)$ above in the convolutional encoder. We have thus found an encoding with constraint length $K = 21$.

IV. Further Problems

- (1) For any $(2n + 2, n + 1)$ QR code, does there exist a polynomial $f(x)$ such that 1 and $f(x)$ can be used as taps in the encoder?
- (2) If (1) is true, do there exist a polynomial $p(x)$ and integer d with $\gcd(p(x), x^n + 1) = 1$ such that $f(x) \equiv (x^d q(x)/p(x)) \pmod{x^n + 1}$, where $q(x) = x^{\deg(p(x))} p(1/x)$?
- (3) If (2) is true, find the smallest K with $\deg(p(x)) = K - 1$.
- (4) If (2) is done, is there any non-QR $(2n + 2, n + 1)$ code that can be generated by some $p'(x)$ and $q'(x)$ with $\gcd(p'(x), x^n + 1) = 1$ and $\deg(p'(x)) \leq K - 1$?

References

- [1] G. Solomon, "Convolutional Encoding of Self-Dual Codes," *The Telecommunications and Data Acquisition Progress Report 42-116*, vol. October-December 1993, Jet Propulsion Laboratory, Pasadena, California, pp. 110-113, February 15, 1994.
- [2] G. Solomon and H. C. A. van Tilborg, "A Connection Between Block and Convolutional Codes," *Siam. J. Appl. Math.*, vol. 37, no. 2, pp. 358-369, October 1979.
- [3] R. W. D. Booth, M. A. Herro, and G. Solomon, "Convolutional Coding Techniques for Certain Quadratic Residue Codes," *Proceedings of the International Telemetry Conference (XI)*, Silver Springs, Maryland, 1975.

9/72
19782
A-11

1995108210
324453
llp

N95-14624

TDA Progress Report 42-118

August 15, 1994

Spin Glasses and Error-Correcting Codes

M. L. Belongie

Communications Systems Research Section

In this article, we study a model for error-correcting codes that comes from spin glass theory and leads to both new codes and a new decoding technique. Using the theory of spin glasses, it has been proven that a simple construction yields a family of binary codes whose performance asymptotically approaches the Shannon bound for the Gaussian channel. The limit is approached as the number of information bits per codeword approaches infinity while the rate of the code approaches zero. Thus, the codes rapidly become impractical. We present simulation results that show the performance of a few manageable examples of these codes.

In the correspondence that exists between spin glasses and error-correcting codes, the concept of a thermal average leads to a method of decoding that differs from the standard method of finding the most likely information sequence for a given received codeword. Whereas the standard method corresponds to calculating the thermal average at temperature zero, calculating the thermal average at a certain optimum temperature results instead in the sequence of most likely information bits. Since linear block codes and convolutional codes can be viewed as examples of spin glasses, this new decoding method can be used to decode these codes in a way that minimizes the bit error rate instead of the codeword error rate. We present simulation results that show a small improvement in bit error rate by using the thermal average technique.

I. Introduction

In a 1989 article in *Nature* [2], Nicolas Surlas claimed that by using an Ising spin glass model he could construct a family of error-correcting codes whose performance asymptotically approached the Shannon coding bound. In 1993, Pal Rujan proposed an idea in *Physical Review Letters* [6] for decoding spin glass codes with a lower resulting bit error rate than could be obtained by finding the most likely codeword, and claimed that the method could also be used for convolutional codes. In this article, we study both of these claims.

This article is organized as follows: In Section II, we introduce Ising spin glasses, which are just collections of particles with spin ± 1 . We also briefly discuss the associated concepts of energy, thermal equilibrium, ground states, magnetization, phase transitions, and gauge invariance. In Section III, we explain the connection between Ising spin glasses and binary error-correcting codes on an additive white Gaussian noise channel. As an example, we will show that spin glasses with a certain type of interactions are equivalent to convolutional codes. We show in Section IV how the physical properties of spin glasses can be used to prove that a family of error-correcting codes based on spin glasses has a bit error rate

approaching zero while the rate approaches the Shannon capacity. Although the construction is simple, it will be clear that the codes rapidly grow too large to be practical. In Section V, we present simulation results that show the performance of a few manageable examples of these codes. Here, decoding is done by finding the ground state of a spin glass, which corresponds to finding the most likely codeword.

In Section VI, we consider a different decoding technique, based on the concept of a thermal average. We show that this method of decoding at an optimum, nonzero temperature minimizes bit error rate, as opposed to codeword error rate. We present simulation results that verify a small decrease in bit error rate for a few examples of spin glass codes, and also for the (8,4) Hamming code and the (24,12) Golay code, both of which can be viewed as spin glass codes. In Section VII, we demonstrate a method for decoding convolutional codes at nonzero temperatures. The method, based on the transfer matrix method of statistical mechanics, is similar to a Viterbi decoder, which it reduces to in the case of zero temperature. We present simulation results that show a small decrease in bit error rate for a convolutional code decoded at the optimum temperature. Finally, in Section VIII, we present our conclusions.

II. Properties of Spin Glasses

An Ising spin glass is a set of N particles with spin ± 1 [1]. The energy of a spin glass depends on the values of the spins and the strengths of the interactions among the particles. For instance, if there is a positive interaction between two particles, then the energy contribution from that interaction will be lower if the spins are the same and higher if they are opposite. In general, the strength of the interaction between any p particles i_1, \dots, i_p is given by the coupling coefficient J_{i_1, \dots, i_p} . Let s_i be the spin of the i th particle and $S = \{s_1, \dots, s_N\}$ a configuration of the N spins. The energy of the whole system when it has configuration S is given by the Hamiltonian

$$H(S) = - \sum_p \sum_{\{i_1, \dots, i_p\} \subset \{1, \dots, N\}} C_{i_1, \dots, i_p} J_{i_1, \dots, i_p} s_{i_1} \dots s_{i_p} \quad (1)$$

where the connectivity matrix C_{i_1, \dots, i_p} is 1 if the p particles i_1, \dots, i_p interact and 0 otherwise. (Each subset is understood to appear only once in the sum.) We will assume that the coupling coefficients are given by independent identically distributed (i.i.d.) random Gaussian variables with mean J_0 and variance σ_J^2 .

The physical situation that we are considering here is that the interaction strengths are fixed while the spins are free to change. Let T be the temperature of the system. Then the probability of the system being in a particular configuration S at equilibrium is given by the Gibbs distribution [1]:

$$p(S) = \frac{e^{-(1/kT)H(S)}}{Z} \quad (2)$$

where k is Boltzmann's constant and the partition function Z (a normalizing constant) is given by

$$Z = \sum_S e^{-(1/kT)H(S)} \quad (3)$$

As $T \rightarrow 0$, we see that $p(S) \rightarrow 0$, except for S such that $H(S)$ is a minimum. Such a minimizing configuration S is known as a ground state. Unfortunately, in many cases the ground state is degenerate, meaning that there may be multiple configurations of spins that have the same minimum energy. For instance, consider the case $p = 2$: For any configuration, the energy of the configuration obtained by reversing all the spins will be the same.

The magnetization $m(S)$ of a configuration S is simply the average spin: $m(S) = (1/N) \sum s_i$. In this article, we will need to consider limits as the number of particles $N \rightarrow \infty$. In this situation, there can occur a phase transition, which is a sort of discontinuity in some global characteristic of the system as a function of some continuous parameter(s). Specifically, for the spin glass model we have described, there is a phase transition at zero temperature at a particular critical value of J_0/σ_J : For J_0/σ_J below this cutoff, the magnetization m (of the ground state, since $T = 0$) is zero, whereas above it, $m > 0$. We will dismiss the problem of degenerate ground states by merely stating that there are ways to make the ground state unique. The existence of the phase transition also requires that the connectivity matrix not be too sparse. This condition will be satisfied in the cases for which we will invoke a phase transition.

We now define one more property of our spin glass model, called gauge invariance. Let $\{\epsilon_1, \dots, \epsilon_N\}$ be an arbitrary configuration of Ising spins, that is, $\epsilon_i = \pm 1$. A system is gauge invariant if the configuration space is invariant under the transformation $s_i \rightarrow s_i \epsilon_i$, and if the Hamiltonian is invariant under this transformation and the simultaneous transformation $J_{i_1, \dots, i_p} \rightarrow J_{i_1, \dots, i_p} \epsilon_{i_1} \dots \epsilon_{i_p}$. Clearly, our model is gauge invariant, since the result of multiplying any sequence of Ising spins by another arbitrary sequence of Ising spins is yet another sequence of Ising spins, and Eq. (1) is unchanged if both transformations are applied simultaneously.

III. Using Spin Glass Models as Error-Correcting Codes

In a 1989 article in *Nature* [2], Nicolas Sourlas suggested using an Ising spin glass model to construct error-correcting codes. In this section, we describe his proposal. For simplicity, he only considered the slightly simpler special case where interactions are restricted to a single value of p . Thus, we have the Hamiltonian

$$H(S) = - \sum_{\{i_1, \dots, i_p\} \subset \{1, \dots, N\}} C_{i_1, \dots, i_p} J_{i_1, \dots, i_p} s_{i_1} \dots s_{i_p} \quad (4)$$

Let $\{a_1, \dots, a_N\}$, $a_i = \pm 1$, be an N -bit information sequence. Let $J_{i_1, \dots, i_p} = J_0 \prod a_{i_1} \dots a_{i_p}$ whenever $C_{i_1, \dots, i_p} = 1$. Then the set of spins corresponding to the data will be the ground state of the Hamiltonian with these coupling coefficients. Thus, our spin glass model yields a code, with codewords given by the computed set of coupling coefficients and decoding done by finding the ground state of the Hamiltonian specified by the coupling coefficients. Before finding the rate, we make one more simplification: Assume that the coordination number $z_i = \sum_{j_2, \dots, j_p} C_{i, j_2, \dots, j_p} = z$ is independent of i . (Notice that C_{j_1, j_2, \dots, j_p} is invariant under permutations of its indices, so that z_i is the number of interacting subsets that include s_i .) Then the code rate is given by $R = p/z$.

Now we consider the issue of noise. Let us assume that the transmitted codeword symbols have magnitude $\pm v$ and duration τ , and are subject to additive white Gaussian noise (AWGN) of spectral density N_0 . Then the noise is included in the model via the already discussed variance σ_J^2 of the coupling coefficients, with corresponding channel $SNR = E_s/N_0 = v^2\tau/N_0 = J_0^2/2\sigma_J^2$. For $J_0 \ll \sigma_J$, or equivalently, $v^2\tau \ll N_0$, the channel thus has capacity $C = (1/\ln 2)J_0^2/2\sigma_J^2$ bits per coupling coefficient [3].

We are ultimately concerned with the probability of decoded bit error P_b , so we now consider the corresponding quantity in the spin glass model. This is where gauge invariance comes in: It allows us to assume, without loss of generality, that the spins are all $+1$. Then, P_b is just the probability that a bit is decoded as -1 . Since the ground state magnetization m is given by $m = (+1)Pr\{s_i = +1\} + (-1)Pr\{s_i = -1\} = (+1)(1 - P_b) + (-1)P_b$, we have $P_b = (1 - m)/2$. In the next section, we will describe a situation where $m \rightarrow 1$, and hence $P_b \rightarrow 0$.

As a familiar example, consider a binary $(n, 1)$ convolutional code [3]. For simplicity, assume that each of its n generating polynomials $\{g_1(x), \dots, g_n(x)\}$ has exactly p terms. It can be described by our model

by letting $N = \infty$, and $C_{i_1+k, \dots, i_p+k} = 1$ if and only if $g_j(x) = x^{i_1} + \dots + x^{i_p}$ for some j . For instance, if $n = p = 2$, with $g_1(x) = 1 + x$ and $g_2(x) = 1 + x^2$, then the corresponding log likelihood formula,

$$\log P \propto \sum_i J_{i,i-1} S_i S_{i-1} + J_{i,i-2} s_i s_{i-2} + \text{constant} \quad (5)$$

that is used in Viterbi decoding is equivalent to the Hamiltonian we have defined. The code can be visualized as a one-dimensional infinite spin glass with short-range, translation invariant interactions.

IV. Approaching the Shannon Bound With a Spin Glass Model

We now consider a special case, known as Derrida's random energy model [4], that is soluble. This means that the behavior of certain measurable quantities, such as the magnetization as a function of J_0/σ_J and temperature T , can be calculated. Again, we restrict interactions to a single value of p , so that our Hamiltonian is given by Eq. (4). We assume that the connectivity is extensive, i.e., $z \sim \binom{N-1}{p-1}$. Because we will be letting $N \rightarrow \infty$, we will use the scaled variables j_0 and σ_j , with $J_0 = (p!/N^{p-1})j_0$ and $\sigma_j^2 = (p!/N^{p-1})\sigma_j^2$, in order for the relevant quantities to remain finite. We then normalize by setting $\sigma_j = 1$, and so the channel $SNR = (1/2)j_0^2 p!/N^{p-1}$. As $N \rightarrow \infty$, the asymptotic rate $R = p!/N^{p-1}$ and the capacity $C = (j_0^2/2 \ln 2)p!/N^{p-1}$ bits per coupling coefficient.

In Derrida's random energy model, the number of particles $p \rightarrow \infty$ and $p/N \rightarrow 0$. He showed that in this case there is a phase transition for $T < 1/(2\sqrt{\ln 2})$ at $j_0 = \sqrt{2 \ln 2}$ from a spin glass phase with $m = 0$ to a ferromagnetic phase with $m = 1$. Thus, for $j_0 > \sqrt{2 \ln 2}$, the probability of error P_e can be made arbitrarily small. Therefore, we can code at a rate arbitrarily close to capacity with $P_e \rightarrow 0$. Although $R \rightarrow 0$, we note that R' , the rate in bits per sec, is given by $R' = R/\tau$. Since $v^2\tau/N_0 = J_0^2/2\sigma_j^2 = (1/2)j_0^2 R = \ln 2 R$, it follows that $R' = (1/\ln 2)v^2/N_0$. This means that the rate in bits per sec remains a constant as a function of transmitter power $P = v^2$ and noise power N_0 as $P_e \rightarrow 0$. The capacity C' in terms of bits per sec is $C' = (1/\ln 2)v^2/N_0$ [3]. The bound is approached for codeword lengths approximately equal to N^p , where both N and p approach infinity, so clearly the codes rapidly become impractical. However, we do have an explicit construction for a family of codes whose performance approaches the Shannon limit, and it is possible to simulate them, as described in the next section. Spin glass theory does give us some hint as to what we can expect: It can be shown that for large p , $m \approx 1 - (2^{-p}/\sqrt{p})$ for codes satisfying the capacity constraint.

V. Decoding by Finding the Ground State

In this section, we discuss simulations of decoding by finding the ground state for a few examples of the family of codes described in the previous section. The size of the codes grows so quickly with N and p that only fairly small values could be used. Two different methods for finding the ground state were used: exhaustive search and simulated annealing. By using efficient recursive algorithms for exhaustive search and letting simulations run for over a week in some cases, it was possible to test codes with parameters as high as $N = 20$ and $p = 5$. Results are shown in Fig. 1, where the curves are labeled as (N, p) . For the four codes with $N = 8$ and 12, each point represents 2500 codeword error events. For the two $N = 16$ codes and the $(N, p) = (20, 3)$ code, each point represents 100 codeword error events, and for the $(20, 5)$ code, only 25 codeword errors were obtained. The reason for using odd values of p was to avoid the degenerate ground states that result when p is even, and no other problems from degenerate ground states appeared.

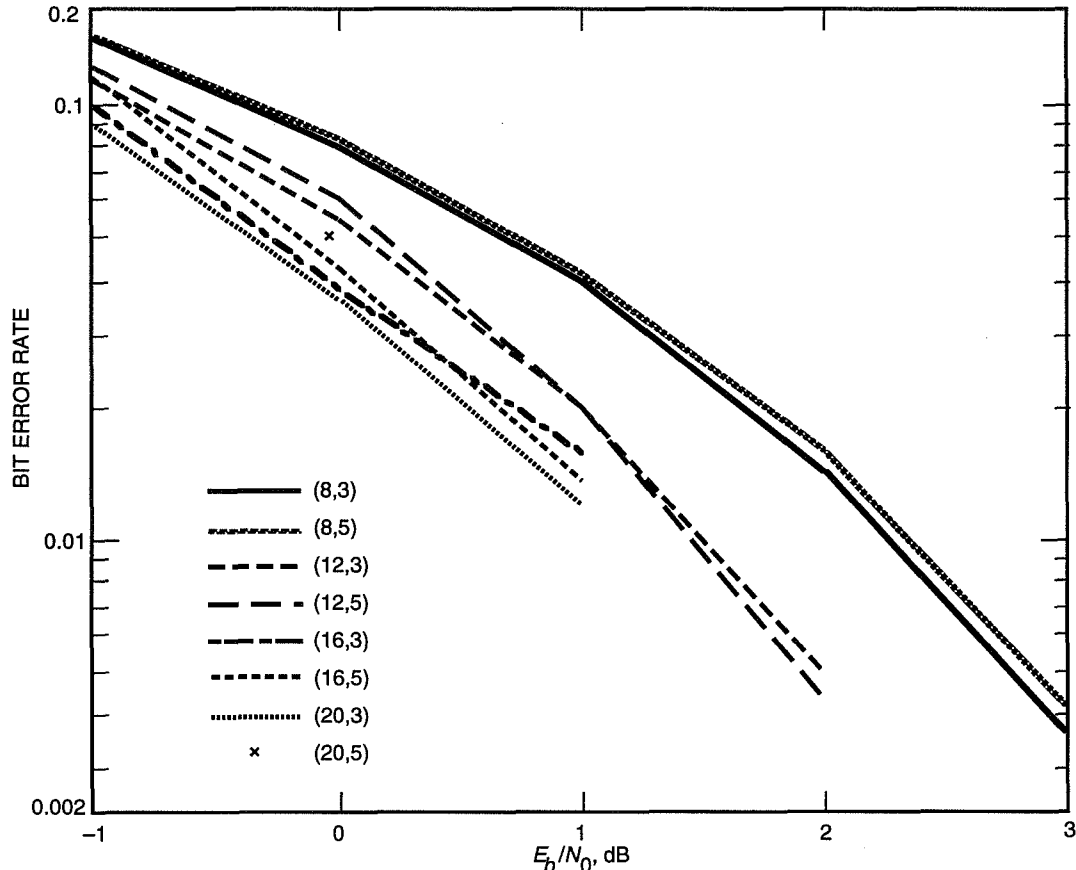


Fig. 1. Bit error rates of spin glass codes with varying parameters (N, p) .

In an effort to speed up decoding, simulated annealing [5] was tried. In a physical spin glass, this corresponds to heating it up to a relatively high temperature and then slowly reducing the temperature asymptotically to 0. If the dwell time, or time spent at each temperature, is large enough for the temperature-decrementing factor used, then the system should reach equilibrium at each temperature, and thus end up in the ground state for T sufficiently close to zero. Results for $N = 12$ and $p = 3$ are shown in Fig. 2, for two different dwell times. Each point on the simulated annealing curves represents approximately 1000 codeword errors, and the exhaustive search curve is taken from Fig. 1. Unfortunately, simulated annealing took even longer than the exhaustive search. This was true even for larger parameters, such as $N = 20$ and $p = 5$, because much longer dwell times were necessary to get reasonable performance. It is possible that further customization of the simulated annealing algorithm for the particular characteristics of this problem could result in significant improvement, but the potential benefits did not seem to justify the additional effort at this time.

VI. Decoding at Nonzero Temperatures

After reading Sourlas' article, Pal Rujan proposed an idea for decoding spin glass codes with a lower resulting bit error rate than could be obtained by finding the ground state [6]. He showed that the effect of the channel was equivalent to heating up a spin glass to a particular temperature T_N (the Nishimori temperature) [7]. For the model we have described with AWGN, $T_N = \sigma^2/kJ_0$. This suggested decoding by computing the thermal average at T_N of the Hamiltonian given by the received codeword. The thermal average is the average over all spin configurations, weighted by the Gibbs distribution, so that the decoded

value of the i th spin, \hat{s}_i , is given by $(1 - m_i)/2$, where m_i is the averaged magnetization of the i th particle, given by

$$m_i = \frac{\sum_S s_i e^{-\beta_N H(S)}}{\sum_S e^{-\beta_N H(S)}} \quad (6)$$

with $\beta_N = 1/(kT_N) = J_0/\sigma_J^2$. Notice that finding the ground state is equivalent to computing the thermal average at $T = 0$.

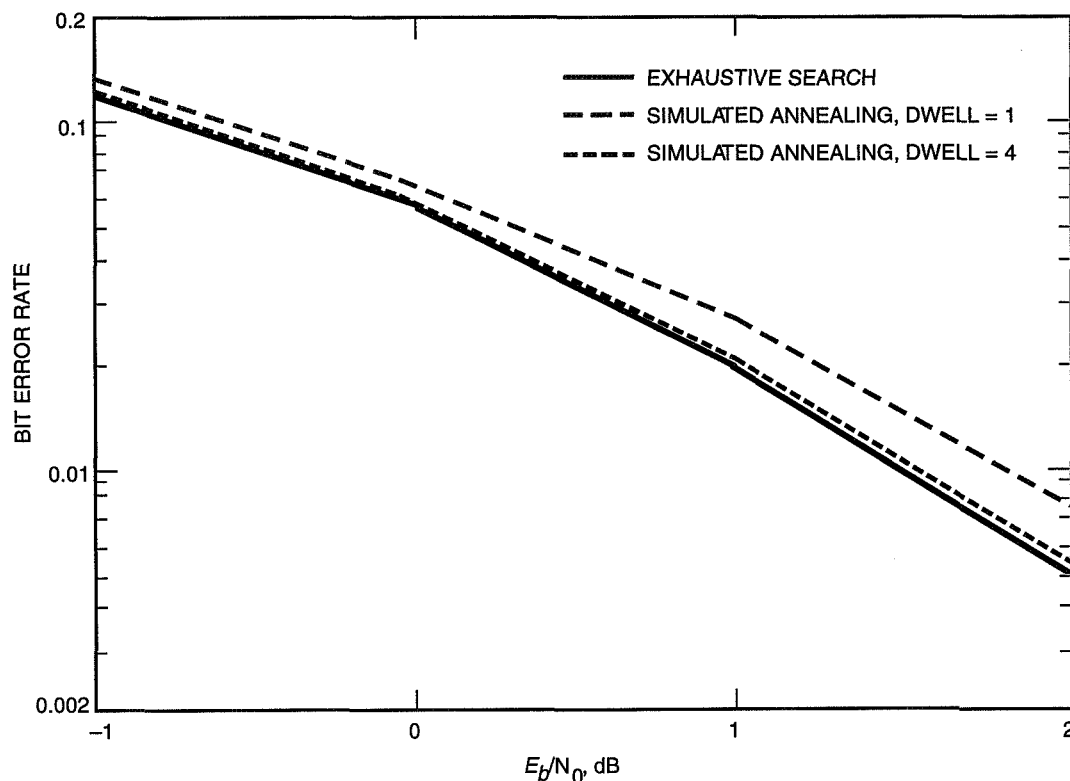


Fig. 2. Performance of simulated annealing versus exhaustive search for decoding a (12,3) spin glass code.

Rujan presented results of a simulation that showed a small decrease in bit error rate at $T = T_N$ compared to $T = 0$ [6]. Hidetoshi Nishimori responded by proving that the bit error rate was indeed lower at $T = T_N$ than at $T = 0$ [9]. In fact, he showed that this is true not only for AWGN, but for any noise with distribution $f(|J|)e^{aJ}$.

Rujan's results seemed suspicious at first glance, because Viterbi decoding is known to be optimum. The difference is that Viterbi decoding finds the most likely sequence of input bits, but not necessarily the sequence of most likely input bits. Although the formula above came from considerations of statistical mechanics, it is easy to derive using just Bayes formula. We start by expressing m_i as

$$m_i = \sum_S s_i Pr\{S|\{J_{i_1, \dots, i_p}\}\} \quad (7)$$

(Again, we are assuming for simplicity of notation a single value of p .) Using Bayes formula, we get

$$Pr\{S|\{J_{i_1,\dots,i_p}\}\} = \frac{Pr\{\{J_{i_1,\dots,i_p}\}|S\}Pr\{S\}}{\sum_S Pr\{\{J_{i_1,\dots,i_p}\}|S\}Pr\{S\}} \quad (8)$$

$Pr\{S\} = 1/2^N$ for all S , and

$$\begin{aligned} Pr\{\{J_{i_1,\dots,i_p}\}|S\} &= \prod_{\{i_1,\dots,i_p\} \subset \{1,\dots,N\}} e^{-(J_{i_1,\dots,i_p} - J_0 s_{i_1} \dots s_{i_p})^2 / 2\sigma_J^2} \\ &= e^{-(1/2\sigma_J^2) \sum_{\{i_1,\dots,i_p\} \subset \{1,\dots,N\}} (J_{i_1,\dots,i_p} - J_0 s_{i_1} \dots s_{i_p})^2} \\ &= A e^{-(1/2\sigma_J^2) \sum_{\{i_1,\dots,i_p\} \subset \{1,\dots,N\}} 2J_{i_1,\dots,i_p} J_0 s_{i_1} \dots s_{i_p}} \\ &= A e^{-\beta_N H(S)} \end{aligned} \quad (9)$$

where A is independent of S (using $s_i^2 = 1$). Finally, substituting Eq. (9) into Eq. (8) and then Eq. (8) into Eq. (7) yields Eq. (6), the desired result.

In fact, we can now show that Rujan's method actually minimizes the bit error rate. From Eq. (7),

$$\begin{aligned} m_i &= \sum_{S:s_i=+1} s_i Pr\{S|\{J_{i_1,\dots,i_p}\}\} + \sum_{S:s_i=-1} s_i Pr\{S|\{J_{i_1,\dots,i_p}\}\} \\ &= (+1)Pr\{s_i = +1|\{J_{i_1,\dots,i_p}\}\} + (-1)Pr\{s_i = -1|\{J_{i_1,\dots,i_p}\}\} \end{aligned} \quad (10)$$

so $m_i > 0$ if and only if $Pr\{s_i = +1|\{J_{i_1,\dots,i_p}\}\} > Pr\{s_i = -1|\{J_{i_1,\dots,i_p}\}\}$.

Figure 3 shows the results of decoding simulations for a few of the spin glass codes described in Section IV. Each point represents 10,000 codeword error events. The bit error rate is lower for $T = T_N$ than for $T = 0$, although the difference is small. Figure 4 shows similar results for the (24,12) Golay code and the (8,4) Hamming code. Again, each point represents 10,000 codeword error events. In these simulations, calculations were done by directly computing the sum in Eq. (6), using efficient recursive algorithms. Of course, for anything but the smallest codes, using Eq. (6) directly is impractical. As mentioned previously, however, for convolutional codes one can use Rujan's transfer matrix method, which will be discussed in the next section.

Although we have shown that Eq. (6) can be derived without reference to spin glasses, the theory behind spin glasses might still be useful in dealing with error-correcting codes. One example, of course, is the use of an algorithm from statistical mechanics for decoding. The simulation results do not demonstrate a great improvement in performance, but theoretically, it would be interesting to have bounds on how much improvement is possible from minimizing the bit error rate instead of the codeword error rate. Perhaps spin glass theory could shed some light on this. Another idea that seems reasonable for decoding at the Nishimori temperature is to use simulated annealing, but only decrease the temperature to T_N instead of all the way to zero.

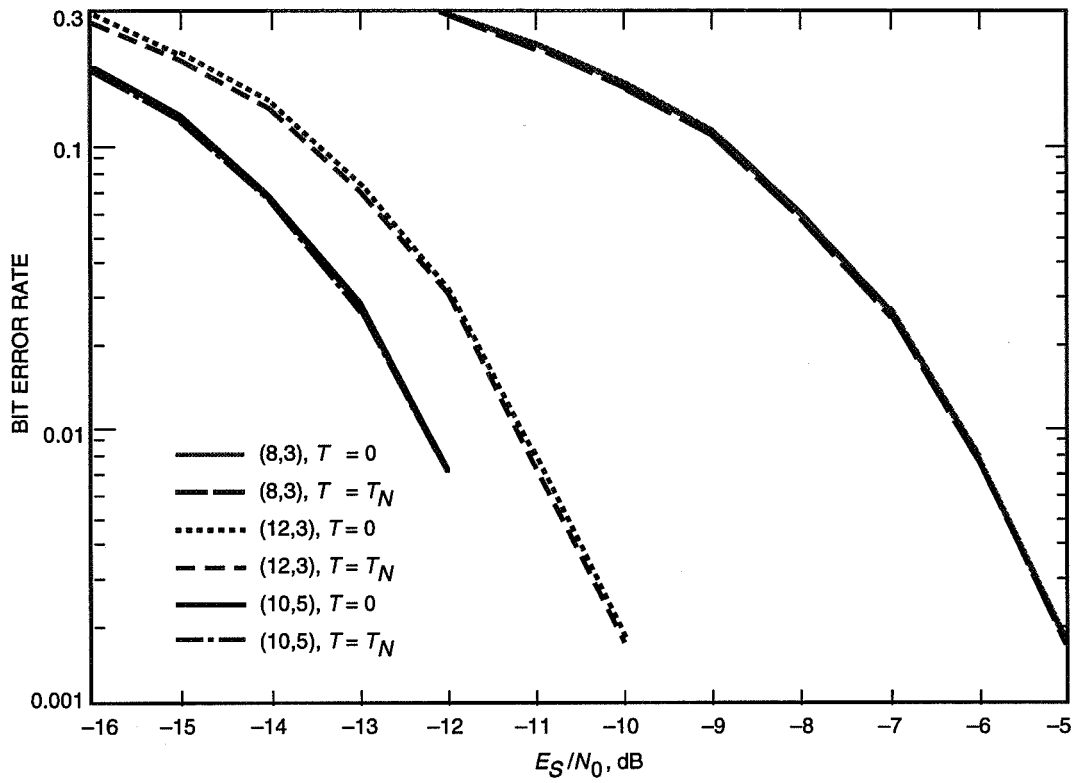


Fig. 3. Comparison of $T=0$ and $T=T_N$ decoding for three spin glass codes.

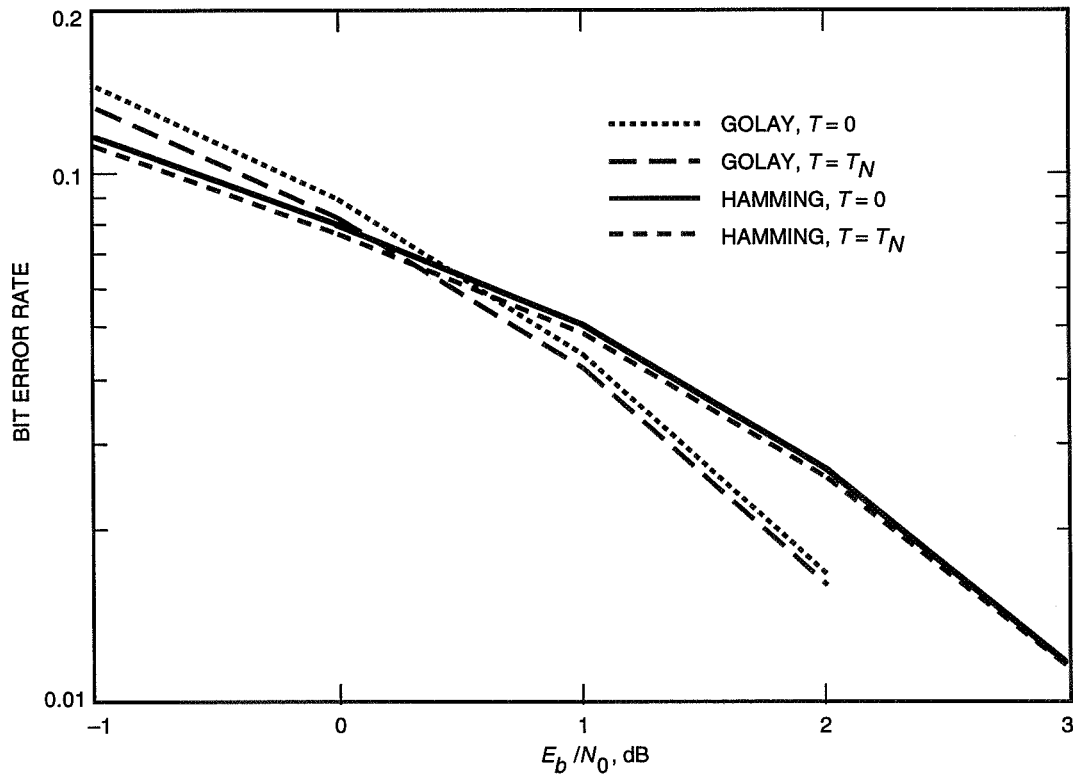


Fig. 4. Comparison of $T=0$ and $T=T_N$ decoding for the (24,12) Golay code and the (8,4) Hamming code.

It also appears that the theory of Markov random fields [1], which is closely related to spin glass theory, might have implications for finite length codes and infinite codes (in one or more dimensions) with only short-range interactions. Codes with short-range interactions are likely to be more practical, since the rate would not decrease so rapidly as the number of information bits increases. Two-dimensional codes might be useful for encoding images, for example.

Another interesting suggestion was pointed out by Sourlas [10]: It is easy to modify Eq. (6) in order to minimize the probability of error of particular blocks of input data. For instance, if the binary input data consisted of a sequence of k -bit symbols, one could minimize the symbol error rate instead of the bit error rate or instead of the sequence error rate.

VII. Decoding Convolutional Codes at Nonzero Temperatures

Rujan [6] showed that for a one-dimensional spin glass with short-range interactions, such as a convolutional code, a variant of the transfer matrix method of statistical mechanics [8] could be used to compute the thermal average. It finds the m_i 's for a given temperature T using a recursive algorithm that reduces to the Viterbi algorithm at $T = 0$, and has similar complexity. We illustrate Rujan's algorithm with a simple rate 1/2 convolutional code with generator matrix $G(x) = [1 + x^2 \ 1 + x + x^2]$. Let $\{K_1(1), K_2(1), K_1(2), \dots, K_2(N)\}$ be the $2N$ received coupling coefficients, $K_1(i) = a_{i-1}a_i a_{i+1} + n_1(i)$ and $K_2(i) = a_{i-1}a_{i+1} + n_2(i)$, where $n_1(i)$ and $n_2(i)$ are i.i.d. Gaussian variable of mean zero and variance σ_J^2 . (Define $a_0 = a_{N+1} = 0$.) Then the energy can be written as

$$H(S) = \sum_{i=2}^{N-1} H_i(s_{i-1}, s_i, s_{i+1}) \quad (11)$$

where $H_i(s_{i-1}, s_i, s_{i+1}) = K_1(i)s_{i-1}s_i s_{i+1} + K_2(i)s_{i-1}s_{i+1}$. The value for m_i is given by

$$m_i = \frac{\sum_{s_{i-1}, s_i} \psi_{i-1}^> s_i \psi_{i+1}^<}{\sum_{s_{i-1}, s_i} \psi_{i-1}^> \psi_{i+1}^<} \quad (12)$$

where the ψ_i 's are defined recursively: Let $\psi_1^>(s_1, s_2) = 1$ and compute

$$\psi_i^>(s_i, s_{i+1}) = \sum_{s_{i-1}} \psi_{i-1}^>(s_{i-1}, s_i) e^{-\beta H_i(s_{i-1}, s_i, s_{i+1})}. \quad (13)$$

for $i = 2, 3, \dots, N$, $s_i = \pm 1$. The inverse temperature is $\beta = 1/(kT)$, so for $T = T_N$, $\beta = J_0/\sigma_J^2$. Then, let $\psi_N^<(s_{N-1}, s_N) = 1$ and compute

$$\psi_i^<(s_{i-1}, s_i) = \sum_{s_{i+1}} \psi_{i+1}^<(s_i, s_{i+1}) e^{-\beta H_i(s_{i-1}, s_i, s_{i+1})} \quad (14)$$

for $i = N - 1, \dots, 2, 1$, $s_i = \pm 1$. Finally, the decoded sequence is obtained by setting $\hat{a}_i = \text{sgn}(m_i)$, $i = 1, 2, \dots, N$, where the m_i 's are computed from Eq. (12).

This algorithm can be visualized on a Viterbi decoder trellis, each column having four states, labelled $(+1, +1), (+1, -1), (-1, +1)$, and $(-1, -1)$. The branch metric from (s_{i-1}, s_i) to (s_i, s_{i+1}) is $H_i(s_{i-1}, s_i, s_{i+1})$, and $\psi_i^>(s_i, s_{i+1})$ is the path metric at (s_i, s_{i+1}) . The difference from the Viterbi

algorithm is that instead of the path metric being solely determined by the best incoming path, it is a weighted sum of the path metrics of the incoming paths. After the $\psi_i^>$'s are computed from left to right, traceback is done by simultaneously computing $\psi_i^<$ and \hat{a}_i from right to left. Unlike the Viterbi algorithm, however, instead of selecting a single best path, the algorithm computes a weighted average of all possible paths. If $T = T_N$, then this weighted average, when quantized to ± 1 , yields the sequence of most likely bits, whereas the Viterbi decoder yields the most likely sequence of bits.

As T decreases, we see that the best (lowest energy) incoming path is weighted increasingly more heavily relative to the other incoming path, with the ratio of the two weights approaching infinity as $T \rightarrow 0$. Thus, the algorithm reduces to the Viterbi algorithm at $T = 0$, although renormalization is necessary to avoid all weights being infinite. The algorithm can also be modified, as the Viterbi algorithm usually is, to allow traceback to begin before reaching the end of the received symbols, at the cost of a slight loss of performance.

Figure 5 shows the results of decoding the convolutional code described above at $T = 0.1T_N$, $T = T_N$ and $T = 2T_N$. Each point represents approximately 10,000 bit errors. The bit error rate is lowest for $T = T_N$, although the difference is minuscule. The case $T = 0$ was not simulated, because the reduction to the Viterbi algorithm is not automatic, since simply using the value $T = 0$ results in dividing by zero. However, the performance at $T = 0$ should be only microscopically worse than at $T = 0.1T_N$.

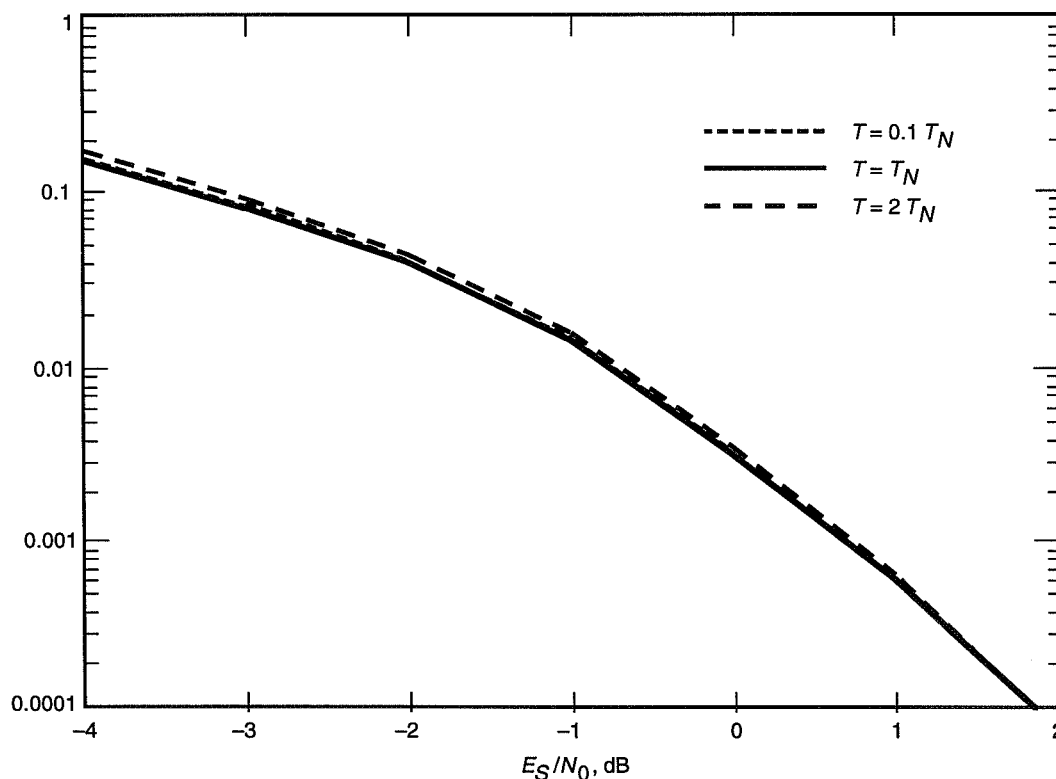


Fig. 5. Bit error rates for a rate 1/2 convolutional code decoded at three different temperatures.

VIII. Conclusion

We simulated the performance of some simple examples of a family of codes whose performance has been shown to asymptotically approach the Shannon bound. The codes have parameters N and p , with codeword length $\binom{N}{p}$ and rate $N/\binom{N}{p}$. The largest code we were able to simulate had a codeword length

of 15,504, a rate of 0.00129, and took over a week to accumulate only 25 codeword errors. Even for this code, the performance was far from capacity. Thus, these codes, although theoretically interesting, are probably not particularly useful, unless radical new decoding methods are developed. One possible such method might be to use an actual spin glass, with coupling coefficients specified by a received codeword, and let it come to equilibrium; then measure the spins to obtain the decoded data. However, this would be, at the very least, technically extremely challenging, and might even be physically impossible.

We also did simulations to measure the improvement in bit error rate achievable by using a decoding method analogous to computing the thermal average of a spin glass. The performance at the optimum temperature, which minimizes bit error rate, was compared to the performance of a standard decoder that minimizes codeword error rate. We tested some examples of the codes described in Section IV and also a (24,12) Golay code, an (8,4) Hamming code, and a simple rate 1/2 convolutional code. For the convolutional code, we used a decoding algorithm based on an algorithm from statistical mechanics for computing thermal averages in one-dimensional systems. For all the codes, there was a measurable but very small improvement in bit error rate. The improvement did not justify the increased decoding complexity, even for the convolutional code, where the decoding algorithm had complexity of the same order as the Viterbi algorithm.

References

- [1] R. Kindermann and J. L. Snell, *Markov Random Fields and their Applications*, Providence, Rhode Island: American Mathematical Society, 1980.
- [2] N. Sourlas, "Spin-Glass Models as Error-Correcting Codes," *Nature*, vol. 338, pp. 693–695, 1989.
- [3] R. McEliece, *The Theory of Information and Coding*, Reading, Massachusetts: Addison-Wesley, 1977.
- [4] B. Derrida, "Random-Energy Model: An Exactly Solvable Model of Disordered Systems," *Physical Review B*, vol. 24, pp. 2613–2626, 1981.
- [5] E. Aarts and J. Korst, *Simulated Annealing and Boltzmann Machines*, Chichester, England: Wiley, 1989.
- [6] P. Rujan, "Finite Temperature Error-Correcting Codes," *Physical Review Letters*, vol. 70, pp. 2968–2971, 1993.
- [7] H. Nishimori, "Internal Energy, Specific Heat and Correlation Function of the Bond-Random Ising Model," *Progress of Theoretical Physics*, vol. 66, pp. 1169–1181, 1981.
- [8] P. Rujan, "Calculation of the Free Energy of Ising Systems by a Recursion Method," *Physica*, vol. 91A, pp. 549–562, 1978.
- [9] H. Nishimori, "Optimum Decoding Temperature for Error-Correcting Codes," *Journal of the Physical Society of Japan*, vol. 62, pp. 2973–2975, 1993.
- [10] N. Sourlas, "Spin Glasses, Error-Correcting Codes and Finite-Temperature Decoding," *Europhysics Letters*, vol. 25, pp. 159–164, 1994.

1995108211
324456

N95-14625

TDA Progress Report 42-118

August 15, 1994

55-32
19783
p. 19 ✓

Linear Quadratic Gaussian and Feedforward Controllers for the DSS-13 Antenna

W. K. Gawronski, C. S. Racho, and J. A. Mellstrom
Ground Antennas and Facilities Engineering Section

The controller development and the tracking performance evaluation for the DSS-13 antenna are presented. A trajectory preprocessor, linear quadratic Gaussian (LQG) controller, feedforward controller, and their combination were designed, built, analyzed, and tested. The antenna exhibits nonlinear behavior when the input to the antenna and/or the derivative of this input exceeds the imposed limits; for slewing and acquisition commands, these limits are typically violated. A trajectory preprocessor was designed to ensure that the antenna behaves linearly, just to prevent nonlinear limit cycling. The estimator model for the LQG controller was identified from the data obtained from the field test. Based on an LQG balanced representation, a reduced-order LQG controller was obtained. The feedforward controller and the combination of the LQG and feedforward controller were also investigated. The performance of the controllers was evaluated with the tracking errors (due to following a trajectory) and the disturbance errors (due to the disturbances acting on the antenna). The LQG controller has good disturbance rejection properties and satisfactory tracking errors. The feedforward controller has small tracking errors but poor disturbance rejection properties. The combined LQG and feedforward controller exhibits small tracking errors as well as good disturbance rejection properties. However, the cost for this performance is the complexity of the controller.

I. Introduction

The DSS-13 antenna, a new-generation 34-m beam-waveguide antenna, is shown in Fig. 1. Future NASA missions will include low-Earth-orbiting satellites, which require significantly higher tracking rates (up to 0.4 deg/sec) than the deep space missions (0.004-0.01 deg/sec). Thus, the servos for the antennas require upgrading in order to follow commands with the required precision. Some upgrade options are presented in this article and are illustrated with simulation results and with field measurements.

The existing proportional integral (PI) controllers, depicted in Fig. 2, satisfy the requirements for deep-space X-band (8.4-GHz) tracking. For a higher tracking rate, a simple and reliable choice is the addition of a feedforward (FF) controller, described in [5,6]. The model-based, linear quadratic Gaussian (LQG) controllers are an alternative to feedforward controllers. The LQG design approach for the DSN antennas is presented in [2,3,4,6]. This article addresses the design and the implementation issues of the feedforward and LQG controllers and compares their performances.

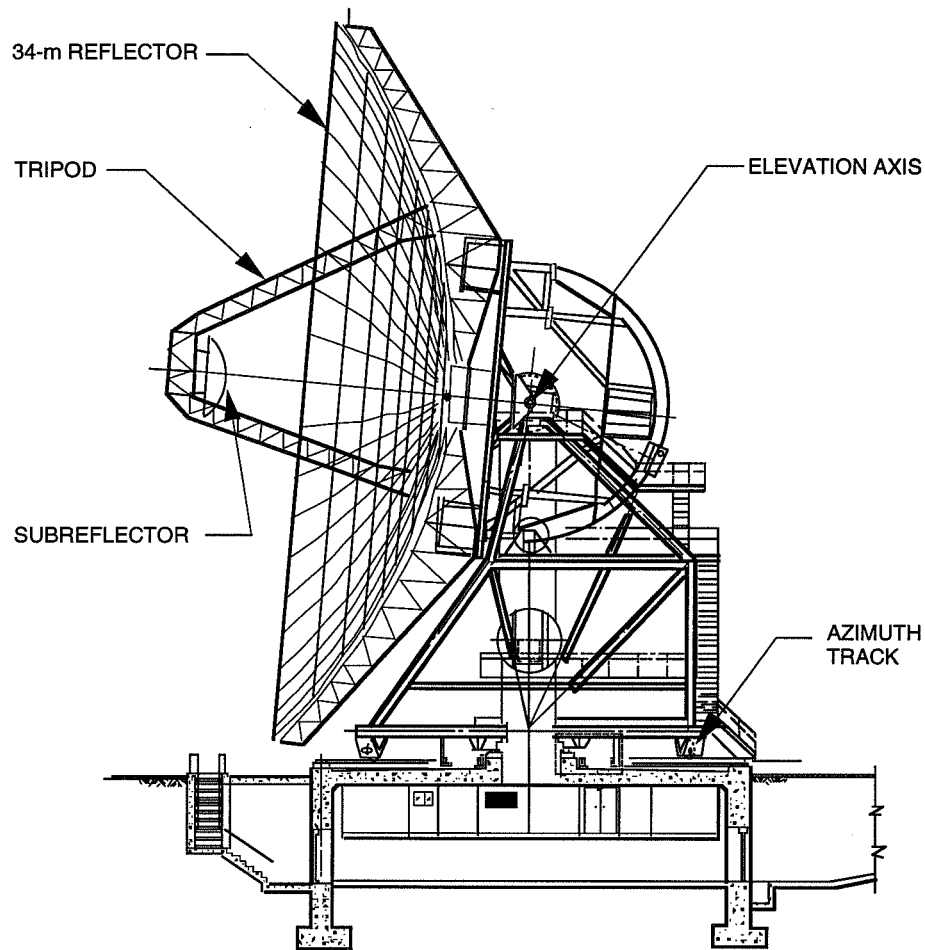


Fig. 1. DSS-13 antenna.

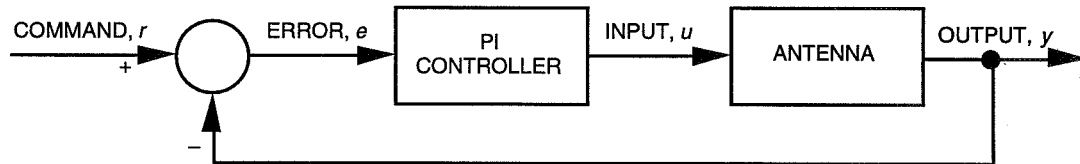


Fig. 2. Antenna PI controller.

The controllers under consideration were designed for a linear plant. However, the antennas can exhibit nonlinear behavior (limit cycling) due to limits imposed on the antenna input. In order to ensure proper performance, a trajectory preprocessor is introduced.

II. Trajectory Preprocessor

In the case of unpredicted commands or severe environmental conditions, the drives could be overloaded and damaged. In order to prevent this from happening, limits are placed on the input rates and

accelerations of DSN antennas. Because of these imposed limits, the antenna dynamics become nonlinear (for the antenna commands exceeding these limits). The antenna tracking commands are usually within these limits. However, the limits are often challenged by antenna slewing commands and by wind disturbances. When slewing commands exceed these limits, this usually results in antenna limit cycling. To avoid limit cycles, a slewing controller, which is different from the tracking controller, was implemented. In order to use the same controller for both tracking and slewing modes, the commands for the slewing mode must be modified so that they do not violate the rate and acceleration limits, yet still move the antenna at the highest rate possible. This command modification can be performed with a trajectory preprocessor located in the control system (Fig. 3). The preprocessor limits the rate and acceleration of the command as described below.

The basic structure of the trajectory preprocessor is derived from the feedforward controller of a DSN antenna [5,6]. This controller has been proven to have good tracking performance. For the preprocessor purposes, the controller is simplified by removing its integral part, and by replacing the linear part of the antenna model with the integrator. The nonlinear part (i.e., the rate and acceleration limiters) remains untouched.

A block diagram of the trajectory preprocessor is shown in Fig. 4(a), where *SAT* denotes saturation, and *RL* denotes rate limiter. Consider a trajectory $r(t)$, and let v_{max} and a_{max} be the maximum rate and acceleration that are allowed for an antenna command. In this figure, r_f is the preprocessed trajectory, $e = r - r_f$ is the preprocessor error, k is its gain, u is the rate command, u_L is the limited rate command, and u_f is the limited acceleration and rate command. The first step in verifying the preprocessor is to check its performance for the lifted limits on rate and acceleration, i.e., for the linear case as shown in Fig. 4(b). Hence, one obtains

$$u = \dot{r} + kr - kr_f, \quad \dot{r}_f = u \quad (1a)$$

and from the above, one obtains $\dot{r}_f + kr_f = \dot{r} + kr$,

$$r_f = r \quad (1b)$$

if the initial conditions for r and r_f are the same. It shows that if the command does not violate the rate and acceleration limits, and if the initial conditions are the same, the preprocessed trajectory is identical to the original one.

In the nonlinear regime, the equations for the discrete-time preprocessor are as follows. The input, $u(i)$, is

$$u(i) = k(r(i) - r_f(i) + v(i)) \quad (2a)$$

where $v(i)$ is the command rate at the i th instant. The input saturation is

$$u_L(i) = \begin{cases} v_{max} & \text{for } u(i) > v_{max} \\ -v_{max} & \text{for } u(i) < -v_{max} \\ u(i) & \text{otherwise} \end{cases} \quad (2b)$$

The input rate limiter is

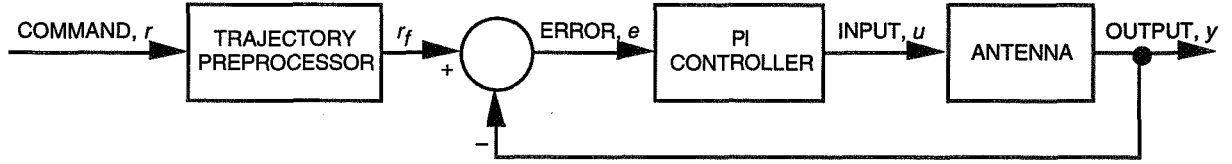


Fig. 3. Antenna PI controller with trajectory preprocessor.

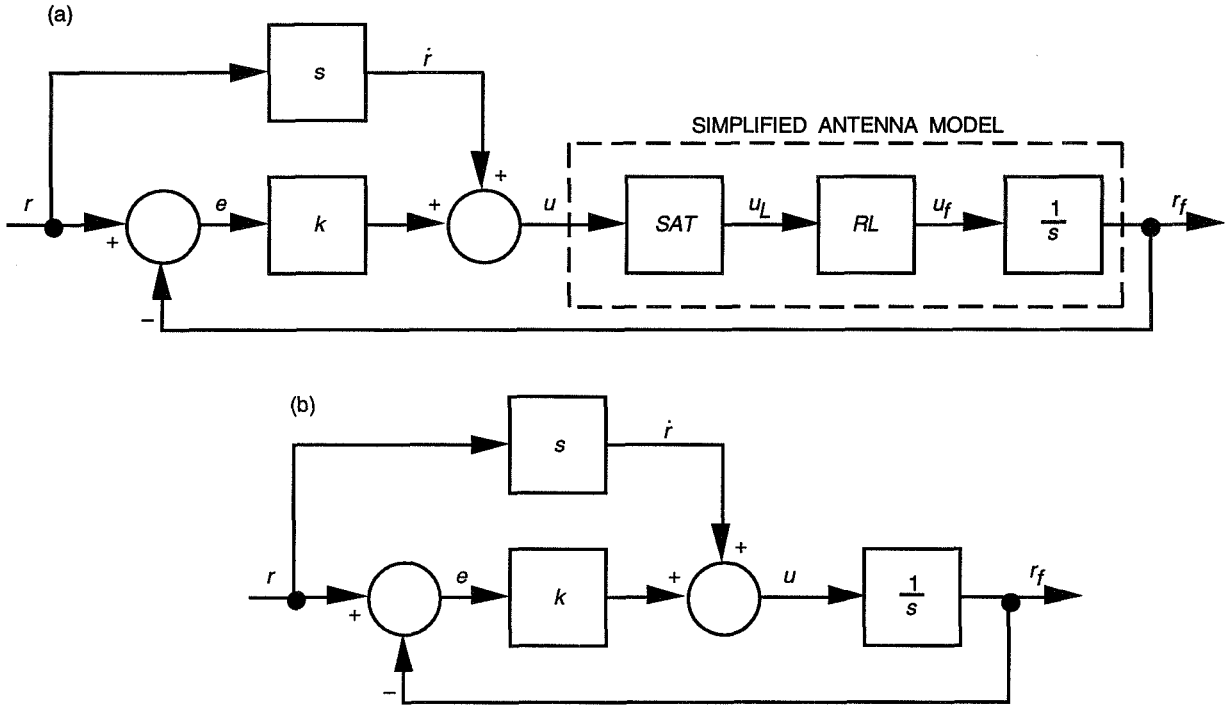


Fig. 4. Trajectory preprocessor: (a) block diagram and (b) linearized variant.

$$u_f(i) = \begin{cases} u_f(i-1) + Ta_{max} & \text{for } u_L(i) > u_f(i-1) + Ta_{max} \\ u_f(i-1) - Ta_{max} & \text{for } u_L(i) < u_f(i-1) - Ta_{max} \\ u_L(i) & \text{otherwise} \end{cases} \quad (2c)$$

The integration of u_f is

$$r_f(i) = r_f(i-1) + Tu_f(i), \quad v_f(i) = u_f(i) \quad (2d)$$

where $v_f(i)$ is the rate of the preprocessed trajectory at the i th instant. In the case of violated limits, it is difficult to analytically evaluate the performance of the preprocessor, but it can be done by simulating commands typical for the DSN antennas. Typical commands are step command (slewing an antenna), rate offset, trajectory acquisition, and medium-rate azimuth trajectory (up to 0.4 deg/sec).

First, the preprocessing of the step command is illustrated. A step command as in Fig. 5(a), solid line, is preprocessed for the maximum rate, $v_{max} = 0.4$ deg/sec, and the maximum acceleration, $a_{max} = 0.6$ deg/sec², which is "acceptable" to a controller. The preprocessed trajectory is shown in Fig. 5(a),

dashed line. Its rate does not exceed v_{max} (Fig. 5(b), dashed line), and its acceleration does not exceed a_{max} (Fig. 5(c), dashed line).

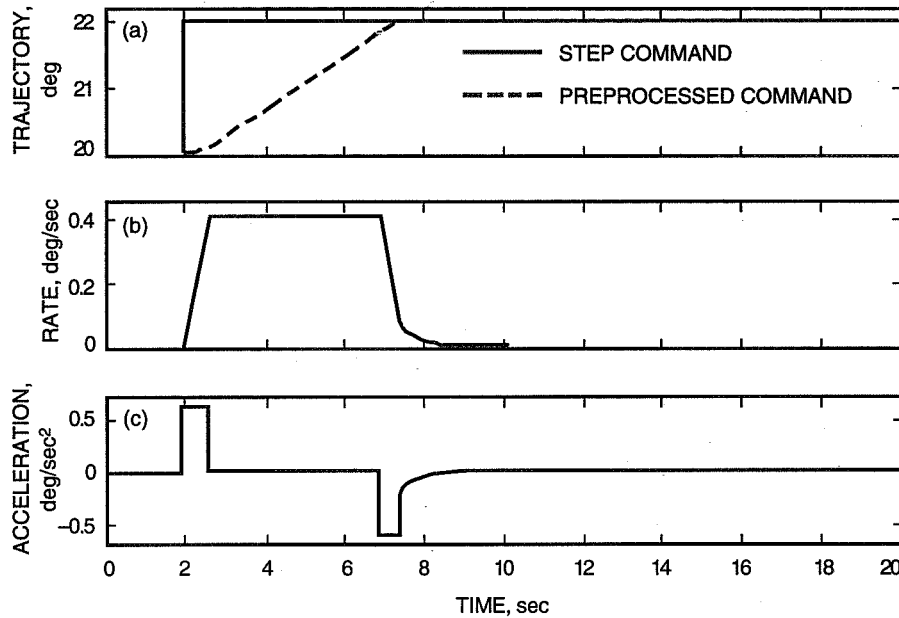


Fig. 5. Preprocessing of the step command: (a) a step command and preprocessed command; (b) rate of the preprocessed command; and (c) acceleration of the preprocessed command.

For the rate offset test, a command with the constant rate of 0.3 deg/sec is preprocessed for the initial position of the preprocessed trajectory identical to the initial position of the original trajectory $r_f(o) = r(0)$ and the zero initial rate of the preprocessed trajectory $v_f(0) = 0$, while the initial rate of the original trajectory is nonzero, i.e., $v(o) = 0.3$ deg/sec (Fig. 6). The original and preprocessed trajectories shown in solid and dashed lines, respectively, demonstrate that the original trajectory is quickly approached by the preprocessed one. For the case where both initial conditions (position and rate) of the preprocessed trajectory are different from those of the original trajectory ($r_f(0) = 1$ deg, $v_f(0) = 0$ deg/sec, and $r(0) = 0$ deg, $v(0) = 0.3$ deg/sec), the preprocessed trajectory is shown in Fig. 6, dashed-dotted line. The original trajectory is acquired with the maximum speed and acceleration, and the difference between them approaches zero.

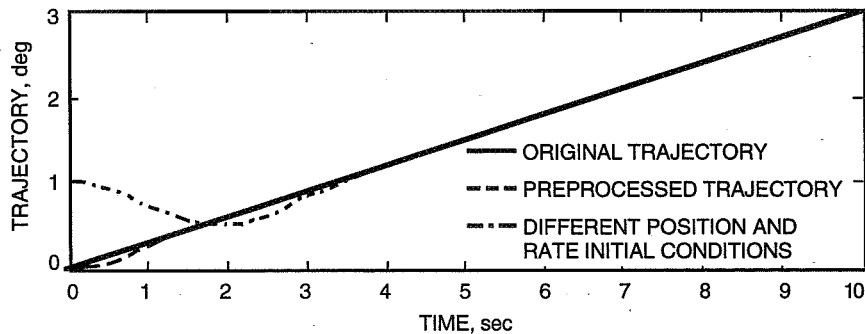


Fig. 6. The rate offset command (solid line) and preprocessed commands: the initial position of the preprocessed and the original commands are identical, but rates are different (dashed line), and the initial positions and rates of the preprocessed and the original commands are different (dashed-dotted line).

Finally, a trajectory, as shown in Fig. 7(a), with a maximum rate of 0.3 deg/sec is preprocessed for $v_{max} = 0.4$ deg/sec, $a_{max} = 0.6$ deg/sec², where the initial conditions ($r_f(0) = 22$ deg, $v_f(0) = 0$ deg/sec) differ from the original trajectory ($r(0) = 24$ deg, $v(0) = 100$ deg/sec). The preprocessed trajectory is shown in the same figure with a dashed line. After acquisition, the maximal difference between the original and the preprocessed trajectories is less than 0.1 mdeg [[Fig. 7(b)], which is much smaller than the noise level in the antenna position error.

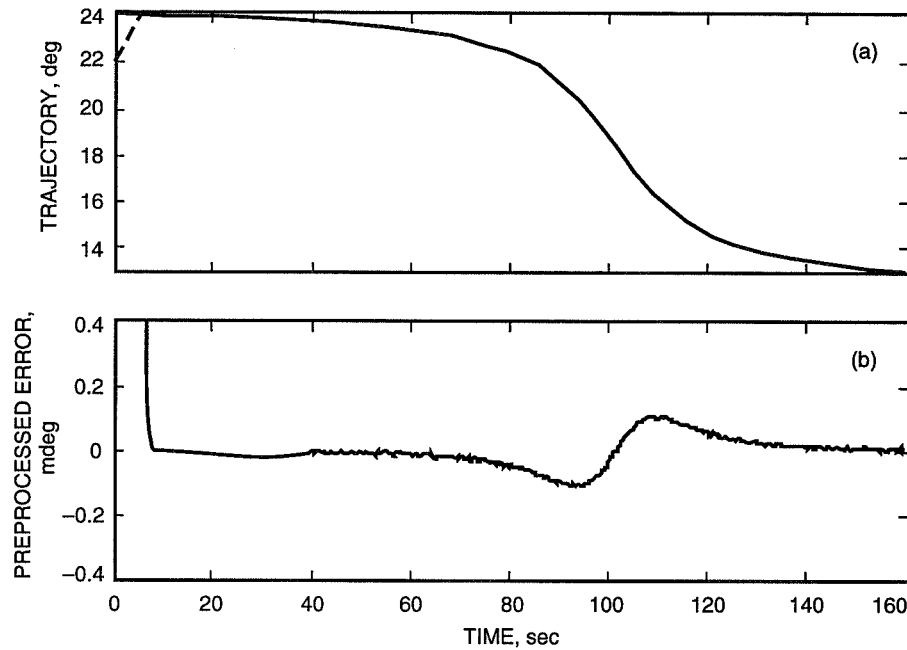


Fig. 7. Preprocessing a trajectory: (a) original and preprocessed trajectories and (b) preprocessing error.

III. LQG Controller

An LQG controller for the antennas (Fig. 8) consists of an estimator, PI gains, flexible mode gains, and the trajectory preprocessor. The identification of an estimator gain determination and the reduction of the controller are described in this section.

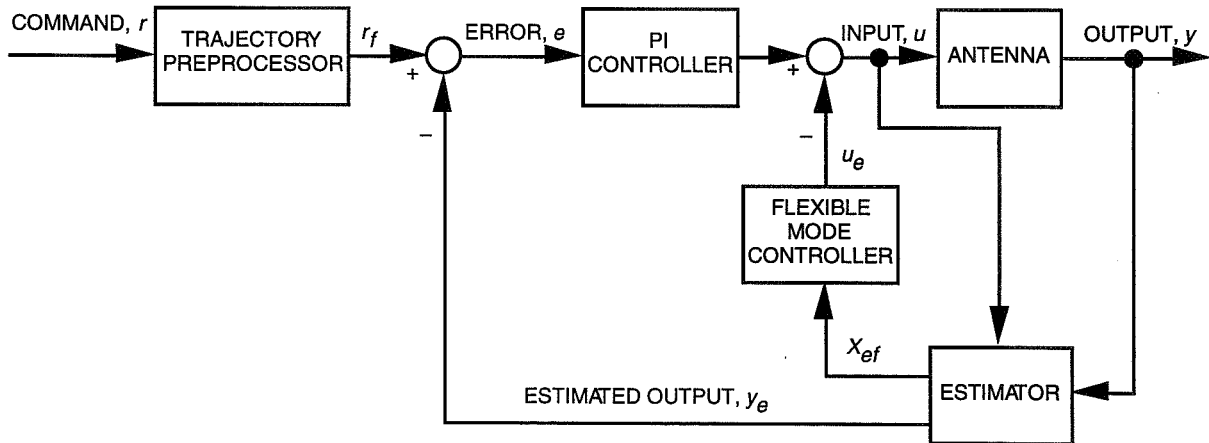


Fig. 8. Antenna LQG controller.

A. Identification of the Estimator Model

The antenna model used for the design of the estimator has two inputs (azimuth and elevation rates) and two outputs (azimuth and elevation positions) [4,6]. However, the cross-coupling between azimuth input and elevation output, and elevation input and azimuth output, is much weaker than the coupling between azimuth input and azimuth output, and elevation input and elevation output (compare Figs. 9 and 10). This fact allows one to ignore the cross-couplings and to use two separate antenna models (for azimuth and elevation). This approach simplifies the design and implementation of the LQG controller. The following test was simulated to justify this approach. An LQG controller A was designed for the plant without cross-couplings, and an LQG controller B was designed for the plant with cross-couplings. The resulting controllers A and B were applied to the plant. The performances of both controllers were nearly identical.

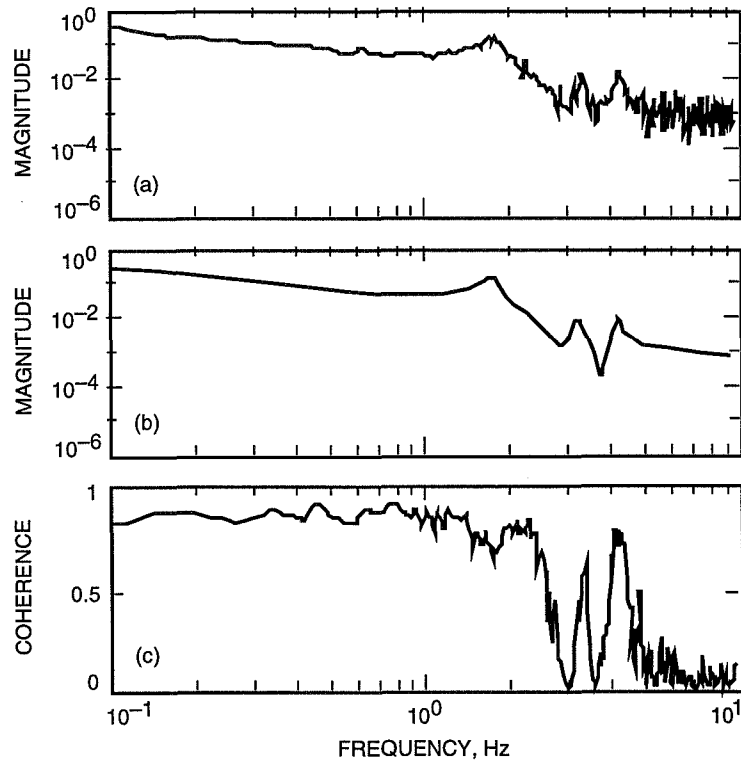


Fig. 9. Antenna transfer function from azimuth input to azimuth output: (a) measured, (b) identified, and (c) coherence of measured data.

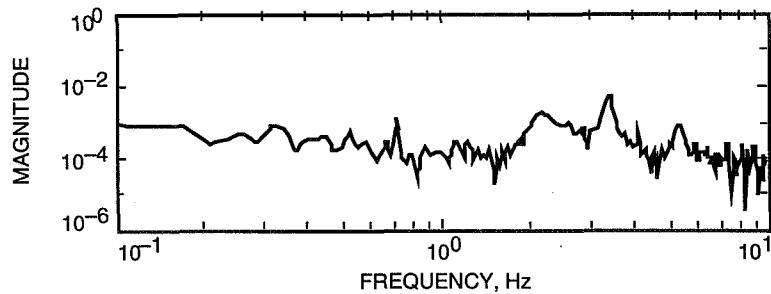


Fig. 10. Measured antenna transfer function from elevation input to azimuth output.

The analytical models for the DSS-13 antenna, such as those in [6], cannot be implemented as an estimator due to their uncertainties (such as finite-element model structural mass, friction, or gearbox stiffness). In order to design a model-based controller, an antenna model must precisely mimic the antenna dynamics. For this reason, an antenna model was identified using field measurements [12]. The field measurements were taken as follows: While the antenna was moving with a constant rate, u_o , a random signal, u , was injected. Then the input, $u_m = u_o + u$, and the output, $y_m = y_o + y$, were measured, where y_o and y were responses to u_o and u , respectively. The signals u and y were determined by detrending u_m and y_m . Next, the time series data were passed through a Hanning filter to prevent spectral leakage during a fast Fourier transformation [1].

The magnitude of the transfer function, $\|T(f)\|$, and the coherence, $\gamma(f)$, were estimated using the filtered and detrended input u and output y vectors of 8192 samples each:

$$\|T(f)\| = \frac{P_{uy}(f)}{P_{uu}(f)} \tag{3}$$

$$\gamma(f) = \frac{\|P_{uy}(f)\|^2}{P_{uu}(f)P_{yy}(f)}$$

where f is the frequency in Hz, $P_{uu}(f)$ is the power spectral density estimate of $u(t)$, $P_{yy}(f)$ is the power spectral density estimate of $y(t)$, and $P_{uy}(f)$ is the cross-spectral density estimate of $u(t)$ and $y(t)$. The magnitude of the transfer function and the coherence are plotted versus frequency in Figs. 9(a) and 9 (c).

The identified azimuth and elevation models were obtained in the state-space form triple (A_i, B_i, C_i) , $i = az$ or el . In later analysis, only the azimuth model is presented in detail, and the subscript i is dropped to simplify notation (details of the elevation model and cross-coupling models can be found in [12]). In this model, the state vector x is of dimension n , the input u is of dimension p , the output y is of dimension q , and the matrices A, B , and C are of dimensions $n \times n, n \times p$, and $q \times n$, respectively.

A model is identified using the identification software SOCIT (System/Observer/Controller Identification Toolbox) [8,9]. A state-space model, (A, B, C) , is identified given the input-output data, sample period, and the number of observer Markov parameters. The order of the system was chosen to be 24, based on the system Hankel singular values. Next, the state-space representation was transformed into balanced coordinates, so that the matrix A was in a diagonally dominant form, with 2×2 diagonal blocks. The diagonal elements of the block represent the system damping, while the off-diagonal elements represent natural frequencies at those modes. The identified transfer function plot is presented in Fig. 9(b).

The antenna model includes an integrator (note that the input is the rate and the output is the position). Thus, some of the system poles are at zero. The SOCIT software, not developed for the systems with poles at zero, consistently identified a model with all nonzero poles. Nevertheless, some of the poles were located close to zero. This feature was corrected by shifting the close-to-zero poles to zero. Also, the identified model showed overdamped modes. This was readily corrected by reducing the modal damping in the balanced representation.

The signals were measured with a sampling frequency of 80 Hz. Since the transfer function of the identified model should reflect the antenna dynamics for frequencies below 10 Hz, these signals were oversampled. The excess data in the oversampled signal were used to reduce noise intensity through averaging. In this way, a typical signal record of 8192 samples was reduced to 1638 samples.

B. Balanced LQG Controller

The design of the balanced LQG controller for the DSN antennas was described in detail in [4,6]. The closed-loop system with an LQG controller is shown in Fig. 8, with the estimator state-space triple (A, B, C) , the estimated state of flexible part x_{ef} , the control input u , the output y , the estimated output y_e , the command r , the servo error e , the process noise v of intensity V , and the measurement noise w of intensity W . Both v and w are uncorrelated $V = E(vv^T)$, $E(ww^T) = I$, $E(vw^T) = 0$, $E(v) = 0$, and $E(w) = 0$, where $E(\cdot)$ is the expectation operator. The triple (A, B, C) is stabilizable and detectable. The identified plant model was augmented with the new state (integral of the error); thus its order is increased to $n = 25$. The task is to determine the controller gain (k_c) and estimator gain (k_e) such that the performance index (J) ,

$$J = E \left(\int_0^{\infty} (x^T Q x + u^T u) dt \right) \quad (4)$$

is minimized, where Q is a positive semidefinite state-weight matrix. The minimum for J is obtained for the feedback $u = -k_c x$, where the gain matrix $k_c = B^T S_c$ is obtained from the solution S of the controller Riccati equation [10]

$$A^T S_c + S_c A - S_c B B^T S_c + Q = 0 \quad (5a)$$

The optimal estimator gain is given by $k_e = S_e C^T$, where S_e is the solution of the estimator Riccati equation

$$A S_e + S_e A^T - S_e C^T C S_e + V = 0 \quad (5b)$$

Denote a diagonal positive definite matrix $M = \text{diag}(\mu_i)$, $i = 1, \dots, n$, $\mu_i > 0$. A state-space representation is LQG balanced if

$$S_c = S_e = M \quad (6)$$

In this case, μ_i , $i = 1, \dots, n$, are the LQG characteristic values of (A, B, C) (see Jonckheere and Silverman [7] and Opdenacker and Jonckheere [11] for weights $Q = C^T C$ and $V = B B^T$, and Gawronski [3] for a general case of weights).

Let (A, B, C) be a state-space triple of the open-loop antenna in the Moore balanced representation. For a diagonal weight matrix $Q = \text{diag}(q_i I_2)$, $i = 1, \dots, n$, the solution S_c of Eq. (5a) is as follows [3]:

$$\begin{aligned} S_c &\cong \text{diag}(s_{ci} I_2) \\ s_{ci} &\cong \frac{(\beta_{ci} - 1)}{2\gamma_i^2} \\ \beta_{ci}^2 &= \frac{1 + 2q_i \gamma_i^2}{\zeta_i \omega_i} \end{aligned} \quad (7a)$$

and for a diagonal $V = \text{diag}(v_i I_2)$, $i = 1, \dots, n$, the solution S_e of Eq. (5b) is

$$\begin{aligned} S_e &\cong \text{diag}(s_{ei} I_2) \\ s_{ei} &\cong \frac{(\beta_{ei} - 1)}{2\gamma_i^2} \\ \beta_{ei}^2 &= 1 + \frac{2v_i \gamma_i^2}{\zeta_i \omega_i} \end{aligned} \quad (7b)$$

It is shown in [3] that for flexible structures the Moore and the LQG balanced representations are approximately collinear, i.e., such that the transformation T from the first to the second requires only rescaling of the components

$$T \cong \text{diag} (t_1 I_2, t_2 I_2, \dots, t_n I_2) \quad (8a)$$

$$t_i = (s_{ci}s_{ei})^{1/4}$$

and the approximate balanced solution is a geometric average of S_c and S_e ,

$$M = \sqrt{S_c S_e} \cong \text{diag} (\mu_i I_2) \quad (8b)$$

$$\mu_i = \sqrt{s_{ci}s_{ei}}$$

$$i = 1, \dots, n$$

a result useful in the controller reduction.

C. Reduced-Order Controller

Although the size of the controller is equal to the size of the plant, it is crucial from an implementation point of view to obtain a controller of the smallest possible dimension that preserves the stability and performance of the full-order controller. In order to ensure the stability of the closed-loop system, the open-loop system (plant model) cannot be excessively reduced in advance. Therefore, controller reduction becomes a part of the controller design.

For a flexible structure, such as a DSN antenna, an LQG balanced approach [3] produces a stable reduced-order controller, for which the reduction index σ_i

$$\sigma_i = \gamma_i^2 \mu_i \quad (9)$$

ranks the importance of the controller states. It combines the open- and closed-loop characteristic values of a system.

The plots of the index σ_i for azimuth and elevation are shown in Fig. 11. In the azimuth-axis case, the index σ_i is small for $i \geq 10$ when compared to σ_i for $i \leq 9$. Thus, the azimuth-axis controller order is chosen to be 9.

The state-space representation (A, B, C) of the reduced azimuth-axis estimator is given in the Appendix, along with the controller gains $k_c = [k_p, k_i, k_f]$ and the estimator gains k_e .

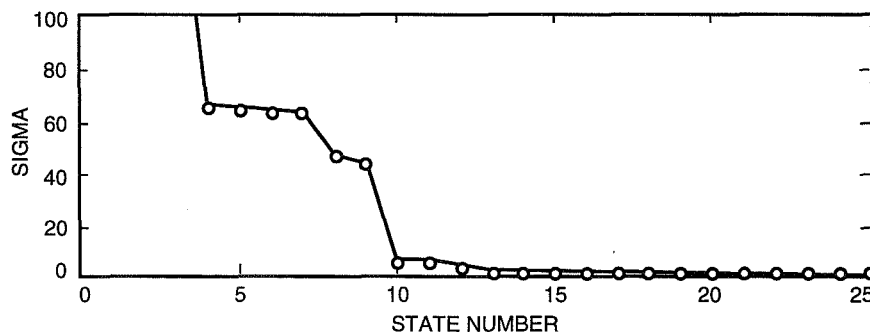


Fig. 11. Reduction index for the estimator model.

IV. Feedforward Controller

The tracking accuracy of fast moving objects can be improved if a PI controller is augmented with a feedforward loop (see [5,6]). A block diagram of the PI controller with the feedforward loop is shown in Fig. 12. In this block diagram, G , K , and F denote transfer functions of the antenna's rate loop, PI controller, and feedforward gain, respectively; r is a command; y is the output (elevation and azimuth angles); e is the tracking error in azimuth and elevation; and u is the plant input.

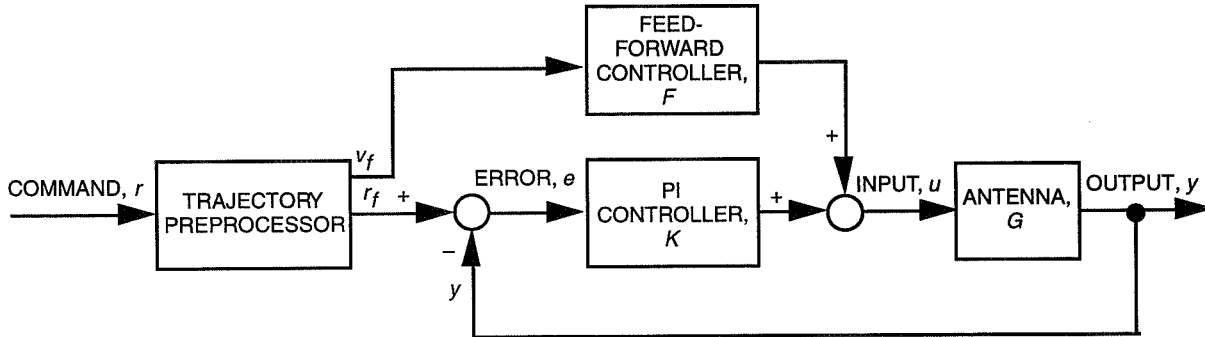


Fig. 12. Antenna PI-and-feedforward controller

In the absence of disturbances, perfect tracking ($e = 0$) is obtained for the feedforward gain F such that $GF = I$. In the case of the DSN antennas, this condition is satisfied in a low frequency range of $0 \leq f \leq 1$ Hz for $F = s$, since for these frequencies the plant transfer function G can be approximated with an integrator $G = 1/s$.

The DSS-13 antenna PI controller, with proportional gain $k_p = 0.5$ and integral gain $k_i = 0.5$ in azimuth and elevation, was investigated. The closed-loop transfer function (azimuth command to azimuth encoder) for a system with and without the feedforward gain is compared in Fig. 13.

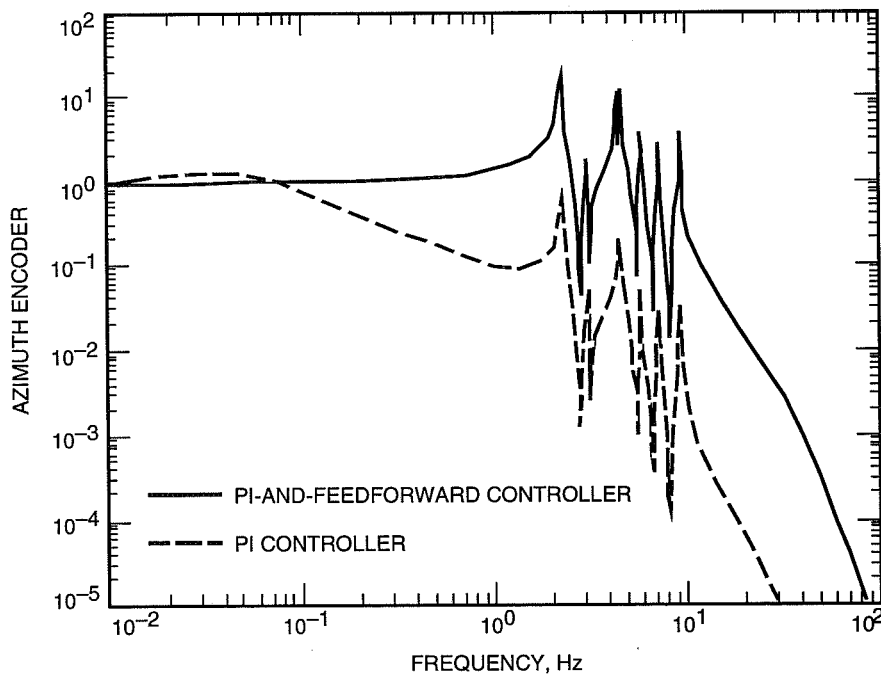


Fig. 13. Magnitude of transfer function of the PI-and-feedforward controller and the PI controller.

The figure shows that for frequencies up to 1 Hz, the system with the feedforward gain has better tracking properties when compared to the system without feedforward gain (good tracking properties are characterized by the unit value of the magnitude of the transfer function).

V. LQG-and-Feedforward Controllers

The controller performance is usually tested for tracking errors when following a command and for servo errors due to wind disturbances. Therefore, the tracking and disturbance rejection properties have to be traded off. The feedforward controller for the DSN antennas has good tracking properties, confirmed by both simulations and field measurements. Also, its performance during the slewing maneuver is satisfactory, since no limit cycling is observed. However, the feedforward controller's ability to compensate for wind action is insufficient, and its disturbance rejection properties are equivalent to those of a PI controller. On the other hand, the LQG controller is effective in suppressing wind-induced vibrations, but has weaker tracking properties.

When comparing the properties of feedforward and LQG controllers, one can conclude that by combining the two it is possible to improve both the tracking and disturbance rejection properties. The properties of a combination of the LQG and feedforward controllers were derived for a system configured as shown in Fig. 14. In this block diagram, G is the plant transfer function, G_y is the estimator transfer function from y to y_e , G_{yu} is the estimator transfer function from u to y_e , G_{uy} is the estimator transfer function from y to u_e , and G_u is the estimator transfer function from u to u_e . In determining the feedforward transfer function F , note that good tracking properties are required for low frequencies only (in our case, for frequencies up to 1 Hz). For these frequencies, $G_{yu} \cong 0$ and $G_y \cong 1$; thus, $y_e \cong y$. For the system as in Fig. 14 (assume transfer function of the trajectory preprocessor equal to 1, i.e., $r = r_f$),

$$\begin{aligned}
 e &= r - y_e \\
 y &= Gu \\
 u &= Fr + Ke + G_f G_u u + G_f G_{uy} y \\
 y_e &= G_{yu} u + G_y y
 \end{aligned}
 \tag{10}$$

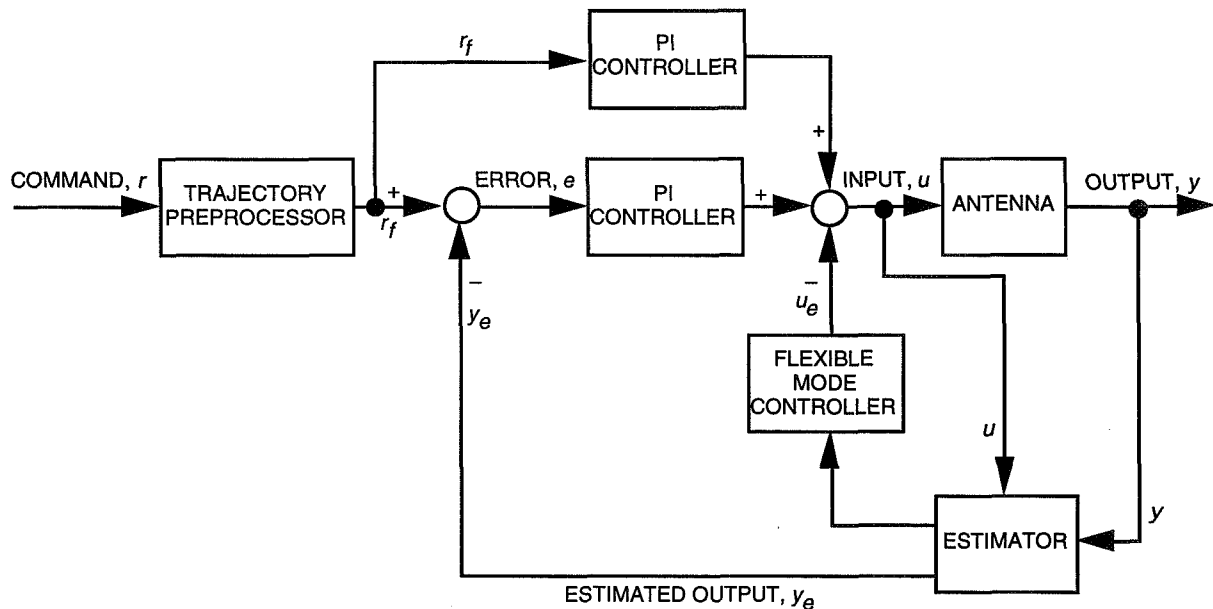


Fig. 14. Antenna LQG-and-feedforward controller.

From these equations, one obtains

$$e = \frac{H - G_{yu}F - G_yGF}{H + G_yGK + G_{yu}K}r \quad (11)$$

$$H = 1 + G_fG_u + G_fG_{uy}G$$

The servo error is eliminated (i.e., $e = 0$) if the numerator of the above transfer function is zero. This is true for the following feedforward transfer function:

$$F = \frac{1 + G_fG_u + G_fG_{uy}G}{sG_{yu} + G_y} \quad (12)$$

For the low frequencies ($f < 2$ Hz), the following is true: $G = 1/s$, G_fG_u is constant ($G_fG_u = k_u$, where k_u is the dc gain of G_fG_u), $G_{yu} \cong 0$, $G_y = 1$, and $G_fG_{uy} \cong k_{uy}s$. Thus, F in Eq. (12) represents a differentiator

$$F = k_{ff}s \quad (13)$$

$$k_{ff} = 1 + k_u + k_{uy}$$

with the gain $k_{ff} = 1 + k_u + k_{uy}$, called the feedforward gain.

The result, Eq. (13), was tested as follows: The LQG controller was configured as in the previous section; the dc gains were $k_u = 2.23$, $k_{uy} = -0.58$. The maximal tracking errors of this LQG controller with a feedforward gain were observed in the simulations for different values of the gain k_{ff} and are shown in Fig. 15. The minimum tracking error is achieved for the feedforward gain $k_{ff} = 1 + k_u + k_{uy} = 2.65$.

VI. Performance Evaluation

The position errors due to disturbances and for a trajectory that approaches antenna rate and acceleration limits are used as performance measures of the antenna position controllers. The performance of the LQG and feedforward controllers for the DSS-13 antenna (Fig. 1) was evaluated through simulations and tested in the field. For this antenna, the rate limit is set to 0.36 deg/sec, and the acceleration limit is set to 0.2 deg/sec². The acquisition and tracking of the trajectory shown in Fig. 7(a) was measured. At time 0 sec, the spacecraft is at position 24 deg, and the antenna is at position 22 deg. The trajectory preprocessor was activated in this case, and the preprocessed trajectory is shown in Fig. 7(a), dashed line.

For the PI controller ($k_p = 0.5$, $k_i = 0.5$), the tracking error is shown in Figs. 16(a) and (b). Figure 16(a) shows the transient tracking error due to the initial step. Figure 16(b) is a zoom of the same tracking error plot in Fig. 16(a), which gives a higher resolution view of the magnitude of the tracking error. The maximal value of the error is 28 mdeg (see also Table 1), which is beyond the required accuracy of 5 mdeg.

The acquisition of the trajectory for the same PI controller with a feedforward gain and without a trajectory preprocessor is shown in Fig. 17(a). After acquiring the target, the maximal tracking error is 2.5 mdeg [Fig. 17(b)]. However, there are poorly damped oscillations present in these data plots.

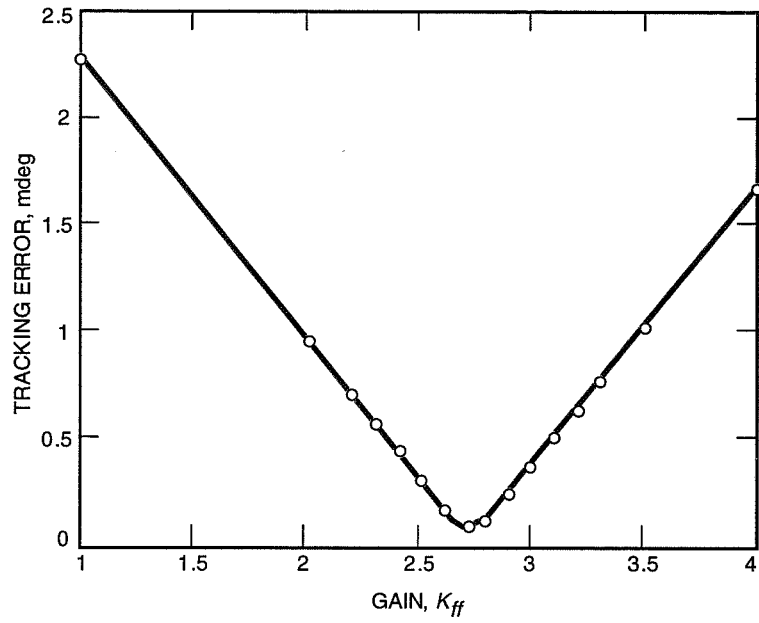


Fig. 15. Servo error versus feedforward gain.

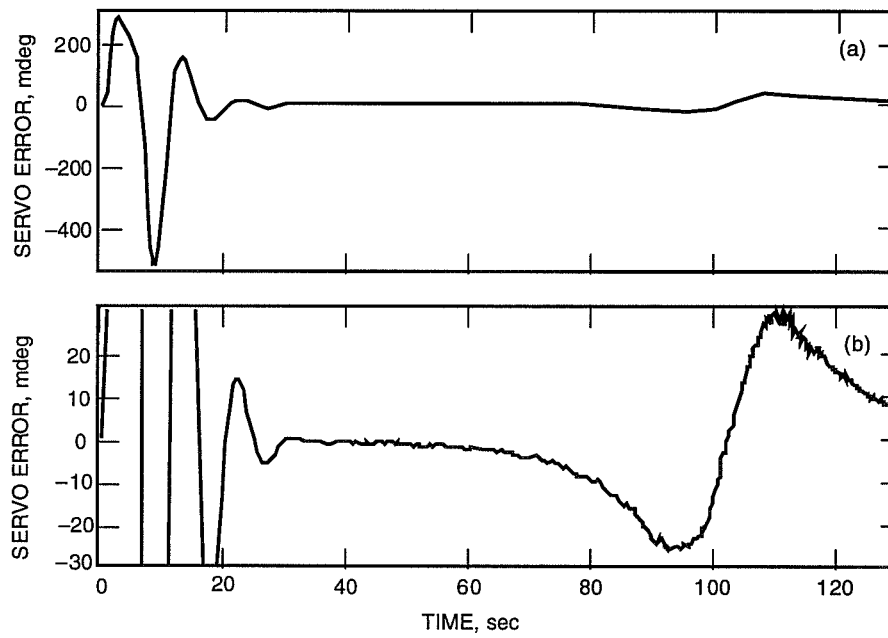


Fig. 16. Servo error of the PI controller: (a) general view and (b) zoomed.

Table 1. Tracking and disturbance errors, mdeg.

	PI	FF	LQG	LQG + FF
Tracking error, maximal	28.6	0.7	3.6	0.1
Disturbance error, rms	3.2	3.6	0.4	0.5
Measured error, maximal	28.0	2.5	3.7	1.5

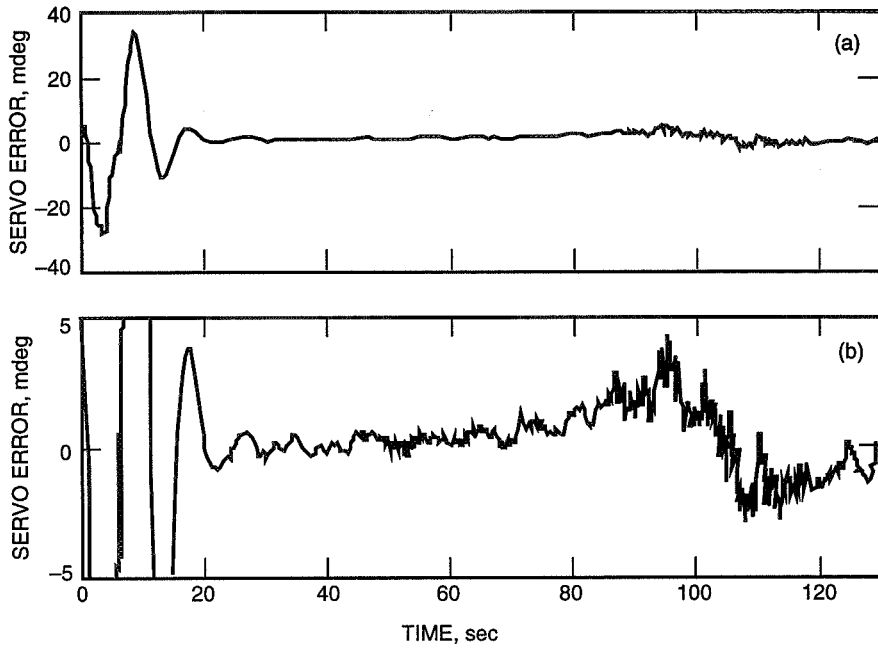


Fig. 17. Servo error of the PI-and-feedforward controller: (a) general view and (b) zoomed.

The performance of the LQG controller with the PI gains $k_p = 12$, $k_i = 10$ was measured and is shown in Fig. 18. The maximal tracking error is 3.7 mdeg, as in the case of the feedforward controller, but the flexible deformations were much more effectively damped by the LQG controller. The LQG controller with the PI parameters $k_p = 12$, $k_i = 10$ and a feedforward loop (for the feedforward gain $k_{ff} = 3$) was tested. The results are shown in Fig. 19. They show a very small tracking error of 1.5 mdeg and flexible mode suppression that is similar to the LQG controller.

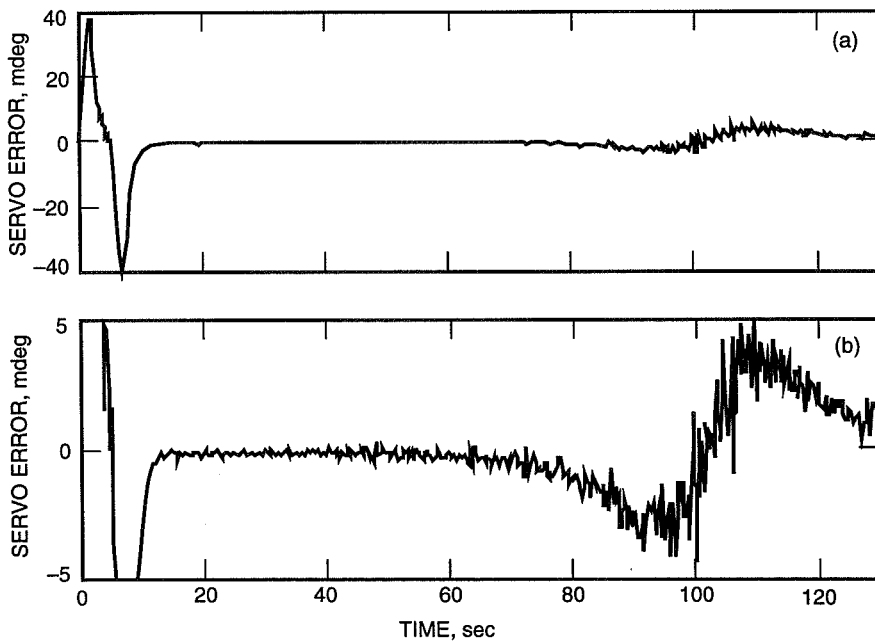


Fig. 18. Servo error of the LQG controller: (a) general view and (b) zoomed.

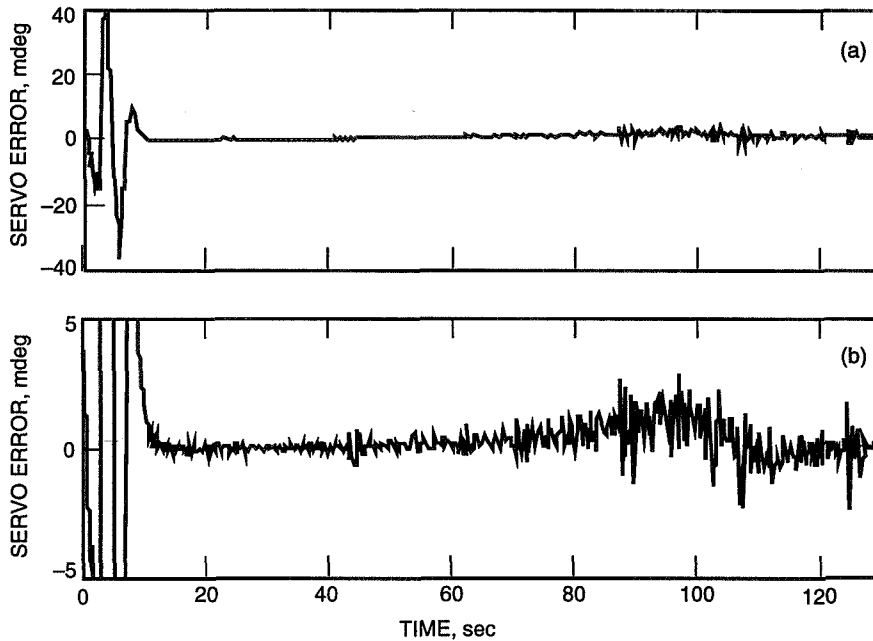


Fig. 19. Servo error of the LQG-and-feedforward controller: (a) general view and (b) zoomed.

The accuracy of the antenna model was tested by comparing measured (solid-line) and simulated (dashed-line) data in Fig. 20 for the case of the LQG controller with PI gains $k_p = 12, k_i = 10$. The figure shows good agreement between the two data sets (which would improve in the absence of encoder faults).

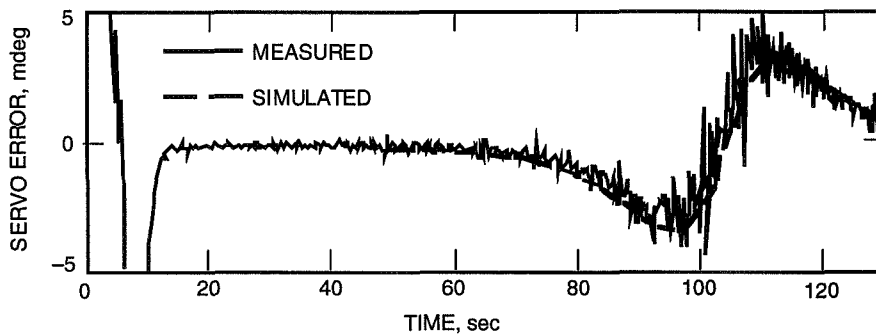


Fig. 20. Comparison of the measured and simulated error of the LQG controller.

The disturbance rejection properties of the presented controllers were simulated. The use of simulations instead of field measurements is justified for two reasons. First, it is difficult, if not impossible, to repeat the same disturbance conditions in the field so that fair comparisons could be made. Secondly, the accuracy of the antenna model has been proved experimentally. The disturbance white noise, w , with standard deviation 0.005 deg/sec, was added to the input u . This noise intensity is approximately equivalent to a 50-km/hr wind acting on the antenna. The simulation results (rms error, mdeg) are shown in the second row of Table 1. The results show good disturbance rejection properties of the LQG and LQG-with-feedforward controllers, when compared with PI and PI-with-feedforward controllers. Note the good coincidence of simulated and measured results for the PI and the LQG controllers. For these

controllers, the signal-to-noise ratio was high. On the other hand, for the feedforward and the LQG-with-feedforward controllers, the signal-to-noise ratio was low. Hence, this signal was engulfed in noise, and the evaluation of tracking error from the noisy measured data could only be approximated within the noise level.

VII. Conclusions

The new controllers were designed and tested to improve the DSN antenna tracking performance. The measures of such improvement are the reduction in position error for a trajectory that approaches antenna rate and acceleration limits, and the reduction in position error due to disturbances. The results of running the new control algorithms on the DSS-13 antenna show an improvement in the performance of the LQG, feedforward, and LQG-with-feedforward controllers over the existing PI controller. On the other hand, the feedforward controller achieves good performance while remaining simple (avoids the complexity of the estimator and preprocessor), but its ability to suppress disturbances is limited. The LQG controller alone shows greatly improved disturbance rejection properties. However, the most improved performance was observed for the combined LQG-and-feedforward controller. It had very small tracking and disturbance-induced errors.

The trajectory preprocessor was introduced as a necessary part of the implementation of the LQG controller, so that tracking and slewing could be accomplished with one algorithm. In the current operation, the PI controller requires separate modes for tracking and slewing, due to the limit cycling that occurs in the latter. However, the preprocessor can also be implemented with the existing PI controller to combine tracking and slewing into a single mode.

Acknowledgments

The authors would like to thank Ben Parvin and Michael Thorburn for their support and encouragement.

References

- [1] J. S. Bendat and A. G. Piersol, *Random Data: Analysis and Measurement Procedures*, 2nd ed., New York: Wiley, 1986.
- [2] W. Gawronski, "Design of a Linear Quadratic Controller for the Deep Space Network Antennas," accepted for publication in *Journal of Guidance, Control, and Dynamics*; also, *Proceedings of the 1992 AIAA Guidance, Navigation, and Control Conference*, Hilton Head, South Carolina, pp. 1399–1408, 1992.
- [3] W. Gawronski, "A Balanced LQG Compensator for Flexible Structures," accepted for publication in *Automatica*; also, *Proceedings of the 1993 IEEE American Control Conference*, San Francisco, California, 1993.
- [4] W. Gawronski, "Design of the Reduced LQG Compensator for the Deep Space Network Antennas," *Proceedings of the 1993 AIAA Guidance, Navigation, and Control Conference*, Monterey, California, pp. 243–253, 1993.

- [5] W. Gawronski and J. A. Mellstrom, "Antenna Servo Design for Tracking Low-Earth-Orbit Satellites," accepted for publication in *Journal of Guidance, Control, and Dynamics*; also, *Proceedings of the 1994 AIAA Guidance, Navigation, and Control Conference*, Scottsdale, Arizona, August 1-3, 1994.
- [6] W. Gawronski and J. A. Mellstrom, "Control and Dynamics of the Deep Space Network Antennas," *Control and Dynamic System*, edited by C. T. Leondes, vol. 67, San Diego, California: Academic Press, 1994.
- [7] E. A. Jonckheere and L. M. Silverman, "A New Set of Invariants for Linear Systems—Application to Reduced Order Compensator Design," *IEEE Trans. Automat. Control*, vol. AC-28, no. 10, pp. 953-964, 1983.
- [8] J.-N. Juang, *Applied System Identification*, Englewood Cliffs, New Jersey: Prentice Hall, 1994.
- [9] J.-N. Juang, M. Phan, L. G. Horta, and R. W. Longman, "Identification of Observer and Kalman Filter Markov Parameters: Theory and Experiment," *Proceedings of the AIAA Guidance, Navigation, and Control Conference*, New Orleans, Louisiana, pp. 1172-1179, 1991.
- [10] H. Kwakernaak and R. Sivan, *Linear Optimal Control Systems*, New York: Wiley-Interscience, 1972.
- [11] P. Opdenacker and E. A. Jonckheere, "LQG Balancing and Reduced LQG Compensation of Symmetric Passive Systems," *Int. J. Control*, vol. 41, no. 1, pp. 73-109, 1985.
- [12] C. S. Racho and W. Gawronski, "Experimental Modification and Identification of the DSS-13 Antenna Control System," *The Telecommunications and Data Acquisition Progress Report 42-115*, vol. July-September 1993, Jet Propulsion Laboratory, Pasadena, California, pp. 42-53, November 15, 1993.

Appendix

Controller Data

The following are the numerical values for the estimator triple (A, B, C) , where $C^T = [C_p^T \ C_f^T]$, and for the gains k_p, k_i, k_f, k_e :

$$A = \begin{bmatrix} 1 & -0.01955 & 0.18642 & -0.03930 & 0.12127 & 0.01232 & 0.08334 & -0.07823 & -0.09326 \\ 0 & 0.95945 & -0.20718 & -0.00937 & -0.00554 & -0.00758 & -0.00154 & -0.00485 & 0.00974 \\ 0 & 0.20718 & 0.97580 & -0.00508 & -0.00194 & -0.00415 & -0.00051 & -0.00222 & 0.00489 \\ 0 & -0.00037 & 0.00508 & 0.85543 & -0.49999 & -0.00046 & -0.01739 & -0.00905 & 0.01219 \\ 0 & 0.00554 & -0.00194 & 0.49999 & 0.85764 & -0.04976 & 0.00209 & -0.01013 & 0.02416 \\ 0 & -0.00758 & 0.00415 & -0.00046 & 0.04976 & 0.91026 & -0.38398 & -0.01464 & 0.03037 \\ 0 & 0.00154 & -0.00051 & 0.01739 & 0.00209 & 0.38398 & 0.92094 & -0.00771 & 0.01805 \\ 0 & 0.00485 & -0.00222 & 0.00905 & -0.01013 & 0.01464 & -0.00771 & 0.93139 & 0.33443 \\ 0 & 0.00974 & -0.00489 & 0.01219 & -0.02416 & 0.02037 & -0.01805 & -0.33443 & 0.83555 \end{bmatrix}$$

$$B^T = 0.01 \times [0.231 \ 1.785 \ -0.395 \ 0.485 \ -0.211 \ 0.395 \ -0.055 \ -0.230 \ -0.479]$$

$$C_p = [1 \ 0 \ 0 \ 0 \ 0 \ 0 \ 0 \ 0 \ 0]$$

$$C_f = [0_{8 \times 1} \ I_8]$$

$$k_p = 12$$

$$k_i = 10$$

$$k_f = [17.163 \ 13.586 \ 6.300 \ 1.829 \ 4.929 \ 1.869 \ 0.231 \ -3.299]$$

$$k_e^T = [0.9955 \ -0.1098 \ 0.2217 \ -0.1710 \ 0.2090 \ -0.1000 \ 0.1682 \ 0.0131 \ -0.0785]$$

20 31
19734
P. 27

1995/08212
324462
27P

A Radio Telescope for the Calibration of Radio Sources at 32 Gigahertz

M. S. Gatti and S. R. Stewart
Ground Antennas and Facilities Engineering Section

J. G. Bowen and E. B. Paulsen
Radio Frequency and Microwave Subsystems Section

A 1.5-m-diameter radio telescope has been designed, developed, and assembled to directly measure the flux density of radio sources in the 32-GHz (Ka-band) frequency band. The main goal of the design and development was to provide a system that could yield the greatest absolute accuracy yet possible with such a system. The accuracy of the measurements have a heritage that is traceable to the National Institute of Standards and Technology. At the present time, the absolute accuracy of flux density measurements provided by this telescope system, during Venus observations at nearly closest approach to Earth, is ± 5 percent, with an associated precision of ± 2 percent. Combining a cooled high-electron mobility transistor low-noise amplifier, twin-beam Dicke switching antenna, and accurate positioning system resulted in a state-of-the-art system at 32 GHz. This article describes the design and performance of the system as it was delivered to the Owens Valley Radio Observatory to support direct calibrations of the strongest radio sources at Ka-band.

I. Introduction

NASA is planning to use the 32-GHz frequency band for communication and navigation of future deep space missions. Precise performance estimates of ground station capability are needed for both mission planning and technology development. To meet this need, a plan has been developed at JPL to determine with high accuracy the absolute gain of Deep Space Network (DSN) antennas.

At the present time, only estimates of the fluxes of celestial objects are available, since there have been no direct observations using highly calibrated telescopes, only extrapolations. A program that utilizes a 5-m-diameter radio telescope at the Owens Valley Radio Observatory (OVRO), operating at 32 GHz, is underway to observe a list of radio sources. If the gain of that antenna is accurately known, then the flux density of the sources may be accurately calculated. It therefore became necessary to calibrate the OVRO antenna to the highest accuracy possible. This article describes the instrument used to perform that calibration.

In order to minimize antenna-gain measurement error, we have developed a radio telescope intended to be a standard gain tool to measure the flux density of celestial radio sources. This telescope uses a highly efficient 1.5-m offset-feed Cassegrainian optics configuration. The aperture efficiency of this telescope

has been measured at nearly 80 percent. The telescope uses a radiometer with a high-electron mobility transistor (HEMT) low-noise amplifier (LNA) and a pair of feeds to operate in a beam-switching mode.

II. System Requirements

The stated goal of the 32-GHz calibration is to improve the accuracy of radio source flux densities from the present value of 20 percent (± 0.8 dB) to 10 percent (± 0.4 dB). However, in order to achieve a final result of this magnitude, the OVRO 5-m radio telescope that performs the direct observations must have knowledge of its gain to approximately 7 percent (± 0.3 dB). Thus, any standard gain calibrator telescope total error must be able to calibrate the flux of a source to approximately 5 percent (± 0.2 dB) total error.

JPL had a 1.5-m offset-feed Cassegrainian antenna left over from previous experimentation. Using this as the basis for our standard gain calibrator fixes many parameters. Specifically, the aperture size of the standard gain antenna is such that at 32 GHz, only the strongest radio sources can be used if a reasonable signal-to-noise ratio (SNR) is expected. We therefore expect the planet Venus to be the best calibrator. A plan was developed for simultaneous observations with both the OVRO 5-m antenna and the 1.5-m standard gain antenna during the summer of 1993, when that planet's approach was closest to Earth. Future articles will detail the results of those measurements.

The selection of a calibrator source and the desire to make 5-percent measurements allow one to calculate the SNR necessary for the system. In this case, it is expected that the measurement precision will be approximately 2.5 percent of the measurement, i.e., a radiometer SNR of 16 dB. In order to derive specific radiometer requirements, we define the minimum detectable signal of the radiometer, ΔT_{min} , and compare it with the expected flux of the source, in our case Venus. This minimum detectable signal is given by [1,2]:

$$\Delta T_{min} = \frac{2T_{sys}}{\sqrt{\tau B}} \quad (1)$$

where T_{sys} is the system operating noise temperature, τ is the system time constant, and B is the system bandwidth. The factor of 2 comes from the use of a Dicke radiometer where the source is observed for only one-half the time.

The signal part of the SNR will be in the form of an increase in system temperature of the radiometer signal when the system is pointed to the source, in our case Venus. The maximum possible signal that can be produced by a radio telescope is given by [1,2]:

$$\Delta T_{100\%} = \frac{SA_p}{2kC_r} \quad (2)$$

where S is the source flux in $\text{Wm}^{-2}\text{Hz}^{-1}$, A_p is the physical area of the receiving antenna, k is Boltzmann's constant (1.38062×10^{-23} J/K), and C_r is the correction for sources that are not true points with respect to the antenna beamwidth. For the 1.5-m antenna, the source size correction factor C_r is never more than 1.001.

The equation for the SNR of our system can now be written

$$SNR = \frac{\Delta T_{100\%}}{\Delta T_{min}} \quad (3)$$

For the expected flux of Venus during the time of our calibrations ($S = 950$ Jy, where $1 \text{ Jy} = \text{Janskys} = 10^{-26} \text{ Wm}^{-2}\text{Hz}^{-1}$) and a desired $\text{SNR} = 16 \text{ dB} = 40$, one may calculate the radiometer minimum detectable signal required from Eqs. (2) and (3) to be 0.0152 K . This will put a strain on any radiometer at this frequency; however, by allowing a large bandwidth, a reasonable 1-sec SNR can be achieved. The expected system temperature of our 1.5-m telescope was 75 K , and the system hardware was operable over a 3-GHz bandwidth, limited mostly by the feedhorn. Therefore, when coupled with the required minimum signal, the selection of 3 GHz indicated that in 1 sec an SNR of 23 dB can be attained. This does not require herculean effort and provides a margin on the SNR for the real-world variations that often degrade the ΔT_{min} . As the signal is reduced due to Venus' increasing distance after April 1, 1993, the SNR will also decrease. This can be easily overcome by more averaging, i.e., integration time. Careful analysis of the standard deviations of the measurements will be required to assure that enough SNR is attained to achieve 2.5-percent measurement precision.

The pointing requirement on this system was developed as a result of the desire that there be no more than a 1-percent loss due to mispointing. This 1-percent loss translates to a beam-pointing error of no more than 0.03 deg . This error is split up between the feed support and the tracking-system tolerances.

The final requirement is on the type of radiometer itself. External effects of the environment, specifically the atmosphere fluctuations, are often on the order of kelvins. To achieve levels in units of millikelvins for the detected signal, a radiometer that is insensitive to external fluctuations is required. In order to overcome the problem of external fluctuations, a radiometric technique known as beam switching will be employed. This technique uses two antenna beams that sense signals on the sky at the same elevation but at different azimuths. By rapidly switching between the two signals and calculating the difference, one can infer the signal level of a source that is in one of the beams but not in the other. A summary of the performance requirements for the system is given in Table 1 below.

Table 1. Performance requirements for the standard calibrator telescope.

Parameter	Required value/type	Comment
Antenna size, m	1.5	Fixed
Signal SNR, dB	16	To provide 2.5% precision
Minimum ΔT , mK	0.0152	From SNR
Bandwidth, GHz	3	From SNR
Time constant, sec	1	May vary as required
System temperature, K	75	Desired best achievable
Total pointing error, deg	0.030	1% loss
Radiometer	Dicke BSR	Eliminate atmosphere

III. High-Gain Antenna

The requirement for having two secondary beams on the sky separated by a fixed angle in azimuth was met by employing two feedhorns that were laterally displaced from the focal point of the reflector system by a fixed amount. Microwave transmission lines (waveguides) then route the two signals to the Dicke circulator switch and on to the low-noise amplifier. This section describes the design of the antenna system, including the feed design, and the placement of the feeds with respect to the reflector focal point.

A. Antenna Description

The antenna used in this system consists of an offset-feed Cassegrainian reflector system, which is shown in Figs. 1 and 2. This type of configuration is also commonly called a clear-aperture antenna

system because there are no blockages due to feed and subreflector supports in the aperture of the antenna. Some of the advantages of this configuration are that it (1) allows for very precise and accurate analytical performance prediction, (2) eliminates the scattering and noise temperature effects common to feed and subreflector support struts, (3) provides higher efficiency systems, and (4) reduces sidelobe levels. A key advantage associated with the ability to make accurate performance predictions is that there is yet another way to eliminate concern regarding the calibration of the system as a whole.

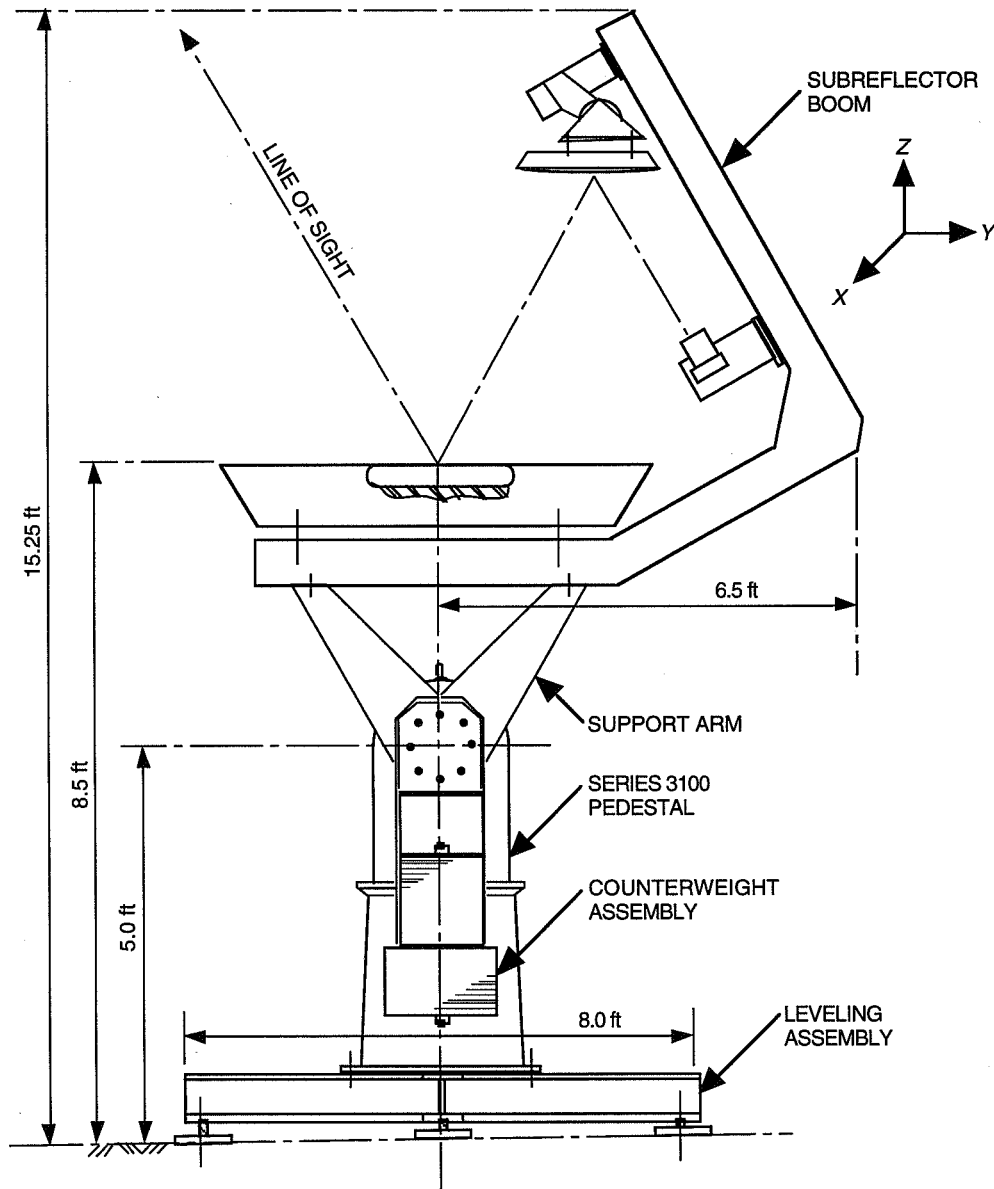


Fig. 1. The standard gain calibrator, 1.5-m diam.

The beamwidth of the antenna is defined by the size of the reflector and the feed pattern. For this system, maximum gain was primary, as the sidelobe levels would be minimized by the lack of aperture blocking in the system. The two antenna beams are reflections of each other about a vertical plane centered at the focal point of the reflector. They have the same beamwidths of 0.430 deg. The beams are separated from each other in azimuth by 1.0 deg and are at the same elevation angle for all positions of the antenna by using an elevation-over-azimuth positioner. The crossover point for each beam occurs on

the mechanical boresight of the antenna and is at a level of approximately -22.6 dB. Due to the electrical scanning of each beam, there are no significant sidelobes from one beam inside the other beam; however, on the opposite side of each beam, the first sidelobe level is -14.8 dB from the peak of the beam. The gain of the antenna at each feed input is 52.8 dBi.

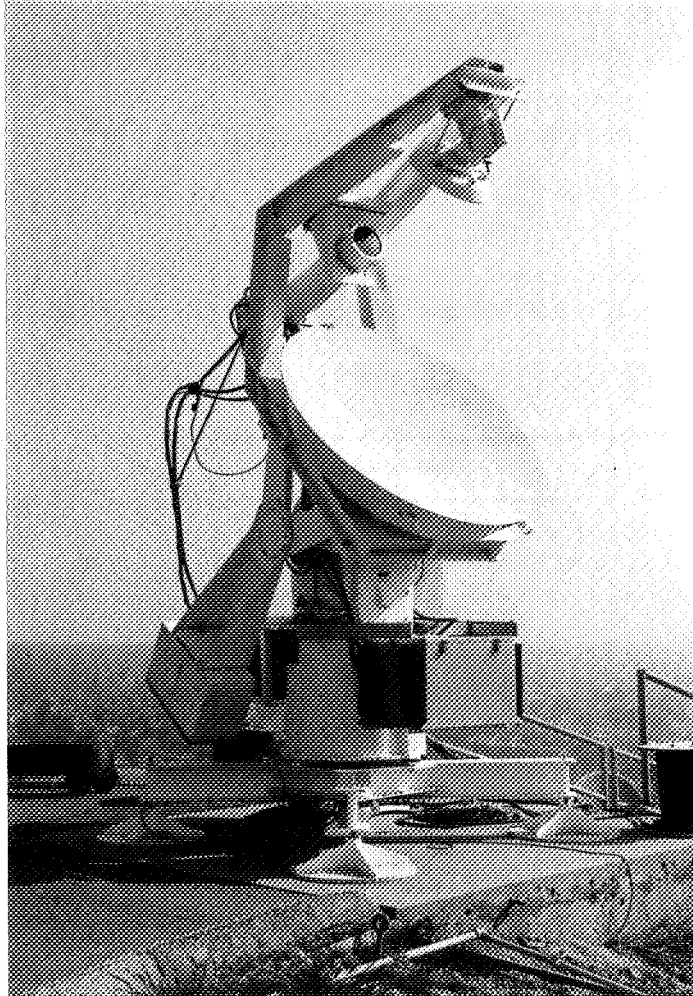


Fig. 2. The reflector system.

B. Structure and Feed Supports

Since this system will be used as a standard with which measurements will be compared, the mechanical stability of the support structure is critical. Analysis was done to determine the maximum allowable deformations of the subreflector support due to gravity. This analysis was based on the requirement to have no more than a 0.025-deg beam-pointing error due to gravity distortions. The analysis used a baseline case of a feed that was placed in a Cassegrainian system with all mirrors exactly aligned. Parametric changes of the subreflector and feed positions were then input and subsequent performance calculations were made. The results of these calculations are shown in Figs. 3-6. Figures 3, 4, and 5 show the beam-pointing error for subreflector movement in the x -, y -, and z -directions, as defined in Fig. 1. Figure 6 shows the gain degradation of the system for motion of the subreflector in the z -direction.

Figures 7 and 8 show the beam-pointing errors for motions of the feed in the x - and y -directions. Note that for these analyses, the nominal case is for a feed that is placed at the focal point of the system, not the final configuration of the feed laterally displaced from the focal point, as required to develop the scanned beam on the sky. As a result of these analyses, the mechanical support for the feed and the subreflector were designed to be stiff enough to meet the requirements given in Table 2.

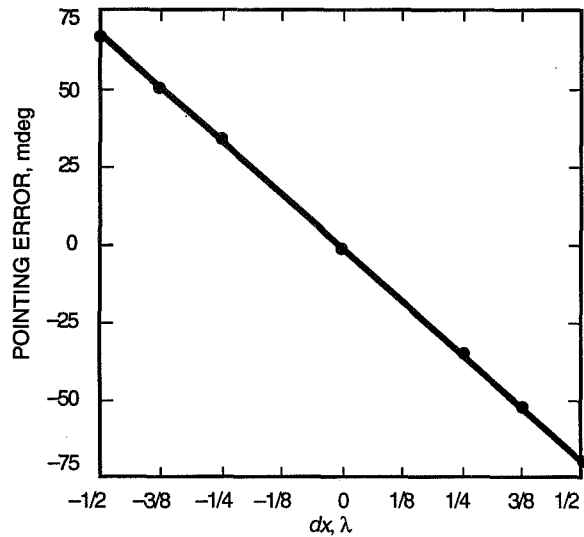


Fig. 3. Clear aperture antenna-beam pointing error due to subreflector movement in the X direction, Y polarized source, E_y field component, $\phi = 0$ deg.

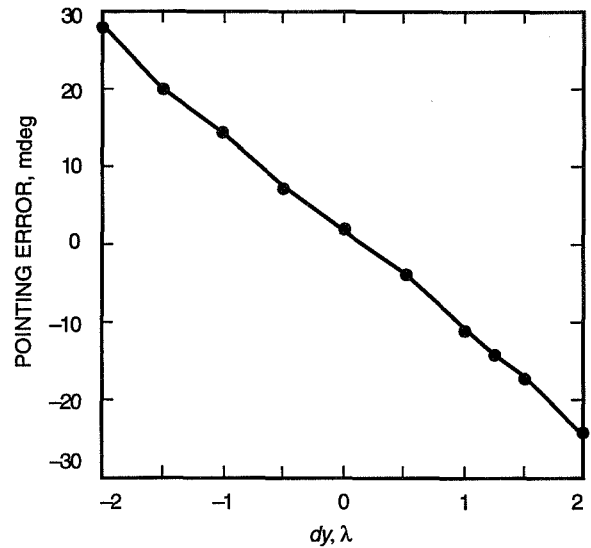


Fig. 4. Clear aperture antenna-beam pointing error due to subreflector movement in the Y direction, $\phi = 90$ deg, E_y field component, Y polarized source.

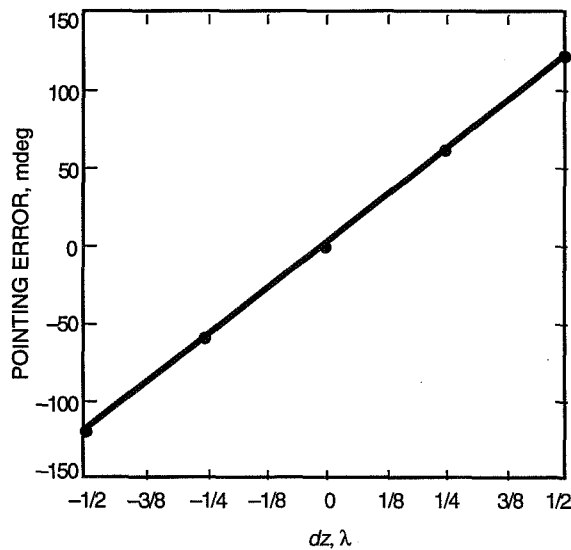


Fig. 5. Clear aperture antenna-beam pointing error due to subreflector movement in the Z direction, $\phi = 90$ deg, E_y field component, Y polarized source.

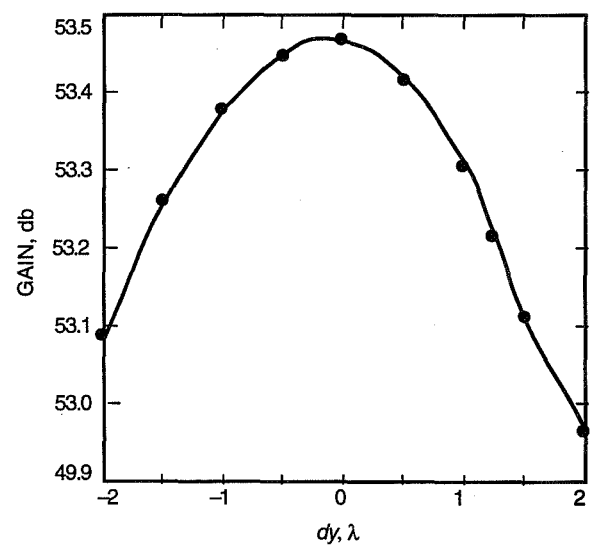


Fig. 6. Clear aperture antenna-gain degradation due to subreflector movement in the Y direction, $\phi = 90$ deg, E_y field component, Y polarized source.

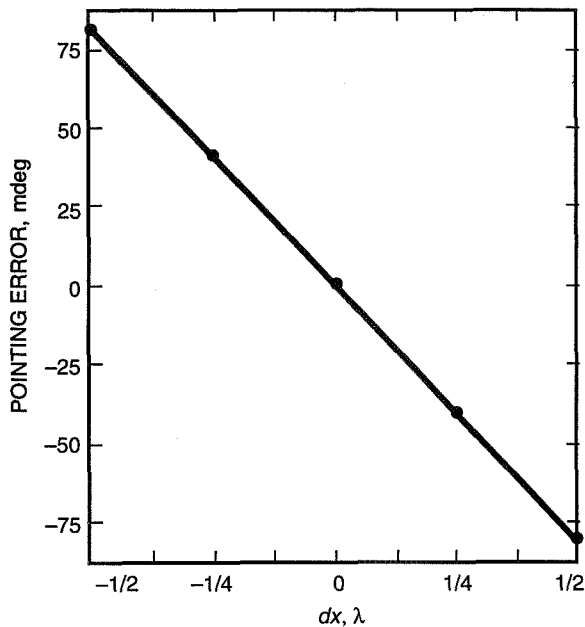


Fig. 7. Clear aperture antenna-beam pointing error due to source horn movement in the X direction, $\phi = 0$ deg, E_y field component, Y polarized source.

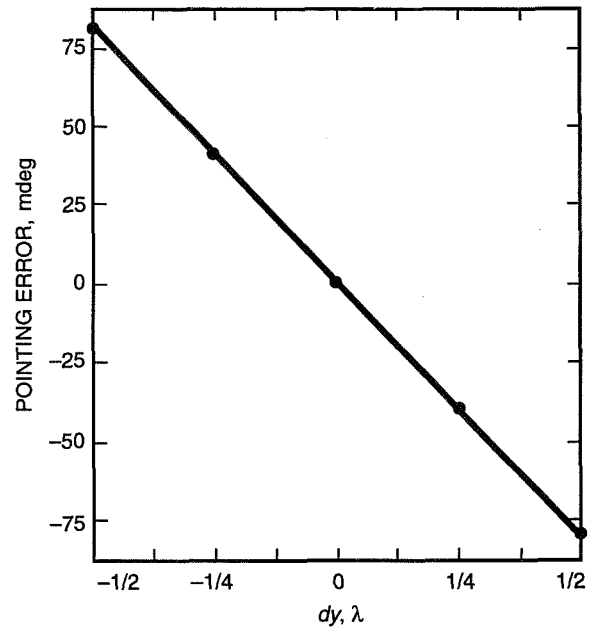


Fig. 8. Clear aperture antenna-beam pointing error due to source horn movement in the Y direction, $\phi = 90$ deg, E_y field component, Y polarized source.

Table 2. Mechanical tolerances for the motion of the subreflector and the feed system.

Direction of motion	Subreflector limits, λ	Feed limits, λ
Δx	± 0.160	± 0.135
Δy	± 0.500	± 0.140
Δz	± 0.100	± 0.250

C. Feed Design and Placement

The main reflector and subreflectors used in this system were inherited from a previous program commissioned to investigate the use of clear-aperture antennas for high-efficiency systems [3]. The focal length-to-diameter ratio, f/D , of the system had, therefore, been previously set. In order to obtain maximum gain, the feed must provide the proper illumination function, and for this system a 22.6-dBi gain feed is required. However, there is some choice of the type of feed that can be made to provide this illumination. For this system a Potter horn [4] was chosen. This horn typically provides ± 5 percent bandwidth, or ± 1.6 GHz, for a center frequency of 32 GHz, which is acceptable for the ± 1.5 -GHz bandwidth of the radiometer; however, it is the limiting factor in the system. The design of the feedhorn is shown in Fig. 9. This horn is circular in cross section and provides nearly uniform illumination in orthogonal planes due to its multimode aperture distribution. The generation of the two modes is done by the mode generator at the input of the horn, and proper phasing of the modes is accomplished by selection of the proper combination of the mode generator length and the step height of the horn input. These details are described by Potter [4].

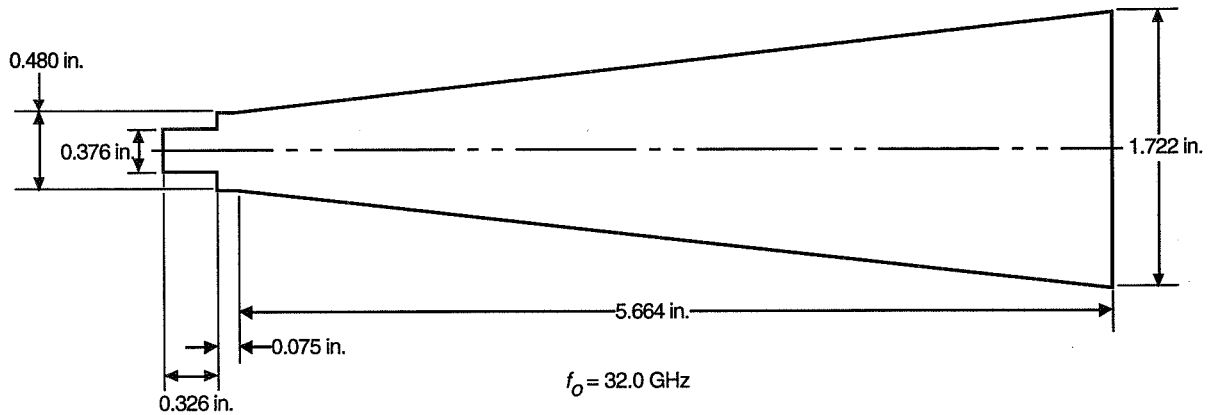


Fig. 9. Potter horn used as feed for 1.5-m antenna, $G = 21.95$ dBi.

By using the results of the previous tolerance analysis on beam scan versus x -axis motion (Fig. 3), one can calculate the required displacement necessary for providing a beam on the sky that is 0.5 deg off the mechanical axis of the antenna, so that each beam is 1.0 deg apart from the other. The slope of the line in Fig. 3 is 0.162 deg scan/ λ displacement. Therefore, a 0.5-deg scan requires 3.09λ ($= 2.90$ cm) displacement in the x -direction.

A second concern regarded the axial placement of the feedhorn with respect to the focal point of the reflector system. All the analyses assumed properly focused feeds. As is typical with flared horns, the phase center of the horn is some distance behind the aperture of the horn. A parametric study was done to determine the position of the feed phase center. This was done by calculating the total antenna gain (excluding all losses) as a function of the feed axial focus position. The actual feed pattern calculated for this horn was used in the analysis. Figure 10 shows the result of that study, where all distances are given with respect to the aperture of the feed. The conclusion is that the optimum gain occurs when the feed is placed with its aperture 0.725 in. closer to the subreflector, i.e., the feed phase center is behind the feed aperture by that distance.

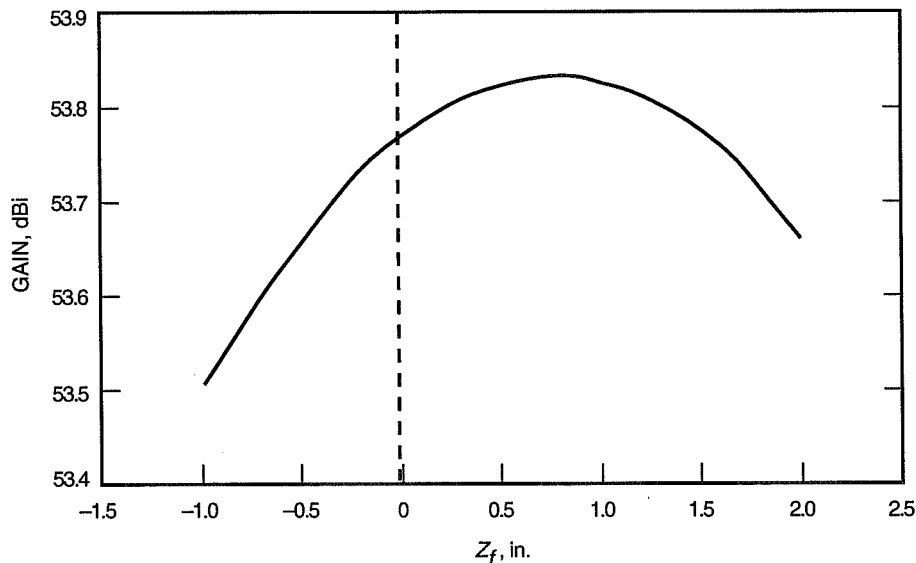


Fig. 10. Antenna gain as a function of feed placement. Position is given with respect to feed aperture; $+Z$ is toward the subreflector.

Figure 11 shows the final configuration of the two horns used to develop the two antenna beams on the sky. To check this, a computer analysis of the antenna system was made in which the feed was displaced by 3λ ($= 2.8$ cm) from the focal point. For the 0.162-deg scan/ λ displacement, the 3λ displacement should yield a scan of 0.486 deg. As seen in Fig. 12, the beam peak occurs at 0.483 deg off the boresight of the antenna—extremely close to what was predicted. This gives us good confidence that the model is accurate and that a 0.5-deg beam scan will be achieved by a displacement of 3.09λ ($= 2.90$ cm).

D. Performance Predicts

The performance predicts were done using a physical optics model of the antenna system. This model uses actual measured data for the main reflector and subreflector, both of which were shaped to provide the maximum possible efficiency. Furthermore, the pattern from a 22.6-dBi gain feedhorn was used as the illuminating source. This is the same model used for the analysis used to determine the mechanical tolerances for the structure described above. An analysis was done with the information regarding the feedhorn size, gain, and placement with respect to the phase center of the reflector system. The gain, beamwidth, and sidelobe predictions are based on the feedhorn being displaced by 3λ from the optical phase center of the reflector system. These results are shown in Fig. 12. Table 3 shows the predicted values of the parameters. The beam location is predicted by using the slope of the scan angle versus lateral displacement, as given by Fig. 3, and is defined to be 0.5 deg from the mechanical boresight. The beam scan of 0.5 deg for each beam implies that the separation of the beams is 1.0 deg.

Table 3. Performance predictions for the 1.5-m telescope.

Parameter	Prediction	NIST calibration
Antenna gain, dB		
Beam A	53.09	53.04
Beam B	53.09	52.96
Antenna efficiency, percent		
Beam A	80.6	79.7
Beam B	80.6	78.25
Half-power beamwidth, deg	0.430	0.430
Azimuth angle between beams, deg	1.0	1.0
Azimuth angle from beam to mechanical boresight, deg	0.5	0.5
Elevation angle between beams, deg	0	0.02
First sidelobe level, dB		
Beam A	-17	-15
Beam B	-17	-14
First sidelobe location, deg	0.58	0.625

E. NIST Calibrations

The fact that very accurate calculations of the system performance can be made does not relieve one from making independent measurements of the system, especially since the system will be used as a standard reference. Therefore, the antenna system and feeds were shipped to the National Institute of Standards and Technology (NIST) in Boulder, Colorado. The system was then characterized in the near-field facility for the parameters of interest, as described in the previous section. As part of the NIST calibrations, a method was devised to disassemble and then reassemble the system with extremely repeatable results. This method depended on placing retroreflectors on all the removable items: the subreflector, the main reflector, the support structure, and the positioning system. Tests at NIST proved that the antenna could be dismantled into its major components and then reassembled with no measurable changes in performance.

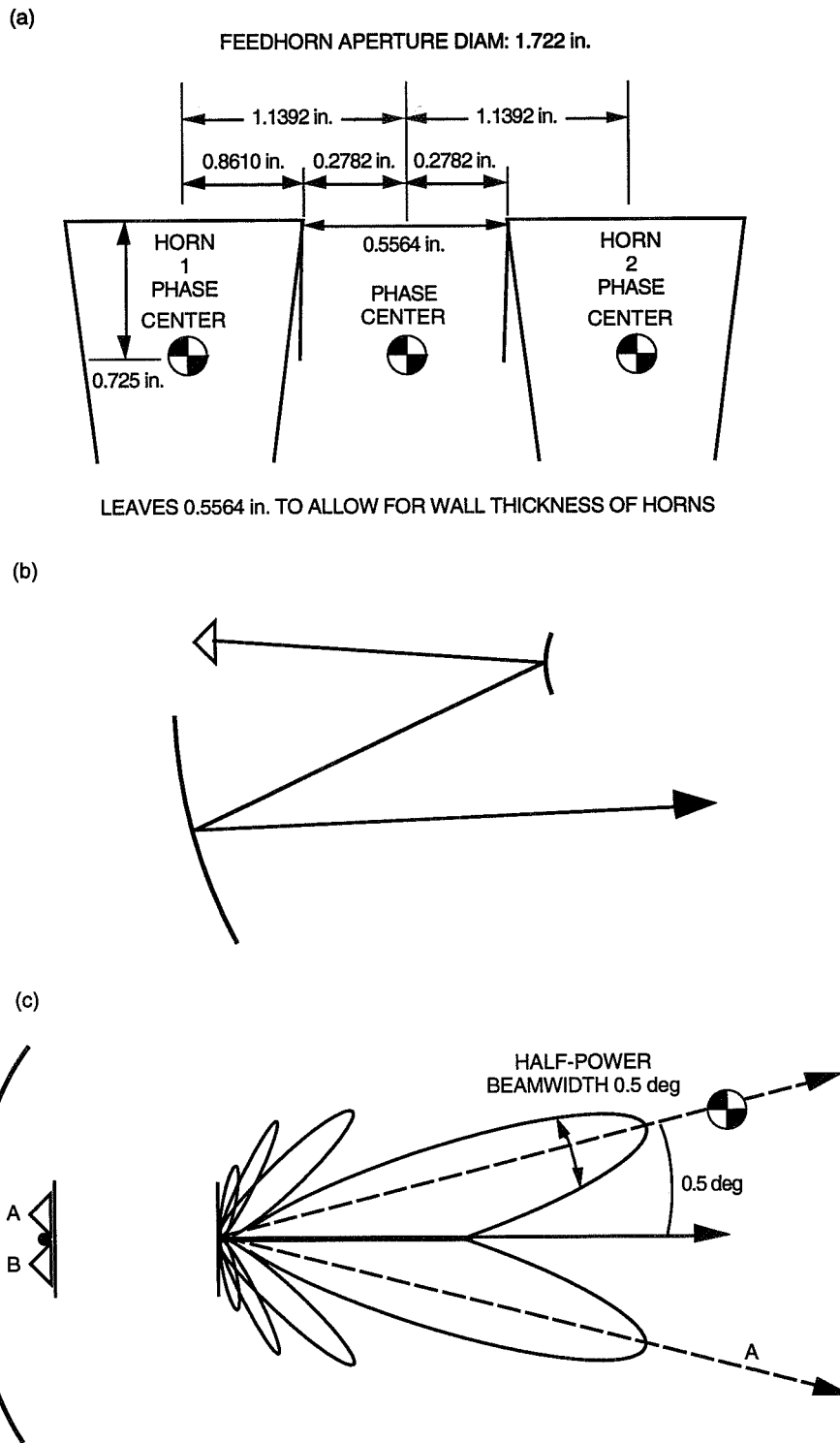


Fig. 11. Twin feedhorn layout to generate scanned antenna beams: (a) detailed layout showing the relationship between horn phase center and reflector system phase center; (b) sideview of the general layout showing the relationship between feeds, the reflector system, and antenna beams on the sky; and (c) top view of the general layout.

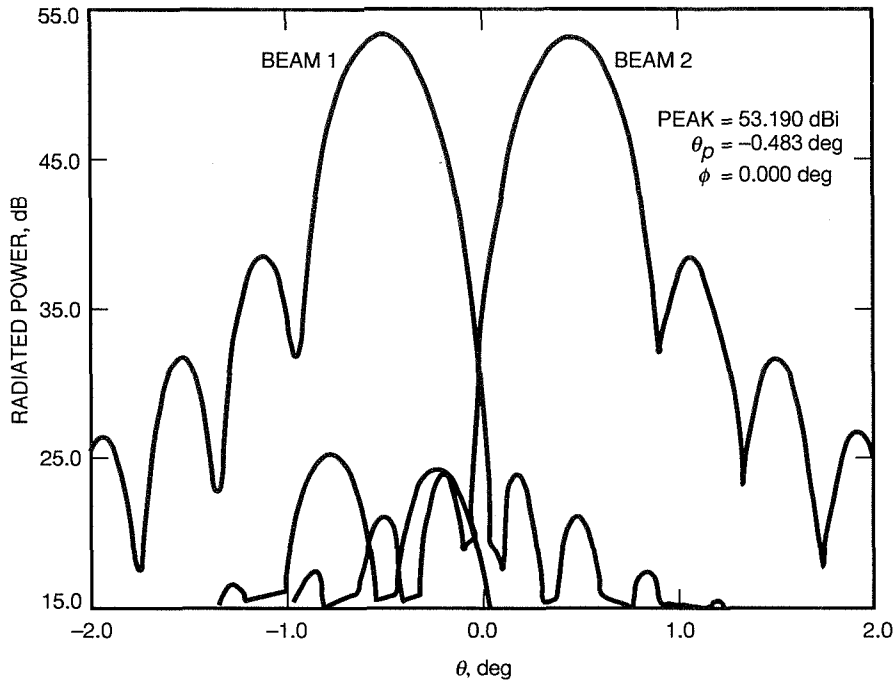


Fig. 12. Predicted telescope antenna patterns for feed lateral displacements of three wavelengths.

The system was characterized at three frequencies and at two elevation angles. The frequencies were at 31.8, 32, and 32.3 GHz. The two elevation angles were 0 and 22.5 deg. The purpose of the multiple elevation-angle measurements was to determine any possible gain dependency with elevation. The measurements did not indicate any measurable gain dependency with elevation, and the only gain dependency with frequency was accounted for by the theoretical expectations, i.e., by $1/\lambda^2$. The results are given in Table 3 and show a very good comparison to the predicted values, as described in the previous section. A typical pattern of the high-gain antenna is given in Fig. 13. Detailed results of the NIST calibrations may be found in [5].

IV. Radiometer Design

A. Radiometer Type

The radiometer to be used is a balanced Dicke radiometer [6], as shown in Fig. 14. Signals from the high-gain antenna are transmitted to the front end of the radiometer via either of two identical antenna beams on the sky. The term for this type of radiometer is a beam-switching radiometer. The radiometer includes a noise diode to perform both the sky signal calibration and radiometer linearity measurements. The front-end controller includes a switch to select one or the other of the two beams. All these items are contained within the cryogenic refrigerator. The back-end equipment consists of a single-stage, double-sideband downconverter that provides an intermediate frequency (IF) of 45–1700 MHz, a 1500-MHz filter, a square-law detector, a Stanford Research Systems SR-510 digital lock-in amplifier, and a square-wave generator. A computer is provided to control the entire system and to acquire and store the measured data.

B. Front-End Section

1. RF Components. The RF receiver consists of a cryogenically cooled 32-GHz high-electron mobility transistor (HEMT), a low-noise amplifier (LNA), and an ambient temperature follow-up amplifier. The LNA is mounted in a vacuum vessel with a closed-cycle refrigerator (CCR). This vacuum vessel is mounted on the antenna below the focal point.

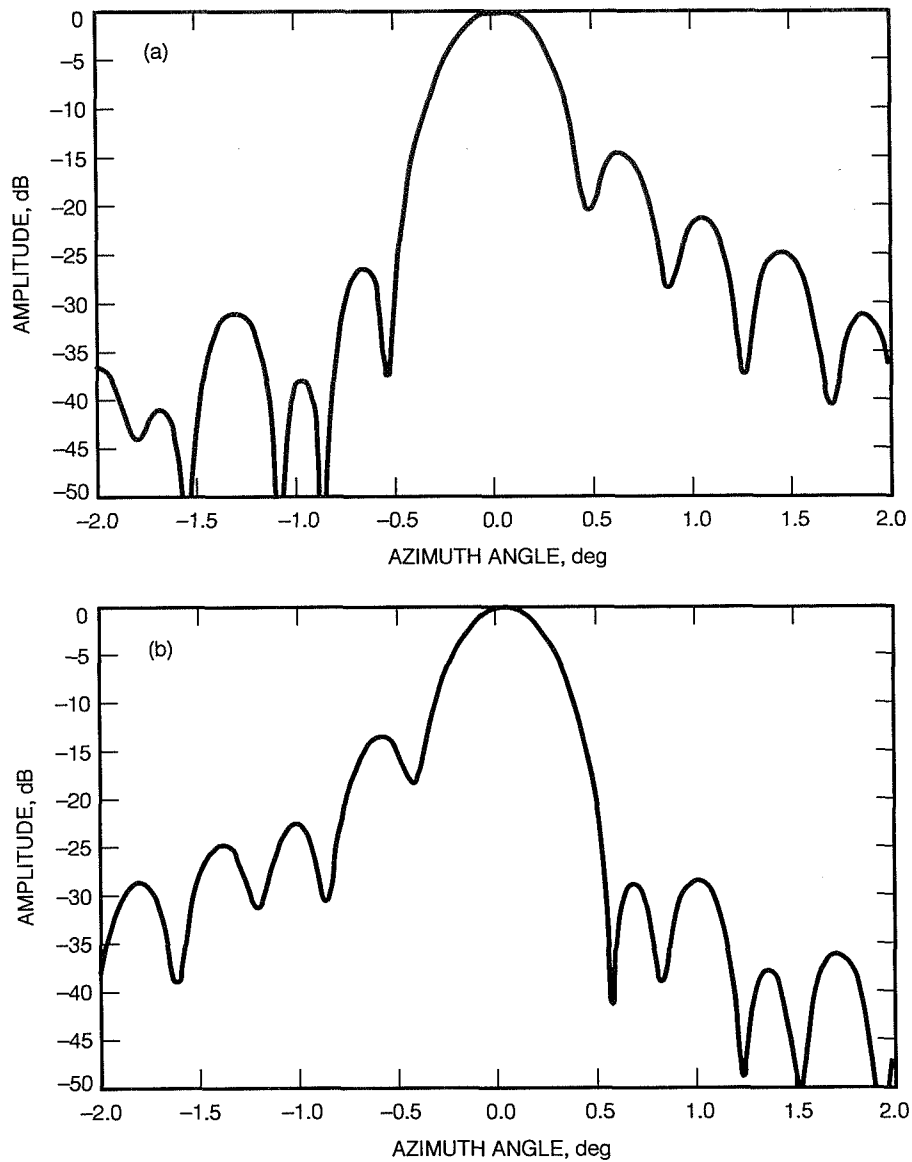


Fig. 13. Clear aperture antenna azimuth patterns as measured by NIST in the near-field facility: (a) beam A and (b) beam B.

The feeds and their associated mode generators, tapers, and vacuum windows are mounted to the top plate of the vacuum vessel. The top plate provides circular waveguide feedthroughs. Inside the vacuum vessel are waveguide sections that provide thermal insulation but are very low loss. This low loss is accomplished by using copper waveguide suspended in a fiberglass tube. The waveguide is only connected at the cooled junction, with the fiberglass tube providing the structural support [7].

Following the waveguide insulators are round-to-rectangular (WR-28) transitions that feed the microwave energy to hybrid polarizers. The left circularly polarized (LCP) port is terminated and the energy is tapped from the right circularly polarized (RCP) port. At this point, 30-dB waveguide cross-guide couplers are placed in the signal paths, which allow signal injection from a noise diode that is located outside the vacuum vessel.

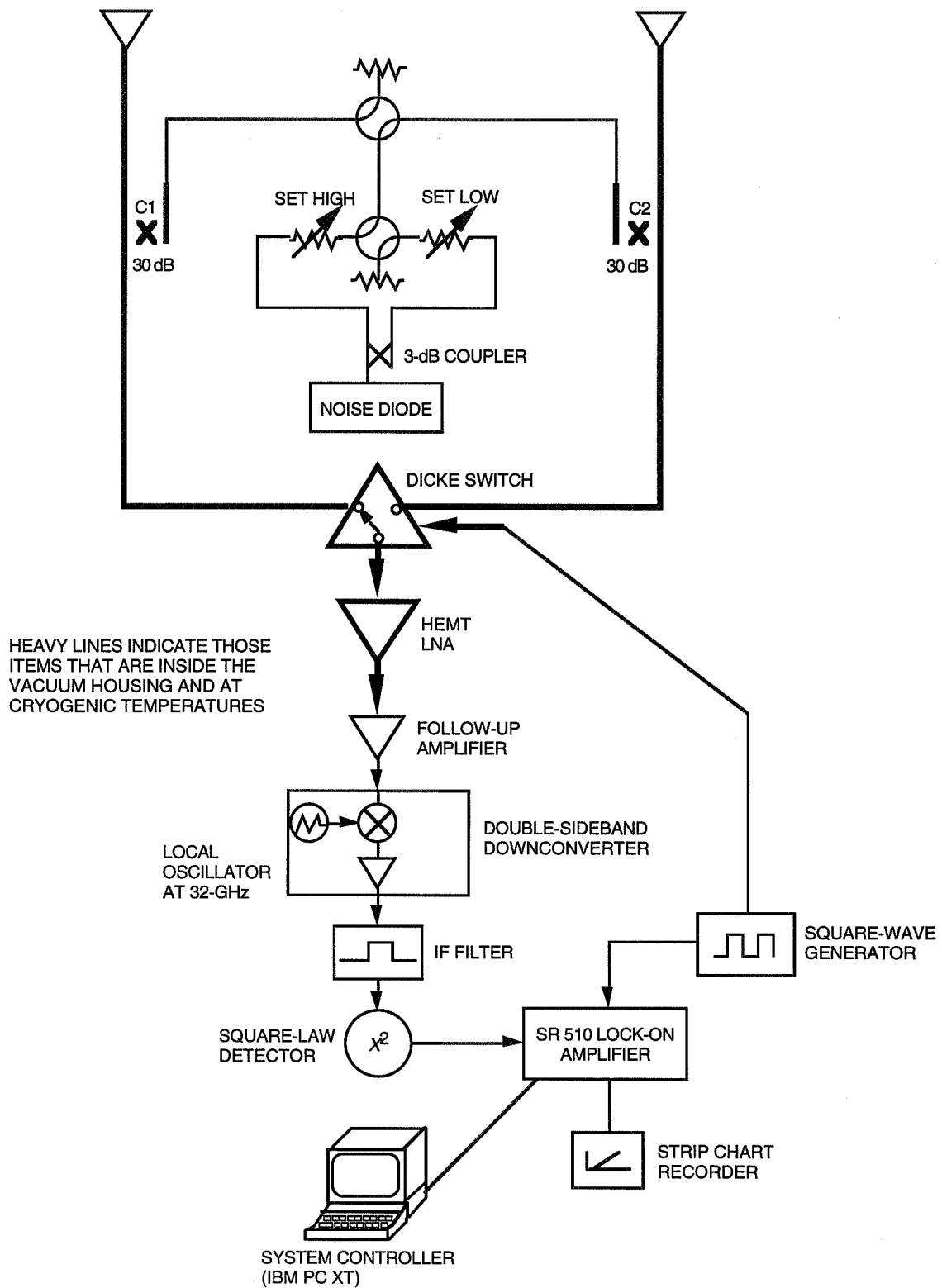


Fig. 14. The 32-GHz clear aperture antenna radiometer.

The outputs of the separate feeds are sent to a (Dicke) switching circulator. This switching circulator is a WR-28 circulator manufactured by Electromagnetic Sciences, Inc. It provides more than 20-dB isolation with less than 0.3 dB of insertion loss and is tuned for 32 GHz at a 77-K physical temperature. From the circulator, the selected feedhorn is coupled to the LNA input isolator. This isolator provides a consistent match for the LNA input while loss is less than 0.25 dB at 12 K.

The LNA is a four-stage amplifier built by the National Radio Astronomy Observatory (NRAO). This amplifier uses four Fujitsu FHX10X transistors in a single-ended design. At 32 GHz and 23 K, the amplifier provides 28 dB of gain at a 49-K noise temperature.

At the output of the amplifier is another isolator. The signal is then coupled out of the vacuum vessel through the bottom plate of the vessel using WR-28 waveguide.

2. Controls. Attached to the pedestal of the telescope is an instrumentation box. This instrumentation box has four major items: a servo power supply for the LNA, a vacuum gauge, a thermometer, and a control panel for routing power to all components and control of waveguide switches. In parallel with the control panel in the instrumentation box is a remote control panel in the control trailer that provides the operator with remote control over all receiver components. There is also a downconverter assembly box that is attached to the front end of the radiometer. This assembly contains the downconverter, a dc control assembly, and the noise injection assembly.

The dc control assembly contains a portion of the control relay switching and power conversion. Attached to this box is the Dicke beam-switching circulator control. This assembly derives its power and control from the dc control assembly. The switching circulator requires a very short, high-voltage pulse to change the field polarity of the circulator. This pulse is controlled by an assembly provided by Electromagnetic Sciences and only requires transistor-transistor logic (TTL) switching levels.

3. Noise Injection. Inside the downconverter assembly is a noise diode with an excess noise ratio (ENR) of 23 dB. Two waveguide switches are in series, which permits selection of one of two sources and selection of which input arm the source is coupled to. The noise diode is mounted to a proportional heater assembly to maintain a fixed temperature. A waveguide switch allows connection of the noise diode to either input feed. A second waveguide switch was incorporated to permit selection of a second signal injection source, if desired. This second port is normally terminated with an ambient 50-ohm waveguide load. The signal sources are transmitted out of the downconverter assembly and into the vacuum vessel in the WR-28 waveguide. Inside the vacuum vessel, the signal is routed to the cross-guide couplers, which are located in front of the switching circulator.

4. Cryogenics. The vacuum vessel consists of an aluminum tube 0.61-m tall with standard 0.20-m flanges at each end. All feedthroughs pass through the end plates. Mounted on the bottom plate is a CTI-Cryogenics model 350, two-stage, Gifford-McMahon refrigerator. This refrigerator cools the low-noise amplifier to 12 K. The refrigerator is driven by a model SC compressor from the same manufacturer. The top plate of the vacuum vessel has bolted to it a housing that covers the feedhorns. This housing has a Kapton window in its top and is charged with nitrogen to prevent condensation. Inside the vacuum vessel, surrounding the microwave components, is a thermal radiation shield, which is kept at 70 K by the first stage of the refrigerator.

5. Performance. As measured by NRAO, the amplifier (serial no. A11) exhibited a gain of 28 dB and a noise temperature of 48.4 K at 32 GHz and a 23-K physical temperature, referenced to the input of the amplifier. After installation in the radiometer, noise temperature was measured with reference to the input feedhorn and was 59.8 K. The physical temperature of the amplifier in this test was 17.6 K.

C. Intermediate Frequency

1. Downconverter. The downconverter assembly is underneath the vacuum vessel. The output from the vacuum vessel runs down through a waveguide filter and into the downconverter box. The signal

is amplified by an Avantek 32-GHz amplifier and coupled to a Watkins-Johnson mixer/YIG oscillator assembly and converted to the IF of 0–1700 MHz. This IF is then passed through a 1500-MHz low-pass filter. The filtered IF then is routed to the control trailer approximately 30 m away by a 7/8-in. hard line, where it is detected by the appropriate detector, as described below.

2. IF Path Performance. There were choices to be made with respect to locating the IF detector. The desire was to detect the IF as close to the downconverter as possible so as to minimize losses and other possible interferences. The detector was, therefore, placed in the downconverter assembly on the output of the low-pass filter. The first hint of a problem occurred when the system stability was found to be unacceptable. This problem was traced to the temperature variations of the detector as the ambient temperature changed. The first attempted fix was to temperature-stabilize the detector by placing it onto a heater unit. There were still problems with this, as the ambient temperature could change from 0 to 25 deg C in the course of a spring-type day at OVRO. We then decided to place the detector in the trailer, where the ambient temperature swings were controlled by the trailer heating and cooling system to ± 3 deg C. The detector was further wrapped in foam to minimize any residual changes in its temperature. The 7/8-in. hard line between the trailer and the antenna was selected in order to minimize the loss versus frequency of the IF signal between the control trailer and the antenna. Figure 15 shows the IF path performance of this system. The curves show the IF loss versus frequency at the output of the low-pass filter on the antenna and at the output of the hard line in the trailer. For reference, the output of the IF is also shown in the case where standard RG59 coaxial cable is used. It is obvious that the hard line essentially brings the IF into the trailer with very little attenuation.

D. Detection

The block diagram in Fig. 14 shows that there are two methods to perform radiometry: in total power mode and in beam-switching mode. While beam switching is the method used during the actual tracking of sources, the total power mode is necessary to determine system performance, noise diode level, linearity, and atmospheric loss. These two modes are described in more detail in this section.

1. Total Power Mode. In total power mode, the IF is switched into the HP 438A power meter. Further, the switching circulator, here called the Dicke switch, is latched into one position. The position is chosen by the operator and the proper control switches are set to cut the square-wave generator out and set the Dicke switch to the desired position. Once this is done, the computer is then run as a total power radiometer, as described in many recent works [8,9].^{1,2} The detector for this mode, an HP 438, is not the same as for the beam-switching mode; however, we would occasionally also employ an HP 3457A multimeter and use the same detector as used in the beam-switching mode to determine the system stability and linearity using that detector. This gave confidence in the system used during the beam-switching mode.

2. Beam-Switching Mode. The beam-switching mode of radiometry used for radio source observations has been described in several references [10–12]. The beam-switching mode is shown in Fig. 14, where the controls are set so that the square-wave generator provides the signal to the switching circulator and to the lock-in amplifier. The configuration of the circulator switch control, IF detection, square-wave generator, and lock-in amplifier are very closely related to the system described in [10]. A brief summary of how this system works follows.

¹C. T. Stelzried, *Microwave Radiometer Calibrations*, JPL D-10496 (internal document), Jet Propulsion Laboratory, Pasadena, California, January 29, 1993.

²L. J. Skjerve, *Preliminary Documentation of DSS-13 Radiometer Program*, JPL D-9292 (internal document), Jet Propulsion Laboratory, Pasadena, California, January 1990.

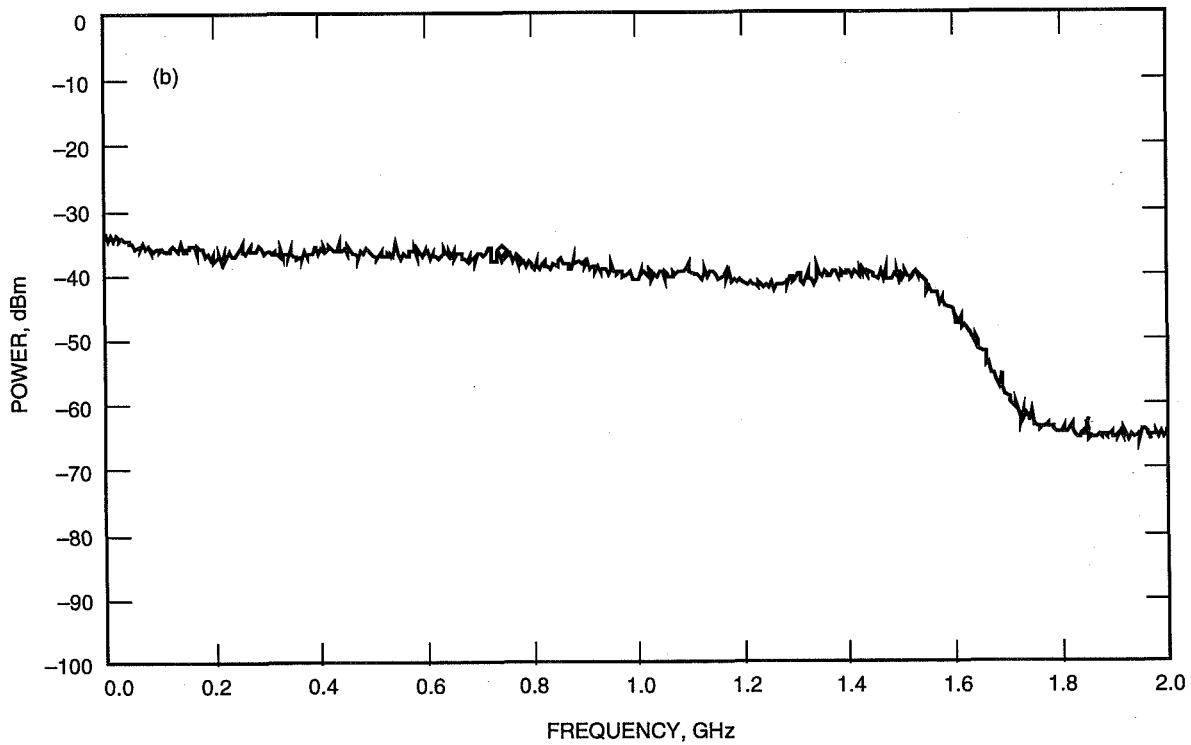
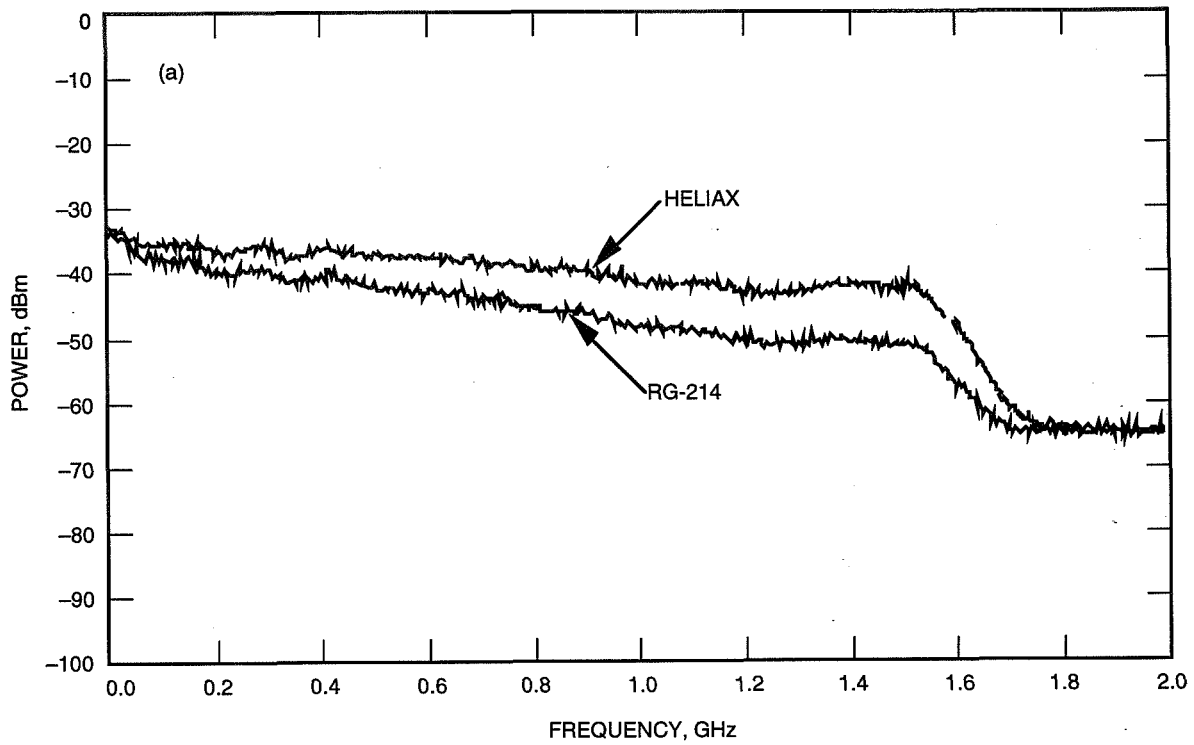


Fig. 15. Performance of the IF loss versus frequency between the antenna and the control trailer: (a) the IF signal as transmitted versus RG-214 to the control room, and (b) signal measured at the antenna pedestal.

The signal from the Dicke switch is a modulated square wave, the amplitude of which is the difference between the signals in the two beams. The lock-in amplifier demodulates this signal and produces the desired amplitude signal level. The computer is connected via a parallel data bus Hewlett Packard

interface bus (HPIB) to the lock-in amplifier. During the beam-switching mode, digital data are taken and a screen is generated that plots the difference signal as a function of time. If each antenna beam is observing the same target, such as the sky, and if the system is perfectly balanced, a zero signal from the lock-in amplifier will be recorded. When beam A is pointed to a radio source and beam B is off the source, the signal is proportional to the increase in system temperature due to the radio source. The output from a diode noise source is coupled into the waveguide of both beams and calibrates the system. The diode calibration was routinely switched on many times each hour as the radio sources were observed. With this procedure, the increase in system temperature produced by each radio source is calibrated and the adverse effects of gain variations in the HEMT and receiver are virtually eliminated.

E. Calibration

The calibration of the radiometer system is second in importance after the high-gain antenna calibration. Unlike the antenna-gain calibration, however, the radiometer calibration is done much more frequently. These calibrations quantify systematic errors and reduce random errors. Furthermore, the calibration of the system is done in both the total power mode and in the beam-switching mode.

In order to discuss the calibration of the radiometer, some quantities need to be defined. Specifically, the quantity that the radiometer measures is the operating system temperature, T_{op} . All other quantities are derived from this basic measurement, depending on the target that is in the beam of the high-gain antenna during the measurement.

The Institute of Electrical and Electronics Engineers (IEEE) definition of T_{op} is given by [13]

$$T_{op} = T_a + T_e \quad (4)$$

where T_a is the effective antenna temperature of the system looking towards the target at the reference plane where the measurement is defined, and T_e is the effective receiver temperature of the system looking towards the receiver at the reference plane where the measurement is defined. In our system, the following definitions are used:

T_{op} = operating system temperature

T_a = effective antenna temperature

T_e = effective receiver temperature

T_{sky} = temperature due to the sky contribution

T_{atm} = temperature due to the atmosphere

T_{gal} = 3.0-K cosmic background radio emission

T_{so} = temperature due to feed spillover

Furthermore,

$$T_a = T_{sky} + T_{so} \quad (5)$$

$$T_{sky} = T_{atm} + T_{gal} \quad (6)$$

The types of calibrations done in each mode, the purpose of each calibration, and the technique used to perform the calibration are described below.

1. Total Power Mode. Receiver Calibration. The receiver calibration is done to determine the effective receiver noise temperature, T_e , of the system.^{3,4} This measurement is important because the receiver noise temperature is assumed to be known in the remainder of the total power radiometer calibrations. This quantity consists of the noise temperature of the transmission lines between the feeds and the LNA, the LNA contribution, and the contribution of the equipment connected to the LNA. The aperture load technique was used in these measurements. A single receiver calibration consists of from 5–10 individual measurements of the system, providing an average and statistics to determine the validity of the data. The details of this measurement technique are described in [10] and are not repeated here. Normally, this quantity does not change over time by more than a few percent. Nevertheless, since the absolute accuracy of the calibrations is paramount, this measurement is done biweekly during observation times.

Total Power Radiometer Calibration. The measure of T_{op} done by the total power radiometer has been extensively described earlier [8,9,14].⁵ The system developed here calculates radiometer constants a_p , b_p , a_c , b_c , and c_c from a precalibration. The a_p and b_p constants are calculated for the case of a radiometer with a linear response. For the radiometer that has some active element in the beginning of its saturation curve, a nonlinear analysis results in the calculation of constants useful in providing corrected values of T_{op} . For this case, one needs to calculate the T_{op} from the linear analysis and then apply the nonlinear analysis coefficients a_c , b_c , and c_c . This is summarized by

$$T_{op} = a_p + b_p(P_m) \quad (7)$$

$$T_{op(nl)} = a_c + b_c(T_{op}) + c_c(T_{op}^2) \quad (8)$$

where the form of Eq. (8) is used when the linearity of the system as defined below is greater than 1.5 percent.

The precalibration consists of measuring the total noise power of the system while the antenna observes different targets. The targets are an ambient aperture load and the sky. Additionally, these measurements are done for two states of the noise diode: on and off. The information that results from these measurements yields not only the radiometer constants, but also the linearity of the system and the noise diode level. The system then performs repeated measurements of the system power, P_m , while applying the radiometer constants to yield T_{op} .

Radiometer Linearity. As mentioned earlier, a linearity metric of the system is a byproduct of the radiometer calibration. This linearity metric is the ratio of the noise diode level in kelvins, as measured while on the ambient load, $T_{nd(load)}$, and while on the sky, $T_{nd(sky)}$. This is written as

$$F_l = \frac{T_{nd(sky)}}{T_{nd(load)}} \quad (9)$$

It is important that only linear results are used in the measurement of radio sources in order to eliminate this effect from the list of possible systematic error sources. During the course of an observation track,

³ C. T. Stelzried, op. cit.

⁴ L. J. Skjerve, op. cit.

⁵ C. T. Stelzried, op. cit.

a set of precalibrations will be periodically done to track this factor (along with the gain and the noise diode calibration). Figure 16 shows a plot of the linearity factor as a function of time during a track done in the summer of 1993.

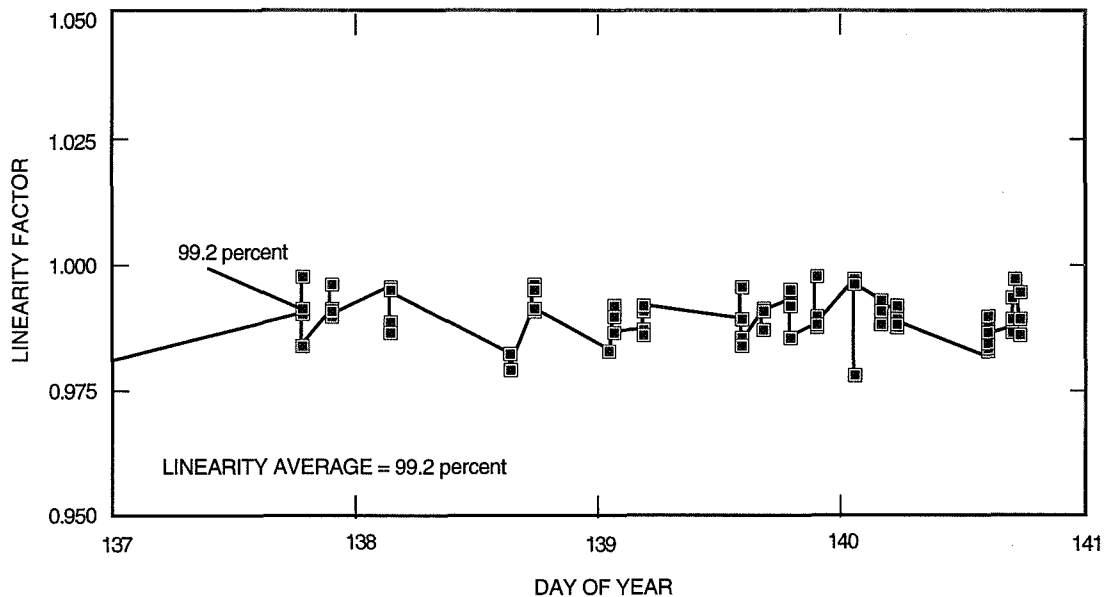


Fig. 16. Clear aperture system linearity for days 137–141 of 1993.

Noise Diode Calibration. Possibly the single most important calibration of the radiometer system is that of the noise diode. The level of noise temperature introduced by the noise diode to the system is critical because it is used to scale the final calibration of the radio-source temperature measurement. The calibration of the noise diode in the total power mode differs from the noise diode *measurement* performed while the radiometer is in the beam-switching mode, as described below. For this calibration, the radiometer constants are calculated as described above, and then the antenna is pointed to the zenith. The radiometer program is then capable of switching the diode on and off successively for a number of times selected by the operator. This number of times was generally chosen to be 15. The noise temperature was measured for each state of diode. The noise diode level was then calculated from the difference in the two system temperature measurements. It is thought that this is the most accurate method for calibrating the noise diode, since the time taken to perform the measurement is on the order of 2 min. For this time frame, the stability of the radiometer would be good and there could be little or no effect due to gain changes in the electronics. Other methods that could be used to calibrate the noise diode level include the measurement of the diode that is a byproduct of the linearity measurement described above; however, that measurement uses several targets and takes a considerably longer time to perform.

Radiometer Stability. For completeness, the stability of the radiometer was checked. The stability was measured while the ambient load was placed over the aperture of the feeds. The radiometer program then measures the load temperature, the system temperature, and noise diode levels. The system gain is calculated from

$$g = \frac{P}{kT_p B} \quad (10)$$

where the measured power on the ambient load is P , the temperature of the ambient load is T_p , the bandwidth of the system is B , and k is Boltzmann's constant. These data are written to files for postanalysis.

Figure 17 shows the results of a stability run. Shown are the gain and physical temperature. The stability of the system was used to define the time between the noise diode calibrations done during observations in the beam-switching mode as described below. For these measurements, a 10-min period between noise diode calibrations was considered conservative enough for our accuracy requirements. Furthermore, a 1.5-hr time frame was chosen to perform all the system calibrations for linearity, gain, and atmospheric effects.

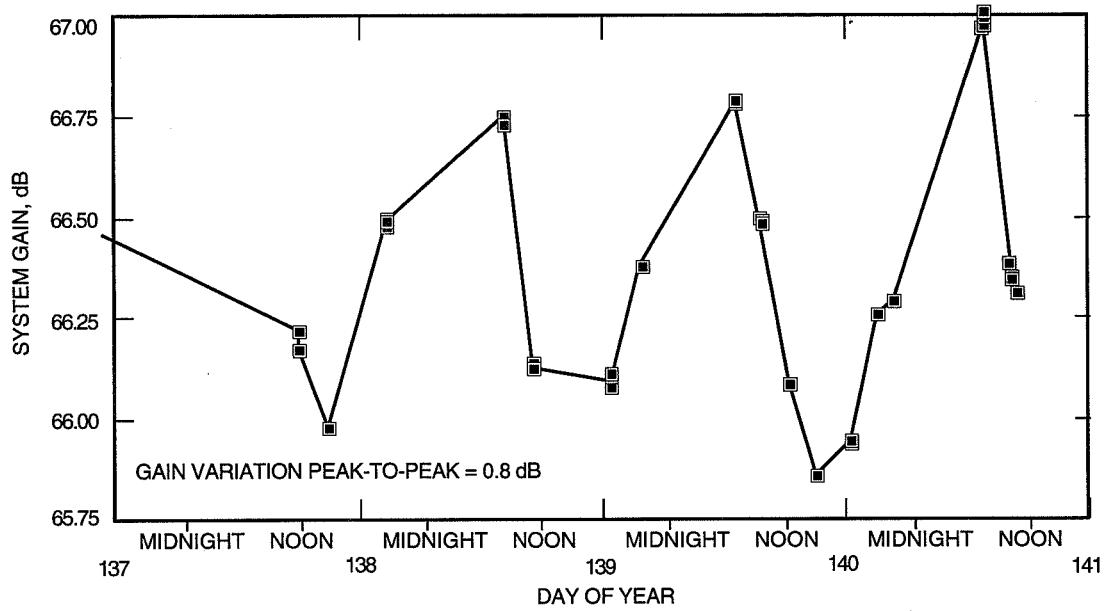


Fig. 17. Clear aperture system gain stability for days 137–141 of 1993.

Tipping Curves. The effects of the atmospheric attenuation to a received signal must be removed in order to correctly calculate either the antenna performance (gain) or the source flux. The most common method to predict the atmospheric effects is to measure the total system temperature as a function of elevation. The measured data can be used to calculate the zenith attenuation. This attenuation can then be used to calculate the attenuation as a function of elevation. The radiometer for this system included an option to perform such measurements and to store the data in files for future analysis. The data can be analyzed in any fashion desired by the observer. Furthermore, if a secondary measurement capability is available, such as a water vapor radiometer, it may be prudent to use it as the primary indication of the atmosphere with the antenna-tipping curves as backup. Figure 18 shows the results of a typical tipping curve. These data are shown as system temperature versus air mass, where the air mass quantity is defined as the amount of air relative to the zenith. At zenith, air mass is defined as 1. At lower elevation angles, the air mass increases. The relationship between air mass at an elevation angle is given by

$$air\ mass = \sec(90 - \theta_{el}) \tag{11}$$

The data are plotted in this way so that, to the first order, one can infer the noise temperature contribution due to the atmosphere (T_{atm}) as the slope of this line in kelvins/air mass. There are second-order effects that may be included in more thorough analyses, but they have been omitted here for simplicity.

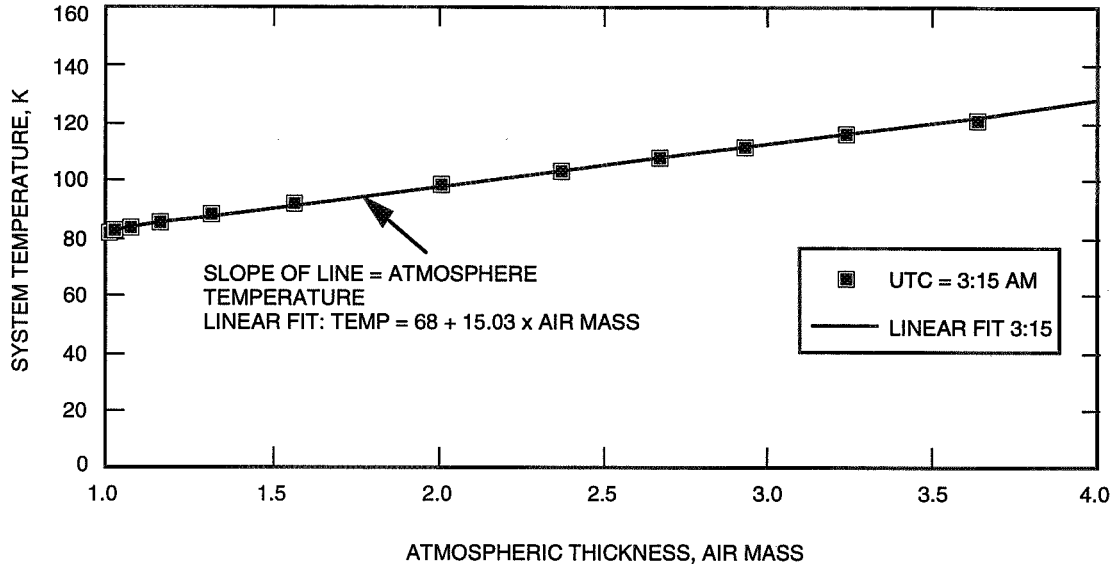


Fig. 18. Tip curve by CAA at OVRO: day of year 138.

The relationship between the noise temperature of the atmosphere, T_{atm} , and the loss of the atmosphere is again simply related as if the atmosphere were an attenuator in the radiometer. This relationship is given by

$$attenuation\ factor = \frac{1}{(T_{atm}/T_p) + 1} \quad (12)$$

where the physical temperature of the atmosphere is given by T_p and can be estimated in a number of ways from other observations, including surface meteorology. Typically, T_p is on the order of 240–270 K. All measured values of flux of a source would be divided by this attenuation factor (< 1) to correct for the loss of the atmosphere.

2. Beam-Switching Mode. Boresight Pointing Calibration. When an antenna is pointed at a source's expected azimuth and elevation, there is often an error due to gravity, refraction, azimuth and elevation constant offsets, and azimuth and elevation misalignments, and so there are tracking system errors. A systematic pointing-error correction model for determining a target's true azimuth and elevation from indicated azimuth and elevation must be generated to accurately point the antenna. In order to do this, several days must be spent scanning the antenna beam through radio sources at various right ascensions and declinations and comparing their actual positions with their indicated positions. To reduce the tedious aspects of this task, an automatic boresighting routine was incorporated into the antenna-tracking software. Details of the antenna-tracking system are discussed in the next section. The automatic boresight routine commands the antenna to track assorted points offset from the calculated center azimuth and elevation of the source and to record average power levels at those points with the radiometer in the beam-switching mode. By defining the offset points along the cross-elevation and elevation axial lines, pointing-correction tables become much easier to produce. Therefore, a software routine was developed to track five points along each axis: the 3-dB and 1-dB offset points on each side of the main lobe and the on-source point. At each of these points, the radiometer records a 20-sec average power level, and after each five-point scan, the software fits a second-order curve through these data points and calculates the pointing offset to the maximum power point on the curve. This pointing offset is then recorded and used to adjust the offsets in the subsequent scan.

By alternately scanning the cross-elevation and elevation axes and recording the accumulated pointing corrections in each axis for various radio sources in all quadrants of the sky, a pointing model was produced that corrected for fixed azimuth and elevation offsets, north/south and east/west azimuth tilt, and gravity and refraction distortions. When these values were then used in subsequent tracks to correct the azimuth and elevation coordinates, the antenna was able to achieve a blind-pointing accuracy of better than 0.02 deg. This is the total pointing error and is significantly less than the 0.03-deg requirement stated earlier.

The pointing model generated was developed using the antenna beam referred to as beam A. After this model was made, tracks of radio sources were done for the antenna beam referred to as beam B. The result of these tracks indicated that the two beams were 1.0 deg apart in azimuth and 0.015 deg different in elevation, indicating excellent agreement with what was measured in the near-field measurements described above.

Flux Measurements. The term "flux measurement" in this section refers to the measurement of the system response in volts due to the increase in system temperature of a source located on the boresight of either antenna beam. Furthermore, what is actually measured is the increase in system temperature in kelvins due to the source. However, until properly scaled by an associated noise diode measurement, given as kelvins/volts, this value is not yet in units of kelvins. The actual flux of the source in Janskys is calculated after the measurement with knowledge of the antenna gain, given by an equation similar to Eq. (2).

Flux measurements are made by observing the signal of the source while it is sequentially presented to both antenna beams. For this discussion, we refer to the beam on the sky providing a signal to its associated feedhorn. Also recall from the discussion above regarding detection in the beam-switching mode, that the signal from the lock-in amplifier is zero for the case when there is no signal in either beam. Furthermore, the signal in beam A differs in sign from a signal in beam B due to the detection method of the lock-in amplifier. With this information, flux measurements can be made and understood.

With the receiver in the beam-switching mode measuring the difference between the signal levels in antenna beams A and B, the antenna is moved so that four measurements could be made with the signal from the radio source focused on feeds B, A, A, and B. The sum of the feed B measurements (a negative value) was subtracted from the sum of the feed A measurements, and the result was divided by four to obtain an average source signal level. The resulting value is a measure in volts of the system response to the source.

All this information is acquired as digital data and is stored in files for further analysis. The computer screen also plots the information in graphical format for the operator to observe. This is often useful in determining if the data are high-precision or not, i.e., clean. A representative example of this display is given in Fig. 19. The larger signals at the beginning of the chart are noise diode signals, as described below. For reference, the noise diode signal is approximately 0.75 K.

Noise Diode Measurement. In order to conduct accurate flux measurements, gain drifts in the receiver must be calibrated out. These calibrations were accomplished throughout the tracks by periodically injecting the signal from a well-calibrated and stable noise diode into the receiver RF path of horn A and measuring the change in detected power level. Since all other variables in the system can be taken as constants during the short calibration period and the effects of atmospheric noise contributions are eliminated in the beam-switching mode, the change in detected power level from the diode is due only to long-term receiver gain variations. The system response due to the injection of the noise diode is measured in volts. With knowledge of the noise diode level, from the total power noise-diode calibrations, one can calculate the scaling factor of the injection signal in kelvins/volts. This measurement is done at the beginning and end of each flux measurement described above. Therefore, system gain drifts on the order of 5 min are continually monitored and the data are used in the calculation of the source temperature.

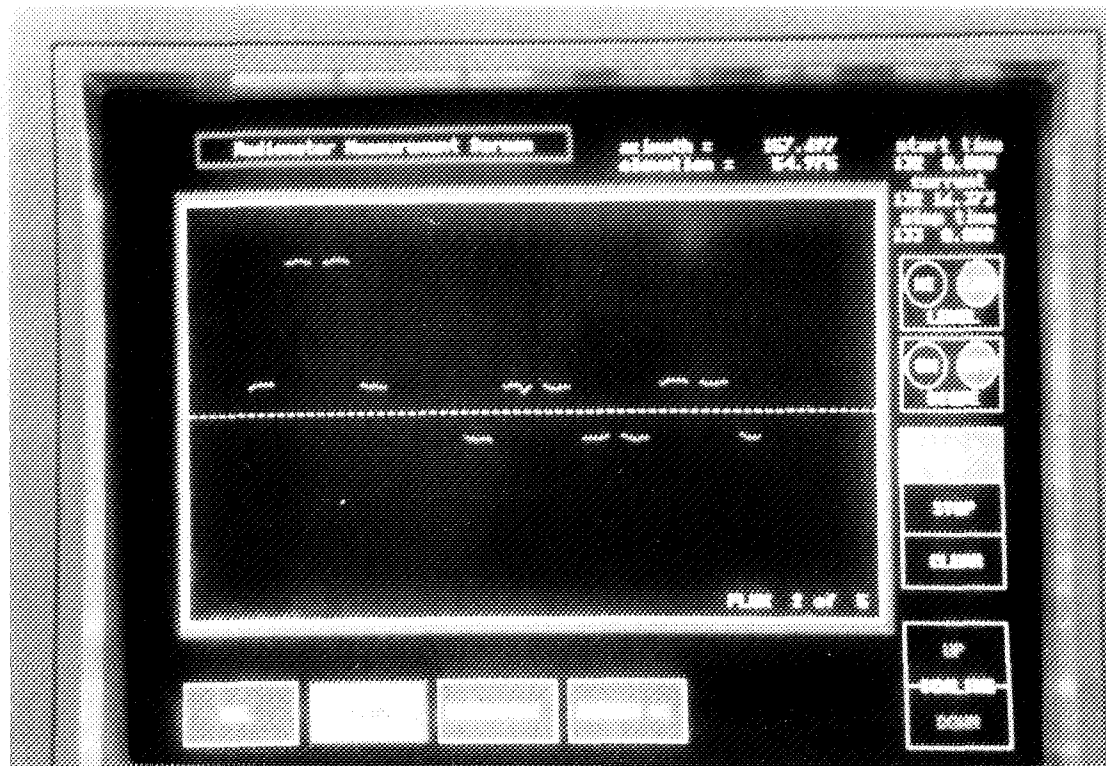


Fig. 19. Display picture of a flux measurement.

The diode measurement method is simple. While tracking, and with the antenna scanned off-source in azimuth, four power level measurements are made. These measurements are made with the diode power injected into horn A and for the diode turned off, on, on, and off. The sum of the diode-off power levels was subtracted from the sum of the diode-on power levels, and the result was divided by 2 to obtain an average diode power level. These four measurements were made in this manner in order to eliminate any error due to short-term variations in the receiver gain during the calibration sequence.

Drift Curves. Drift curves are of use in determining the performance of the antenna. These curves allow the observer to determine the beamwidth of the antenna and can be used in conjunction with other mathematical techniques to determine the source-size correction factors to apply to measurements of sources that are not extremely small with respect to the antenna beamwidth. For this article, the drift curve is used to verify the size of the antenna beams as measured by NIST. These data are taken by driving the antenna to a position that is in advance of the source. For this positioning system, an offset of the time "axis" (also known as hour angle) is allowed. Thus, driving the antenna ahead of the source by a set time and then setting the brakes allows the source to slowly (sidereal rate) drift through the antenna beam. Figure 20 shows the results of one drift curve done using Venus as the source. The beamwidth calculated by this curve is 0.430 deg, which is in very good agreement with the measurements.

V. Tracking System

A. Azimuth/Elevation Positioner System

The antenna is mounted on a Scientific-Atlanta elevation-over-azimuth positioner that has a range of 100 and 540 deg of rotation in the elevation and azimuth axes, respectively. Servo motors on each axis are driven by a model 3840 positioner controller from the same manufacturer. This controller accepts a

variety of commands from its front panel or a remote computer, reads the encoders on each axis of the positioner, and drives the antenna in response to these commands and indications. The 3840 also displays these commanded and indicated positions on its front panel and sends them to a remote computer.

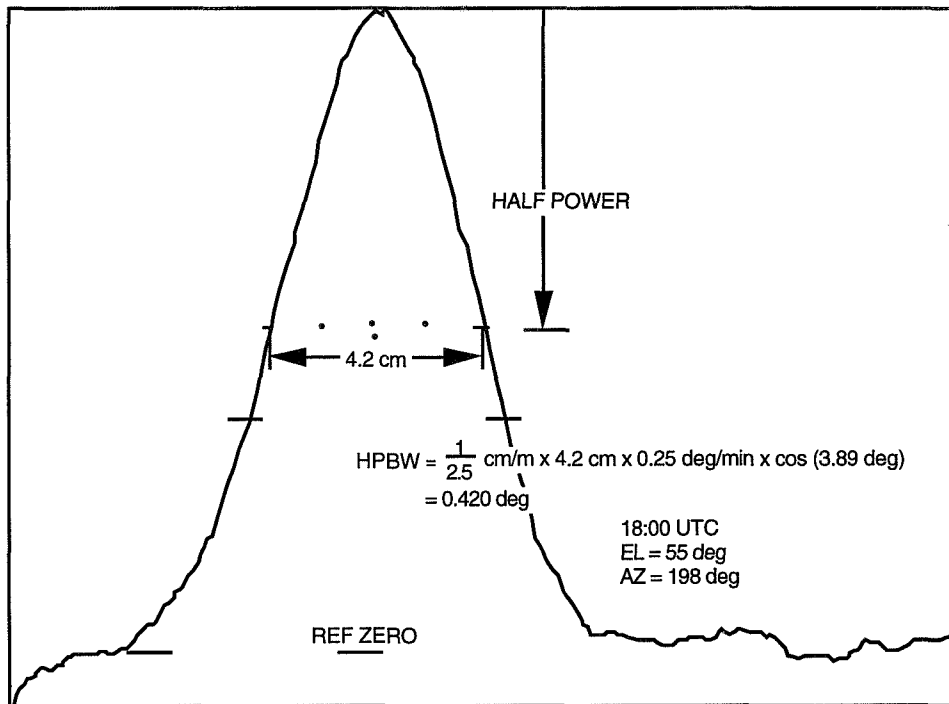


Fig. 20. Drift curve of beam A using Venus. Venus declination = 3.89 deg, April 29, 1983, chart speed = 2.5 cm/min.

The four active modes of this 3840 controller, which are available for this telescope, are stow, slew, position, and scan. In its stow mode, the controller drives the antenna servos at full rate to a zero position defined internally by user-selectable jumpers. In the slew mode, the antenna servos are driven at a variable rate in the direction selected by the user. In the position mode, the antenna servos are driven at a moderate tracking rate until the indicated position matches the commanded position. And in the scan mode, the antenna is driven to oscillate around the current position between user-defined limits at a user-defined rate. A fifth mode, standby, is used to disengage the drive motors and set the brakes on the positioner when tracking is done. It should be noted that no firmware exists in this controller to conduct antenna tracks in either sidereal or planetary mode; therefore, a remote computer is required to send continuous new commanded positions to conduct these tracks.

The remote computer used for tracking is a Hewlett-Packard Vectra 386 with a touch screen. This computer serves as a virtual device by displaying the equivalent of the 3840 controller's front panel on the screen, and through the use of the touch screen, it allows the user to activate any command button just as one would on the 3840 front panel. In addition, the user is also capable of scanning through several data-display and system-configuration screens on this computer. By way of touch screen and keyboard inputs, the experimenter may select the source to be tracked, the tracking mode to use, and the type of data collection to conduct.

B. Tracking Software

As stated above, the Scientific-Atlanta 3840 positioner controller cannot of itself conduct antenna tracks. It requires an external computer to continuously send new position commands. The software on

this computer must therefore be able to produce position commands for the necessary tracking modes. It was decided at the start of this project that two tracking modes were necessary, sidereal and planetary. Furthermore, there should be a capability to superimpose a scan on top of the tracking mode to perform secondary measurements. These requirements were met by a combination of software provided by the Scientific Atlanta as part of the delivery of the 3840 positioner controller and software added by JPL to perform specific boresighting and tracking capabilities common to JPL deep space tracking systems.

1. Tracking Modes. Sidereal. In the sidereal mode, the antenna tracks a radio source at a fixed right ascension (RA) and declination (DEC), and the antenna moves to compensate for the rotation of the Earth. The RA and DEC of the source to be tracked are supplied to the tracking software by the user. Although the user occasionally supplies these coordinates for the current day, they are usually retrieved from an ephemeris listing with coordinates at some past or future date which need to be corrected for the Earth's precession to the current date. For this reason, the software requires four inputs to conduct a sidereal track: the right ascension and declination, the epoch of the RA and DEC coordinates, and whether or not to apply precession correction. Once these values have been input, the computer will compute azimuth and elevation command positions.

Planetary. In the planetary mode, the antenna tracks a radio source at a variable RA and DEC, and the antenna moves to compensate for the rotation of the Earth and the motion of the source. In this mode, the user is required to supply three data sets consisting of a date and time and the RA and DEC of the source for that date and time. Through these three points, the computer fits a second-order curve. Using the current date and time and this curve, the computer then calculates the current RA and DEC of the source and calculates azimuth and elevation command positions from these coordinates. It should be noted that as the time between these three points increases, a significant error in the calculation of the current RA and DEC can result. Therefore, for this experiment, we consistently supplied coordinates that were only 6 hr apart.

2. Scanning Capability. In addition to the sidereal and planetary tracking modes that have been added to the positioner controller software, there are modes available that allow for scanning the antenna in elevation, azimuth, and in the time base (hour angle). These scan modes can be applied while the antenna is stationary or while it is tracking. This feature is useful in searching for targets upon initial acquisition. Prior to the development of pointing models for a particular part of the sky, a search may be made by superimposing a scan in any or all of the axes while observing a strip chart display of the detected signal. Another use of this capability would be to measure the antenna patterns or to measure source sizes in the development of non-point-source correction factors. This useful mode of operation is not widely used other than for initial source acquisition.

VI. Performance

The telescope has been assembled and was used in a side-by-side observation of Venus along with the OVRO 5-m antenna during the summer of 1993. During this period, the performance parameters of the system were calibrated, often many times. Table 4 summarizes all performance parameters measured during this period and their predicted values where a prediction was made. For completeness, the performance parameters measured at NIST are included in this table.

VII. Summary

A radio telescope has been developed and delivered to the field that can accurately measure the flux density of the brightest radio sources. This telescope uses an antenna system that has been calibrated to high absolute accuracy. The calibration matches well with the predicted performance for this system. This telescope uses a Dicke beam-switching radiometer that can provide 8-mK sensitivity in a 1-sec integration time. This radiometer is extremely stable and linear, and by virtue of its beam switching eliminates the

transitory effects of the atmosphere during observations. The calibration and supporting documentation suggest that this is the most highly accurate standard gain system for radiometric observations at 32 GHz yet reported. The system supported a set of side-by-side observations of Venus, the purpose of which was to determine very accurately both the gain of the associated telescope, an OVRO 5-m antenna, and the disk temperature of Venus. Those measurements were highly successful and will be reported in a future article.

Table 4. The 1.5-m telescope performance.

Parameter	Measured value	Predicted value
System noise temperature, K	75	75
Receiver temperature, K	65	65
Stability, dB/hr	0.06 (maximum)	—
Maximum blind pointing error, deg	0.022	0.030
Minimum ΔT (noise floor), mK	8	10
Separation of beams, deg		
Azimuth (NIST)	1.00	1.00
Azimuth (OVRO)	0.99	—
Elevation (NIST)	0.02	0.00
Elevation (OVRO)	0.02	—
Linearity, percent	99.2	—
Half-power beamwidth, deg		
NIST calibrations	0.430	0.43
OVRO calibrations	0.420–0.440	—

Acknowledgments

The principal author would like to thank his coauthors for their dedicated support during this multiyear development. Also, this system would not have been completed without the help of Dudley Neff, Richard Hodges, Manuel Esquivel, Gary Glass, Leon Alvarez, Hal Ahlstrom, Fred Menninger, Ron Heuerman, George Resch, and Rob Hartop of JPL, and Wil Klemperer and Andy Repjar of NIST.

References

- [1] G. Evans, *RF Radiometer Handbook*, Dedham, Massachusetts: Artech House, 1977.
- [2] N. Skou, *Microwave Radiometer Systems Design and Analysis*, Dedham, Massachusetts: Artech House, 1989.
- [3] A. Cha, "An Offset Dual Shaped Reflector With 84.5 Percent Efficiency," *IEEE Transactions on Antennas and Propagation*, vol. AP-31, no. 6, November 1983.
- [4] P. D. Potter, "A New Horn Antenna With Suppressed Sidelobes and Equal Beamwidths," *Microwave Journal*, vol. VI, no. 6, pp. 71–78, June 1963.

- [5] A. J. Repjar, *Final Project Report, Calibration of the JPL 1.5 Meter Clear Aperture Antenna*, Report Number SR-723-61-90, National Institute of Standards and Technology, Boulder, Colorado, December 31, 1990.
- [6] R. H. Dicke, "The Measurement of Thermal Radiation at Microwave Frequencies," *The Review of Scientific Instruments*, vol. 17, pp. 268-275, July 1946.
- [7] J. Bowen and D. Neff, "A Cryogenic Seven-Element HEMT Front End for DSS 13," *The Telecommunications and Data Acquisition Progress Report 42-114*, vol. April-June 1993, Jet Propulsion Laboratory, Pasadena, California, pp. 51-60, August 15, 1993.
- [8] C. T. Stelzried and M. J. Klein, "Precision DSN Radiometer Systems: Impact on Microwave Calibrations," *Special Issue of the IEEE Proceedings on Design and Instrumentation of Antennas for Deep Space Telecommunications and Radio Astronomy*, February 1994.
- [9] C. T. Stelzried, *The Deep Space Network—Noise Temperature Concepts, Measurements, and Performance*, JPL Publication 82-33, Jet Propulsion Laboratory, Pasadena, California, September 15, 1982.
- [10] M. S. Gatti, M. J. Klein, and T. B. H. Kuiper, "32-GHz Performance of the DSS-14 70-Meter Antenna: 1989 Configuration," *The Telecommunications and Data Acquisition Progress Report 42-99*, vol. July-September 1989, Jet Propulsion Laboratory, Pasadena, California, November 15, 1989.
- [11] S. D. Slobin, W. V. T. Rusch, C. T. Stelzried, and T. Sato, "Beam Switching Cassegrain Feed System and Its Applications to Microwave and Millimeterwave Radioastronomical Observations," *The Review of Scientific Instruments*, vol. 41, no. 3, pp. 439-443, March 1970.
- [12] A. C. S. Readhead, C. R. Lawrence, S. T. Myers, W. L. W. Sargent, H. E. Hardebeck, and A. T. Moffet, "A Limit on the Anisotropy of the Microwave Background Radiation on Arc Minute Scales," *The Astrophysical Journal*, vol. 346, pp. 566-587, November 15, 1989.
- [13] "IRE Standards on Electron Tubes: Definition of Terms," 1962 (62 IRE 7.S2 IEEE Standard No. 161), *Proceedings of the IEEE*, March 1963.
- [14] C. T. Stelzried, "Non-Linearity in Measurement Systems: Evaluation Method and Application to Microwave Radiometers," *The Telecommunications and Data Acquisition Progress Report 42-91*, vol. July-September 1987, Jet Propulsion Laboratory, Pasadena, California, pp. 57-66, November 15, 1987.

1995/08213
324465
32p

N95-14627

17105

August 15, 1994

p. 32

TDA Progress Report 42-118

The Block V Receiver Fast Acquisition Algorithm for the Galileo S-Band Mission

M. Aung, W. J. Hurd, C. M. Buu, and J. B. Berner
Radio Frequency and Microwave Subsystems Section

S. A. Stephens
Tracking Systems and Applications Section

J. M. Gevargiz
Telecommunications Systems Section

A fast acquisition algorithm for the Galileo suppressed carrier, subcarrier, and data symbol signals under low data rate, low signal-to-noise ratio (SNR) and high carrier phase-noise conditions has been developed. The algorithm employs a two-arm fast Fourier transform (FFT) method utilizing both the in-phase and quadrature-phase channels of the carrier. The use of both channels results in an improved SNR in the FFT acquisition, enabling the use of a shorter FFT period over which the carrier instability is expected to be less significant. The use of a two-arm FFT also enables subcarrier and symbol acquisition before carrier acquisition. With the subcarrier and symbol loops locked first, the carrier can be acquired from an even shorter FFT period. Two-arm tracking loops are employed to lock the subcarrier and symbol loops with the carrier loop open. In addition, a new method is introduced for loop parameter modification to achieve the final (high) loop SNR in the shortest time possible. The fast acquisition algorithm is implemented in the Block V Receiver (BVR). This article describes the complete algorithm design, the extensive computer simulation work done for verification of the design and the analysis, implementation issues in the BVR, and the acquisition times of the algorithm. In the expected case of the Galileo spacecraft at Jupiter orbit insertion, $P_D/N_o = 14.6$ dB-Hz, $R_{sym} = 16$ symbols per sec, and the predicted acquisition time of the algorithm (to attain a 0.2-dB degradation from each loop to the output symbol SNR) is 38 sec.

I. Introduction

Due to the Galileo high-gain antenna failure, the spacecraft will be transmitting very low data-rate signals with very low signal-to-noise ratios (SNRs). For a significant portion of the mission, including the time of the Jupiter orbit insertion (JOI), the S-band (2.3-GHz) carrier signal will have high phase instability due to solar plasma process noise. Under these conditions, fast acquisition is extremely important both to minimize data loss and because slower acquisition methods fail when the phase is not stable over the (long) acquisition time. An additional complication to the acquisition process is that, for the first time for the Deep Space Network, the received signal modulation type will be a fully suppressed

carrier with a fully suppressed subcarrier, which requires new algorithms. A fast acquisition algorithm for Galileo suppressed carrier, subcarrier, and data symbol signals under low data rate, low SNR, and high carrier phase-noise conditions has been developed. The algorithm is implemented in the Block V Receiver (BVR) [1] and is under consideration for implementation in the buffered telemetry demodulator (BTD). This article describes the complete algorithm design. Details of the various algorithms are given in the referenced internal memoranda and will be published in future issues of this report.

A. The Approach

The approach of the fast acquisition algorithm is to implement nonlinear detection algorithms to generate signals with sinusoidal components related to the subcarrier, symbol, and suppressed carrier signals, and then to estimate the signal frequencies and phases from the signals via fast Fourier transform (FFT) methods. This part of the fast acquisition algorithm will be referred to as the FFT acquisition. The corresponding tracking loops are then closed with initial frequencies and phases set to the FFT-estimated values. Each tracking loop is closed with a minimal initial loop SNR, and the final (high) loop SNR, necessary for negligible output-symbol SNR loss, is achieved by gradually narrowing the loop bandwidth (and transition window width if applicable) to final values resulting in the low SNR loss. (The transition window in the subcarrier and symbol loops is the window region about the data transition that is integrated [2]. The window has a value in the range (0,1]. Windowing is implemented for noise reduction whenever square signals are tracked. Hence, windowing is used for subcarrier and symbol tracking, but not for carrier tracking.) This part will be referred to as the loop acquisition. Therefore, the fast acquisition algorithm can be described as a composition of two parts: the FFT acquisition and the loop acquisition.

Multiple novel enhancement methods were incorporated into the fast acquisition algorithm design to acquire the subcarrier, symbol, and suppressed carrier in a much shorter acquisition time than if using the existing methods. In the FFT acquisition, a novel combination of the carrier and subcarrier in-phase (I) and quadrature-phase (Q) demodulated signals is utilized. This approach reduces the number of symbols required for the FFT at the required SNR by a factor of two. The new signals are a combination of all four II, IQ, QI, and QQ, where the II, IQ, QI, and QQ are the I and Q carrier and subcarrier demodulated signals as shown in Fig. 1, instead of the traditional combination of only two signals. Using a complex FFT results in a single-tone, sign-correct frequency estimate. Therefore, further testing for the polarity of the frequency estimate is eliminated. In frequency estimation from the FFT, a sinc interpolation method (Appendix) is used that results in refined estimates of the frequency and phase.

In loop acquisition, a new approach to the entire loop acquisition process, from choosing the initial bandwidth and window values through narrowing these parameters at the fast rate, is introduced. Also, due to the design to initialize both the phase and frequency of the tracking loops with refined (FFT) estimates, the loops start out essentially in lock immediately after closure. An additional advantage of the loop starting in lock is that the bandwidth and window narrowing process can be activated immediately after loop closure.

A new approach to suppressed carrier acquisition is employed when the carrier phase noise is high. In this case, the subcarrier and symbol are acquired first with the carrier loop open, which can be done because the subcarrier and symbol signals have lower phase noise due to the lower frequencies relative to the carrier. This approach of first acquiring the subcarrier and symbol is taken because, when the subcarrier tracking loop (SCL) and symbol synchronization loop (SSL) are locked, the SNR loss in the carrier acquisition FFT is significantly reduced, resulting in a shorter acquisition FFT time requirement during which the effects of high carrier phase noise are expected to be less significant.

Two-arm SCL and SSL have been introduced for tracking the subcarrier and symbol with the carrier loop open. The two-arm loops (which use both the carrier I and Q arms) provide a 3-dB gain over the traditional one-arm loops in the low SNR case (to be reported on in a future article of this report). When

the carrier loop is closed, only additional noise is introduced by the use of the second arm; therefore, the conventional one-arm SCL and SSL are used.

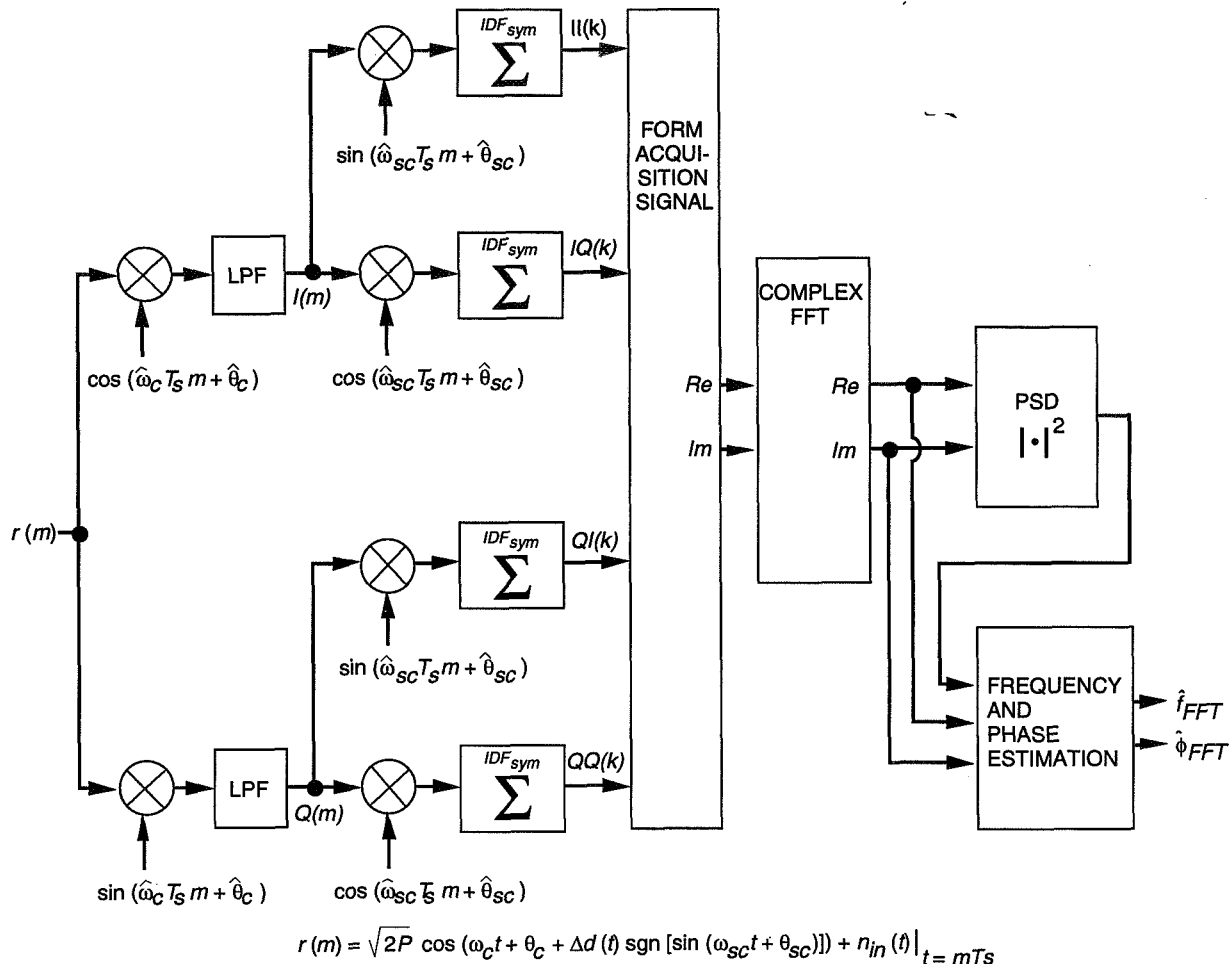


Fig. 1. FFT-acquisition setup for the fast acquisition algorithm in the BVR.

B. Outline

In Section II, the fast acquisition algorithm process is described. In Section III, the FFT acquisition algorithm is described. The loop acquisition is described in Section IV. In Section V, the issues for implementing the algorithm in the Block V Receiver are discussed. Results of computer simulations are presented in Section VI. Finally, in Section VII, the acquisition times of the algorithm are presented.

II. Algorithm Flowchart

The flows of the algorithm are shown in Figs. 2 and 3 for two cases: when the carrier phase noise is high and when it is low, respectively.

A. Algorithm Flowchart When Carrier Phase Noise Is High

For a significant portion of its mission, the Galileo spacecraft is expected to have high carrier phase noise (e.g., the carrier phase and frequency can be moved significantly during the initial acquisition FFT time due to solar plasma). In this case, the subcarrier and symbol, which are relatively more stable due to lower frequencies relative to the carrier, are acquired first. By doing so, losses to the carrier acquisition

signal due to the subcarrier and symbol are reduced. One source of loss is from the fact that, before subcarrier acquisition, only the first harmonic of the subcarrier signal is captured for the FFT acquisition, compared to after subcarrier acquisition when all the harmonics are captured. Additional losses arise from the subcarrier and symbol phase errors. After reduction of the subcarrier and symbol losses, the SNR in the carrier acquisition is enhanced. As a result, a shorter acquisition time is required for the carrier acquisition FFT, during which the effects of the carrier dynamics are expected to be less significant.

For this case, the flowchart of the acquisition algorithm is shown in Fig. 2. Step (1) will be to FFT-acquire the subcarrier. The subcarrier is acquired using $N_{sc,acq}$ FFTs with $N_{sc,acq}$ different, equally spaced symbol phase offsets. We use $N_{sc,acq}$ symbol phase offsets so that losses due to symbol phase error are minimized if the error in predicted symbol rate is small (Section III.A). In step (2), subcarrier acquisition is verified (see Section III.D). If the subcarrier was not acquired, a larger FFT size will be determined in step (9), and the acquisition process restarts from step (1).

After subcarrier FFT acquisition, a decision is made if the symbol rate is known accurately. For automating this decision, a method utilizing the relationship between the amplitudes of the $N_{sc,acq}$ subcarrier acquisition FFTs is currently under development. If the symbol rate is known, symbol phase is estimated via interpolation of the subcarrier acquisition FFTs [step (4)]. If the symbol rate is not known, the symbol frequency and phase are estimated via an FFT approach [step (11)]. For the symbol acquisition FFT, the data stored from the subcarrier FFT acquisition are reused after refitting the stored data with the FFT-estimated subcarrier phase error. If a longer data set is required for symbol acquisition, the stored data set will be complemented with consecutively collected new data. By mainly using the stored data, little or no additional time is required for data collection [step (10)].

After estimation of the subcarrier and symbol frequency and phase via the FFT acquisition, the SCL and the SSL are initialized with the FFT-estimated frequencies and phases and closed. The bandwidth and window narrowing process is started immediately [steps (5) and (6)]. Note that the initial phase used to start the loop is the phase estimated for time $t = t_{cl,loop}$, the time at which the loop is closed. The subcarrier loop is closed with a square subcarrier reference; hence, all harmonics of the square wave are used after this point. Because the subcarrier and symbol are tracked while the carrier is open, two-arm SCL and SSL are used, which provide a 3-dB gain over the one-arm loops in the low SNR case.

Next, the carrier is FFT acquired [step (7)]. New data can be collected for this step immediately after the subcarrier and symbol loops are closed, as these loops are then assumed to be in lock. Finally, when the carrier is FFT-acquired successfully, the carrier tracking loop will be initiated with the estimated frequency and phase and closed, and the bandwidth narrowing process will be started immediately [step (8)].

B. Algorithm Flowchart When the Carrier Phase Noise Is Low

The flowchart of the acquisition algorithm when the carrier phase noise is relatively low, e.g., when the Sun–Earth–probe (SEP) angle is large, is shown in Fig. 3. In this case, the carrier frequency and phase are expected to be stable for the duration of the longer initial FFT time. (Recall that a long FFT time is required without the subcarrier and symbol lock, i.e., with the losses from using only the first harmonic of the subcarrier and from the subcarrier and symbol phase errors.) Then, the carrier and the subcarrier can be acquired simultaneously [step (1)]. (The acquisition signals for the carrier and the subcarrier are formed from analogous combinations of the same set of II, IQ, QI, and QQ and have the same detection statistics.) The rest of the flowchart is analogous to that for the case of a high carrier phase noise. Note that in step (9) both the carrier and subcarrier errors estimated from FFT acquisitions are refitted to the stored data from step (1).

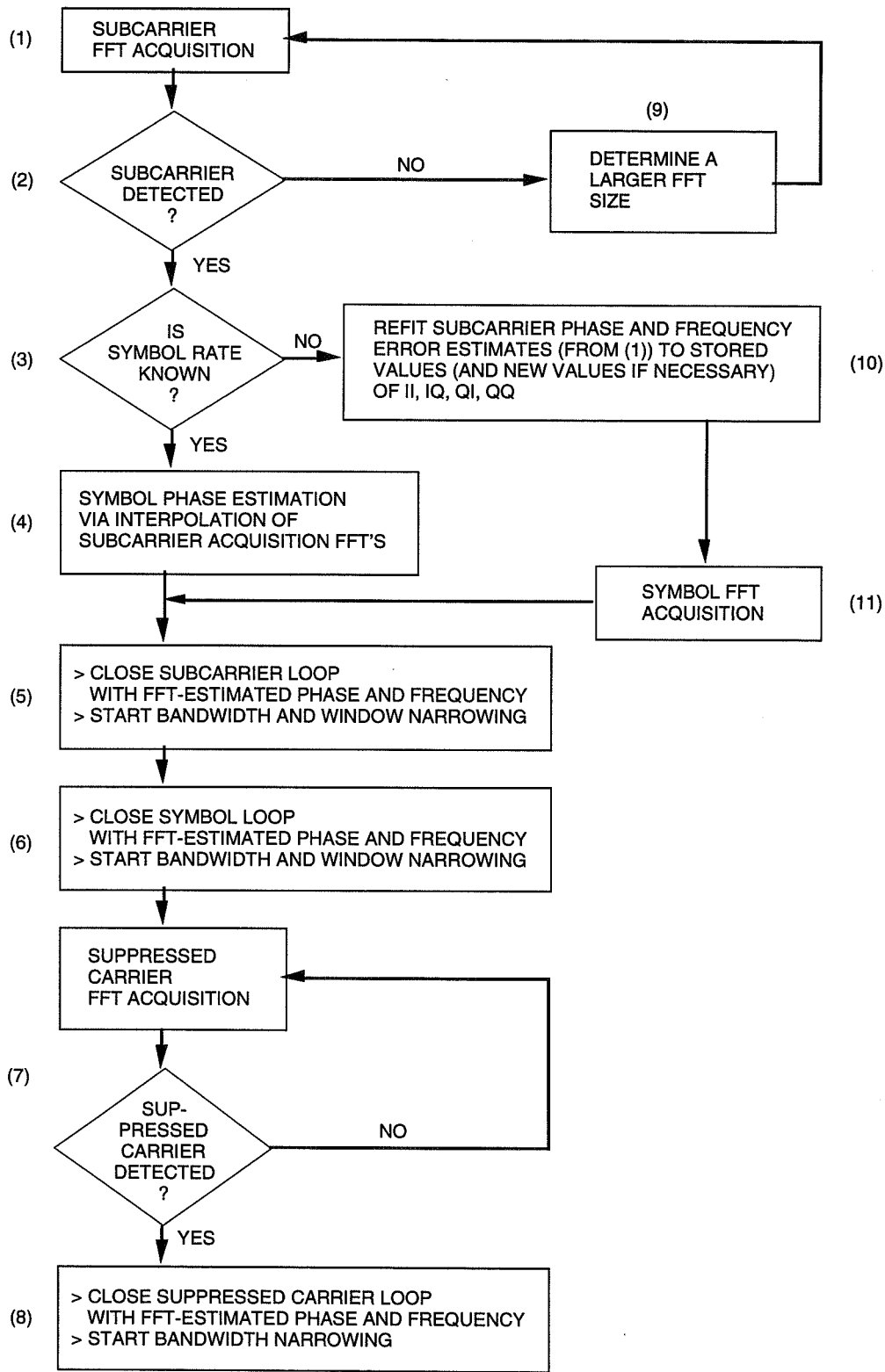


Fig. 2. Algorithm flowchart when the carrier phase noise is high.

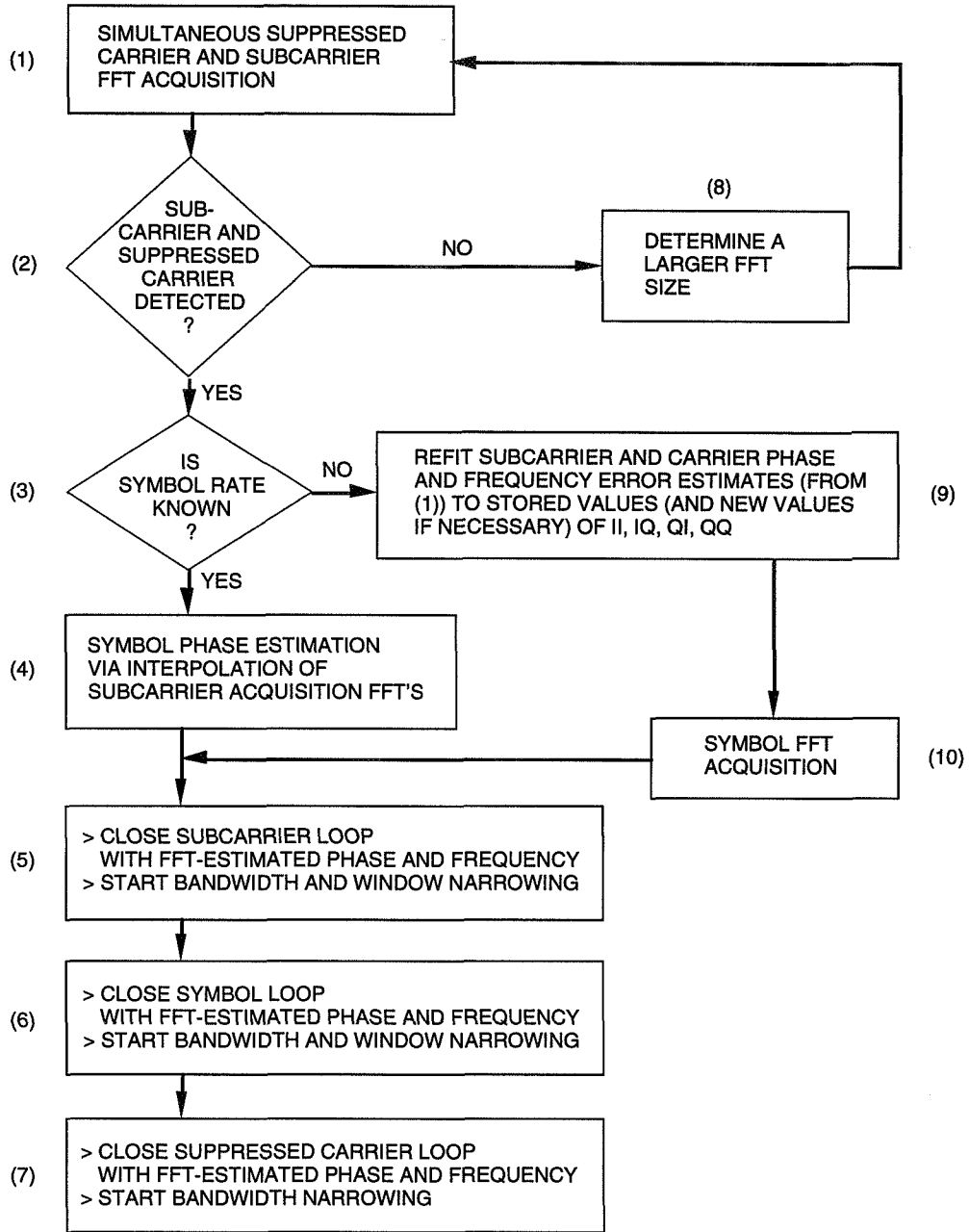


Fig. 3. Algorithm flowchart when the carrier phase noise is low.

III. FFT Acquisition

In this section, the FFT acquisition component of the fast acquisition algorithm is discussed. The setup of the receiver for the FFT acquisition is shown in Fig. 1. The input signal is modeled to be

$$r(m) = \sqrt{2P} \cos(\omega_c t + \theta_c + \Delta d(t) \operatorname{sgn}[\sin(\omega_{sc} t + \theta_{sc})]) + n_{in}(t) |_{t=mT_s} \quad (1)$$

where

- $\omega_c = 2\pi f_c =$ carrier frequency
- $\theta_c =$ carrier phase
- $\Delta = 90$ deg (modulation index for suppressed carrier)
- $d(t) =$ data symbol of rate R_{sym} symbols per sec
- $\omega_{sc} = 2\pi f_{sc} =$ subcarrier frequency
- $\theta_{sc} =$ subcarrier phase
- $n_{in}(t) =$ input noise, modeled as white Gaussian noise in analysis
- $T_s =$ sampling period of the signal
- $m =$ sample index corresponding to a sampling period of T_s sec

The $I(\cdot)$ and $Q(\cdot)$ signals are defined as

$$\begin{aligned} I(m) &\triangleq r(m) \cos(\hat{\omega}_c m T_s + \hat{\theta}_c) |_{LPF} \\ Q(m) &\triangleq r(m) \sin(\hat{\omega}_c m T_s + \hat{\theta}_c) |_{LPF} \end{aligned}$$

where $|_{LPF}$ indicates low-pass filtering, and

$$\begin{aligned} \hat{\omega}_c &= 2\pi \hat{f}_c = \text{predicted carrier frequency used in the carrier numerically controlled oscillator (NCO)} \\ \hat{\theta}_c &= \text{predicted carrier phase used in the carrier NCO} \end{aligned}$$

The II, IQ, QI, and QQ signals are defined as

$$\begin{aligned} II(k) &\triangleq I(m) \sin(\hat{\omega}_{sc} m T_s + \hat{\theta}_{sc}) |_{IDF_{sym}} \\ &= AD(k) \sin(\phi_{e,c}(k)) \cos(\phi_{e,sc}(k)) + N_{II}(k) \end{aligned} \quad (2)$$

$$\begin{aligned} IQ(k) &\triangleq I(m) \cos(\hat{\omega}_{sc} m T_s + \hat{\theta}_{sc}) |_{IDF_{sym}} \\ &= AD(k) \sin(\phi_{e,c}(k)) \sin(\phi_{e,sc}(k)) + N_{IQ}(k) \end{aligned} \quad (3)$$

$$\begin{aligned} QI(k) &\triangleq Q(m) \sin(\hat{\omega}_{sc} m T_s + \hat{\theta}_{sc}) |_{IDF_{sym}} \\ &= AD(k) \cos(\phi_{e,c}(k)) \cos(\phi_{e,sc}(k)) + N_{QI}(k) \end{aligned} \quad (4)$$

$$\begin{aligned} QQ(k) &\triangleq Q(m) \cos(\hat{\omega}_{sc} m T_s + \hat{\theta}_{sc}) |_{IDF_{sym}} \\ &= AD(k) \cos(\phi_{e,c}(k)) \sin(\phi_{e,sc}(k)) + N_{QQ}(k) \end{aligned} \quad (5)$$

where $|_{IDF_{sym}}$ indicates integration over the estimated symbol period \hat{T}_{sym} ; k is the sample index corresponding to the k th overlapped integration period as shown for $N_{sc,acq} = 4$ in Fig. 4(a), and

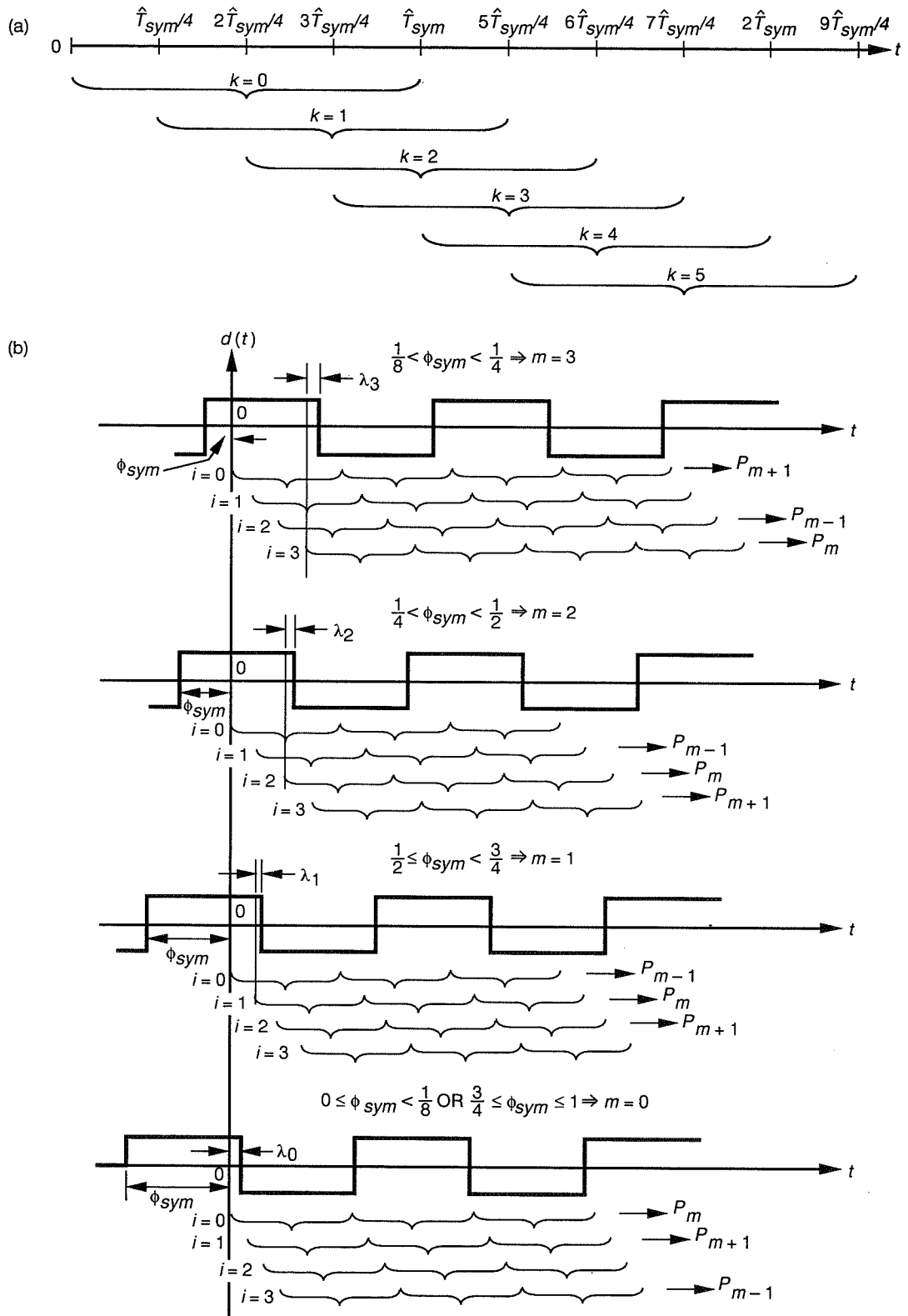


Fig. 4. Symbol acquisition: (a) overlapped integration intervals of II, IQ, QI, and QQ for $N_{sc, acq} = 4$; and (b) relationship between ϕ_{sym} and the symbol integration interval (i) which results in the PSD with the largest peak (P_m).

$$\begin{aligned}
\hat{\omega}_{sc} &= 2\pi\hat{f}_{sc} = \text{predicted subcarrier frequency used in the SCL NCO} \\
\hat{\theta}_{sc} &= \text{predicted subcarrier phase used in the SCL NCO} \\
\phi_{e,c}(k) &= \text{carrier demodulation error} \\
\phi_{e,sc}(k) &= \text{subcarrier demodulation error} \\
A &= -\sqrt{2P}/\pi \\
D(k) &= \text{the data symbol integrated over the estimated symbol period}
\end{aligned}$$

Note that to avoid significant degradation due to integration of the signals over the estimated symbol period, \hat{T}_{sym} (in the IDF_{sym} in Fig. 1), the subcarrier and carrier frequency predict errors are required to be much less than the symbol rate. A rule of thumb is to require $\Delta f_{carr-or-sc} < (R_{sym}/20)$ Hz, where $\Delta f_{carr-or-sc}$ is the maximum carrier or suppressed carrier frequency error. Note also that only the first harmonic of the square subcarrier is retained in the I's and Q's.

The first letters in II, IQ, QI, and QQ indicate the in-phase (I) or quadrature-phase (Q) carrier demodulation, and the second letters indicate the I or Q subcarrier demodulation in the receiver. The definition of the I and Q demodulation (whether cosine or sine for I or Q) is arbitrary. A different definition of the I's and Q's leads to a different combination of the I's and Q's in forming the acquisition signals. However, if from end to end the signal definition of the I's and Q's and the combinations of the I's and the Q's are consistent, and if the FFT estimated phase and frequency are applied to the loops with the correct polarization, the final FFT-acquisition result will be the same.

The $II(k)$, $IQ(k)$, $QI(k)$, and $QQ(k)$ are generated for $N_{sc,acq}$ overlapping, shifted integration periods of \hat{T}_{sym} sec. The number of overlapped integrations per symbol, $N_{sc,acq}$, is an arbitrary integer value greater than or equal to 4. In the Block V Receiver, the minimum required value of $N_{sc,acq} = 4$ will be used. Hence, in the remainder of the article, $N_{sc,acq} = 4$ is assumed. For this case, the overlapped symbol integration periods are shown in Fig. 4(a).

The subcarrier, symbol, and suppressed carrier are FFT acquired (as shown in Fig. 1) using the four I's and Q's. The subcarrier, symbol, and suppressed carrier acquisition signals, $X_{sc}(\cdot)$, $X_{sym}(\cdot)$, and $X_{carr}(\cdot)$, are formed from combinations of $II(\cdot)$, $IQ(\cdot)$, $QI(\cdot)$, and $QQ(\cdot)$. From each acquisition signal, a power spectral density (PSD) is formed as the magnitude square of the complex FFT of the signal, and the peak bin with PSD value above the detection threshold and bin location within the range of frequency search is detected (Section III.D). From the peak bin and two bins about it, the frequency and phase (at $t = 0$) of the tone, \hat{f}_{FFT} and $\hat{\phi}_{FFT}$ are estimated using a sinc interpolation method (Appendix). Combining FFT-estimated \hat{f}_{FFT} and $\hat{\phi}_{FFT}$ and predicted f and $\hat{\theta}$, refined estimates of the subcarrier, symbol, and suppressed carrier are obtained.

In this section, for the I and Q demodulation setup of the BVR shown in Fig. 1, the acquisition signals are defined for the subcarrier, symbol, and suppressed carrier. For each FFT acquisition, the SNR in the acquisition FFT, SNR_{FFT} , defined as,

$$SNR_{FFT} \triangleq \frac{\text{tone power}}{\text{noise power}} \triangleq N_{data} \frac{E_s^*}{N_o} \triangleq N_{data} \frac{E_s}{N_o} S_L \quad (6)$$

is presented. (Note that SNR_{FFT} can be defined as N_{data} times an equivalent symbol SNR, E_s^*/N_o , which is the symbol SNR times a signal degradation factor, S_L , in the acquisition signal.) Also for each case, the variances of the FFT-estimated frequency and phase are given. Finally, the determination of FFT parameters in the FFT acquisition is discussed.

A. Subcarrier FFT Acquisition

Subcarrier acquisition is performed in step (1) of Figs. 2 and 3. At this point of the acquisition, the symbol frequency is assumed to be known, but the symbol phase is unknown. (Note that if ΔR_{sym} , the error in the predicted symbol rate, is not negligible, the SNR of the acquisition FFT will be degraded, resulting in either the subcarrier being detected with a weaker SNR, or not being detected in the first FFT.) For the case in which ΔR_{sym} is negligible, the integration of II, IQ, QI, and QQ over the estimated symbol period will have a constant symbol phase error, λ (in cycles), during the FFT and contribute a loss $\overline{D_\lambda^2}$ in SNR_{FFT} :

$$\overline{D_\lambda^2} = \frac{1}{2}[1 + (1 - 2\lambda)^2] \quad (7)$$

where $\overline{D_\lambda^2}$ is the expected symbol phase-error loss averaged over symbol probability.

To minimize the loss due to $\overline{D_\lambda^2}$, the subcarrier acquisition signals will be formed for four ($N_{sc,acq}$) symbol phase offsets, 1/4 cycle apart as $X_{sc,0}$, $X_{sc,1}$, $X_{sc,2}$, and $X_{sc,3}$. The SNR_{FFT} 's of $X_{sc,0}$, $X_{sc,1}$, $X_{sc,2}$, and $X_{sc,3}$ will be proportional to $\overline{D_{\lambda_0}^2}$, $\overline{D_{\lambda_1}^2}$, $\overline{D_{\lambda_2}^2}$, and $\overline{D_{\lambda_3}^2}$, respectively, where λ_i ($i = 0, 1, 2, 3$) is the phase error between the actual input symbol epoch and the i th integration interval. The four symbol offset integration intervals and the λ_i 's are shown in Figs. 4(a) and (b). Loss due to $\overline{D_\lambda^2}$ is minimized in the subcarrier acquisition by estimating the subcarrier and frequency from the PSD with the largest peak (minimum value of $\overline{D_\lambda^2}$), i.e., the largest peak out of the four PSDs is detected and the FFT containing the largest peak is used for FFT frequency and phase estimation, \hat{f}_{FFT} and $\hat{\phi}_{FFT}$ (at $t = 0$), respectively.

The four subcarrier FFT acquisition signals, $X_{sc,i}(n)$ ($i = 0, 1, 2, 3$), with the four equally spaced symbol offsets, are

$$X_{sc,i}(n) = (II(i + 4n) + jIQ(i + 4n))^2 + (QI(i + 4n) + jQQ(i + 4n))^2 \quad (8)$$

where $n = 0, 1, 2, \dots, N_{data} - 1$, and N_{data} is the number of data samples in the acquisition FFT. Using Eqs. (2)–(5), these equations reduce to

$$X_{sc,i}(n) = (AD(i + 4n))^2 e^{j2\phi_{e,sc}(n)} + n_{sc,i}(n) \quad (9)$$

Each PSD of $X_{sc,i}(n)$ ($i = 0, 1, 2, 3$) will have a peak tone at the bin closest to twice the error in the predicted frequency, i.e., the frequency estimated from the FFT (as in the Appendix), \hat{f}_{FFT} , is

$$\hat{f}_{FFT} \approx 2(f_{sc} - \hat{f}_{sc}) \quad (10)$$

where \hat{f}_{sc} is the predicted subcarrier frequency. Similarly, the FFT-estimated phase, $\hat{\phi}_{FFT}$ (estimate of phase at $t = 0$, as in the Appendix), is doubled:

$$\hat{\phi}_{FFT} \approx 2(\theta_{sc} - \hat{\theta}_{sc}) \quad (11)$$

Therefore, the estimate of subcarrier frequency and phase are

$$\hat{f}_{sc,FFT} = \hat{f}_{sc} + \frac{\hat{f}_{FFT}}{2} \quad (12)$$

$$\hat{\phi}_{sc,FFT}(t) = \hat{\theta}_{sc} + \frac{\hat{\phi}_{FFT}}{2} + 2\pi\hat{f}_{sc,FFT}t \quad (13)$$

This new method of combining all four II, IQ, QI, and QQ (using both I and Q channels of the carrier) in the FFT-acquisition signal, instead of the traditional use of only the carrier Q channel, results in a 3-dB improvement in the SNR_{FFT} . Hence, the number of data points necessary to attain a given SNR_{FFT} is reduced by a factor of two. Furthermore, the frequency error estimate is sign correct, eliminating the need to further test for the polarity of the estimated frequency value.

The SNR in each of the subcarrier acquisition FFTs is as follows:¹

$$SNR_{FFT,i} = N_{data} \frac{E_s}{N_o} S_{L,bin} \frac{\left(\frac{2}{\pi}\right)^4 \overline{D_{\lambda_i}^2} S_{L,\Delta f}^2}{2 \left[\left(\frac{2}{\pi}\right)^2 \overline{D_{\lambda_i}^2} S_{L,\Delta f} + \frac{1}{2(E_s/N_o)} \right]} \quad (14)$$

where

N_{data} = number of symbols in the FFT

$$\frac{E_s}{N_o} \triangleq \frac{P_D T_{sym}}{N_o} \text{ (symbol SNR)}$$

$\overline{D_{\lambda_i}^2}$ = symbol integration loss in the i th FFT, Eq. (7)

$S_{L,bin}$ = power loss due to the tone not falling exactly on an FFT bin²

$$= \frac{1}{N_{data}^2} \frac{\sin^2(\pi\Delta_{bin}/\alpha)}{\sin^2(\pi\Delta_{bin}/(\alpha N_{data}))} \approx \frac{\sin^2(\pi\Delta_{bin}/\alpha)}{(\pi\Delta_{bin}/\alpha)^2}$$

Δ_{bin} = fractional bin offset between the true tone bin and the peak FFT bin

α = zero-padding factor in the FFT

$S_{L,\Delta f}$ = power loss due to the tone being away from dc

$$= \frac{\sin^2(\pi\Delta f_{sc} T_{sym})}{(\pi\Delta f_{sc} T_{sym})^2}$$

$$\Delta f_{sc} = f_{sc} - \hat{f}_{sc}$$

The estimated frequency and phase will have the following variances:³

¹ The SNRs in the FFT acquisition of the subcarrier and carrier are derived in M. Aung, "Derivation of the SNR's in the Subcarrier and Carrier FFT Acquisition in the Fast Acquisition Algorithm," JPL Interoffice Memorandum 3338-94-054 (internal document), Jet Propulsion Laboratory, Pasadena, California, June 6, 1994.

² The $S_{L,bin}$, $S_{L,\Delta f}$, and FFT frequency interpolation algorithm (Appendix) are derived in S. A. Stephens, "An Analysis of FFT Tone Acquisition," JPL Interoffice Memorandum 335.1-92-14 (internal document), Jet Propulsion Laboratory, Pasadena, California, May 14, 1992.

³ The variances of the FFT-estimated frequencies and phases, the probability of FFT detection, and the detection threshold are discussed in S. Stephens and M. Aung, "FFT Estimation Variances," JPL Interoffice Memorandum 335.1-94-DRAFT (internal document), Jet Propulsion Laboratory, Pasadena, California, August 1994.

$$\sigma_{f,FFT}^2 = \frac{1}{4} \frac{0.16}{T_{FFT}^2} \frac{1}{SNR_{FFT}} \text{ Hz}^2 \quad (15)$$

$$\sigma_{\phi,FFT}^2(t) = (2\pi)^2 \left(\frac{1}{4} \frac{0.01345}{SNR_{FFT}} + \sigma_{f,FFT}^2 \times \left(t - \frac{T_{FFT}}{2} \right)^2 \right) \text{ rad}^2 \quad (16)$$

B. Symbol Acquisition

After the subcarrier FFT acquisition, it is determined if the error in the predicted symbol rate error, ΔR_{sym} , is negligible. If so, only the symbol phase is estimated from the subcarrier acquisition FFTs; otherwise, both the frequency and phase are estimated with a new FFT.

1. Determination If Symbol Frequency Is Known Accurately. In step (3) of Figs. 2 and 3, a decision has to be made if the symbol rate is known accurately. If it is not known a priori, a possible method of making this decision is to compare the relative amplitudes of the $N_{sc,acq}$ subcarrier acquisition FFTs. The basic idea is that when the symbol frequency is known, the $N_{sc,acq}$ FFTs will have amplitudes proportional to $D_{\lambda_i}^2$, where λ_i 's are phase errors $1/N_{sc,acq}$ cycles apart. On the other hand, when the symbol frequency is not known, the $N_{sc,acq}$ FFTs will have comparable amplitudes. (A method utilizing this principle is under development and will be reported on in a future article.)

2. Symbol Phase Acquisition From Subcarrier Acquisition FFTs. When ΔR_{sym} is negligible, symbol phase can be estimated from the four FFTs with λ_i ($i = 0, 1, 2, 3$) as follows. In Fig. 4(b), the integration intervals of the input symbol stream, $d(\cdot)$, are shown for integration phase offsets of 0, 0.25, 0.5, and 0.75 cycle (labeled interval index $i = 0, 1, 2$, and 3, respectively, and λ_i is the phase difference between the input symbol epoch and the i th integration interval). Define m as the interval index of the integration interval that results in the PSD with the largest peak, P_m . It can be seen that m varies depending on the input symbol phase ϕ_{sym} (ϕ_{sym} is defined with respect to the estimated symbol phase $\hat{\phi}_{sym} = 0$ at $t = 0$ at the beginning of the first symbol integration interval), as

$$m = \begin{cases} 3, & \text{if } 1/8 \leq \phi_{sym} < 3/8 \text{ cycle} \\ 2, & \text{if } 3/8 \leq \phi_{sym} < 5/8 \text{ cycle} \\ 1, & \text{if } 5/8 \leq \phi_{sym} < 7/8 \text{ cycle} \\ 0, & \text{otherwise} \end{cases}$$

Index m for various values of ϕ_{sym} is shown in Fig. 4(b), where the label P_m is used to indicate the integration interval that results in the PSD with the largest peak.

Hence, the symbol phase at $t = 0$ (with respect to the integration interval $i = 0$) can be estimated as

$$\hat{\phi}_{sym,FFT}(0) = \left(1 - \frac{m}{4} \right) + \hat{\lambda}_m \quad (17)$$

where $\hat{\lambda}_m$ is the estimate of λ_m , the phase error between the input symbol epoch and the integration interval m . One derives $\hat{\lambda}_m$ by writing the peak amplitudes of the four PSDs (P_i , $i = 0, 1, 2, 3$) as being proportional to $D_{\lambda_i}^2$, which is a quadratic function of λ_i [Eq. (7)]. Using the quadratic relationship plus the additional information that phase errors λ_i 's ($i = 0, 1, 2, 3$) are one-quarter of a cycle apart, λ_m is estimated as⁴

⁴ Details of symbol phase estimation and FFT phase estimation discussed in the Appendix are available in M. Aung and S. Stephens to E. W. Stone, "Fast Acquisition Algorithm Developed for the Block V Receiver Support of the Galileo Low Data-rate Mission," JPL Interoffice Memorandum 3338-93-167 (internal document), Jet Propulsion Laboratory, Pasadena, California, August 25, 1993.

$$\hat{\lambda}_m = \frac{b + \sqrt{b^2 - 4ac}}{2a} \quad (18)$$

where

$$a = 4d$$

$$b = -4 \left(1 - \frac{2}{N_{sc,acq}} g \right)$$

$$c = \left(1 + \left(1 - \frac{2}{N_{sc,acq}} g \right)^2 \right) d$$

$$d = \frac{\sqrt{P_{m+g}} - \sqrt{P_{m-g}}}{\sqrt{P_{m+g}} + \sqrt{P_{m-g}}}$$

P_l = peak value of the l th PSD

$$g = \text{floor} \left[\frac{N_{sc,acq}}{4} \right]$$

In summary, for this case, the estimated symbol parameters are

$$\hat{f}_{sym,FFT} = R_{sym,pred} \quad (19)$$

$$\hat{\phi}_{sym,FFT}(t) = \hat{\phi}_{sym,FFT}(0) + 2\pi \hat{f}_{sym,FFT} t \quad (20)$$

The variance of the estimated phase will be approximately

$$\sigma_{\phi,FFT}^2 \approx \frac{(2\pi)^2}{16 \times SNR_{FFT}} \text{ rad}^2 \quad (21)$$

where SNR_{FFT} is the SNR in the subcarrier acquisition FFT given in Eq. (14).

3. Symbol FFT Acquisition When R_{sym} Is Unknown. When the symbol rate is not known, the symbol frequency and phase are estimated from one FFT of the acquisition signal. The acquisition signal is formed using the I's and Q's stored from the subcarrier acquisition, complemented with consecutively collected data if a larger number of symbols are required. Because most or all of the data are already available, little or no addition data collection time is required. Note from Eqs. (2)–(5) that the stored I's and Q's have subcarrier and carrier demodulation error, $\phi_{e,c}$ and $\phi_{e,sc}$, respectively. Using estimates of these demodulation errors available from the subcarrier FFT acquisition (and carrier FFT acquisition if performed prior to symbol acquisition), the errors in the stored data are demodulated out before the data are used for the symbol acquisition signal.

The overview of the algorithm is given here.⁵ The approach is to form a signal $X_{sym}(n)$ (for $n = 0, 1, 2, \dots, N_{data} - 1$) proportional to $D^2(i + 4n)$ ($i = 0, 1, 2, \text{ or } 3$) that can be shown to be periodic with

⁵ Details of the algorithm and the SNR in the FFT are given in M. Aung to E. W. Stone, "FFT Acquisition of Symbol Frequency and Phase After Subcarrier Acquisition With the Carrier Loop Open in the Fast Acquisition Algorithm," JPL Interoffice Memorandum 3338-94-075 (internal document), Jet Propulsion Laboratory, Pasadena, California, July 19, 1994, and in M. Aung to E. W. Stone, "FFT Acquisition of Symbol Frequency and Phase After Carrier and Subcarrier Acquisition in the Fast Acquisition Algorithm," JPL Interoffice Memorandum 3338-94-076 (internal document), Jet Propulsion Laboratory, Pasadena, California, July 19, 1994.

a frequency equal to ΔR_{sym} Hz [Fig. 4(a)]. Therefore, the FFT of $D^2(i + 4n)$ returns harmonic tones at $l\Delta R_{sym}$ ($l = 0, 1, 2, \dots$), and the frequency and phase can be estimated (Appendix) from the first harmonic. To eliminate the sign ambiguity in the frequency estimate, a complex FFT is formed from the signal and its quadrature as

$$X_{sym,z}(n) = X_{sym,I}(n) + jX_{sym,Q}(n) \quad (22)$$

For $N_{sc,acq} = 4$, it can be shown [Fig. 4(a)] that

$$X_{sym,z}(n) = X_{sym}(n+1) + jX_{sym}(n) \quad (23)$$

because the sequence $X_{sym,I}(n) \triangleq X_{sym}(n+1)$ is in quadrature with the sequence $X_{sym,Q}(n) \triangleq X_{sym}(n)$, as they differ by 90 deg in phase, as shown in Fig. 4(a).

A further modification is added to the algorithm where the acquisition signal is formed as $X_{sym}(n)$ proportional to $D^2(n)$. Then, note from Fig. 4(a) that the consecutive samples of $X_{sym}(n)$ have overlapping integration intervals. The outcome of overlapping is an improvement in the FFT SNR, and the estimated frequency and phase are

$$\hat{f}_{sym,FFT} = \hat{f}_{FFT} \quad (24)$$

$$\hat{\phi}_{sym,FFT}(t) = \hat{\phi}_{FFT} + 2\pi\hat{f}_{sym,FFT}t - \frac{\pi}{2} \quad (25)$$

where \hat{f}_{FFT} and $\hat{\phi}_{FFT}(t)$ are the frequency and phase estimates from the FFT of the acquisition signal $X_{sym}(k)$.

4. Case A: Symbol FFT Acquisition, Retrofitting Only the Subcarrier. When the symbol FFT acquisition is performed after the subcarrier is acquired, with the carrier loop still open [Fig. 2, steps (10) and (11)], the estimated subcarrier frequency and phase errors are rotated out from each sample of the stored I's and Q's, and the acquisition signal is formed as

$$\begin{aligned} X_{sym}(n) &= |Re \left\{ (QI(n) + jQQ(n))e^{-j\hat{\phi}_{e,sc}(n)} \right\} + jRe \left\{ (II(n) + jIQ(n))e^{-j\hat{\phi}_{e,sc}(n)} \right\}|^2 \\ &= \left\{ QI(n) \cos(\hat{\phi}_{e,sc}(n)) + QQ(n) \sin(\hat{\phi}_{e,sc}(n)) \right\}^2 \\ &\quad + \left\{ II(n) \cos(\hat{\phi}_{e,sc}(n)) + IQ(n) \sin(\hat{\phi}_{e,sc}(n)) \right\}^2 \\ &= A^2 D^2(n) \cos^2(\phi_{e,sc}(n) - \hat{\phi}_{e,sc}(n)) + n_{sym,FFT} \\ &\approx A^2 D^2(n) + n_{sym,FFT} \end{aligned} \quad (26)$$

where $\hat{\phi}_{e,sc}(\cdot)$ is the estimate of the subcarrier demodulation error $\phi_{e,sc}(\cdot)$ in the stored II, IQ, QI, and QQ [Eqs. (2)–(5)], estimated from the subcarrier FFT acquisition.

5. Case B: Symbol FFT Acquisition, Retrofitting the Subcarrier and the Carrier. When symbol acquisition is performed after the subcarrier and the carrier are acquired [Fig. 3, steps (9) and (10)], the symbol frequency and phase are estimated in a manner analogous to case A, with the following acquisition signal. The estimated subcarrier and carrier errors are rotated out from each sample of the stored I's and Q's, and the acquisition signal is

$$\begin{aligned}
X_{sym}(n) &= \left(Re \left[e^{-j\hat{\phi}_{e,c}(n)} \left[Re \left\{ (QI(n) + jQQ(n))e^{-j\hat{\phi}_{e,sc}(n)} \right\} + jRe \left\{ (II(n) + jIQ(n))e^{-j\hat{\phi}_{e,sc}(n)} \right\} \right] \right] \right)^2 \\
&= \left(\left[QI(n) \cos(\hat{\phi}_{e,sc}(n)) + QQ(n) \sin(\hat{\phi}_{e,sc}(n)) \right] \cos(\hat{\phi}_{e,c}(n)) \right. \\
&\quad \left. + \left[II(n) \cos(\hat{\phi}_{e,sc}(n)) + IQ(n) \sin(\hat{\phi}_{e,sc}(n)) \right] \sin(\hat{\phi}_{e,c}(n)) \right)^2 \\
&= A^2 D(n)^2 \cos^2(\phi_{e,sc}(n) - \hat{\phi}_{e,sc}(n)) \cos^2(\phi_{e,c} - \hat{\phi}_{e,c}) + n_{sym,FFT} \\
&\approx A^2 D(n)^2 + n_{sym,FFT}
\end{aligned} \tag{27}$$

where $\hat{\phi}_{e,sc}(\cdot)$ and $\hat{\phi}_{e,c}(\cdot)$ are the estimates of the subcarrier and carrier demodulation errors in the stored data, estimated from the subcarrier and carrier FFT acquisitions.

For cases A and B, the estimated frequencies and phases will have the following variances:

$$\sigma_{f,FFT}^2 = \frac{0.16}{T_{FFT}^2} \frac{1}{SNR_{FFT}} \text{ Hz}^2 \tag{28}$$

$$\sigma_{\phi,FFT}^2(t) = (2\pi)^2 \left(\frac{0.01345}{SNR_{FFT}} + \sigma_{f,FFT}^2 \times \left(t - \frac{T_{FFT}}{2} \right)^2 \right) \text{ rad}^2 \tag{29}$$

C. Carrier FFT Acquisition

The suppressed carrier is acquired after the subcarrier and symbol acquisition when the carrier phase noise is high and simultaneously with the subcarrier when the carrier phase noise is low. The carrier acquisition is described for the two cases.

1. Case A: Carrier Acquisition After the Subcarrier and Symbol Have Been Acquired.

If the carrier is acquired after the subcarrier and symbol loops are in lock [Fig. 2, step (7)], the carrier frequency and phase are estimated from one FFT. Note that at this point of the acquisition process, the I and Q subcarrier demodulation is performed with square-wave references. The acquisition signal is

$$X_{carr}(n) = (QI(4n) + jII(4n))^2 = \frac{P}{2} e^{j2\phi_{e,c}(n)} + n_{carr,acq}(n) \tag{30}$$

The SNR in the FFT will be

$$SNR_{FFT} = N_{data} \frac{E_s}{N_o} S_{L,bin} \frac{S_{L,\Delta f}^2}{8 \left[S_{L,\Delta f} + \frac{1}{2(E_s/N_o)} \right]} \tag{31}$$

2. Case B: Simultaneous Acquisition of the Carrier and the Subcarrier. For simultaneous subcarrier and carrier acquisition [Fig. 3, step (1)], the four carrier FFT acquisition signals are analogous to the subcarrier acquisition signal:

$$\begin{aligned} X_{carr,i}(n) &= (QI(i+4n) + jII(i+4n))^2 + (QQ(i+4n) + jIQ(i+4n))^2 \\ &= (AD(i+4n))^2 e^{j2\phi_{e,c}(n)} + n_{carr,acq}(n) \end{aligned} \quad (32)$$

where $i = 0, 1, 2, 3$, and $n = 0, 1, \dots, N_{data} - 1$. The SNR of the tone in the FFT and the variances of the estimated frequency and phase are the same as those for subcarrier acquisition, given in Eqs. (14)–(16).

Analogous to the subcarrier FFT acquisition, the estimated carrier frequency and phase for both cases A and B are

$$\hat{f}_{c,FFT} = \hat{f}_c + \frac{\hat{f}_{FFT}}{2} \quad (33)$$

$$\hat{\phi}_{c,FFT}(t) = \hat{\theta}_c + \frac{\hat{\phi}_{FFT}}{2} + 2\pi\hat{f}_{c,FFT}t \quad (34)$$

where \hat{f}_{FFT} and $\hat{\phi}_{FFT}$ are the estimates of frequency and phase (at $t = 0$) of the peak tone in the FFT (Appendix), and \hat{f}_c and $\hat{\phi}_c$ are the predicted carrier frequency and phase. The estimated frequency and phase will have the same variance as in Eqs. (15) and (16).

D. Determination of the FFT Parameters

In this section, the FFT parameters, namely N_{data} , detection threshold, and the zero-padding factor, are discussed.

1. Determination of N_{data} . The number of data points to be used in the FFT, N_{data} , is determined from choosing a desired confidence of detection, C , and solving for N_{data} . The confidence of detection, which is the probability of detecting the correct signal bin in the FFT in the presence of noise, is

$$C \approx \left(1 - 0.5e^{-0.5(E_s^*/N_o)N_{data}}\right)^{2(\Delta f_{search}/R_{sym})N_{data}} \quad (35)$$

where E_s^*/N_o is the equivalent symbol SNR in the acquisition FFT, defined in Eq. (6). The Δf_{search} determines the frequency search region, $\pm\Delta f_{search}$ Hz about the predicted frequency, i.e., the peak bin in the PSD is detected as the bin with the largest PSD value among the bins corresponding to the search frequency range $[\hat{f} - \Delta f_{search}, \hat{f} + \Delta f_{search}]$ Hz. It should be noted that Eq. (35) is only an approximation of the confidence of detection.

2. Detection Threshold. In the FFT acquisition, FFT detection is declared if the peak bin in the search frequency range $[\hat{f} - \Delta f_{search}, \hat{f} + \Delta f_{search}]$ Hz exceeds a lower threshold, P_{thresh} . The lower threshold is set as

$$P_{thresh} \triangleq \xi P_s \quad (36)$$

where

P_s = the expected signal power

$$\xi = \left(1 - \frac{1}{\sqrt{SNR_{FFT}}} \text{Erf}^{-1}[2C - 1]\right)^2$$

C = confidence of detection

$\text{Erf}^{-1}(\cdot)$ = inverse error function

3. The Zero-Padding Factor. The nominal value of the zero-padding factor, α , will be 4. However, N_{data} is chosen according to Eq. (35), which may not be a 2^n value. In general, the FFT size, N_{FFT} , will be determined as

$$N_{FFT} = 4 \times N_{nearest}$$

where $N_{nearest}$ is the nearest 2^n value greater than or equal to N_{data} . Data points N_{data} plus $(N_{FFT} - N_{data})$ zeros will be used to form the N_{FFT} point FFT. Therefore, the actual zero-padding factor, which should be the value used in all equations requiring α (e.g., frequency interpolation), will be

$$\alpha = \frac{N_{FFT}}{N_{data}} \geq 4 \quad (37)$$

IV. Loop Acquisition

This section discusses loop acquisition. First, initialization of the tracking loop frequency and phase is described. The use of two-arm versus one-arm loops is also briefly discussed, and the majority of the section describes the process of initializing and gradually narrowing the loop bandwidths (and windows if applicable) until the final loop SNR is achieved.

A. Initializing the NCOs of the Tracking Loops

After the FFT acquisition, the (subcarrier, symbol, and carrier if applicable) tracking loops are closed with the FFT estimated parameters. In each loop (indicating subcarrier, symbol, or carrier as $Y = \text{"sc," "sym," or "carr"}$ in the following), the initial frequency in the numerically controlled oscillator (NCO) is set to $f_{NCO,init}$:

$$f_{NCO,init} = \hat{f}_{Y,FFT} \quad (38)$$

and the initial phase of the NCO is set to $\phi_{NCO,init}$:

$$\phi_{NCO,init} = \hat{\phi}_{Y,FFT}(t_{cl,loop}) \quad (39)$$

where $t = t_{cl,loop}$ is the time at which the loop is closed with respect to $t = 0$ at the beginning of the first symbol integration, shown in Fig. 4(a).

B. Two-Arm and One-Arm Tracking Loops

New two-arm tracking loops have been introduced for subcarrier and symbol tracking while the carrier loop is open. The two-arm loop forms the loop phase error estimate $\hat{\phi}_{e,loop}$ from two phase detector outputs, one output using the carrier I input and the other output using the carrier Q input, as shown

in Fig. 5. When tracking the subcarrier and/or symbol loop while the carrier is open-loop demodulated, and when the symbol SNR is low, using two arms provides a 3-dB gain in the loop SNR as the signals in both channels are used. When the carrier is in lock, no additional information and only additional noise is gained by using the second channel and, therefore, a conventional one-arm loop is used.

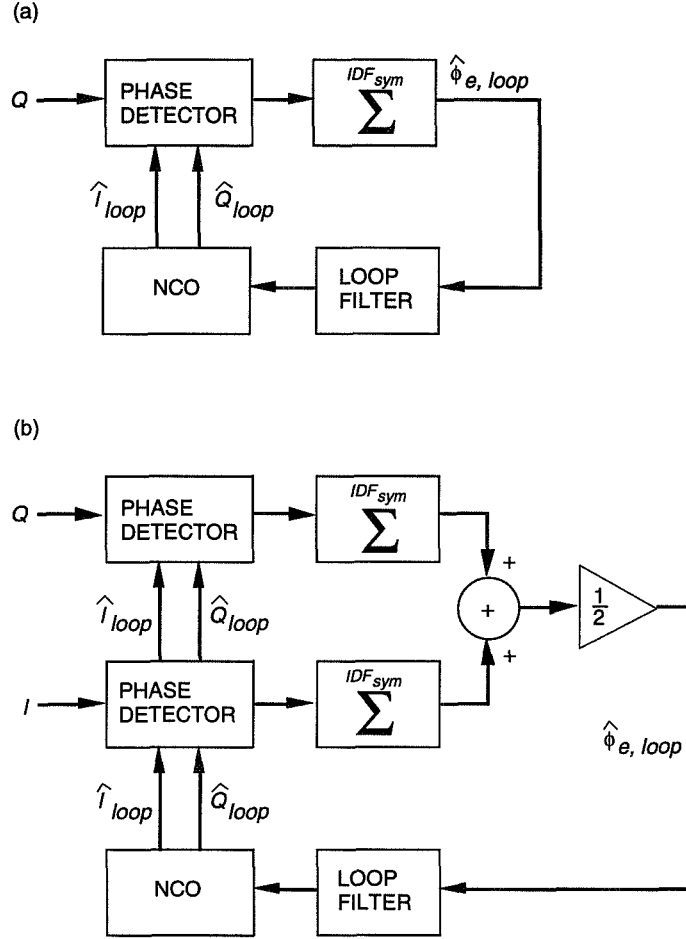


Fig. 5. Subcarrier or symbol tracking loops: (a) one arm and (b) two arm.

C. Initial Bandwidths and Windows

When FFT acquisition is complete, each estimate of signal phase and frequency will have associated with it a variance, $\sigma_{\phi, FFT}^2$ and $\sigma_{f, FFT}^2$, respectively (given in the last section). The initial tracking loop bandwidth (and transition window if applicable) is chosen by matching the loop phase variance, σ_{ϕ}^2 , with the FFT-estimated phase variance, $\sigma_{\phi, FFT}^2$. This is analogous to a constant-bandwidth tracking loop handing over to the acquisition loops, which will start at the bandwidth and window and begin narrowing.

The tracking variance σ_{ϕ}^2 for each type of loop can be written in the form

$$\sigma_{\phi}^2 = \begin{cases} (2\pi)^2 c_{\phi}^2 B_L w \text{ rad}^2, & \text{for loops with transition windows (SCL and SSL)} \\ (2\pi)^2 c_{\phi}^2 B_L \text{ rad}^2, & \text{otherwise (suppressed carrier loop)} \end{cases}$$

where B_L is the loop noise bandwidth, w is the window width size, and c_ϕ^2 is a constant that depends on the signal SNR and the tracking loop. For loops with transition windows, the window is specified in terms of the tracking variance with the parameter c_w :

$$w = \frac{c_w \sigma_\phi}{(2\pi)}$$

$$c_w = \begin{cases} 4c'_w, & \text{for subcarrier loops} \\ 2c'_w, & \text{for symbol loops} \end{cases}$$

The parameterization of c_w in terms of c'_w is for physical significance: c'_w gives the tracking error that reaches the edge of the transition window, expressed in tracking standard deviations. For example, with $c'_w = 4$, the (unlikely) tracking error of $4\sigma_\phi$ is necessary to cause the signal transition to fall outside of the phase extractor window.

We can now solve for the initial bandwidth and window width:

$$w(0) = \frac{c_w \sigma_{\phi,FFT}}{2\pi}$$

$$B_L(0) = \frac{\sigma_{\phi,FFT}^2}{(2\pi)^2 c_\phi^2 w(0)}$$

For a loop with no transition window, the initial bandwidth is

$$B_L(0) = \frac{\sigma_{\phi,FFT}^2}{(2\pi)^2 c_\phi^2}$$

The windowing allows the initial bandwidth to be w times larger than with no windowing for a given loop SNR.

D. Bandwidth and Window Narrowing

In the continuous bandwidth and window narrowing methods used,⁶ the loop time constant $\tau \triangleq 1/(2B_L)$ is linearly increasing in time with rate $d\tau/dt$. Bandwidth as a function of time then has the form

$$B_L(t) = \frac{1}{2 \left(\frac{1}{2B_L(0)} + \frac{d\tau}{dt} t \right)} \quad (40)$$

In tracking loops with transition windows, window as a function of time is given by

$$w(t) = w(0) \frac{B_L(t)}{B_L(0)}$$

⁶ The bandwidth and window narrowing method is introduced and analyzed in S. Stephens, "Bandwidth and Window Modification in Phase-locked Loops," JPL Interoffice Memorandum 335.9-94-010 (internal document), Jet Propulsion Laboratory, Pasadena, California, June 1994.

From simulation⁷ and analysis, values of $d\tau/dt$ and c'_w that minimize the loop phase variance after a fixed time span are specified for loops⁸ of order N and damping parameter η^2 and are given in Table 1.

Table 1. Optimum values of $d\tau/dt$ and c'_w for loops of order N and damping parameter η^2 .

Loop	$d\tau/dt$	c'_w
Subcarrier loop, $N = 2, \eta^2 = -1$	0.181	4.0
Symbol loop, $N = 1$	1.0	4.0
Symbol loop, $N = 2, \eta^2 = -1$	0.181	4.0
Carrier loop, $N = 2, \eta^2 = -1$	0.383	

From solving Eq. (40), the time, T_{fin} , to reach $B_{L,fin}$ from $B_L(0)$ is

$$T_{fin} = \frac{1}{2\frac{d\tau}{dt}} \left(\frac{1}{B_{L,fin}} - \frac{1}{B_L(0)} \right) \approx \frac{1}{2\frac{d\tau}{dt} B_{L,fin}} \quad (41)$$

Note that for $d\tau/dt = 0.181$,

$$T_{fin} \approx \frac{2.8}{B_{L,fin}} \text{ sec}$$

For digital loops, bandwidth and window width values can be changed no faster than the update rate. Processor limitations may impose an even tighter constraint: for the Block V Receiver, the loop parameters may only be modified once per second. If the continuous equations above are used to generate discrete values of bandwidths and windows at rates (f_u) much larger than the loop bandwidth, then the analysis should still hold; this is confirmed by simulation in Section VI. However, if f_u is comparable to or larger than the loop bandwidth, the analysis in Footnote 6 specifies a maximum allowable change in the value per update time of $1/f_u$ sec. In this case, the bandwidths and windows are narrowed in the limited step sizes allowed per update time. For Galileo fast-acquisition in the BVR ($f_u = 1$ Hz), where the bandwidths are less than $f_u = 1$ Hz for all loops, we can always use the continuous approximation.

The bandwidth function versus time is illustrated in Fig. 6(a). The dark line shows the actual bandwidth values applied to the tracking loop. The steps reflect the update rate $f_u = 1$ Hz, at which the bandwidth is modified. The following sections discuss $B_{L,min}$ and $B_{L,fin}$.

The window function versus time is illustrated in Fig. 6(b). The dark line shows the actual window width values applied to the tracking loop. The limitation of the window value (in the BVR) to a 2^{-n} value (discussed in Section V) results in quantized window values, as in the figure. A discussion of w_{fin} and w'_{fin} follows.

⁷ The implementation and simulation of Footnote 6 is discussed in M. Aung, S. Stephens, and C. Buu to J. Berner, "Block V Receiver Implementation and Simulation of Bandwidth and Window Narrowing Methods in [1]," JPL Interoffice Memorandum 3338-94-042 (internal document), Jet Propulsion Laboratory, Pasadena, California, June 3, 1994.

⁸ S. A. Stephens and J. B. Thomas, "First-Principles Analysis of Digital Phase-Locked Loops with Controlled-Roots, Transient-Response-Specific Parameterization," JPL Interoffice Memorandum 335.1-91-032 (internal document), Jet Propulsion Laboratory, Pasadena, California, November 22, 1991.

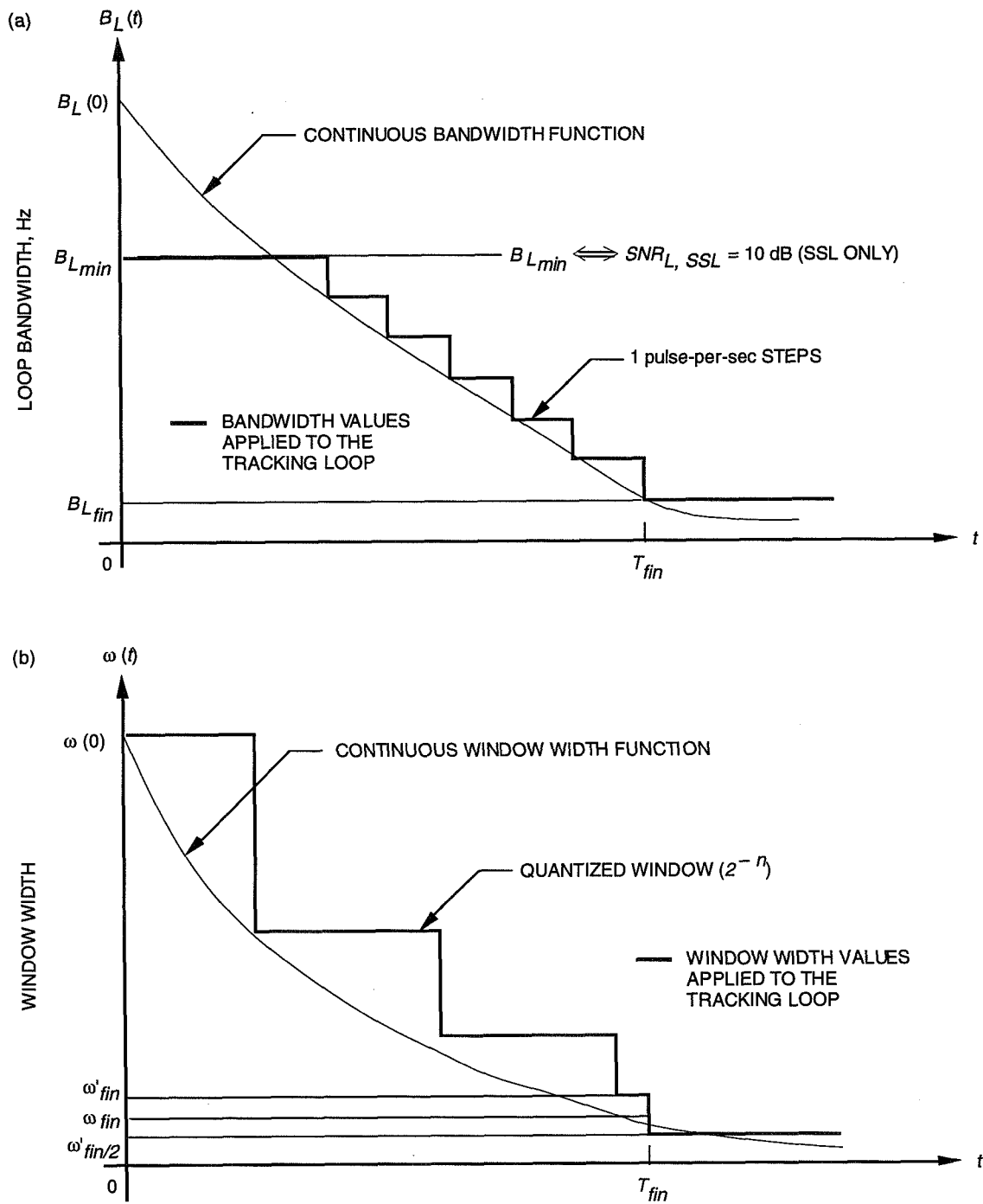


Fig. 6. Bandwidth and window narrowing: (a) loop bandwidth versus time t and (b) $\omega(t)$ versus time t .

E. Final Bandwidths and Windows

The final bandwidth, $B_{L,fin}$, is determined from a specified maximum output symbol SNR loss; the bandwidth narrowing routine stops narrowing when it reaches the final required bandwidth at time $t = T_{fin}$. However, window quantization will cause the final quantized window value ω'_{fin} to be larger than ω_{fin} , specified by the continuous equations above. This in turn yields a lower final loop SNR

than desired. For compensation, the window or bandwidth must be narrowed an additional amount. During narrowing, the tracking variance at any given time can be twice as large as that implied by the bandwidth alone, due to transients in the narrowing process. Thus, the optimum windowing factor c'_w during narrowing will be larger than the factor used once narrowing transients have died away. The method implemented for reaching the final design loop SNR makes use of this smaller c'_w when the narrowing process is completed; the window is narrowed by an additional factor of two at the end of the narrowing process, which is when the final bandwidth is reached, as shown in Fig. 6(b), i.e., at $t = T_{fin}$, the window is set to $w_{fin}/2$.

F. Special Considerations

For the symbol loop, the initial bandwidth specified above may cause the initial loop SNR of the SSL to be somewhat low (e.g., when $SNR_{FFT} = 12$ dB and symbol phase is estimated from a set of subcarrier acquisition FFTs (Section III.B.2), the initial SSL SNR is about 8 dB). For this case, the bandwidth is limited to $B_{L,min}$, which corresponds to a loop SNR of 10 dB; the window width calculation uses the continuous bandwidth function before it is limited, so that the window is kept larger for transients caused by the narrow bandwidth [Fig. 6(a)].

V. Implementation in the Block V Receiver

The fast acquisition algorithm has been implemented in the BVR; this section discusses the issues regarding its implementation. The BVR high-speed digital signal-processing hardware consists of five application-specific integrated circuits (ASICs) that are used to demodulate the carrier and up to two subcarriers and two symbol streams. There are three unique ASIC designs: carrier processing, subcarrier processing, and symbol processing. The two telemetry processing channels (subcarrier and symbol loops) are provided by independent sets of the subcarrier and symbol ASICs, each set receiving the in-phase (I) and quadrature-phase (Q) carrier demodulation outputs (the subcarrier ASIC can internally reverse the I and Q inputs). All tracking loop NCOs are frequency and phase updatable. The software processing of each telemetry channel is also independent of the other.

Implementation of the fast acquisition algorithm involved changing the software tasking structure of the BVR subcarrier and symbol tracking loops and modifying the algorithm for the software implementation. The carrier, subcarrier, and symbol tracking loops are implemented as independent software tasks. As such, the loop acquisitions are independent processes; it is possible to acquire the subcarrier and symbol loops sequentially or simultaneously. The fast acquisition algorithm requires that the subcarrier and symbol loops be controlled together. To accomplish this, a separate task was created for the fast acquisition process. The subcarrier and symbol loops have two acquisition tasks each, the normal acquisition, which is independent for each loop, and the fast acquisition, which controls both loops.

Upon receipt of the acquisition command, the task zeroes out the subcarrier and symbol NCO phases and sets the subcarrier NCO frequency to the predicted subcarrier frequency and the symbol NCO frequency to the predicted symbol rate times $N_{sc,acq}$. The subcarrier reference signal type is set to sine wave (as opposed to the normal square wave). Because there are no accumulators to sum the symbol integration outputs, the symbols must be read into software for processing. This means that the symbol NCO frequency used must be less than the symbol hardware interrupt rate (1 or 2 kHz). This places a limit on the product of $N_{sc,acq}$ and the symbol rate. For this part of the acquisition process, only one set of telemetry ASICs is used, since all four outputs (II, IQ, QI, and QQ) are available.

The FFT size is determined from the input predicted signal parameters. The data are collected, and the complex subcarrier FFT inputs for the $N_{sc,acq}$ FFTs are generated. A Sky Computer Skybolt array processor board is used to compute the FFTs, which can be as large as 2^{17} points. After the (subcarrier, symbol, and carrier) phase and frequency are estimated from the FFT acquisition, the tracking loop

NCOs, which are frequency and phase updatable, are initialized with the FFT-estimated values, and the loops are closed. The subcarrier reference signal type is changed to the square wave.

If the carrier loop has not yet been acquired, the subcarrier and symbol loops must be operated in the two-arm mode. This uses both sets of telemetry ASICs to generate the windowed subcarrier and symbol tracking loop inputs (the second set of ASICs has the I and Q inputs reversed, providing the needed signals to give windowed versions of the II, IQ, QI, and QQ signals). If the carrier is locked, only one telemetry channel is required.

The implementation of the transition window-narrowing and bandwidth-narrowing algorithms also required some trade-offs, due both to hardware and software concerns. The subcarrier and symbol windows are implemented in the ASICs and are quantized to a factor of two. In other words, the hardware window widths are step selectable in increments of 2^{-n} , where n is an integer in the range of 0 to 15. So, the algorithm could not continuously vary the window width; it had to quantize the windows to the hardware capabilities.

The update rates of the narrowing algorithms (both window and bandwidth) were also quantized in time. All tracking loops have two update rates: the hardware interrupt rate, which is the rate that the software reads in the data off of the ASICs and processes the tracking loop, and the once-per-second pulse, which is the rate at which the performance data are reported and the loop configuration parameters are updated. It was determined that the narrowing algorithms could be updated at the lower rate (once per second), which allowed a simpler implementation that did not require lowering the interrupt rate (the higher the interrupt rate, the less time there is to process the software instructions required to close the loop).

VI. Computer Simulation

Extensive computer simulations were performed to verify the design and analysis of the fast acquisition method.⁹ The simulations examine the following aspects of the fast acquisition algorithm:

- (1) Subcarrier FFT acquisition
- (2) Symbol FFT acquisition
- (3) Carrier FFT acquisition
- (4) Subcarrier, symbol, and carrier loop acquisition

In order to verify case 1 [step (1) of Figs. 2 and 3], the subcarrier FFT acquisition is simulated in the presence of demodulation errors, and the resulting frequency and phase estimates are compared to the input parameters. The theoretical performance of the algorithm is also evaluated in terms of the probability of FFT detection and statistics on the frequency and phase estimates. Specifically, the simulations verify agreement between measured and predicted values for the following:

- (1a) Subcarrier tone SNR when the symbol rate error is negligible and the subcarrier is acquired using four initial symbol phase offsets
- (1b) Subcarrier tone SNR when the symbol rate error is significant

⁹ References for the simulation results are summarized in M. Aung to E. W. Stone, "Computer Simulation Work Supporting the Design and Analysis of the Block V Receiver Fast Acquisition Algorithm," JPL Interoffice Memorandum 3338-94-053 (internal document), Jet Propulsion Laboratory, Pasadena, California, June 1, 1994, which gives an overview of the simulation work and lists all interoffice memoranda reporting the simulation results.

- (1c) FFT detection confidence
- (1d) Subcarrier frequency and phase estimates
- (1e) Subcarrier frequency and phase estimate variances

Verification of (1e) is important since the SCL is closed with the initial bandwidth, and the window values are calculated as functions of the predicted standard deviation of the FFT-estimated phase. In addition, (1a) and (1d) were verified for actual Galileo downlink data recorded at Goldstone. Good agreement to within one or two standard deviations of the measured value was seen for (1a), (1b), (1d), and (1e). For (1c), an approximate predict was used, resulting in some divergence with the simulated value.

In symbol FFT acquisition, when the error in the predicted symbol frequency is negligible, the symbol phase can be estimated from the subcarrier acquisition by interpolating the $N_{sc,acq}$ PSDs of the subcarrier FFT acquisition. If the symbol phase detection fails due to a symbol rate error, the symbol frequency and phase are acquired via FFT methods. Hence, for steps (4), (10), and (11) of Fig. 2 and steps (4), (9), and (10) of Fig. 3, the simulations verify agreement between measured and predicted values for the following:

- (2a) Symbol phase when the symbol rate error is negligible and the phase is estimated from the four subcarrier acquisition FFTs
- (2b) Symbol phase estimate variances for (2a)
- (2c) Symbol frequency and phase and the variances of these estimates when the symbol rate is unknown
- (2d) Symbol error tone SNR when the symbol rate is unknown

Verification of variance of the FFT estimate is important since the SSL is closed with the initial bandwidth and window values, which are calculated as functions of the predicted standard deviation of the FFT-estimated phase. For (2a) through (2d), good agreement to within one or two standard deviations of the measured value was seen. Agreement varied slightly for (2b), but the uncertainty lies in the computation of the predicted standard deviation (an approximation of the true standard deviation was used).

Simulations of the subcarrier and carrier simultaneous FFT acquisition [step (1), Fig. 3] confirm that carrier FFT acquisition is analogous to subcarrier FFT acquisition in terms of tone SNRs. Therefore, results obtained for case (1) can be applied to case (3).

The loop acquisition in case (4) was simulated separately by initializing the loop NCO phase and frequency with errors equal to one standard deviation of the FFT estimates. The loops are then closed with initial bandwidths and window widths as described in Section IV.C. The bandwidths are narrowed as described in Section IV.D until the desired symbol SNR degradation is achieved. The window widths are narrowed in quantized increments of 2^{-n} to reflect hardware implementation constraints in the BVR. In addition, the simulation update rate of the narrowing algorithm is set to 1 pulse per sec in accordance with the BVR loop configuration parameter update rate. The simulations measure acquisition times for the following cases:

- (4a) The subcarrier, symbol, and carrier loops are closed simultaneously using the one-arm approach [steps (5) through (7) in Fig. 3].

- (4b) The two-arm SCL and SSL are closed, followed by carrier FFT acquisition first and then the carrier loop acquisition [steps (5) through (8) in Fig. 2]. This is simulated by closing all three loops simultaneously, assuming that the carrier FFT acquisition time is negligible compared to the SCL and SSL loop acquisition times.
- (4c) The two-arm SCL and SSL are closed while the carrier loop is left open [steps (5) and (6) in Fig. 2].

Good agreement is observed between measured and predicted acquisition times as discussed in Section VII.

VII. Acquisition Times

The acquisition time of the fast acquisition algorithm is defined as the length of time required until all the loops (subcarrier, symbol, and carrier if applicable) have attained loop SNRs high enough to contribute only a tolerable amount of degradation to the output symbol SNR. For the high carrier phase-noise case (Section II.A) when the carrier is acquired after the subcarrier and symbol acquisition, the acquisition time is

$$T_{acq} = \text{MAX}\{T_{sc,acq}, T_{sym,acq}\} + T_{carr,acq} \text{ sec} \quad (42)$$

where $T_{Y,acq}$ ($Y = sc, sym, \text{ or } carr$, indicating subcarrier, symbol or carrier) is the acquisition time of the indicated signal. For the low carrier phase-noise case (Section II.B) when the subcarrier, symbol, and carrier are acquired simultaneously, the acquisition time is

$$T_{acq} = \text{MAX}\{T_{sc,acq}, T_{sym,acq}, T_{carr,acq}\} \text{ sec} \quad (43)$$

In the following, individual acquisition times for the subcarrier, symbol, and suppressed carrier ($T_{sc,acq}$, $T_{sym,acq}$, and $T_{carr,acq}$, respectively) are presented. For each case, $T_{Y,acq}$ is defined as

$$T_{Y,acq} = T_{Y,FFT} + T_{Y,loop} \quad (44)$$

where $T_{Y,FFT}$ is the FFT acquisition time and $T_{Y,loop}$ is the loop acquisition time.

The FFT acquisition time, $T_{Y,FFT}$, is

$$T_{Y,FFT} = N_{data}T_{sym} = \frac{SNR_{Y,FFT}}{E_s^*/N_o}T_{sym} \quad (45)$$

where $SNR_{Y,FFT}$ is the SNR in the FFT-acquisition of the signal under consideration.

The loop acquisition time for each loop, $T_{Y,loop}$, is defined as the length of time for narrowing the bandwidth and window width until the design loop SNR, $SNR_{L,fin}$, is achieved. The $SNR_{L,fin}$ is determined by the maximum allowed degradation, $Deg(\phi)$, to the output symbol SNR due to the loop phase jitter, ϕ . The relationships between $Deg(\phi)$ and ϕ are listed in Table 2 for the SSL, SCL, and the suppressed carrier loop. The expected degradation, $\overline{Deg(\phi)}$, calculated as the statistical expectation of $Deg(\phi)$ assuming a Gaussian distribution for ϕ , is also listed in Table 2 where $SNR_L \triangleq 1/\sigma_\phi^2$.

Table 2. Degradation, $Deg(\phi)$, to the output symbol SNR due to loop phase error ϕ , and expected values of $Deg(\phi)$ and $\overline{Deg(\phi)}$ for the SCL, SSL, and carrier loops.

Loop	$Deg(\phi)$	$\overline{Deg(\phi)}$
SCL	$\left(1 - 4\frac{ \phi }{2\pi}\right)^2$	$1 - 8\sqrt{\frac{1}{2SNR_L\pi^3} + \frac{4}{SNR_L\pi^2}}$
SSL	$\frac{1}{2}\left(1 + \left(1 - 2\frac{ \phi }{2\pi}\right)^2\right)$	$1 - 4\sqrt{\frac{1}{SNR_L(2\pi)^3} + \frac{2}{SNR_L(2\pi)^2}}$
Suppressed carrier loop	$\cos^2(\phi)$	$\frac{1}{2}\left(1 + e^{-\frac{2}{SNR_L}}\right)$

The $SNR_{L,fin}$ is calculated as the minimum SNR_L required for a given expected degradation. In Table 3, $SNR_{L,fin}$ is calculated for expected degradation values of $\{0.1, 0.2, 0.5, 1\}$ dB, i.e., for final degradation of $\{0.1, 0.2, 0.5, 1\}$ dB to the output symbol SNR due to each loop, the loop bandwidth and window width are to be narrowed until the loop SNR of $SNR_{L,fin}$ of Table 3 is achieved. When designing for low final loop SNRs, the $SNR_{L,fin}$ derived should be padded conservatively, e.g., by 1 dB, to compensate for nonlinear effects not modeled in the equations used for loop SNRs.

Table 3. Minimum required loop SNRs, $SNR_{L,fin}$'s, as a function of $\overline{Deg(\phi)}$.

$\overline{Deg(\phi)}$, dB	SCL $SNR_{L,fin}$, dB	SSL $SNR_{L,fin}$, dB	Suppressed carrier loop $SNR_{L,fin}$, db
0.1	33	21	16
0.2	27	15	13
0.5	19	6.5	9
1.0	13.0	0	6

Recall that the initial loop SNR is set equal to $1/\sigma_{\phi_{FFT}}^2$, the inverse of the variance of the FFT-estimated phase at the time the loop is closed. For the acquisition time plots presented in this section, it is assumed that SNR_{FFT} is 12 dB, and that the tracking loop is closed at $t_{cl,loop} = T_{FFT}$. In this case, the initial SNR_L 's are listed in Table 4. For the SSL, $1/\sigma_{\phi_{FFT}}^2$ is less than the minimum loop SNR of 10 dB required to avoid cycle slipping; therefore, the loop will be started with a bandwidth such that the initial loop SNR is 10 dB, as described in Section IV.F. By comparing Tables 3 and 4, it is seen that the carrier loop starts out very close to or above the $SNR_{L,fin}$ required. Hence, the carrier loop acquisition time is essentially 0, leaving only the FFT acquisition time. As larger degradations to the output symbol SNR are tolerated, the required $SNR_{L,fin}$ are smaller and the loop acquisition times are shorter. In fact, for a degradation of 0.5 dB, the loop acquisition times for both the symbol and the suppressed carrier are 0 sec, leaving only the FFT acquisition time. For a 1-dB degradation, the loop acquisition time is 0 for all three loops.

The loop acquisition time, $T_{Y,loop}$, is calculated as the time to reach the required final bandwidth, $B_{L,fin}$, corresponding to the required $SNR_{L,fin}$, Eq. (41), plus $1/2B_{L,fin}$ sec. The latter term is an approximation of the additional time the loop transients will require to die out after the final window narrowing by an extra factor of two at the end of the narrowing process (Section IV.E). Hence,

$$T_{loop} = \frac{1}{2(d\tau/dt)} \left(\frac{1}{B_{L,fin}} - \frac{1}{B_{L,init}} \right) + \frac{1}{2B_{L,fin}} \quad (46)$$

where

$$B_{L,fin} = \begin{cases} \frac{1}{c_w c_\phi^2} \frac{1}{\sqrt{SNR_{L,fin}}} \frac{1}{2\pi} & \text{SCL and SSL} \\ \frac{1}{c_\phi^2 SNR_{L,fin} (2\pi)^2} & \text{suppressed carrier loop} \end{cases}$$

and

$$B_{L,init} = \begin{cases} \frac{1}{2\pi} \frac{\sigma_{\phi_{FFT}}}{c_w c_\phi^2} & \text{SCL and SSL} \\ \frac{\sigma_{\phi_{FFT}}^2}{c_\phi^2 (2\pi)^2} & \text{suppressed carrier loop} \end{cases}$$

Table 4. Initial loop SNRs when $SNR_{FFT} = 12$ dB.

Loop	$SNR_{L,init} = 1/\sigma_{\phi_{FFT}}^2$, dB
SCL	14.8
SSL (symbol phase estimation by interpolation)	8 (10 dB used to avoid cycle slips)
SSL (FFT frequency and phase estimation)	8.8 (10 dB used to avoid cycle slips)
Suppressed carrier loop	14.8

Acquisition times vary with the types of loops: one-arm versus two-arm and different loop orders.¹⁰ In this section, $T_{sc,acq}$, $T_{sym,acq}$, and $T_{carr,acq}$ are presented for the high carrier phase-noise case. In Figs. 7(a), 8(a), and 9(a), $T_{sc,acq}$ is plotted for final degradations of 0.1, 0.2, and 0.5 dB, respectively. Similarly, in Figs. 7(b), 8(b), and 9(b), $T_{sym,acq}$ is plotted. The suppressed carrier acquisition time plotted in Fig. 7(c) is presented as $T_{carr,acq} = T_{carr,FFT}$ (with the assumption that $T_{carr,loop} \approx 0$ sec) for final degradations of 0.1, 0.2, and 0.5 dB.

In these figures, $T_{Y,acq}$ is a function of P_D/N_o and E_s/N_o (or R_{sym}). Hence, families of curves of $T_{Y,acq}$ versus P_D/N_o are plotted for various values of E_s/N_o . Note the decrease in the acquisition times for larger final degradations.

The total acquisition time of the algorithm, T_{acq} , for the final degradation of 0.1, 0.2, or 0.5 dB from each loop, is estimated as in Eq. (41). For example, for $P_D/N_o = 14.6$ dB-Hz and $R_{sym} = 16$ symbols per sec ($E_s/N_o = 2.56$ dB) expected when the Galileo spacecraft is at JOI, the acquisition time, $T_{acq,JOI}$, for a final degradation of 0.2 dB is

$$T_{acq,JOI} = MAX\{26.4, 33.1\} + 5.9 = 38 \text{ sec}$$

¹⁰ A complete set of acquisition times for the different loops is in C. Buu, S. Stephens, and M. Aung to J. Berner, "Acquisition Times of the Fast Acquisition Algorithm," JPL Interoffice Memorandum 3338-94-052 (internal document), Jet Propulsion Laboratory, Pasadena, California, June 4, 1994.

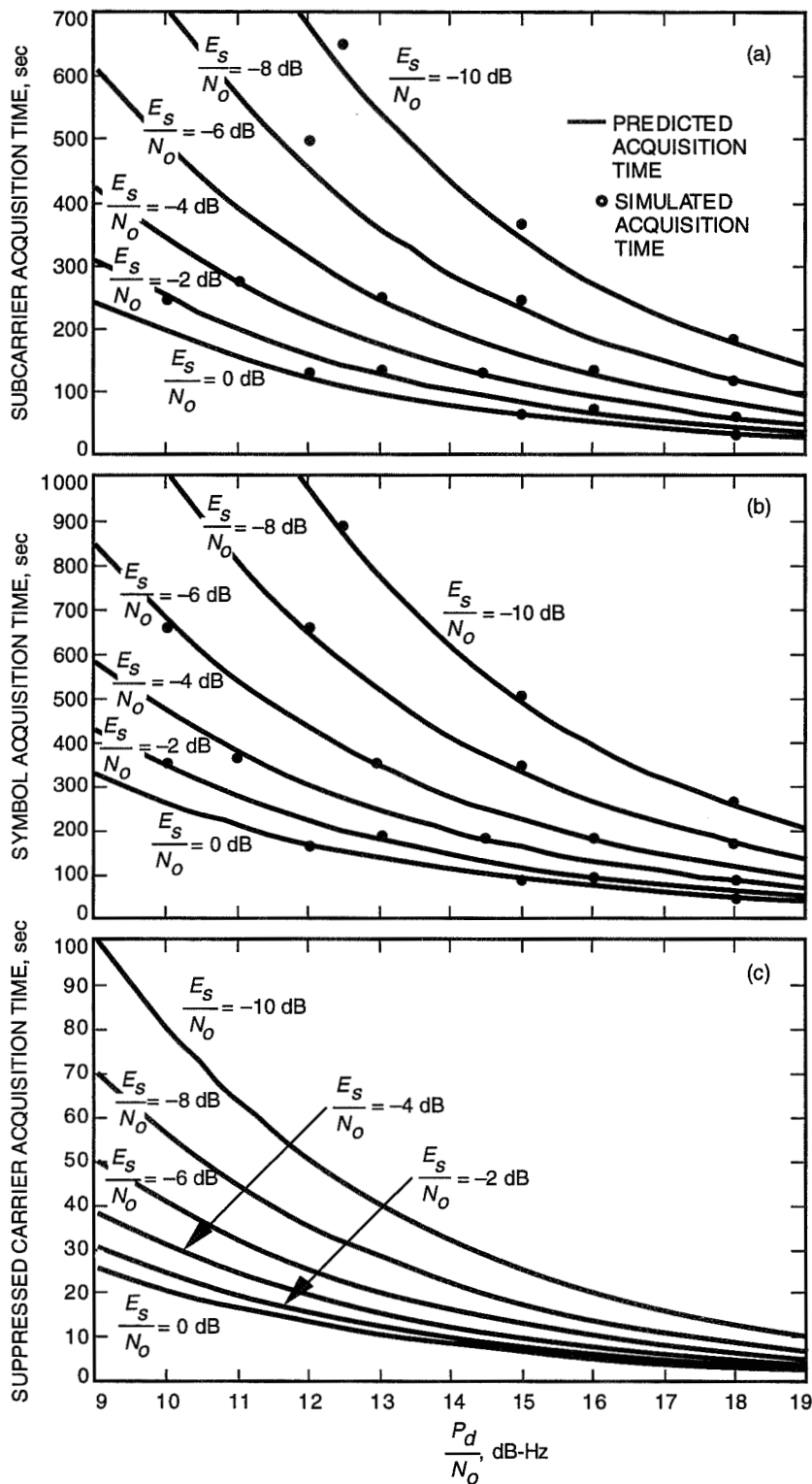


Fig. 7. Acquisition time to reach 0.1-dB degradation in output symbol SNR due to phase jitter in each loop: (a) subcarrier $T_{sc,acq}$, and (b) symbol $T_{sym,acq}$, and for (c) suppressed carrier $T_{carr,acq}$ to reach 0.1, 0.2, or 0.5-dB degradation.

The simulated acquisition times are also included in Figs. 7-9, shown in discrete points. In the simulations, $SNR_{L,fin}$ padded by 1 dB was used. Relatively good agreement is seen between the predicted and the simulated times. The seemingly larger divergence in the plots for a 0.5-dB degradation is largely due to the vertical scale of the plot. In Figs. 7(c) and 9(b), no simulation points are included as $T_{acq} = T_{FFT}$.

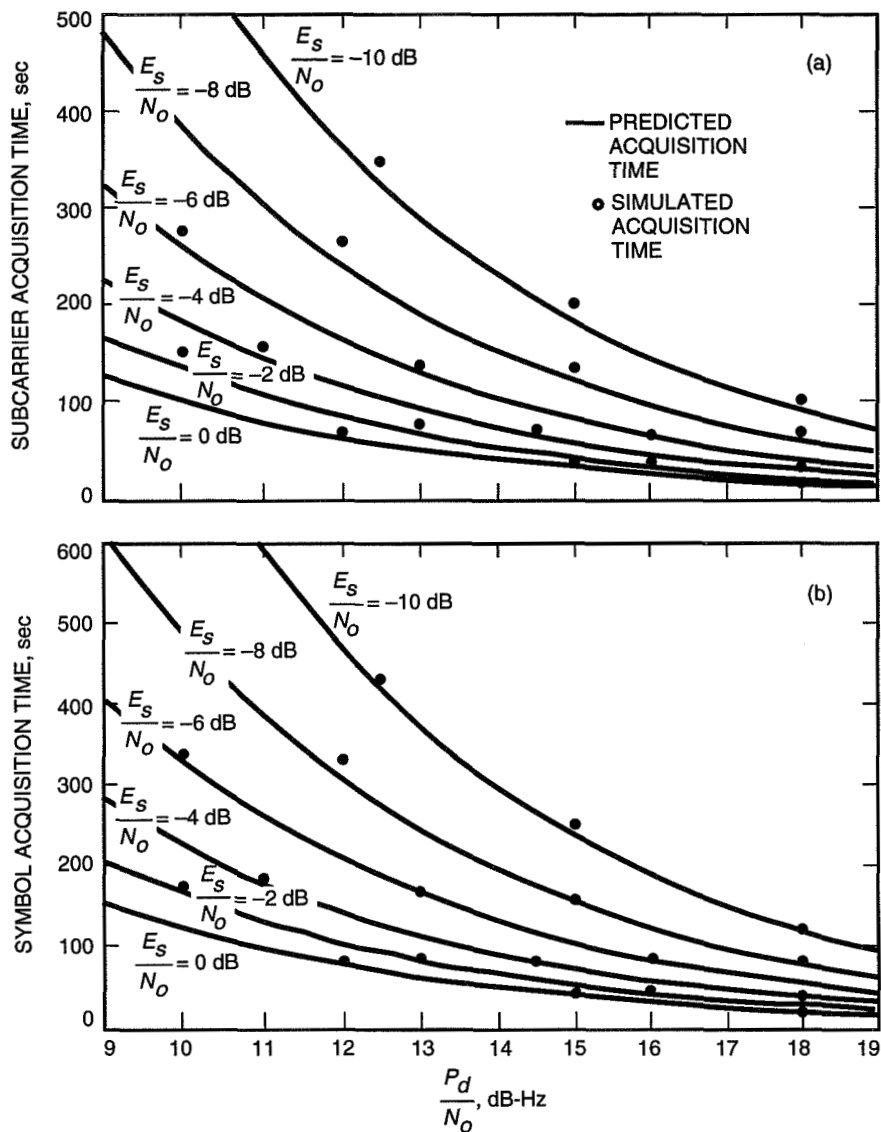


Fig. 8. Acquisition time to reach 0.2-dB degradation in the output SNR due to phase jitter in each loop: (a) subcarrier $T_{sc, acq}$ and (b) symbol $T_{sym, acq}$.

VIII. Conclusion

The fast acquisition algorithm developed for the Galileo S-band mission that is expected to encounter low data rate, low SNR, and high carrier phase-noise conditions is presented in this article. Multiple schemes resulting in faster acquisition times are introduced. Implementation of the algorithm in the Block V Receiver is described. Simulation work supporting the algorithm is discussed. Finally, the acquisition times of the algorithm are presented. In the expected case for the Galileo spacecraft at

JOI ($P_D/N_o = 14.6$ dB-Hz and $R_{sym} = 16$ symbols per sec), the acquisition time to attain a 0.2-dB degradation from each loop to the output symbol SNR is estimated to be 38 sec.

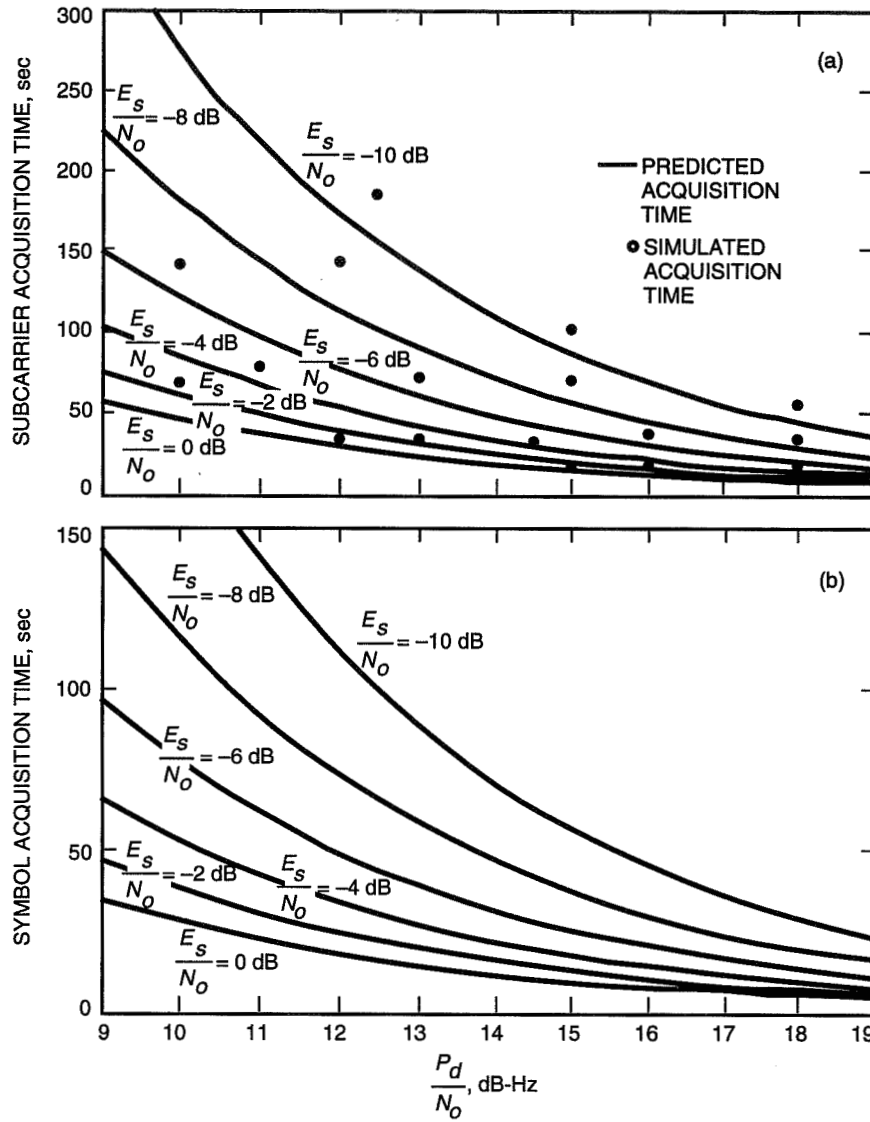


Fig. 9. Acquisition time to reach 0.5-dB degradation in the output symbol SNR due to phase jitter in each loop: (a) subcarrier $T_{sc, acq}$ and (b) symbol $T_{sym, acq}$.

Acknowledgments

The authors would like to express their appreciation to A. Mileant, J. M. Layland, P. W. Kinman, Y. H. Son, J. Rayas, M. Leung, C. Bearden, M. McCormick, K. Knights, E. W. Stone, and R. Tung for their technical support in the development of the BVR fast acquisition algorithm.

References

- [1] J. Berner and K. Ware, "An Extremely Sensitive Digital Receiver for Deep Space Satellite," *Eleventh Annual International Phoenix Conference on Computers and Communications 1992 Proceedings*, Scottsdale, Arizona, pp. 577–585, April 1–3, 1992.
- [2] W. J. Hurd and S. Aguirre, "A Method to Dramatically Improve Subcarrier Tracking," *The Telecommunications and Data Acquisition Progress Report 42-86, vol. April–June 1986*, Jet Propulsion Laboratory, Pasadena, California, pp. 103–110, August 15, 1986.

Appendix

Frequency Interpolation and Phase Estimation From the FFT

In this appendix, the technique adopted for estimation of the frequency and phase of an exponential tone from its FFT is discussed. Expressing the input exponential tone signal, $s(m)$, sampled every $T_{s,FFT}$ sec as

$$s(m) = Ae^{j(2\pi f_{in}t + \phi_o)} \Big|_{t=mT_{s,FFT}} \quad (\text{A-1})$$

the technique for estimating the frequency and phase (f_{in} and ϕ_o , respectively) is described.

A. Frequency Estimation Using Sinc Interpolation

An N_{FFT} -point complex FFT of the signal $s(m)$ will have a peak at bin number k_{peak} . By interpolation between the complex FFT values of the peak bin and two bins about the peak, n bins away, the frequency f_{in} can be estimated as \hat{f}_{FFT} . The interpolation assumes an underlying sinc function relation between the three points (rather than a simple quadratic one), resulting in an improved estimate of frequency. The interpolated FFT estimate, \hat{f}_{FFT} , is

$$\hat{f}_{FFT} = \frac{k_{peak} + \Delta k}{N_{FFT}} \frac{1}{T_{s,FFT}}$$

where

Δk = frequency bin interpolation

k_{peak} = bin number of the peak tone

N_{FFT} = FFT size

$T_{s,FFT}$ = FFT sampling time

The Δk is calculated as

$$\Delta k = n \times \text{Re} \left[\frac{\gamma Z_{(k_{peak}+n) \bmod N_{FFT}} + \gamma^* Z_{(k_{peak}-n) \bmod N_{FFT}}}{\gamma Z_{(k_{peak}+n) \bmod N_{FFT}} - \gamma^* Z_{(k_{peak}-n) \bmod N_{FFT}} + (\gamma^* - \gamma) Z_{k_{peak}}} \right] \quad (\text{A-2})$$

where

Z_k = complex FFT value of the k th bin

$$\gamma = e^{j2\pi n/\alpha} - 1$$

$$\alpha = \frac{N_{FFT}}{N_{data}}$$

= zero-padding factor, may not be an integer

$$n = \text{MAX} \left\{ \text{Floor} \left[\frac{\alpha}{2} \right], 1 \right\}$$

When $\alpha = 1$, Eq. (A-2) becomes in the limit

$$\Delta k = \text{Re} \left[\frac{Z_{(k_{peak}+1) \bmod N_{FFT}} - Z_{(k_{peak}-1) \bmod N_{FFT}}}{Z_{(k_{peak}+1) \bmod N_{FFT}} + Z_{(k_{peak}-1) \bmod N_{FFT}} - 2Z_{k_{peak}}} \right] \quad (\text{A-3})$$

B. Phase Estimation

The phase ϕ_o of the signal at $t = 0$ can be estimated from its FFT as $\hat{\phi}_{FFT}$:

$$\hat{\phi}_{FFT} = \Delta \hat{\phi}_{FFT} - 2\pi \hat{f}_{FFT} \frac{T_{s,FFT}}{2} \quad (\text{A-4})$$

where

$$\Delta \hat{\phi}_{FFT} = \text{Arg} [Z_{k_{peak}}] - 2\pi \Delta k \frac{(N_{data} - 1)}{2\alpha N_{data}} \quad (\text{A-5})$$

and $T_{s,FFT}$ is the sample rate of the FFT input signal.

1995/08214
32448

N95- 14628

TDA Progress Report 42-118

19786
August 15, 1994

4-10

Research and Development Optical Deep Space Antenna Sizing Study

D. Wonica

Communications Systems Research Section

Results from this study provide a basis for the selection of an aperture size appropriate for a research and development ground-based receiver for deep space optical communications. Currently achievable or near-term realizable hardware performance capabilities for both a spacecraft optical terminal and a ground terminal were used as input parameters to the analysis. Links were analyzed using OPTI, our optical link analysis program. Near-term planned and current missions were surveyed and categorized by data rate and telecommunications-subsystem prime power consumption. The spacecraft optical-terminal transmitter power was selected by matching these (RF) data rates and prime power requirements and by applying power efficiencies suitable to an optical communications subsystem. The study was baselined on a Mars mission. Results are displayed as required ground aperture size for a given spacecraft transmitter aperture size, parametrized by data rate, transmit optical power, and wavelength.

I. Introduction

This study builds upon and continues work performed to develop a ground-based optical terminal for deep space communications, the Deep Space Optical Receiving Antenna (DSORA) [1-3]. Deep space links can utilize pulse position modulation schemes very effectively, which implies the information is contained in the energy per pulse and not in the phase of the optical beam. Thus, DSORA can use a large aperture, incoherent, photon-bucket type of telescope that is much less expensive to construct [4] than the phase-preserving Keck I and II telescopes (\$93M). The nominal DSORA aperture size is 10 m. This size of aperture was found to be both technologically achievable and reasonably affordable [5]. The present study reexamined what was technologically achievable both from the spacecraft side as well as the ground receiver side and used performance parameters in a link analysis that are achievable now or in the near future (5 years) with continued development. Mission planning was reexamined as well, and this led to consideration of nominal data rate requirements much less than 1 Mbps, with a Mars mission providing the most likely opportunity of placing an optical communications subsystem on a deep space probe in the near future.

II. Mission Database

The mission database currently being maintained by the Telecommunications and Data Planning Office¹ was used as the basic source of information regarding current and near-term future mission data

¹ Data compiled and maintained by R. Cesarone, Telecommunications and Data Acquisition Planning Office, Jet Propulsion Laboratory, Pasadena, California.

rates. Of the planetary missions in the database (as of December 1993), 29 had either firm data rate requirements or projected estimates available. A distillation of this information is contained in Table 1, which categorizes missions into flyby, orbiter, lander, probe, or other, and shows the mean rate and spread. Additional mission data rates projected well into the next century (to the year 2075) were obtained from the JPL-sponsored Deep Space Relay Satellite System (DSRSS) study contracts.^{2,3} Table 2 summarizes telemetry data rate requirements for primary planetary encounter science, as derived by Stanford Telecom (S-TEL).⁴

Table 1. Data rates for mission categories (29 missions total).

Mission type	Number, percent	Data rates		
		Maximum, kbps	Minimum, kbps	Mean, kbps
Flyby	31	640	0.008	86
Orbiter	38	500	3	135
Lander	7	10	1	6
Probe	7	0.5	0.35	0.5
Other	17	400	8	200

From Tables 1 and 2, it is seen that the majority of missions can be serviced by telecommunications subsystems providing 200-kbps data rates or less. Large spacecraft with multiple imaging cameras (or a smaller number of high-resolution cameras) will require data rates approaching 1 Mbps. Current NASA plans do not indicate that large, heavy spacecraft, such as Cassini, will be flown in the near future, as the trend is toward a larger number of smaller and lighter payloads. For this study, a data rate of 250 kbps was selected as a reasonable upper limit.

III. Spacecraft Optical Transmitters

To size the ground aperture, a spacecraft optical transmitter had to be conceptually devised and parametrized. Key parameters include laser power output at a specified wavelength, transmitter aperture size, and beam pointing accuracy.

The most mature technology for laser transmitters are Nd-based laser gain media operating at 1.06 μm , and the same laser frequency doubled to 0.532 μm . Adequate powers are presently available at these wavelengths (3.5 W pulsed at 0.532 μm , 11 W continuous wave (CW) at 1.06 μm [6]), the atmospheric transmittances are good, and high-performance detectors exist. A realistic transmitted optical power was obtained by first identifying the prime power required for several RF telecommunications subsystems already designed (or in process) to provide a specified data rate for the categories of missions indicated above. It was assumed that the same power was allocated to the optical communications subsystem and the same data rate requirement imposed. The laser power output was obtained by applying appropriate power efficiencies for optical and electro-optical hardware to the prime electrical power.

² Stanford Telecom, *DSRSS Mission Requirements TR90090 Final Report*, DSRSS Study Contract No. 958734, January 21, 1991.

³ TRW, *Deep Space Relay Satellite System Study Final Report*, DSRSS Study Contract No. 95833, July 22, 1993.

⁴ Stanford Telecom, op. cit., pp. 1-13.

Table 2. Data rate requirements projected for future missions.

Encounter type/ representative mission	Likely science objectives	Likely instrumentation	Data rate considerations and rationale	Relationship to timeline element	Derived requirements	
					Data rate, kbps	Variability
Flybys/ Pluto Flyby	Planetary figure, mass, density, magnetic field. Surface character. Atmospheric character. Solar wind interactions.	Imaging camera. Magnetometer. Plasma wave spectrometer. Ultraviolet spectrometer.	Camera data rate is 6-350 Mbps. If camera episodes are short, then data recording can be used to lower effective data rate.	4 months around primary target encounter event.	100	Moderate
Landers/ Mars Global Network	High resolution of localized sites. Perform in-situ soil analyses. Seismic studies. Meteorological studies.	Camera. Soil sampler. Magnetometer. Meteorological. Seismological.	Long-term data generation. Continuous low rate. Occasional high rate. Use of data recorders. Data transfer to Earth based on view period.	Corresponds to surface operations phase.	20	Moderate
Sample return/ Mars Rover Sample Return	Collect soil samples. Collect rock samples. Meteorological studies. Seismic studies.	Camera. Rover. Meteorological.	Low rate. Relatively short duration (several months). Communication may be relayed via an orbiting spacecraft.	8 months around primary target encounter event.	50	Moderate
Probe, penetrator/ Cassini Probe	Atmospheric studies. Lightning characteristics. Surface state composition.	Imager spectral radiometer. Gas chromatograph. Atmospheric structure instruments.	Low rate. Short duration.	20 days around primary target encounter event.	10	Moderate

Table 3 indicates four specific missions, their respective power allocations, data rates, and spacecraft attitude control capabilities. An optical communications subsystem shall require an onboard beam control assembly to increase pointing accuracy. For reference, the Defense Support Program (DSP) optical crosslink subsystem achieved optical pointing accuracy in ground simulation tests of $1.3 \mu\text{rad}$ at $1.06 \mu\text{m}$ (1σ value) [7]. The design data rate was 1.28 Mbps at crosslink distances of 71-84 Mm and for a ground link distance of 38 Mm. This represents older technology, frozen at approximately 10 years ago. For the link analyses of this study, 100 nrad was used [8].

Table 4 shows four optical transmitters, their power requirements, and the estimated total power consumption for the subsystem, including laser and gimbal. The 10-W class transmitter is from TRW's DSRSS study,⁵ included for comparison and reference only and not used in the link analyses. The three transmitters at 0.5, 1.0, and 2.0 W use conversion efficiencies of 13 percent. The estimated total power consumed is from previous work⁶ and currently ongoing work performed by JPL's Optical Communications Group. For this article, it is assumed that a gimbal for the telescope is needed. A gimbal is

⁵ TRW, op. cit., pp. 5-54-5-55.

⁶ H. Hemmati and C. C. Chen, "Report on the Pluto Flyby Laser Transmitter Study," JPL Interoffice Memorandum 331-92.6-143 (internal document), Jet Propulsion Laboratory, Pasadena, California, July 1, 1992.

estimated to consume 15 W.⁷ The remaining electronics use about 27 W. An optical transmitter at 2 W consumes at most 16 W of prime power, and the total subsystem consumption is 58 W, less than the power allocated to the communications subsystems of several categories of missions. For many missions, a gimbal will not be required; thus, the power for the 0.5-, 1.0-, and 2.0-W transmitters of Table 4 will each be reduced by 15 W.

Table 3. Representative missions for spacecraft categories, RF data rates, and prime power allocations.

Parameter	Spacecraft category			
	Flyby	Orbiter	Orbiter/probe	Lander
Representative mission	Pluto	Cassini	Galileo	MESUR Pathfinder
Time frame	2014–2015	2004–2008	1995–1998	1997
Distance, km/AU	$6.15 \times 10^9/41$	$1.58 \times 10^9/10.5$	$9 \times 10^8/6$	$3.75 \times 10^8/2.5$
Telecommunications rate	80 bps	250 kbps	134 kbps	1200 bps
Band	X	X	X	X
Control accuracy	1.5 mrad (1σ)	2 mrad (3σ)	3.4 mrad (3σ)	12 mrad (1σ)
Control stability	10 μ rad/1 sec	4 μ rad/0.5 sec	125 μ rad/1 sec	1.7 μ rad (knowledge)
Total spacecraft power, W	60	800	500	200
RF subsystem power, W	24	88	—	83
RF transmitted power, W	3	20	20	17

Table 4. Spacecraft transmitter power requirements.

Optical power output, W at 1.06 μ m	Prime power into laser, W	Total prime power required for optical communications subsystem, W
0.5	4	46
1.0	8	50
2.0	16	58
10.0	91	133

The final parameter is the optical aperture size, and three sizes were selected: 10, 30, and 50 cm. There are several designs for 10-cm aperture telescopes in existence, and this size is appropriate for missions where size and weight are given highest priority and where the data rate is low. SSG Inc. is currently being funded under the NASA Phase II Small Business Innovative Research Program (SBIR) through the JPL Optical Communications Group to build a 30-cm silicon carbide telescope that could eventually be space qualified. It is estimated that it will weigh about 6 kg, without a gimbal. Additionally, successful demonstration of this 30-cm mirror technology would enable fabrication of a 50-cm telescope.

⁷ L. A. Voisinet, "OCD Gimbal Discussion," JPL Interoffice Memorandum 331-93.6-209 (internal document), Jet Propulsion Laboratory, Pasadena, California, December 13, 1993.

IV. Link Analyses

OPTI was used for all link analyses. Inputs are shown in Table 5. Mars was selected as the candidate target for hypothetical missions: orbiters, landers, and probes. In view of the recent NASA decision to explore Mars over the coming decade [9], Mars will undoubtedly present the largest number of opportunities in the near term for a possible deep space optical communications payload.

Links were first modeled using a wavelength of $1.06\ \mu\text{m}$. A frequency-doubling conversion efficiency of 50 percent was then applied to the transmitter power at $1.06\ \mu\text{m}$ and the links recomputed at a wavelength of $0.532\ \mu\text{m}$, making appropriate changes in atmospheric transmittance and detector quantum efficiency. Avalanche photodiode detectors (APDs) in a direct detection mode were used for both wavelengths. Parameters listed for hardware performance are realizable. All links are for daytime conditions and assume an atomic resonance filter is used to suppress atmospherically scattered background light.

A. Ground Aperture Sizes for $\lambda = 1.06\ \mu\text{m}$

Table 6 gives the ground aperture diameter required in meters for values of the spacecraft transmitter aperture of 10, 30, and 50 cm, for four different data rates, and for ranges of 2.5 and 0.4 AU (for Earth-Mars at nearly the furthest separation and at the closest approach, respectively) at a communication wavelength of $1.06\ \mu\text{m}$. Figure 1 graphically displays these same results for the 2.5-AU range.

As expected, the required receiving aperture size increases with data rate and decreases with transmitter power. The U.S. Air Force Phillips Laboratory/Starfire Optical Range (SOR) operates a 3.5-m-diam imaging telescope in Albuquerque that is available to NASA and JPL. A line is drawn at 3.5 m in Figure 1 as a reference point to indicate this as the largest ground receiver immediately available for communications links (of course, apertures smaller than 3.5 m are available at a number of locations, including the Table Mountain Facility).

Results show that for a 250-kbps data rate, at least a 17-m-diam receiver is needed for the powers considered with a 10-cm transmitter at 2.5 AU. This size of receiver is not presently available. The largest optical telescope primary mirror presently in operation is 10 m. Current mirror fabrication methods may extend this size to about 12 m. For a 12-m receiver, a 10-cm/2-W transmitter provides a maximum data rate of 131 kbps. For a 3.5-m telescope, the data rate is 283 kbps for a 50-cm/2-W transmitter.

For 2-W output powers, a 30-cm spacecraft transmitter requires at least a 6-m ground receiver to attain 250-kbps data rates, and a 50-cm transmitter will reduce this ground aperture size to 3.3 m for the same data rate. A photon bucket can be made at either size of receiver aperture. The 30- and 50-cm spacecraft telescopes are under development; the 2-W power is currently available at $1.06\ \mu\text{m}$; and initial research is now proceeding on the atomic resonance filter.

For 1 W of transmitted power, the 3.5-m telescope is limited to about 150 kbps with the 50-cm spacecraft telescope. A rate of 250 kbps is achievable with a 30-cm transmitter if an investment is made in an 8.4-m ground receiver.

For 0.5 W of transmitted power, a 50-cm transmitter and 6.6-m receiver are required to attain 250-kbps rates. The small-aperture, low-power transmitter, 10 cm/0.5 W, is useful with the 3.5-m ground receiver when size and power on the user spacecraft are severely restricted; this configuration is limited to about 3 kbps.

Table 5. OPTI inputs.

Parameter	Value
Transmitter	
Power, W	0.5, 1.0, and 2.0
Wavelength, μm	1.06 and 0.532
Antenna diam, m	0.1, 0.3, and 0.5
Obscuration diam, m	0, 0.067, and 0 with respect to antenna diameters above
Efficiency	0.70
Pointing bias, 1σ , μrad	0.1
Jitter, 1σ , μrad	0.05, 0.02, and 0.01 with respect to antenna diameters above
Modulation extinction ratio	1×10^5
Receiver	
Diam, m	Variable
Obscuration diam, m	18 percent of diam (≈ 3 percent of primary area)
Efficiency	0.70
Quantum efficiency	0.36 (at 1.06 μm) and 0.72 (at 0.532 μm)
Filter transmittance	0.30
Filter bandwidth, \AA	0.01 (atomic resonance filter at 1.06 and 0.532 μm)
Detector diam, field of view, μrad	100
APD gain	200
Noise temperature, K	300
Load resistance, ohms	2000
APD ionization ratio	0.002
APD surface leakage current, nA	1.0
APD bulk leakage current, pA	1.0
Operational parameters	
Alphabet size	1024
Data rate, kbps	1.2, 50, 150, and 250
Link distance, AU	2.5
Bit error rate	0.01 (without coding)
Atmospheric transmittance	0.50 (at 1.06 μm) and 0.34 (at 0.532 μm), both at 60-deg zenith angle at 2.3 km
Dead time, μsec	Fixed; depends on alphabet, slot width
Slot width, nsec	10
Additional parameters	
Link margin, dB	3
Day sky radiance, $\text{W}/\text{m}^2/\text{sr}/\text{\AA}$	0.054
Mars	In field of view of detector at 2.5 AU

Table 6. Ground aperture sizes for selected data rates and spacecraft transmitters at $\lambda = 1.06 \mu\text{m}$ for daylight conditions and ranges = 2.5/0.4 AU.

Spacecraft transmitter		Ground receiver aperture size, m							
Average power, W	Aperture, cm	1.2 kbps		50 kbps		150 kbps		250 kbps	
		2.5 AU	0.4 AU	2.5 AU	0.4 AU	2.5 AU	0.4 AU	2.5 AU	0.4 AU
0.5	10	2.3	0.37	15.0	2.40	26.6	4.26	35.2	5.63
	30	0.82	0.13	5.3	0.85	9.2	1.47	12.0	1.92
	50	0.46	0.07	2.9	0.46	5.1	0.82	6.6	1.06
1.0	10	1.6	0.26	10.5	1.68	18.3	2.93	24.0	3.84
	30	0.59	0.09	3.8	0.60	6.5	1.04	8.4	1.34
	50	0.32	0.05	2.1	0.34	3.6	0.58	4.6	0.74
2.0	10	1.1	0.18	7.3	1.17	12.8	2.05	16.7	2.67
	30	0.41	0.07 ^a	2.7	0.43	4.6	0.74	6.0	0.96
	50	0.23 ^a	0.04 ^a	1.5	0.24 ^a	2.6	0.42	3.3	0.53

^a Performance will be degraded by scintillation.

At 0.4 AU, a 250-kbps rate can be attained using the small (10-cm) transmitter with a ground receiver of less than 6 m. Using 2 W of power with this transmitter, the receiver can be reduced to 2.7 m. This indicates that with careful mission planning, high data rates (>250 kbps) comparable to that contemplated for the Cassini mission may be sustained utilizing the existing 3.5-m ground telescope as a receiver.

B. Ground Aperture Sizes for $\lambda = 0.532 \mu\text{m}$

Table 7 and Fig. 2 present results for a wavelength of $0.532 \mu\text{m}$. The $1.06\text{-}\mu\text{m}$ laser transmitter powers of Table 4 were retained and a frequency-doubling conversion efficiency factor of 50 percent was applied, thus halving the transmitter powers for the shorter wavelength. As the doubler does not consume prime power, the spacecraft subsystem power allocation at this wavelength will not change from the values in Table 4.

Comparing results for the two wavelengths at 2.5 AU, the ground receiver size needed at $0.532 \mu\text{m}$ is in every case smaller than that required at $1.06 \mu\text{m}$ for the same transmitted power, a consequence of the smaller divergence at the shorter wavelength. To provide the capability for 250-kbps data rates at this wavelength, a 0.25-W/30-cm transmitter must be used with a 10.3-m ground receiver. Alternatively, increasing the power to 1 W with the same 30-cm transmitter reduces the required ground receiver size to 5.3 m and in principle lowers the cost of the ground receiver by a factor of 4. The 10-cm transmitter cannot provide 250 kbps for any currently available ground receiver size at maximum range, the smallest required size being a 14.2-m diameter.

Examining what may be done with the 3.5-m telescope, we see that at the small spacecraft transmitter extreme, 0.25 W/10 cm, the link is capable of a data rate of 3.9 kbps. At the other extreme, 1 W/50 cm, the link is capable of 379 kbps. The 30-cm telescope used with the 3.5-m ground receiver will provide 29, 57, and 116 kbps for powers of 0.25, 0.5, and 1 W, respectively.

At 0.4 AU, the receiver can be even smaller than that required at $1.06 \mu\text{m}$ at 0.4 AU, again indicating that high rates can be obtained for most missions of current interest by utilizing technology readily available.

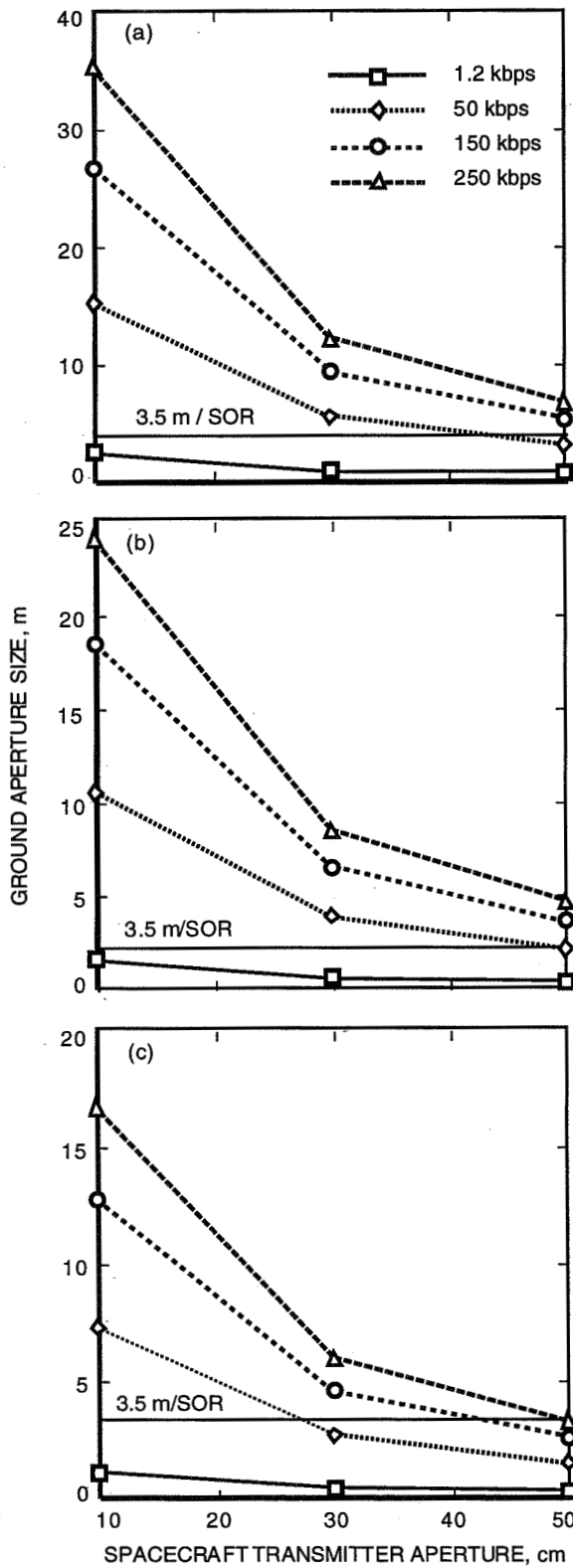


Fig. 1. Ground aperture sizes for a $1.06\text{-}\mu\text{m}$ link distance of 2.5 AU (daylight conditions) with transmitter power at (a) 0.5 W, (b) 1.0 W, and (c) 2.0 W.

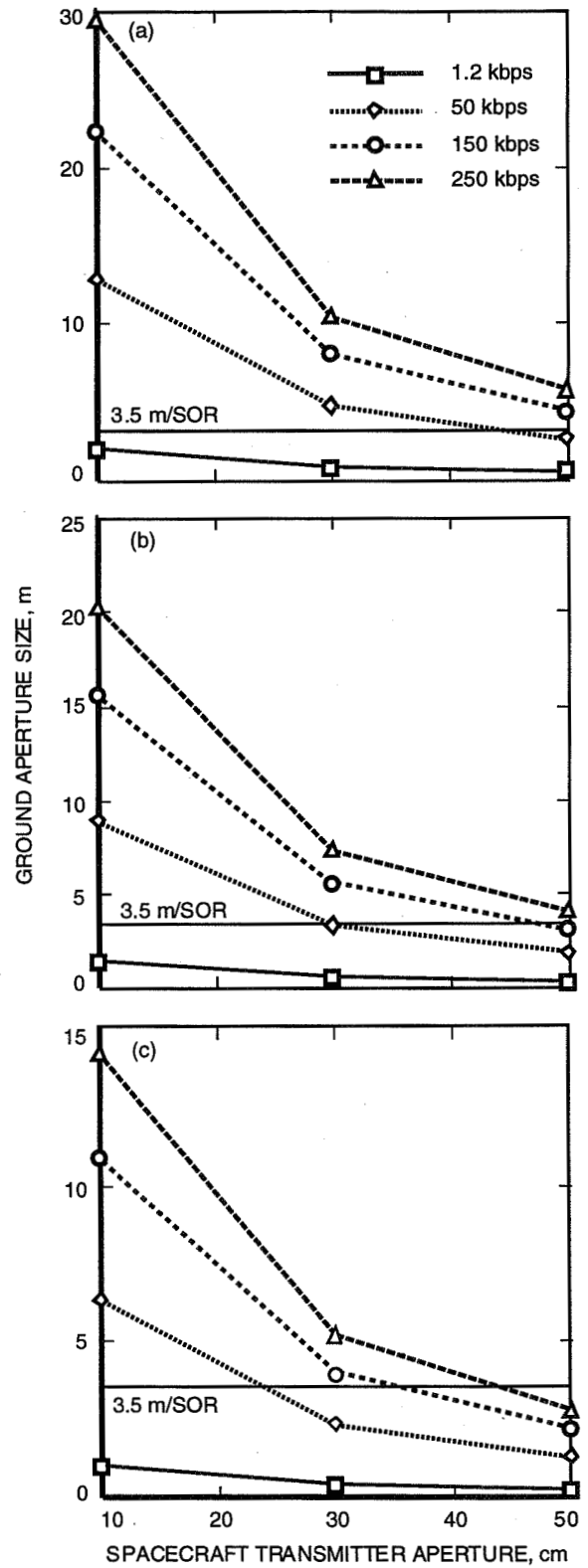


Fig. 2. Ground aperture sizes for a $0.532\text{-}\mu\text{m}$ link distance of 2.5 AU (daylight conditions) with transmitter power at (a) 0.25 W, (b) 0.5 W, and (c) 1.0 W.

Table 7. Ground aperture sizes for selected data rates and spacecraft transmitters at $\lambda = 0.532 \mu\text{m}$ for daylight conditions and ranges = 2.5/0.4 AU.

Spacecraft transmitter		Ground receiver aperture size, m							
Average power, W	Aperture, cm	1.2 kbps		50 kbps		150 kbps		250 kbps	
		2.5 AU	0.4 AU	2.5 AU	0.4 AU	2.5 AU	0.4 AU	2.5 AU	0.4 AU
0.25	10	2.0	0.32	12.7	2.0	22.2	3.5	29.2	4.51
	30	0.71	0.11	4.6	0.74	8.0	1.28	10.3	1.65
	50	0.39	0.06	2.6	0.42	4.4	0.70	5.7	0.91
0.5	10	1.4	0.22	8.9	1.42	15.6	2.50	20.3	3.25
	30	0.50	0.08	3.3	0.53	5.6	0.90	7.3	1.17
	50	0.28	0.04	1.8	0.29	3.1	0.50	4.0	0.64
1.0	10	0.98	0.16	6.3	1.01	10.9	1.74	14.2	2.27
	30	0.36	0.06	2.3	0.37	4.0	0.64	5.2	0.83
	50	0.20	0.03	1.3	0.21	2.2	0.35	2.8	0.45

V. Summary

A spaceborne segment consisting of a 2-W, 1.06- μm laser transmitter with a 30-cm telescope and an onboard beam control assembly capable of at least 100-nrad pointing accuracy can provide at least an 86-kbps data rate from Mars at 2.5 AU using a 3.5-m receiver and an avalanche photodiode detector in the ground segment. An atomic resonance filter provides daytime operation capability. The same configuration will provide a data rate as high as 2.9 Mbps from Mars at its closest approach to Earth (0.4 AU).

By converting the wavelength to 0.532 μm while still retaining the total prime power consumption, a 1-W transmitter with a 30-cm telescope and the same pointing capability will provide 115 kbps from Mars at 2.5 AU using a 3.5-m telescope. The detector (APD) and filter (atomic resonance) are categorically the same but operate at this shorter wavelength. At the closest approach, the data rate capability is as high as 3.6 Mbps.

These optical communications segments would provide the capability to meet the telemetry data rate requirements currently envisioned for many lander, orbiter, and probe missions.

References

- [1] K. Shaik and E. Kerr, "A Ten-Meter Optical Telescope for Deep Space Communications," *SPIE, Advanced Technology Optical Telescopes IV*, vol. 1236, Tucson, Arizona, pp. 347-350, 1990.
- [2] E. Kerr, "Architectural Design of a Ground-Based Deep-Space Optical Reception Antenna," *Optical Engineering*, vol. 30, no. 4, pp. 446-451, 1991.
- [3] K. Shaik, "Progress on Ten-Meter Optical Receiver Telescope," *SPIE, Proc. of Free Space Laser Communication Technologies IV*, vol. 1635, Los Angeles, California, pp. 109-117, 1992.

- [4] D. Wonica, "Economical 10-Meter-Class Ground-Based Receiver for Deep Space Optical Communications," to be published in *SPIE, Proc. Free Space Laser Communication Technologies VI*, Los Angeles, California, 1994.
- [5] J. Lesh and D. Robinson, "A Cost-Performance Model for Ground-Based Optical Communications Receiving Telescopes," *The Telecommunications and Data Acquisition Progress Report 42-87, vol. July-September 1986*, Jet Propulsion Laboratory, Pasadena, California, pp. 56-64, November 15, 1986.
- [6] H. Hemmati and J. Lesh, "A 3.5 W Q-Switched 532 nm Nd:YAG Laser Pumped With Fiber-Coupled Diode Lasers," to be published in *Optics Letters*, 1994.
- [7] R. Deadrick and W. Deckelman, *SPIE, Proc. of Free Space Laser Communication Technologies IV*, vol. 1635, Los Angeles, California, pp. 225-235, 1992.
- [8] R. Fugate, "Observations of Faint Objects With Laser Beacon Adaptive Optics," to be published in *SPIE, Proc. of Conference on Astronomical Telescopes for the 21st Century*, Kona, Hawaii, 1994.
- [9] D. Ainsworth, "Lab Will Embark on New Mars Mission," *JPL Universe*, vol. 24, no. 3, p. 1, February 11, 1994.

1995/08215

N95-14629

324470

1998 1

August 15, 1994

TDA Progress Report 42-118

✓ p. 14

Pilot Retrofit Test of Refrigerant R-134a for GDSCC

J. Albus

Ground Antennas and Facilities Engineering Section

B. Brown, M. Dungao, and G. Spencer

TDA Mission Support and DSN Operations Section

NASA has issued an interim policy requiring all of its Centers to eliminate consumption (purchase) of stratospheric ozone-depleting substances, including chlorofluorocarbons (CFCs), by 1995. Also, plans must be outlined for the eventual phaseout of their usage. The greatest source of CFC consumption and usage at the Goldstone Deep Space Communications Complex is refrigerant R-12, which is used in many of the facility's air-conditioning systems. A pilot retrofit test shows that retrofitting R-12 air-conditioning systems with hydrofluorocarbon R-134a would be a workable means to comply with the R-12 portion of NASA's policy. Results indicate acceptable cost levels and nearly equivalent system performance.

I. Introduction

Some researchers believe that the release of manufactured chlorofluorocarbons (CFCs) into the atmosphere plays a substantial role in depletion of the stratospheric ozone layer. This layer, located at an altitude of 15 to 55 km, shields our planet from harmful solar ultraviolet rays. In 1987, representatives of both industrialized and developing nations set forth a timetable for reduction and elimination of stratospheric ozone-depleting substances, including CFCs, in a document known as *The Montreal Protocol for Protection of Stratospheric Ozone*. Twenty-four nations signed the initial document, which has since been modified with stricter phaseout schedules for these substances. Today, *The Montreal Protocol* has been ratified by more than 100 nations.

NASA's policy calls for eliminating ozone-depleting substance consumption (purchase) and planning for the quickest practical phaseout of their usage at all Centers. The Goldstone Deep Space Communications Complex (GDSCC) annually consumes approximately 3086 kg of the CFC R-12 to maintain refrigerant charges on 20 R-12 air-conditioning systems.

The ozone depletion potential (ODP) of a chemical compares its tropospheric lifetime, upward atmospheric diffusion rates, and photolyzability into chlorine with that of CFC R-11 (reference ODP of 1.0). A chemical with an ODP of 0.5 has one-half the ozone-depletion potential of R-11 [1]. Refrigerant R-12 has an ODP of 1.0.

Closed R-12 systems may continue to operate past 1995 using in-house stocks of refrigerant. Stockpiling sufficient R-12 to operate the systems for their remaining lifetimes would be costly. Refrigerant R-12 cost approximately \$3.30/kg in 1986, but in February 1994 it had increased in price to \$27.90/kg, due in part

to federal taxation on CFC compounds. Taxes on R-12 are \$9.57/kg for 1994 and will rise to \$11.77/kg in January 1995. Its production will cease in the United States in December 1995.

II. Alternatives to CFC R-12

The term “capacity” refers to the maximum amount of British thermal units (BTUs) that a refrigerant in a compressor of fixed displacement can remove from the air (or other medium) under a given set of conditions. “Efficiency” refers to the amount of energy required to remove a given amount of heat from the air (or other medium) under a given set of conditions.

Viable alternatives to CFC R-12 include hydrochlorofluorocarbon (HCFC) R-22, HFC R-134a, and MP39. These refrigerants were the only commercially available alternatives suggested by GDSCC compressor manufacturers and major refrigerant manufacturers (Allied Signal, Du Pont, and ICI). Each is classified as A1 for lower toxicity and no flame propagation by the American National Standards Institute—American Society of Heating, Refrigeration and Air Conditioning Engineers (ANSI-ASHRAE) standards. Class A is a designation for refrigerants whose toxicities have not been identified at concentrations less than or equal to 400 parts per million. Class 1 is a designation for refrigerants showing no flame propagation when tested in air at one atmosphere and 18.3 deg C.

A. The R-22 Retrofit

R-12 systems may be modified to use HCFC R-22, an “interim solution” refrigerant with a complete phaseout date of 2030. R-22 has a low 0.05 ODP. Its present cost of \$4.03/kg is considerably less than that of R-12. An R-12 system can gain capacity when retrofitted to use R-22. Conversion to R-22 usually requires expensive and time-consuming modifications (downsizing refrigerant lines, compressor replacement, etc.) due mainly to R-22’s significantly higher operating pressures (a condensing pressure higher than 1548 kPa) and a condensing temperature of 38 deg C.

B. System Replacement

R-12 systems may be removed and replaced with those using acceptable refrigerants. This is advantageous when the current R-12 system requires greater capacity or is scheduled for replacement in the near future. It would allow installation of the most energy-efficient system design available. Removing and replacing a system, however, is costly, time-consuming, and usually very disruptive to operations.

C. The R-134a Retrofit

R-12 systems may be retrofitted to hydrofluorocarbon (HFC) R-134a with less disruption and cost than with R-22. As R-134a contains no chlorine, its ODP is 0. Usually, no major components in a reciprocating compressor system need replacement. R-134a’s present cost of \$14.00/kg (as of February 1994) is less than that of R-12 and should decline somewhat as commercial production capacity increases. System capacity and efficiency should be equivalent to R-12 in systems running evaporator temperatures above -6.7 deg C (GDSCC’s R-12 systems operate above -1.1 deg C). Special procedures must be followed, however, to ensure lubricant and materials compatibility with R-134a.

D. The MP39 Retrofit

R-12 systems may be retrofitted to use MP39 (Du Pont) with little or no modification other than an oil change to an alkylbenzene lubricant. Efficiency should be equivalent to R-12 and R-134a. Because of higher operating pressures (than with R12), some GDSCC systems, however, may require receiver tank replacement. MP39 is a blend of HCFC R-22, HCFC R-124, and HFC R-152a, with an ODP of 0.03. MP39’s current price of \$12.78/kg (as of February 1994) is similar to that of R-134a. An R-12 system may gain capacity when retrofitted with MP39. MP39 is an acceptable alternative refrigerant that should not be phased out until 2030.

E. The Field Retrofit Test

Because of its good characteristics, R-134a was chosen to replace R-12 in an air-conditioning system at the Echo site's building G-38. This provided experience and data involving a refrigerant conversion. R-22 was not chosen because of the anticipated complexity and expense of system modifications. MP39 was not chosen because of two concerns. First, MP39 contains R-22, and at the time there was concern that the phaseout date of 2030 might be moved up. Second, performance of MP39 can change if significant leakage occurs on a repeated basis. While such performance changes are considered within acceptable ranges for most commercial uses, it was decided that no changes would be acceptable in systems supporting NASA mission-critical operations.

III. The R-12 to R-134a Retrofit Test

An R-12 air-conditioning system at building G-38 was retrofitted to use R-134a. Selected variables were monitored to compare qualitative and quantitative system performance with both refrigerants. A Fluke 2620A hydra data acquisition unit, a personal computer (PC), and an Elcontrol energy analyzer were used to collect and record information.

The variables monitored included current, voltage, suction-line pressure, discharge-line pressure, suction-line temperature, liquid-line temperature, cold-deck temperature, discharge-line temperature, mixed return-air temperature, second-stage suction temperature, compressor-head temperature, first-stage suction temperature, hot gas bypass temperature, ambient temperature, subcooling temperature, second-stage expansion valve temperature, return air temperature, air handler temperature, air off of condenser coils, pre-evaporator coil humidity, and post-evaporator coil humidity.

Allied-Signal Technical Services Corporation, Du Pont, GDSCC, and Trane maintenance personnel assisted in determining these variables. Measurements were made point-in-time with the interfaced hydra 2620A and PC, usually at 1- or 5-min intervals. The energy analyzer recorded (on demand) the kilowatt consumption rate.

Temperatures were measured with JPL-made thermocouples; pressures were measured with Fluke pressure transducers; voltage was read directly from a compressor transformer; current was measured with a Fluke current transducer; and relative humidity was measured with Omega humidity transducers. All output was fed to the 2620A. The energy analyzer monitored energy consumption directly from the system's 3-phase 480-V panel. All measuring devices were either calibrated and/or tested alongside portable instruments to ensure accuracy.

IV. Retrofit Considerations

A. Lubricants

Prior to converting from R-12 to R-134a, the compressor lubricant must be changed from the mineral oil commonly used in R-12 systems to a synthetic polyol ester oil. Mineral oils are not miscible with R-134a. Nonmiscibility, resulting in oil pooling in various parts of the system, can impede performance. In the worst case, such pooling can result in compressor oil starvation and severe damage or failure. The heating, ventilation, and air conditioning (HVAC) industry, lubricant manufacturers, and refrigerant manufacturers recommend a maximum of 3- to 5-percent mineral oil contamination of the new polyol ester oil before converting to R-134a.

Manufacturers, such as Castrol and ICI, offer synthetic polyol ester lubricants that are well suited for use with R-134a. Lubricant additive packages ensure good lubricity of the HFC R-134a/oil mixture, even though it lacks the chlorine found in CFCs (chlorine forms metal chlorides which provide a significant measure of lubrication).

The oil change procedure is as follows:

- (1) The mineral oil is drained from the compressor.
- (2) The compressor is filled with polyol ester oil and run for 24 hr or more. A longer run time provides better flushing of the oil from the system.
- (3) A sample of the oil is removed and tested either by the oil manufacturer or by HVAC personnel (with a test kit) for contamination levels of mineral oil. The manufacturer can test the oil for metal wear and other factors that most test kits cannot test.
- (4) The system is again drained, refilled, and run with fresh polyol ester oil for 24 hr or longer. Contamination levels are once again determined.

This procedure is repeated, if necessary, until mineral oil contamination is under 5 percent (usually 2 or 3 oil changes in total). The system may then be evacuated of R-12 and charged with R-134a, assuming that all necessary modifications have been made. The G-38 system required three oil changes to reach a 2-percent contamination level (industry consensus at the time had not yet agreed upon 5-percent maximum allowable contamination). Two changes would have been sufficient to reach a sub-5-percent level.

B. Material Compatibility

Refrigerant and lubricant manufacturers have tested R-134a and polyol ester lubricants for a variety of factors, such as material swell, material shrinkage, hardening, elasticity changes, refrigerant permeation, and so on. Published results are usually noted without a generic approval for a material to be used in all applications. In general, the following applies:

- (1) Metals. R-134a and polyol esters are compatible with all metals typically found in air-conditioning systems.
- (2) Plastics. R-134a and polyol esters are compatible with most plastics found in R-12 systems. Acrylics and celluloses are among those that should not be used with R-134a.
- (3) Elastomers (seals, gaskets, o-rings, etc.). R-134a and polyol esters are compatible with many elastomers found in R-12 systems. Adiprene L and Viton A should not be used with R-134a. Because Buna S and butyl rubber exhibit borderline characteristic changes, their use with R-134a is not recommended. Styrenated butadiene (SBR) exhibits a high swell with polyol ester and is not recommended for use with the lubricant.

An inventory was made of all system components (hoses, solenoids, compressor, etc.) for the G-38 system. Component manufacturers were contacted to determine material compatibility of their parts with R-134a and polyol ester lubricants. All materials in the G-38 system were determined to be compatible. According to Trane, Carrier, and Vilter (manufacturers of the GDSCC air-conditioning system compressors), all GDSCC compressors should be compatible with R-134a.

C. Equipment Modifications

The air-conditioning equipment requiring compatibility evaluation before being converted to another type of refrigerant includes compressors, expansion valves, hot gas valves, condenser coils, evaporator coils, filter-driers, capillary tubes, pressure switches, and system piping. Centrifugal R-12 compressors often experience significant capacity loss as impeller design and rotational speed are exactly matched to the properties of R-12. Replacement of the impeller and/or pulley is usually required to regain lost capacity. Reciprocating R-12 compressors in systems operating above evaporator temperatures of -6.7 deg C usually experience equivalent performance with R-134a. The GDSCC R-12 compressor systems are reciprocating and operate at evaporator temperatures above -1.1 deg C. No piping material or diameter changes are required when retrofitting with R-134a because its physical characteristics are similar to those of R-12.

Some expansion valve manufacturers may recommend replacing the expansion valves because of somewhat higher operating pressures with R-134a. ALCO and Sporlan manufacture most of the expansion valves found in the GDSCC R-12 systems. ALCO recommended that the expansion valve power heads be changed for the G-38 retrofit. Sporlan states that its expansion valve assemblies are compatible with R-134a unless the system is already running a significantly oversized valve. The solenoid valves, pressure switches, and hot gas valve for the G-38 system were determined to operate satisfactorily with R-134a (confirmed by manufacturers). The expansion valve power heads were replaced at the recommendation of the manufacturer. Filter driers were replaced with an R-134a-compatible type. No compressor modifications were required.

D. Capacity

According to Du Pont, at evaporator temperatures over -6.7 deg C, R-134a exhibits an equivalent capacity compared with R-12.¹ Some systems running at these temperatures may show slightly higher capacities with R-134a because of its higher heat of vaporization (ability of a liquid to absorb heat prior to vaporizing to a gas).

E. Energy Efficiency Ratio

The energy efficiency ratio (EER) is the ratio of the net cooling capacity of a device, in BTU/hr, to the electric power input to that device, in watts, under designated operating conditions. Based on computer modeling by Du Pont, R-134a has a slightly lower EER than R-12 (1.5 percent and 0.5 percent less at evaporator temperatures of -40 and $+4.4$ deg C, respectively).² In actual practice, however, R-134a's greater heat transfer value provides better temperature transfer at the evaporator and condenser, resulting in an EER as good as with R-12.

F. Coefficient of Performance

The coefficient of performance (COP) is the ratio of heat removed to the energy used. Theoretically, the COP of R-134a is roughly 3 percent less than that of R-12. Both the G-38 retrofit and discussions with manufacturers indicate, however, that R-134a's greater heat transfer value can provide an equivalent or slightly higher COP in systems operating at evaporator temperatures over -6.7 deg C.

V. Retrofit of the G-38 Air Conditioning System to R-134a

The retrofitting of building G-38's air conditioning system to R-134a is summarized as follows:

- (1) The Trane 8-cylinder reciprocating compressor was completely overhauled to standard specifications, including replacement of all elastomeric parts, such as gaskets, seals, and o-rings. Rebuilding allowed testing with a "new" compressor, eliminating potential confounding variables introduced by worn equipment.
- (2) The compressor was reinstalled, filled with polyol ester oil, and run for more than 24 hr. Two more oil changes and runs with polyol ester were performed, which resulted in a residual mineral oil contamination below 2 percent. All samples were sent to Castrol for contamination analysis. As previously mentioned, a higher contamination level could have been tolerated.
- (3) Baseline data were recorded on the R-12 charged system.
- (4) The R-12 refrigerant was evacuated with a Thermoflow refrigerant recovery unit.
- (5) The 660 kg of recovered R-12 was recycled and stored for use in other R-12 systems.

¹ Personal communication with R. Dlugopolski, Technician, Du Pont Technical Services, Wilmington, Delaware, January 1994.

² Ibid.

- (6) The following parts were changed: ALCO power heads were changed to an R-134a-compatible model of the manufacturer's recommendation and desiccant filter blocks were replaced with an R-134a-compatible model.
- (7) The system was evacuated to a vacuum of 500 μm .
- (8) The system was charged with R-134a and run. Superheat was checked and adjusted.
- (9) Data were recorded on the retrofitted system.

VI. Retrofit Comments and Observations

No gasket or o-ring leakage has been observed in the converted G-38 system. The mechanical shaft seal cannot be observed without compressor tear down. Vilter reported that similar mechanical seals remained leak-free in laboratory extended-run testing with R-134a.

Oil samples analyzed by Castrol showed no unusual compressor wear or undesirable lubricant chemistry in the R-134a charged system. Flushing the system with polyol ester oil to a contamination level of under 5-percent mineral oil is a fairly simple procedure with about 4 to 6 hours of system downtime per oil change. Polyol ester oil is an expensive synthetic lubricant costing about \$14/liter (as of February 1994). The G-38 compressor uses approximately 23 liters of oil per change (\$320 oil cost). The drained oil cannot be reused and is disposed of as a hazardous waste. Disposal of used oil should not add extra expense to the GDSCC's current hazardous waste disposal costs. The R-134a/polyol-ester oil mixture foamed considerably less than the R-12/mineral oil mixture.

Changing the power-head assemblies of the ALCO expansion valves required minimal effort due to their design. Changing power heads in other systems may require significantly more time if they are not as easily disassembled. Some systems will not require power-head changes if fitted with Sporlan power heads.

Trane reviewed the performance data and noted that the first- and second-stage suction pressures wander more than expected. As measurements were taken point-in-time, either when the compressor was loading or was unloading, readings gave the appearance of random wandering. It was also noted that R-134a exhibited cooler discharge temperatures than with R-12. The different enthalpy values of the two refrigerants likely caused the temperature differences, which are within expected ranges. All other variables indicate that the G-38 system is operating satisfactorily with both refrigerants.

The time and cost for the retrofit are as follows:

- (1) Labor time: Approximately 95 hr were required to complete the retrofit to R-134a. This works out to a \$2,850 labor cost. Table 1 shows the labor breakdown.
- (2) Materials cost: Materials for the retrofit to R-134a cost approximately \$3,152. Table 2 shows the materials cost breakdown.

VII. Retrofit Performance Results

Quantitative comparisons were made among 5- to 15-minute performance runs with both refrigerants. Pairs, each consisting of an R-12 run and an R-134a run, were selected for similar running conditions (less than 4-percent variation in ambient and pre-evaporator air temperature). The pairs were then separated into their own refrigerant categories, providing two comparable groups of 10 each. COPs were calculated and plotted from lowest to highest values in each group (Fig. 1). Because of the lack of controlled heat and ventilation loads, these factors were not included in the calculations. As the G-38 test retrofit building was unoccupied, the system was run under low loading conditions. Compressor efficiency is usually measured

at high load conditions in the laboratory. Thus, this field test shows the relative performance with each refrigerant, rather than actual system COP.

The efficiency and capacity of R-134a and R-12 appear to be comparable. Slightly more energy was used with R-134a (Fig. 2) to remove moderately more heat from the air (Fig. 3). R-134a exhibited an average postevaporator temperature that was -2.2 deg C lower than that of R-12. The R-134a group runs and the R-12 group runs exhibited COPs of 3.21 and 3.06, respectively. Thus, the relative COP of R-134a was 5 percent greater than that of R-12 for these specific data. When retrofitting to R-134a, some impurities were found to have accumulated in the liquid line filter, which may have somewhat impeded the performance with R-12.

Table 1. Labor time for the G-38 retrofit to R-134a.

Task	Time, hr
System materials listing and compatibility research	8
Drain mineral oil and recharge with polyol-ester oil (2 oil changes to <5% contamination—6 hr each)	12
Remove 600 kg R-12 refrigerant to 0 gauge pressure	16
Replacement of hardware (power head, etc.)	13
Vacuum system to 500 μ m	12
Recharge system with 660 kg R-134a	8
Run system and make adjustments	12
Change filter driers and check in-line screens	5
Take system readings and evaluate performance	6
Leak check and repair	3
Total labor time: (equivalent cost = \$2,850 at \$30/hr)	95

Table 2. Materials cost for the G-38 retrofit to R-134a.

Material	Cost, dollars
660 kg Du Pont R-134a refrigerant (adjusted to retail price 2/94)	\$1,908
2 cases Castrol Icematic SW-68 lubricant (adjusted to retail price 2/94)	631
2 ALCO XB1014MV-1B power assemblies	108
1 Henry 3-way dual shutoff valve	146
2 Henry relief valves	92
1 Henry seal cap valve	47
2 ALCO HX-48 desiccant blocks	40
Miscellaneous shop materials	200
Total materials cost:	\$3,152

VIII. Other R-134a Retrofit Field Cases

In general, the G-38 retrofit results are similar to results observed in field and laboratory tests of other R-12 air-conditioning systems.

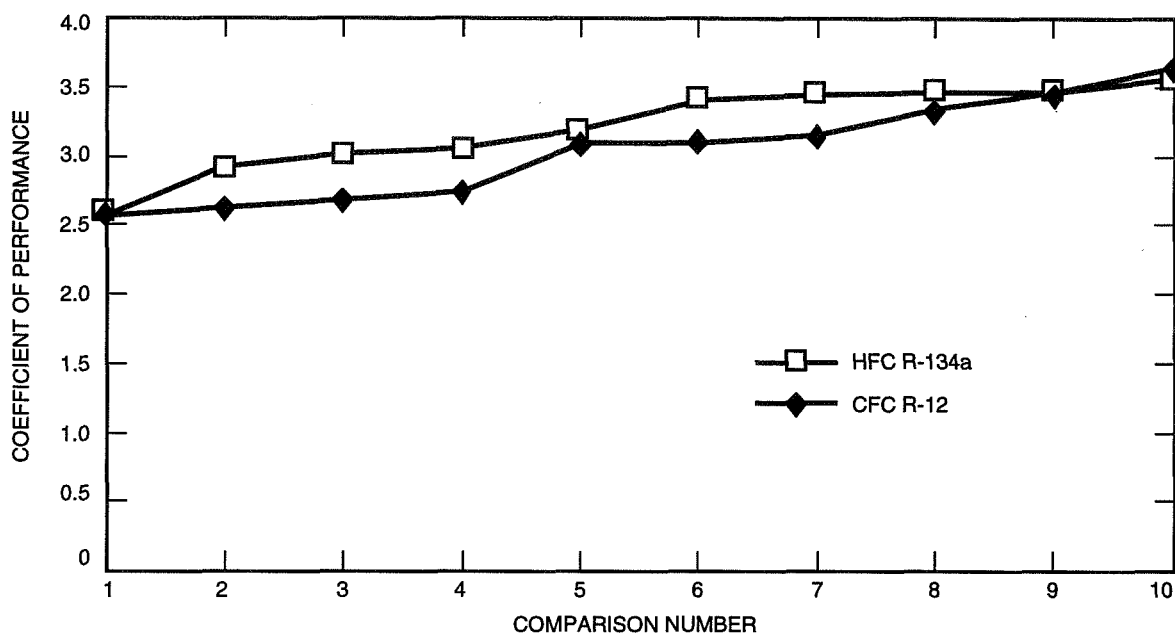


Fig. 1. Coefficient of performance.

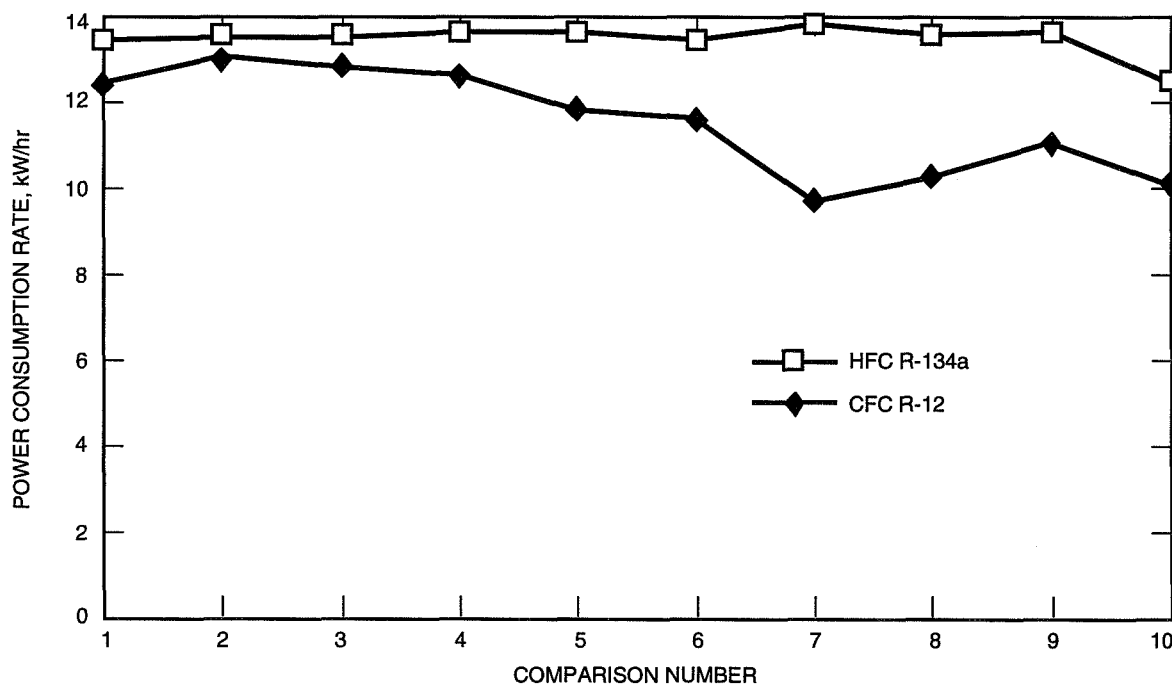


Fig. 2. Power consumption rate (kW/hr).

Vilter Corporation has retrofitted a Unichiller system (similar to the two at building G-86) to R-134a under laboratory conditions. Their test system exhibited capacities and efficiencies nearly identical to both refrigerants. Internal components and seals were in satisfactory condition after an extended run test. The main shaft seal exhibited a slight, but acceptable, swelling.

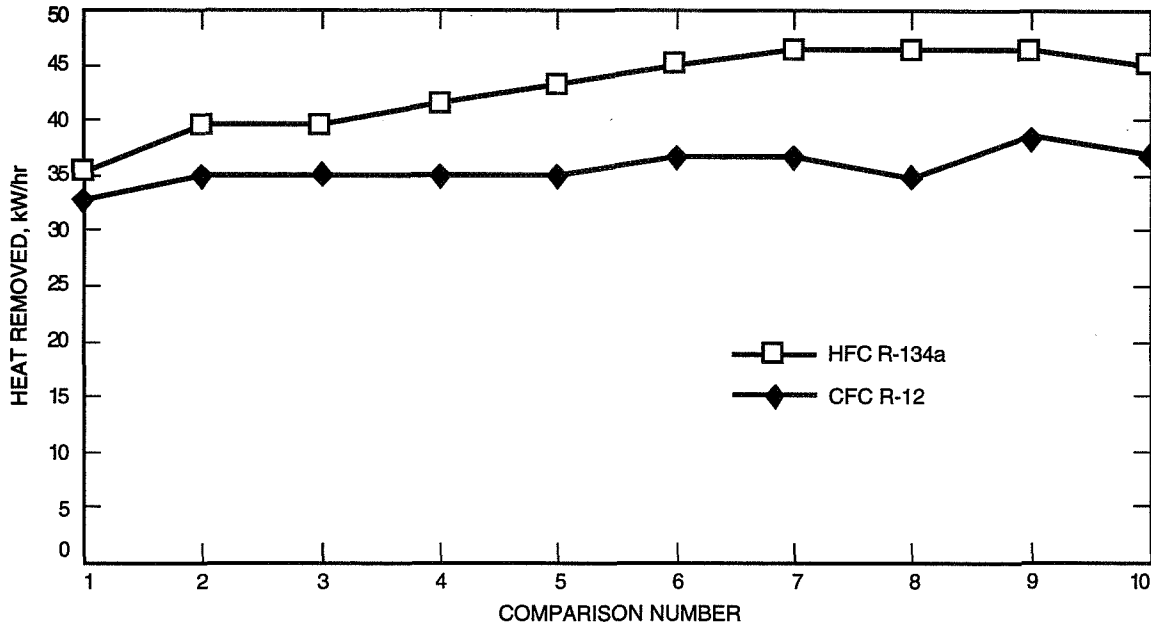


Fig. 3. Heat removed (kW/hr).

Trane has retrofitted an R-12 8-cylinder reciprocating compressor (similar to the G-38 unit) to R-134a under laboratory conditions and has run it in a 1-year endurance test. The unit has operated satisfactorily with no significant deviation from the reliability, capacity, or efficiency experienced with R-12. ICI, a major producer of R-134a, has published results of several R-12 to R-134a retrofits showing very similar performance for both refrigerants in all instances [2].

IX. Alternative Refrigerant MP39

Prior to the pilot retrofit, MP39 was assessed as a replacement for R-12. In most retrofits, no mechanical or material changes are required when converting to MP39. Usually only the oil must be changed once to an inexpensive alkylbenzene lubricant. In contrast, two or three changes with an expensive polyol ester oil are required when converting to R-134a.

Two concerns prevented MP39 from being chosen for the pilot retrofit: First, MP39 contains HCFC R-22, which is scheduled for phaseout in 2030. There was concern that this date may occur sooner. There has yet to be any indication, however, that the date will change (probably because of R-22's low ODP of 0.05). Second, MP39 is a near-azeotropic blend of three components: HCFC R-22, HCFC R-124, and HFC R-152a. They form a physical mixture (no new chemical compounds are formed) that has distinct vapor pressures corresponding to each component. An azeotrope's components have consistent vapor pressures. When a nonazeotrope leaks from a system in the gaseous phase, the components leak at different rates, altering the original ratio. There was concern that after several cycles of refrigerant leakage and refill (most air-conditioning systems leak to some extent), the composition of MP39 would change enough to affect system performance. Du Pont has run 20 leak (gaseous state) and recharge cycles with MP39 to find the effect on system capacity. Four such cycles caused a capacity loss of about 9 percent, resulting in overall capacity equivalent to that with R-12. Six more cycles caused a further 5-percent loss and 10 more cycles caused only a 1-percent further loss. Several substantial leaks (i.e., a broken fitting leaking overnight) in a system operating at or near maximum capacity levels may require that the remaining refrigerant be evacuated and replaced with fresh MP39 to maintain capacity.

Observations by a Du Pont refrigerant distributor and retrofit specialist have indicated capacity gains averaging 6 to 8 percent in R-12 air-conditioning systems retrofitted to MP39.³ Du Pont confirms that up to 10-percent system-capacity gains can be expected. Thus, MP39 can provide system capacity gains as long as leakage is maintained within limits. As MP39's capacity decreases with sustained leakage and/or refill cycles, its EER increases. A computer simulation of leak recharging shows that a slight gain in efficiency is observed, as shown in Table 3.

**Table 3. Energy efficiency ratios
(at 1.7 deg C evaporator temperature).**

Refrigerant	EER	EER after 20 percent refrigeration loss
MP39	15.823	15.985
R-12	15.992	15.992 (same)
R-134a	15.896	15.896 (same)

Du Pont claims that charging an R-12 system with MP39 requires only 80 to 85 percent of the usual R-12 charge by weight. Some field observations have shown even lower average numbers of 75 percent.⁴ Using less refrigerant would save money. It is estimated that retrofitting the G-38 R-12 system with MP39 would incur a materials cost of \$2,097 versus \$3,152 for R-134a (using an estimated 85-percent charge for the MP39). Labor for retrofitting with MP39 is estimated at 84 hr versus 95 hr for R-134a. Material and labor costs may be higher with MP39, depending on the system configuration. Some GDSCC R-12 systems would require an expensive receiver tank replacement to accommodate MP39's higher pressures.

X. Systems Not Included

Not included in this retrofit plan and schedule are a walk-in refrigerator, walk-in freezer, and five small food-cooling units at the Echo site cafeteria; several small wall air conditioners; and the complex water fountains. Those units have shown insignificant R-12 consumption and, as sealed systems, pose very low leakage potential. A small supply of in-house R-12 stock would ensure sufficient refrigerant for their remaining lifetimes. The time and cost of converting these units to R-134a is not justified.

The Carrier system in G-38 (room 115) does not contain any refrigerant. As the building is vacant and has no known occupancy plans, the system is not included in this retrofit plan and schedule. The Carrier system in G-52 (Venus antenna) and the rooftop unit in G-33 (Photo Lab) are no longer being used and are not included either.

XI. Potential R-12 Replacement Plan and Schedule

A. Plan

The following plan could allow the GDSCC to meet NASA's interim policy with respect to consumption and use of CFC R-12. It is recommended that the GDSCC R-12 air-conditioning systems be retrofitted with R-134a. Several factors justify the possible additional costs of converting to R-134a (as compared with MP39). In some systems, the higher operating pressures of MP39 (and R-22 as well) would necessitate installation of higher pressure receiver tanks, eliminating or reversing projected cost savings. Table 4 shows some pressure comparisons of refrigerants referred to in this article. At higher discharge temperatures, relief valves in 172-kPa receiver tanks (found in some GDSCC R-12 systems) could vent

³ Personal communication with R. Sazewicz, Air Cold Supply, Irwindale, California, January 1994.

⁴ Ibid.

refrigerant to the atmosphere. A system audit would be required to determine the number of tanks needing replacement. R-134a should operate within the relief valve limit.

Table 4. Comparison of refrigerant pressures.

Temperature, deg C	Pressure, kPa			
	R-12	R-134a	MP39	R-22
10	322	312	499	579
24	530	542	749	912
38	808	856	1083	1351
52	1166	1272	1521	1916
66	1618	1812	2075	2632

Using a blend of refrigerants, such as MP39, would require training and maintenance procedures different from those of the single-component refrigerants used at GDSCC. Systems must be liquid-charged instead of gas charged, as usual. Two sets of subcooling and superheat calculations must be used in routine servicing (as opposed to using one set with R-12 or R-134a) to account for "temperature glide." As the liquid refrigerant boils into a gas, the components will boil at different rates, depending on their vapor pressures. This causes a change in the mixture's composition, which results in a temperature glide or change for the boiling point.

Recycling MP39 recovered from systems is not as straightforward as with a single-component refrigerant. Short of a chemical analysis, component ratios in the recovered refrigerant cannot be accurately estimated if an exact leakage record is kept because of the differing leakage rates of the components. Additionally, some refrigerant reclaimers will not accept used-blend refrigerants. This presents a disposal issue not normally encountered with single-component refrigerants. Du Pont will accept used blends, however, in its Refrigerant Reclamation Program.

B. Schedule

This plan and schedule attempts to reduce the risk of equipment problems with air-conditioning units used to cool critical locations. No indications of problems have been seen in either the pilot test, other field retrofits (reported by refrigerant manufacturers), or equipment manufacturers retrofit experiences with R-134a. The retrofit process should proceed cautiously by first converting equipment less critical to tracking support. This would give more experience and run time in each system type before converting critical units. Using a small data-acquisition unit and laptop computer (included in the total cost estimate), systems would be monitored for performance before and after converting to R-134a. This would provide detailed information for optimizing performance of the retrofitted systems.

A five-phase, 1-year retrofit schedule (Fig. 4) would be performed by Allied Signal Technical Services Personnel if an additional temporary workforce is provided. Three units per phase would be retrofitted, with the flexibility of rearranging the schedule within the phase. Completion in 1 year is suggested, but that period may be extended considerably while still complying with the interim NASA policy directive.

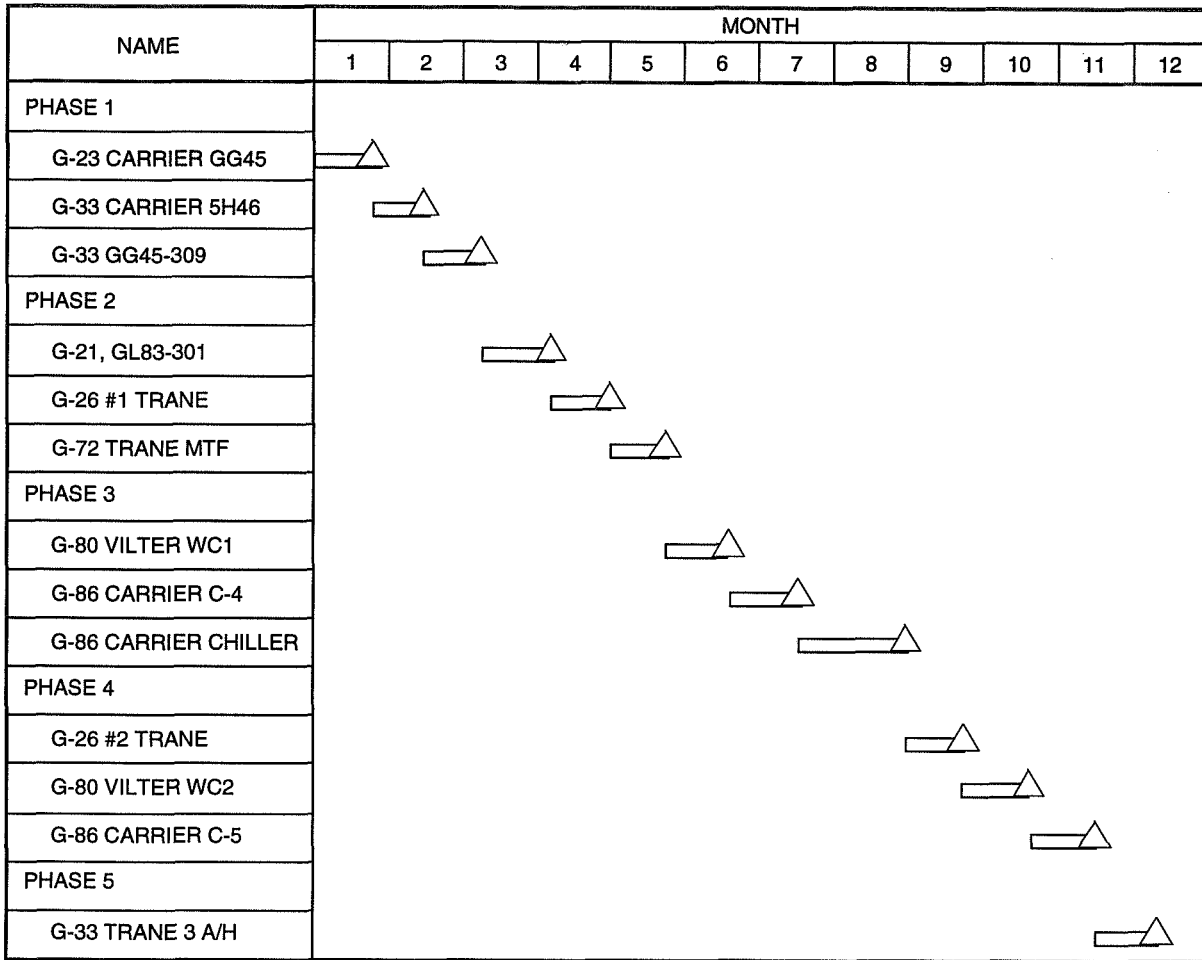


Fig. 4. Potential GDSCC R-12 replacement schedule.

XII. Cost Estimate of Potential R-12 Replacement

The total estimated cost for retrofitting the GDSCC R-12 systems to R-134a is approximately \$136,000 (Fig. 5). Labor and material costs were itemized for each system. Included in the total cost estimate are recovery and recycling equipment, data-acquisition and recording equipment, and R-12 recovery certification training required by the Environmental Protection Agency (EPA).

XIII. In-House R-12 Stocks

Approximately 3080 kg of R-12 are consumed annually by the 20 GDSCC R-12 systems. As systems are converted to R-134a, the recovered R-12 would be recycled and stored in-house to meet the progressively decreasing consumption demand. The accumulating stock (Table 5) would be more than sufficient to maintain operation of the unconverted systems.

BUILDING	No. 274 kg CYLINDERS R-134a	KILOGRAMS OF R-134a	LITERS OF POLYOL ESTER OIL	No. FILTER DRIERS	No. POWER ASSEMBLIES	No. TEST VALVE DRAINS	No. OIL TESTS	No. REFRIGERANT TESTS	No. OIL FILTERS	MATERIAL COST	No. 3-WAY VALVES	No. RELIEF VALVES	LABOR HOURS	LABOR COST	TOTAL COST
G-21 GL83-301	3	142	114	4	2	1	3	2	1	\$6,815	1	2	175	\$5,250	\$12,065
G-26 #1 TRANE	4	160	57	4		1	3	2		\$5,070	1	2	127	\$3,810	\$8,880
G-26 #2 TRANE	3	160	57	4		1	3	2		\$5,070	1	2	128	\$3,840	\$8,910
G-23 CARRIER GG45-469	1	36	34	2	1	2	3	2	1	\$2,141	1	2	123	\$3,690	\$5,831
G-33 CARRIER 5H46	3	159	27	4		2	3	2	1	\$3,967	1	2	112	\$3,360	\$7,327
G-33 GG45-309	1	45	34	2		2	3	1		\$2,037	1	2	141	\$4,230	\$6,267
G-72 TRANE MTF	2	91	38	2		1	3	2		\$3,108	1	2	129	\$3,870	\$6,978
G-80 VILTER WC1	4	205	80	1	2	2	3	2		\$5,996			138	\$4,140	\$10,136
G-80 VILTER WC2	4	205	80	1	2	2	3	2		\$5,996			138	\$4,140	\$10,136
G-86 CARRIER C-4	4	227	38	4	4	2	3	2	1	\$5,550	1	2	169	\$5,070	\$10,620
G-86 CARRIER C-5	4	227	38	4	4	2	3	2	1	\$5,550	1	2	169	\$5,070	\$10,620
G-86 CARRIER CHILLER #1	5	284	83	4		4	3	2	3	\$7,154	1	2	230	\$6,900	\$14,054
G-33 TRANE 3 A/H	2	114	57	4	1	4	3	2		\$3,485	1	2	162	\$4,860	\$8,345
TOTALS:	40	2056	734	40	16	26	39	25	8	\$61,939	11	22	1941	\$58,230	\$120,169
RECOVERY UNITS (2)	\$9,000														
TECHNICIAN TRAINING AND CERTIFICATION	\$3,000														
DATA COLLECTION AND ANALYSIS UNIT	\$4,000														
GRAND TOTAL	\$136,169														

Fig. 5. Estimates for retrofitting the GDSCC R-12 systems to R-134.

Table 5. R-12 inventory as GDSCC systems are retrofitted to R-134a.

System	Cumulative R-12 recovered, kg
G-23 Carrier GG45-469	142
G-33 Carrier 5H46	302
G-33 Carrier GG45-309	463
G-21 GL83-301	499
G-26 #1 Trane	658
G-72 Trane MTF	704
G-80 Vilter WC1	795
G-86 Carrier C-4	999
G-86 Carrier chiller #1	1204
G-26 #2 Trane	1431
G-80 Vilter WC2	1658
G-86 Carrier C-5	1942
G-33 Trane 3 A/H	2056

XIV. Conclusion

To comply with NASA's policy, HVAC systems at GDSCC must be retrofitted with an alternative refrigerant. Retrofitting with HFC R-134a would require fewer work hours, less system downtime, and would be less expensive than retrofitting with HCFC R-22 or replacing entire systems. It is preferable to retrofit with R-134a rather than with MP39 for factors discussed previously. Most of MP39's advantages (compared with R-134a) are not anticipated to be substantial with respect to the GDSCC's systems. All systems recommended for retrofitting operate in the temperature ranges best suited for R-134a performance. The efficiency and capacity with R-134a are expected to be equivalent to those with R-12. Compatibility of system materials and equipment does not appear to be a concern. Retrofitting the GDSCC R-12 air-conditioning systems with R-134a is a workable means of complying with the NASA policy directive while maintaining equivalent systems performance.

Acknowledgments

The authors thank the following individuals, listed in alphabetical order; Allied-Signal—Bill Bonson, Tony Brydon, Steve Duran, Tim Gorman, Bob Johnson, Steve Jonas, Kevin King, Paul Liverman, and William Noffsinger; Castrol Corporation—David Jones; Du Pont Corporation—Bob Dlugopolski and Fred Kielhorn; ICI Corporation—George Haines and Melissa Sorrell; Jet Propulsion Laboratory—Fred Battle and Jack Jones; PRC—Peter Stelzmuller; and Trane Corporation—Dave Fontanini. Special mention is due to Kevin King and Paul Liverman for their contribution to retrofitting the G-38 test system.

References

- [1] D. D. Dawn, *Saving Stratospheric Ozone: Putting the Problem in Perspective and Evaluating Hydrohalocarbons and Their Mixtures as Potential Solutions*, California Institute of Technology, Division of Chemistry and Chemical Engineering, Pasadena, California, May 10, 1990.
- [2] ICI Americas, Inc., "ICI KLEA Case Studies of R-12 to R-134a Field Retrofits," Wilmington, Delaware.

199108216
324472

N95-14630

TDA Progress Report 42-118

19100
August 15, 1994
p. 24 ✓

A Trajectory Preprocessor for Antenna Pointing

S. R. Tyler

Ground Antennas and Facilities Engineering Section

A trajectory-preprocessing algorithm has been devised which matches antenna angular position, velocity, and acceleration to those of a target. This eliminates vibrations of the antenna structure caused by discontinuities in velocity and acceleration commands, and improves antenna-pointing performance by constraining antenna motion to a linear regime. The algorithm permits faster acquisition times and preserves antenna-tracking capability in situations where there would otherwise be an unacceptably sudden change in antenna velocity or acceleration. A simulation of DSS 13 shows that this preprocessor would reduce servo error to 1 mdeg during acquisition of a low-Earth-orbiting satellite.

I. Introduction

When a large antenna is moved in a sudden or jerky manner, the ensuing vibration of the structure can adversely affect pointing accuracy. A fast-moving antenna which stops in a precipitous manner upon acquiring a target may vibrate enough to lose lock. Even in situations for which the vibration amplitude does not immediately produce an unacceptable pointing error, the servo control may enter a nonlinear, and possibly unstable, region. This problem can arise when the servo controller attempts to apply an excessive velocity or acceleration in an attempt to track a sudden command change [1].

In the past, Deep Space Network pointing requirements have been for slow antenna motion. While DSN antennas are required to track at up to 0.4 deg per sec, they are not required to meet pointing requirements for other than sidereal targets.¹ The prospect of very accurate acquisition of low-Earth-orbiting satellites (with angular velocities in excess of even 0.4 deg per sec) is a relatively new idea. The anticipation of such requirements has led to the present work.

Trajectory preprocessing is one method used to preserve antenna-pointing integrity. The principal idea is to make antenna motion smoother during target acquisition, although the algorithm can be applied to all antenna motion commands. The present antenna control system is nonlinear. Its behavior is governed by the nonlinearity (acceleration and velocity limits), its inputs, the initial conditions, and the linear subsystem frequency response (the controller bandwidth). This has resulted in a system with complicated switching rules for changing the controller bandwidth as a function of inputs. A change in a velocity or acceleration limit affects the switching rules. The system can still work poorly for some sets of inputs, initial conditions, and parameters.

¹ W. Scherr, *Deep Space Communications Complex Subsystem Functional Requirements, Antenna Mechanical Subsystem (1991 through 1997)*, JPL D-1179, Rev. C (internal document), Jet Propulsion Laboratory, Pasadena, California, September 1, 1992.

Since commands which are in violation of these limits cause the system to behave nonlinearly, a simple method for allowing the system to operate in a linear regime is to force command angles to conform to the limits. Trajectory preprocessing performs this task.

Even if an antenna were perfectly rigid and could be moved at will at accelerations of up to 1 deg/sec^2 , it could still overshoot a target during a high-speed acquisition. When the difference in speeds between average acquisition velocity and tracking velocity can easily exceed a deg/sec , some algorithm is needed to ensure that the acquisition time remains reasonable for a target which may not be visible for more than a minute or two in the first place. This provides a further motivation for considering trajectory preprocessing.

The problem to be solved by this preprocessor is to find an optimal, or at least an adequate, path from an initial antenna position, velocity, and acceleration to some target trajectory. The first idea that was considered for finding this path was to use the calculus of variations. This idea was abandoned for three reasons. First, the method is overly complex. Second, the calculation time can be large. The method is iterative, and the calculation time is indeterminate, making it unsuitable for a real-time system. Finally, although the calculus of variations can give a least-time solution, it is not easy to include constraints that will prevent sudden changes in the slopes of the antenna velocity and acceleration profiles.

II. The Three-Region Method

The method described in this article involves three regions of antenna motion and was inspired by the following scenario. A target is far away and one wishes to move the antenna towards the target trajectory as quickly as possible. So one begins by accelerating the antenna to its maximum speed; that is region 1. Then, in region 2 one moves the antenna at maximum speed until one is near the target. Finally, in region 3, the antenna is decelerated until it matches the apparent target angular position and angular velocity.

As applied to a low-Earth-orbiting satellite, the initial scenario envisioned the following preprocessor steps:

- (1) Input a set of target positions and velocities (θ and v) for both local azimuth and elevation as a function of time using known orbital parameters (updated by optical detection).
- (2) Choose an intercept (acquisition) $\theta_{el} = \theta_{0,el}$. From this obtain the time interval, T , from the start of region 1 to the intercept time, as well as θ_{az} and both v_{az} and v_{el} . Input the initial antenna pointing (θ_0 and v_0) and the maximum angular velocity for the antenna (v_{max}). Input or calculate maximum angular accelerations for the antenna ($a_{max} > 0$).
- (3) If necessary, try a different maximum acceleration (remaining less than or equal to the specified limit) or a later acquisition time. Set a flag if acquisition is not possible before $\theta_{el} > \theta_{max}$.

The same algorithm can be used for reacquisition during tracking (without the flag). One does not need to start by choosing the acquisition elevation. A total acquisition time can be input instead. This time can be chosen by noting the distance in position and the change in velocity that must occur. Using one's experience from previous acquisitions, it will often be possible to choose an acquisition time within a second of the minimum. Should one's choice be too small, the algorithm can be rerun with steadily increasing total times input. In practice, the maximum acceleration may simply be set to the specified acceleration limit.

For acquisition, in both azimuth and elevation, it is best to chase the target rather than approach it head-on; this lessens the required change in velocity. That means that θ_0 should be a little less than θ . Thus, while waiting for the target to appear, the antenna will generally be pointing at a place in the trajectory close to that anticipated by an optical acquisition aid. The antenna will typically have an

initial velocity of approximately zero in elevation (or it might badly overshoot the target). When the target shows up “late,” the Earth’s rotation will cause it to move in azimuth as a function of lateness, so the antenna may initially be moving slowly in azimuth. The formula for the minimum time to acquire is then $T = v_f/A$, where A is the average acceleration.

When $A = a_{max}$, we get the fastest acquisition. An a_{max} in elevation of 0.5 deg/sec gives $T = 2v_f$, where v is in deg/sec and T is in sec.

In our acquisition schemes, the average A will often be $a_{max}/2$ or less, giving a minimum acquisition time of $4v_f$ sec. When v_f is about 0.5 deg/sec, this results in a minimum acquisition time on the order of 2 sec.

This minimum acquisition time applies only when

$$\Delta\theta_{el} = \frac{v_f^2}{2A}$$

If, for example, we initially aim at the acquisition point instead of a point $v_f^2/2A$ below it, the minimum time increases from T to $T/\sqrt{2} - 1$.

Figure 1 shows the matching in elevation of antenna pointing with that of a target. Figure 2 shows the antenna angular velocity for this example. In these figures, the antenna is aimed a little above the acquisition point. Figure 3 shows how the algorithm matches angular position when the antenna is initially aimed a little below this point.

The acquisition time will often be determined by the change in v_{el} . The final azimuthal velocity is usually much smaller, and there may even be an initial azimuthal velocity. However, if the antenna is simply waiting several degrees from the acquisition, θ_{az} , the azimuthal acquisition time can easily become the total acquisition time.

III. Acquisition Schemes

Four acquisition schemes are considered in this article:

- Scheme 1: Match initial and final angular position and velocities. Use the maximum allowable acceleration throughout each acceleration region.
- Scheme 2: The same as scheme 1, but use a sinusoidal acceleration pattern to avoid large discontinuities in acceleration.
- Scheme 3: The same as scheme 2, but match the final acceleration as well.
- Scheme 4: The same as scheme 2, but match both initial and final accelerations.

Each of these ideas has some merit. The calculations needed to implement the trajectory-preprocessing algorithm are similar for any of the first three schemes.

A. The First Acquisition Scheme

Scheme 1 has the advantage of speed. By using the maximum acceleration, the target can be reached more quickly. Even when the increased initial overshoot and ensuing oscillations are taken into account, the total acquisition time may be minimized in some situations. On the other hand, when the angular distance to the target is large and the maximum allowable pointing error is small, this scheme is inappropriate.

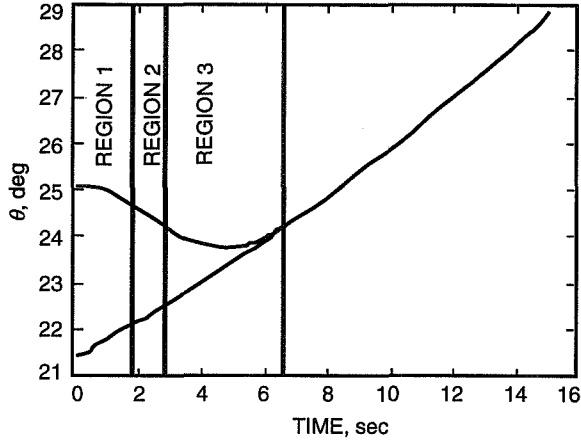


Fig. 1. Matching of antenna and target positions for constant accelerations (elevation only).

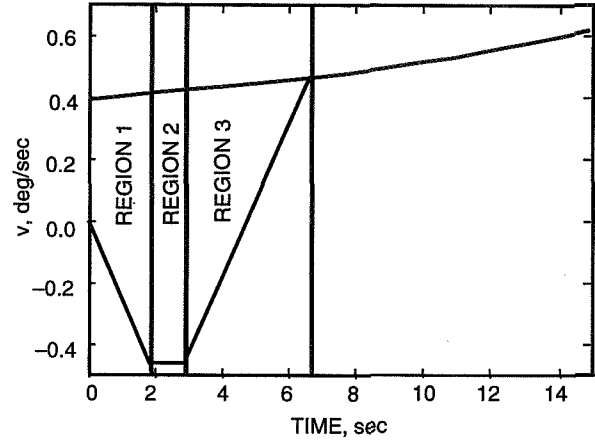


Fig. 2. Matching of antenna and target velocities for constant accelerations (elevation only).

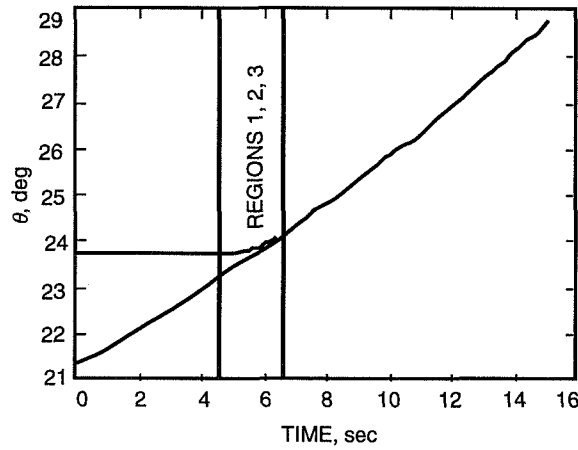


Fig. 3. Matching of antenna and target positions for elevation only (chasing target).

This scheme uses the maximum acceleration in each acceleration region. Although this introduces discontinuities in acceleration, it permits a straightforward calculation of the acquisition parameters. Then $a = \pm a_m = \pm a_{max}$ in regions 1 and 3. By integrating twice, we get the velocities and positions as a function of time in all three regions. The following calculations must be performed both for elevation and for azimuth:

For region 1,

$$v = v_0 + a_1 t \quad (1)$$

$$\theta = \theta_0 + v_0 t + \frac{a_1 t^2}{2} \quad (2)$$

For region 2,

$$v = v_2 = v_0 + a_1 t_1 = v_f - a_3 t_3 \quad (3)$$

$$\theta = \theta_0 + v_0 t_1 + v_2 (t - t_1) + \frac{a_1 t_1^2}{2} \quad (4)$$

where $T = t_1 + t_2 + t_3$.

For region 3,

$$v = v_f - a_3(T - t) \quad (5)$$

$$\theta = \theta_f - v_f(T - t) + a_3 \frac{(T - t)^2}{2} \quad (6)$$

1. Calculation of Acquisition Parameters. In the above equations, we do not yet know the signs of a_1 or a_3 . Nor do we know the durations, t_1 or t_3 , or the constant velocity, v_2 . These are calculated as follows. Input the initial and final antenna positions (azimuth and elevation), θ_0 and θ_f ,

$$\Delta\theta = \theta_f - \theta_0$$

as well as the initial and final antenna velocities (azimuth and elevation), v_0 and v_f ,

$$\Delta v = v_f - v_0$$

and the total time,

$$T = t_1 + t_2 + t_3$$

as well as the maximum acceleration, a_m , and velocity, v_m (in both azimuth and elevation), which must be less than or equal to the requirements, a_{max} and v_{max} (in both azimuth and elevation).

From the above inputs, output t_1, t_2, t_3 , and v_2 and also determine a_1 and a_3 . To obtain these outputs, the following formulas are used. First, a normalized angular position, x , and a normalized angular velocity, y , are calculated:

$$x = \frac{\Delta\theta}{a_m T^2} - \frac{v_0}{a_m T} \quad (7)$$

$$\frac{y}{a_m T} = \frac{\Delta v}{a_m T} \quad (8)$$

Next, ε_0 and ε_f , intermediate variables that are used to find the signs of the accelerations in regions 1 and 3, are determined:

$$\varepsilon_0 = \varepsilon_f = -1 \text{ when } y \leq 0 \text{ and } y + \frac{y^2}{2} \leq x \leq -\frac{y^2}{2} \quad (9)$$

$$\varepsilon_0 = \varepsilon_f = 1 \text{ when } y < 0 \text{ and } \frac{y^2}{2} \leq x \leq -y - \frac{y^2}{2} \quad (10)$$

$$\varepsilon_0 = 1 \text{ and } \varepsilon_f = -1 \text{ when } y > 0 \text{ and } x > y - \frac{y^2}{2} \text{ or } y \leq 0 \text{ and } x > -\frac{y^2}{2} \quad (11)$$

$$\varepsilon_0 = -1 \text{ and } \varepsilon_f = 1 \text{ when } y > 0 \text{ and } x < \frac{y^2}{2} \text{ or } y \leq 0 \text{ and } x < y + \frac{y^2}{2} \quad (12)$$

These give us a_1 and a_3 :

$$a_1 = \varepsilon_0 a_m \quad (13)$$

$$a_3 = \varepsilon_f a_m \quad (14)$$

Now the velocity in region 2 can be found:

$$\text{for } \varepsilon_0 = \varepsilon_f, \quad y_2 = \frac{y^2 \varepsilon_f - 2x}{2(y\varepsilon_f - 1)} \quad (15)$$

$$\text{for } \varepsilon_0 \neq \varepsilon_f, \quad y_2 = \frac{y\varepsilon_f - 1 + \sqrt{y^2 \varepsilon_0 \varepsilon_f - 2y\varepsilon_f + 2x(\varepsilon_f - \varepsilon_0) + 1}}{\varepsilon_f - \varepsilon_0} \quad (16)$$

$$v_2 = a_m T y_2 + v_0 \quad (17)$$

Finally, the time intervals can be deduced:

$$t_1 = \frac{v_2 - v_0}{a_1} \quad (18)$$

$$t_3 = \frac{v_f - v_2}{a_3} \quad (19)$$

$$t_2 = T - t_1 - t_3 \quad (20)$$

Once the above parameters have been obtained, position and velocity commands are determined from Eqs. (1) through (6).

The main problem with this acquisition scheme is the discontinuity in antenna acceleration at the borders of regions 1 and 3. The problem is most serious at the border of region 3, where transient phenomena may significantly affect antenna-pointing accuracy immediately after acquisition. To see this, consider the example of Figs. 1 and 2. In this, Example (1),

$$\begin{aligned} \theta_0 &= 25.104 \text{ deg} \\ \theta_f &= 24.253 \text{ deg} \\ v_0 &= -0.001 \text{ deg/sec} \\ v_f &= 0.479 \text{ deg/sec} \\ T &= 6.6 \text{ sec} \\ |a| &= 0.25 \text{ deg/sec}^2 \end{aligned}$$

which has the solution

$$\begin{aligned}
v_2 &= -0.46 \text{ deg/sec} \\
t_1 &= 1.85 \text{ sec} \\
t_2 &= 1 \text{ sec} \\
t_3 &= 3.75 \text{ sec}
\end{aligned}$$

Figure 4 shows anticipated servo error during and immediately following acquisition for this example using a simulation in which a PI controller is applied to a model of a 34-m Deep Space Network antenna, namely DSS 13 in Goldstone, California. This servo controller, which uses both proportional (P) and integral (I) feedback terms, is in use at DSS 13. The controller and the model of the antenna are described in [2].

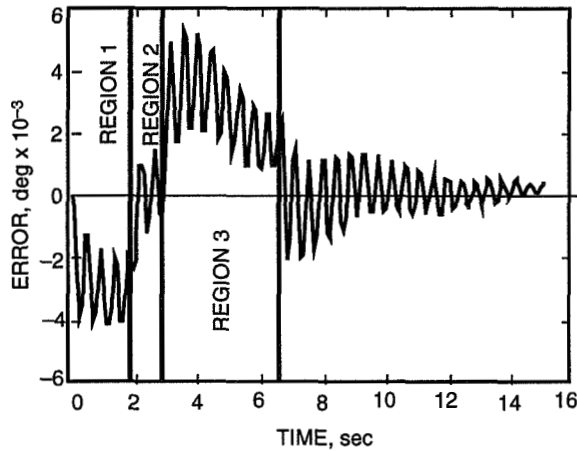


Fig. 4. Anticipated servo error for Example (1) with constant acceleration in regions 1 and 3 (elevation only).

2. Derivation of Results. This section gives a derivation of the results of Eqs. (7) through (20). Begin by conserving the total angular distance:

$$v_1 t_1 + v_2 t_2 + v_3 t_3 = \Delta\theta \quad (21)$$

The values t_1 and t_3 are obtained from the change in velocity divided by the acceleration. This immediately gives Eqs. (18) and (19).

The values v_1 and v_3 are the average angular velocities in regions 1 and 3. Since the acceleration is constant in each of these regions,

$$v_1 = \frac{v_2 + v_0}{2} \text{ and } v_3 = \frac{v_2 + v_f}{2} \quad (22)$$

When Eqs. (18), (19), and (22) are substituted in Eq. (21), the result is

$$\frac{v_2^2 - v_0^2}{2a_1} + v_2 t_2 + \frac{v_f^2 - v_2^2}{2a_3} = \Delta\theta \quad (23)$$

By substituting $T - t_1 - t_3$ for t_2 in Eq. (23), we get

$$-\frac{(v_2 - v_0)^2}{a_1} + 2v_2T + \frac{(v_f - v_2)^2}{a_3} = 2\Delta\theta \quad (24)$$

Further substitution of the definitions of x, y, y_2, ε_0 , and ε_f from Eqs. (7), (8), (17), (13), and (14) gives

$$y_2^2(\varepsilon_f - \varepsilon_0) + 2y_2(1 - y\varepsilon_f) + y^2\varepsilon_f - 2x = 0 \quad (25)$$

When $\varepsilon_0 = \varepsilon_f$, which is often the case, Eq. (15) follows directly from Eq. (25). When $\varepsilon_0 \neq \varepsilon_f$, Eq. (16) immediately results from applying the quadratic formula to Eq. (25). However, the sign in front of the square root in Eq. (16) is yet to be determined. This is done as follows. Note that

$$t_2 = T - \frac{v_f}{a_3} + \frac{v_0}{a_1} - \frac{v_2}{a_1} + \frac{v_2}{a_3} + \frac{v_0}{a_3} - \frac{v_0}{a_3}$$

which gives

$$\frac{t_2}{T} = 1 - y\varepsilon_f + y_2(\varepsilon_f - \varepsilon_0)$$

The square root term in Eq. (16) is also equal to $1 - y\varepsilon_f + y_2(\varepsilon_f - \varepsilon_0)$. Since t_2/T must be positive, the plus sign must be chosen in front of the square root.

The next step is to find out where the solutions for y_2 described in Eqs. (15) and (16) are valid. The values of x and y for which a solution can be found will be referred to as an "area of validity," which can be plotted on a graph of y versus x . This area is in "phase space," and as it increases, a larger number of combinations of target positions and velocities can be matched. Starting from Eq. (16), the minimum and maximum values of x as a function of y_2 are obtained by setting $dx/dy_2 = 0$. This gives $y_2 = (y\varepsilon_f - 1)/(\varepsilon_f - \varepsilon_0)$ and $t_2 = 0$. This means that the discriminant of the square root in Eq. (16), t_2^2 , is 0 at the borders of the area of validity of solutions to Eq. (25). Setting the discriminant to zero gives

$$x = \frac{1 - 2y\varepsilon_f + y^2\varepsilon_0\varepsilon_f}{2(\varepsilon_0 - \varepsilon_f)} \quad (26)$$

At the external boundaries of the area of validity, $\varepsilon_0 \neq \varepsilon_f$. Thus, the area of valid solutions is bounded by the curves

$$x = \frac{y^2 + 2y - 1}{4} \quad (-1 \leq y \leq 1)$$

and

$$x = \frac{1 + 2y - y^2}{4} \quad (-1 \leq y \leq 1)$$

This area of validity is shown in Fig. 5. Notice that solutions for which x and y have the same sign are favored (have more phase space) than those which do not.

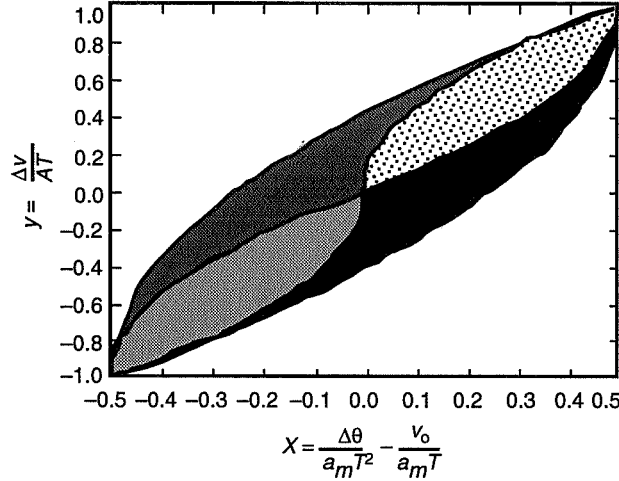


Fig. 5. Area of valid solutions ($a_m = a_{max}/2$ and $a_o = a_f = 0$).

In these calculations, we have ignored the situation in which v_{max} corresponds to $|y_{max}| < 1$, which would cut off the region of valid solutions at $y < 1$ or $y > -1$. This can be dealt with as follows: Note that for the antenna velocity to exceed a velocity limit, either v_o , v_f , or v_2 must exceed that limit. If v_o exceeds the limit, we already have a problem, but it is one that has little to do with the trajectory preprocessor. If v_f exceeds the limit, we cannot acquire at that point, but we can try other values of T for which v_f may be smaller. If v_2 is the only culprit, we increase T to a point at which v_2 is acceptable.

Figure 5 also shows internal borders in the area of validity. These borders define the regions where a_1 and a_3 are both negative, both positive, of opposite sign with a_1 positive, and of opposite sign with a_1 negative, respectively. At these borders, $t_1 = 0$ (which gives $y_2 = 0$) or $t_3 = 0$ (which gives $y_2 = y$). Substituting in Eq. (25),

$$y_2 = 0 \Rightarrow x = \frac{y^2 \varepsilon_f}{2} \quad (27)$$

while

$$y_2 = y \Rightarrow x = y - \frac{y^2 \varepsilon_0}{2} \quad (28)$$

By defining the borders of each of the four internal regions, Eqs. (27) and (28) permit us to write down Eqs. (9) through (12), completing our derivation of the formulas used in the first acquisition scheme.

B. The Second Acquisition Scheme

To avoid the discontinuities in acceleration, one can choose a sinusoidal acceleration pattern. This trades acquisition rate for pointing accuracy; the price that is paid for improved accuracy is a factor of two in average antenna angular acceleration. The preprocessor matches position and velocity as before. The antenna angular acceleration is still not matched to that of the target, but it is zero rather than the maximum allowable acceleration at acquisition. The idea is to let $a = \pm a_m (1 - \cos 2\pi\omega t)$ for some ω and for $a_m < a_{max}/2$. In particular, for region 1,

$$a = a_1 \left(1 - \cos \frac{2\pi t}{t_1} \right)$$

Integrating with respect to t ,

$$v = v_0 + a_1 \left(t - \frac{t_1}{2\pi} \sin \frac{2\pi t}{t_1} \right) \quad (29)$$

Integrating again,

$$\theta = \theta_0 + v_0 t + a_1 \left(\frac{t^2}{2} - \frac{t_1^2}{4\pi^2} + \frac{t_1^2}{4\pi^2} \cos \frac{2\pi t}{t_1} \right) \quad (30)$$

For region 2,

$$a = 0$$

$$v = v_2 = v_0 + a_1 t_1 = v_f - a_3 T_3 \quad (31)$$

$$\theta = \theta_0 + v_0 t_1 + v_2(t - t_1) + \frac{a_1 t_1^2}{2} \quad (32)$$

For region 3,

$$a = a_3 \left(1 - \cos \frac{2\pi(T-t)}{t_3} \right)$$

Integrating with respect to $(T-t)$,

$$v = v_f - a_3 \left(T-t - \frac{t_3}{2\pi} \sin \frac{2\pi(T-t)}{t_3} \right) \quad (33)$$

$$\theta = \theta_f - v_f(T-t) + a_3 \left(\frac{(T-t)^2}{2} - \frac{t_3^2}{4\pi^2} + \frac{t_3^2}{4\pi^2} \cos \frac{2\pi(T-t)}{t_3} \right) \quad (34)$$

Note that da/dt is not merely finite everywhere; it goes to 0 at the borders of each region.

At first, these equations seem more complicated than those for constant accelerations, but the solutions for their parameters are identical. Equations (7) through (20) still hold. The acceleration is not constant, but Eq. (22) is still valid. The maximum value of a_m is reduced by a factor of 2, but Eqs. (13) and (14) are unchanged. The same four solutions exist with the same boundaries in x and y , as represented by Fig. 5. The only difference is that Eqs. (1) through (6) have been replaced by Eqs. (29) through (34).

Example (1) still has the same solution for t_1 , t_2 , t_3 , and V_2 . However, the anticipated servo error has been reduced because the acceleration changes more smoothly.

Figure 6 shows the matching of antenna and target angular positions in Example (1) for acquisition scheme 2. Figure 7 shows the corresponding matching of velocities. Note that the velocity slope is zero at acquisition for the antenna but not for the target; there is still a slight discontinuity in acceleration at acquisition. Figure 8 gives the anticipated servo error for Example (1) using the second acquisition scheme.

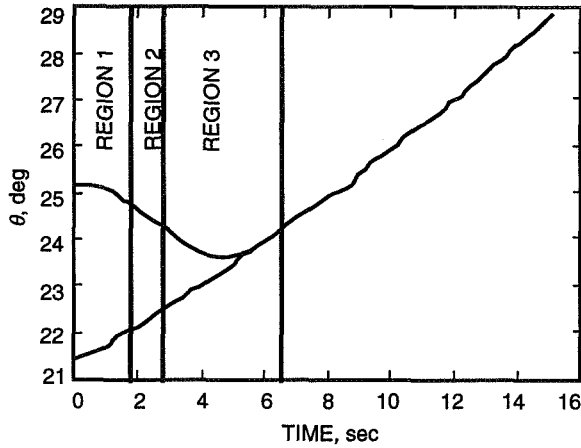


Fig. 6. Matching the target position for raised cosine acceleration (elevation only).

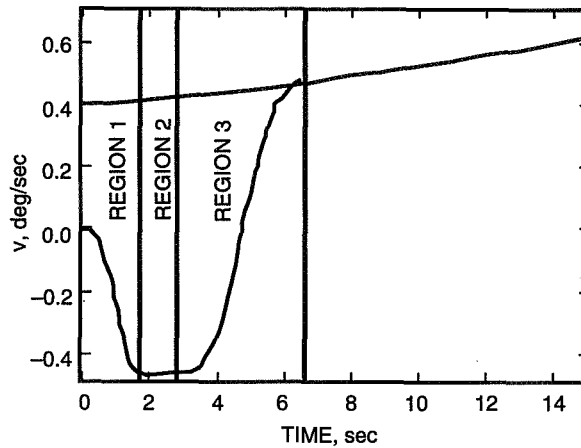


Fig. 7. Matching the target velocity for raised cosine acceleration (elevation only).

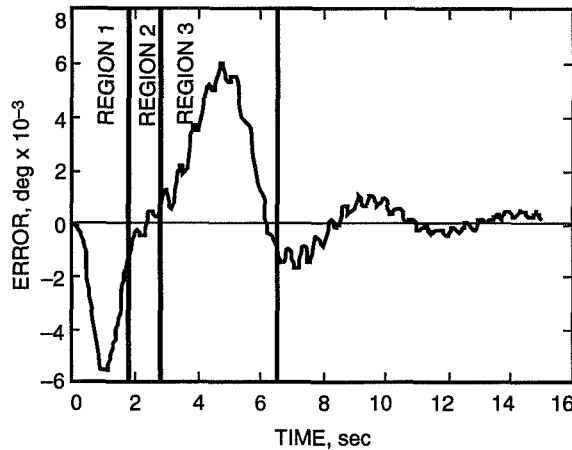


Fig. 8. Anticipated servo error (for Example (1) with raised cosine acceleration in regions 1 and 2 (elevation only).

Since T has already been chosen prior to the calculation of t_1 and t_3 , it may seem unnecessary to set a_m to $a_{max}/2$ when a smaller a_m would suffice. Also, potentially huge values of da/dt (jerk) can arise in this trajectory preprocessing scheme. These high values of jerk are produced when one is near the internal borders within the region of valid solutions in Fig. 5, since t_1 or t_3 approaches 0. Since $|a|$ goes from 0 to $2a_m$ and back in each region, the average $|da/dt|$ is $4a_m/t_3$ in region 3. The maximum $|da/dt|$ is $8a_m/t_3$ in region 3, and as t_3 approaches 0, this number becomes larger until the increase is filtered out by the servo mechanism. Actually, this gives us a very small servo error because for the PI controller, the maximum error caused by a sudden pulse does not exceed the total displacement caused by the pulse. Thus, the PI controller does not react much to a t_3 of 0.1 sec because $1/2a_{av}t^2$ for an average a of 0.125 deg/sec² is only 0.6 mdeg, which is an upper bound on the servo transient error. This is illustrated by Example (2), for which

$$\begin{aligned}\theta_0 &= 23.7618 \text{ deg} \\ \theta_f &= 24.253 \text{ deg} \\ v_f &= 0.479 \text{ deg/sec} \\ v_0 &= -0.001 \text{ deg/sec}\end{aligned}$$

$$\begin{aligned}
|a| &= 0.25 \text{ deg/sec}^2 \\
T &= 2 \text{ sec} \\
t_1 &= 1.9 \text{ sec} \\
t_2 &= 0.0 \text{ sec} \\
t_3 &= 0.1 \text{ sec} \\
v_2 &= 0.4665 \text{ deg/sec}
\end{aligned}$$

Figure 9 shows the anticipated servo error for Example (2) with acquisition scheme 2.

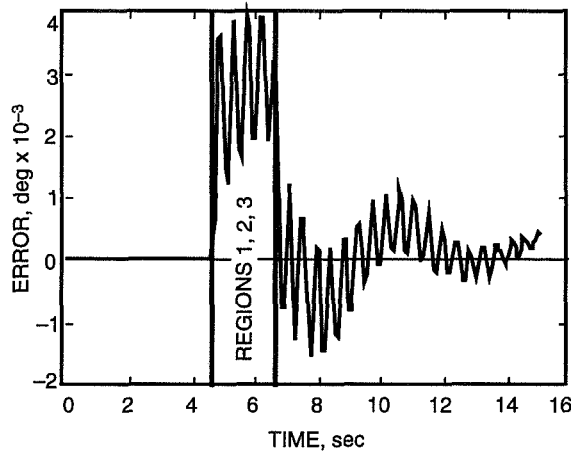


Fig. 9. Anticipated servo error during acquisition for Example (2), ($t_3 = 0.1$ sec, $t_2 = 0$) (elevation only).

If it is thought that the servo controller would react adversely to such a sharp acceleration pulse, one can modify a_m so that neither t_1 nor t_3 is small, or at least choose a reasonable a_m to begin with and modify either a_m or t if necessary. For example, one can choose an a_m that gives $t_2 = 0$ and if t_1 or t_3 is small anyway, one simply increases T . From Eq. (26), $t_2 = 0$ gives

$$y^2 \varepsilon_0 \varepsilon_f - 2y \varepsilon_f + 1 = 2(\varepsilon_0 - \varepsilon_f)x$$

Picking $\varepsilon_0 \varepsilon_f = -1$,

$$y^2 + 2y \varepsilon_f \left(1 - \frac{2x}{y}\right) - 1 = 0$$

Let

$$\Omega = 1 - \frac{2x}{y} = \frac{\Delta v T - 2\Delta\theta + 2v_0 T}{\Delta v T}$$

Then

$$\frac{\Delta v}{a_m T} = y = -\varepsilon_f \Omega \pm \sqrt{\Omega^2 + 1} \quad (35)$$

The sign in front of the square root in Eq. (35) and the value of ε_f are readily determined by observing that y has the same sign as Δv and that $|y| \leq 1$. This determines y and gives

$$a_m = \frac{\Delta v}{y T}$$

The $a = 0$ region can also be omitted from the algorithm entirely. The resulting scheme would have no intermediate region of maximum velocity for large changes in antenna position and would increase acquisition time as a result. If by some chance,

$$\frac{\Delta v}{T} = \frac{v_f^2 - v_0^2}{2\Delta\theta}$$

(and even with some latitude in choosing t , it is unlikely that this will occur), then a one-region solution is possible where

$$a = \frac{T}{\Delta v} \left(1 - \cos \frac{2\pi t}{T} \right)$$

If not, then $\varepsilon_0\varepsilon_f = -1$, and y is determined from Eq. (35), which also gives a_m , while

$$y_2 = \frac{y \pm 1}{2}$$

By leaving out the $a = 0$ region, overall accelerations are reduced. However, there is an increased flexibility in maintaining a three-region algorithm, and picking a_m prior to solving for y_2 may be impractical in some situations.

C. The Third Acquisition Scheme

In our examples, the target acceleration and servo controller are such that the sudden discontinuity in acceleration at acquisition does not significantly increase the pointing error. However, there is a straightforward way to avoid this discontinuity by modifying the previous acquisition scheme so that it matches the target acceleration at acquisition instead of acquiring with zero acceleration. One simply switches to a frame of reference which has an acceleration equal to that of the target. Figure 10 shows the anticipated servo error for Example (1) in this case.

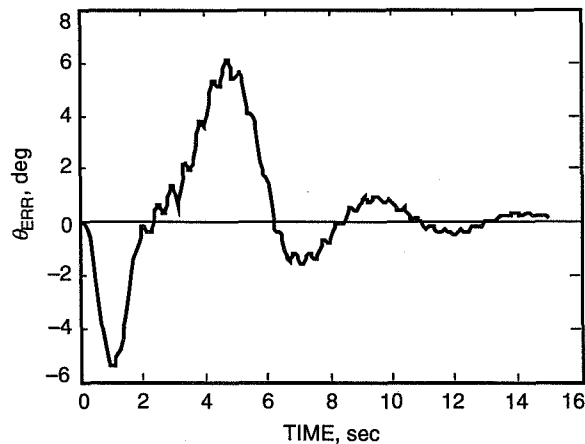


Fig. 10. Servo error for acquisition scheme 3 and constant velocity track. Acquisition is at $t = 6.6$ sec.

Let a_f be the acceleration of the target at $t = T$. Then match a position of $\theta_f - 1/2aT^2$ and a velocity of $v_f - aT$.

This means that $\Delta\theta$ now equals $\theta_f - \theta_0 - ((1/2)aT^2)$ and $\Delta v = v_f - v_0 - aT$. Once again, Eqs. (7) through (20) remain valid. However, care must be taken to ensure that the actual antenna accelerations

and velocities never exceed the maxima. The acceleration can be kept within bounds by choosing $a_m = a_{max} - |a_f|/2$. But the velocity is trickier, as the actual velocity in region 2 is no longer constant. For a situation in which the antenna must traverse a large angular distance to acquire a target, it might at first appear that the maximum velocity will be reached at the end of region 2. This is not the case. At the end of region 2, the antenna has an acceleration of a_f , so the velocity is still increasing. The maximum velocity is reached when the acceleration first reaches zero in region 3.

The difference between this scheme and the first scheme is that Eqs. (1) through (6) are now replaced with the following equations:

For region 1,

$$a = a_1 \left(1 - \cos \frac{2\pi t}{t_1} \right) + a_f$$

$$v = v_0 + a_1 \left(t - \frac{t_1}{2\pi} \sin \frac{2\pi t}{t_1} \right) + a_f t \quad (36)$$

$$\theta = \theta_0 + v_0 t + a_1 \left(\frac{t^2}{2} - \frac{t_1^2}{4\pi^2} + \frac{t_1^2}{4\pi^2} \cos \frac{2\pi t}{t_1} \right) + \frac{1}{2} a_f t^2 \quad (37)$$

For region 2,

$$a = a_f$$

$$v = v_2 + a_f t \quad (38)$$

$$\theta = \theta_0 + v_0 t_1 + v_2 (t - t_1) + \frac{a_1 t_1^2}{2} + \frac{a_f t^2}{2} \quad (39)$$

For region 3,

$$a = a_3 \left(1 - \cos \frac{2\pi(T-t)}{t_3} \right) + a_f$$

$$v = v_f - a_3 \left(T - t - \frac{t_3}{2\pi} \sin \frac{2\pi(T-t)}{t_3} \right) + a_f t \quad (40)$$

$$\theta = \theta_f - v_f (T - t) + a_3 \left(\frac{(T-t)^2}{2} - \frac{t_3^2}{4\pi^2} + \frac{t_3^2}{4\pi^2} \cos \frac{2\pi(T-t)}{t_3} \right) + \frac{a_f t^2}{2} \quad (41)$$

D. The Fourth Acquisition Scheme

Our final scheme applies to situations where the antenna has an initial acceleration a_0 and a final acceleration a_f . In this scheme, both the initial and final accelerations are matched by the preprocessor. We will assume that an initial value of a_m is chosen either by setting it to $a_{max}/2$, by looking at Eq. (35) (possibly modified by adding or subtracting a_0 or a_f), or by some as yet undetermined method. Inputs are then θ_0 , θ_f , v_a , v_f , A_0 , A_f , A_m , T , v_{max} , and a_{max} (for both azimuth and elevation). Equations (1) through (6) are now replaced by the following:

For region 1,

$$a = a_1 \left(1 - \cos \frac{2\pi t}{t_1}\right) + \frac{a_0}{2} \left(1 + \cos \frac{\pi t}{t_1}\right)$$

Note that $da/dt = 0$ both at $t = 0$ and $t = t_1$. By integrating,

$$v = v_0 + \left(a_1 + \frac{a_0}{2}\right) t + \frac{t_1}{2\pi} \left(a_0 \sin \frac{\pi t}{t_1} - a_1 \sin \frac{2\pi t}{t_1}\right) \quad (42)$$

$$\theta = \theta_0 + v_0 t + \left(a_1 + \frac{a_0}{2}\right) \frac{t^2}{2} + \frac{t_1^2}{4\pi^2} \left[2a_0 \left(1 - \cos \frac{\pi t}{t_1}\right) - a_1 \left(1 - \cos \frac{2\pi t}{t_1}\right)\right] \quad (43)$$

For region 2,

$$a = 0$$

$$v = v_2 = v_0 + \left(a_1 + \frac{a_0}{2}\right) t_1 = v_f - \left(a_3 + \frac{a_f}{2}\right) t_3 \quad (44)$$

$$\theta = \theta_0 + v_0 t_1 + v_2(t - t_1) + \left(a_1 + \frac{a_0}{2}\right) \frac{t_1^2}{2} + \frac{a_0 t_1^2}{\pi^2} \quad (45)$$

For region 3,

$$a = a_3 \left(1 - \cos \frac{2\pi(T-t)}{t_3}\right) + \frac{a_f}{2} \left(1 + \cos \frac{\pi(T-t)}{t_3}\right)$$

$$v = v_f - \left(a_3 + \frac{a_f}{2}\right) (T-t) - \frac{t_3}{2\pi} \left(a_f \sin \frac{\pi(T-t)}{t_3} - a_3 \sin \frac{2\pi(T-t)}{t_3}\right) \quad (46)$$

$$\theta = \theta_f - v_f(T-t) - \left(a_3 + \frac{a_f}{2}\right) \frac{(T-t)^2}{2} - \frac{t_3^2}{4\pi^2} \left[2a_f \left(1 - \cos \frac{\pi(T-t)}{t_3}\right) - a_3 \left(1 - \cos \frac{2\pi(T-t)}{t_3}\right)\right] \quad (47)$$

When $\text{sign}(a_0) = \text{sign}(a_1)$,

$$|a_1| = \frac{1}{2}(2a_m - |a_0|)$$

Otherwise $|a_1| = a_m$. When $\text{sign}(a_f) = \text{sign}(a_3)$,

$$|a_3| = \frac{1}{2}(2a_m - |a_f|)$$

Otherwise $|a_3| = a_m$.

The solution from the previous acquisition schemes no longer applies. Although y_2 has a similar form, ϵ_0 and ϵ_f are changed. The parameters are derived as follows. Once again, $v_1 t_1 + v_2 t_2 + v_3 t_3 = \Delta\theta$. Let

$$\beta_0 = \frac{1}{a_1 + (a_0/2)}$$

$$\beta_f = \frac{1}{a_3 + (a_f/2)}$$

Then

$$t_1 = \beta_0(v_2 - v_0)$$

$$t_3 = \beta_f(v_f - v_2)$$

From Eq. (45) we can calculate the change in position from $t = 0$ to $t = t_1$. Dividing by t_1 , we get v_1 :

$$v_1 = \frac{v_0 + v_2}{2} + \frac{t_1 a_0}{\pi^2}$$

Equation (22) is no longer valid, so the calculation becomes more complex:

$$v_3 = \frac{v_f + v_2}{2} + \frac{t_3 a_f}{\pi^2}$$

Plugging in,

$$(v_f - v_2)^2 \left[\beta_f + \frac{2\beta_f^2 a_f}{\pi^2} \right] - (v_0 - v_2)^2 \left[\beta_0 - \frac{2\beta_0^2 a_0}{\pi^2} \right] = 2\Delta\theta - 2v_2 T$$

Let

$$\epsilon_f = a_m \left(\beta_f + \frac{2\beta_f^2 a_f}{\pi^2} \right) \quad \text{and} \quad \epsilon_0 = a_m \left(\beta_0 - \frac{2\beta_0^2 a_0}{\pi^2} \right)$$

Then

$$(v_f - v_2)^2 \epsilon_f - (v_0 - v_2)^2 \epsilon_0 = 2a_m(\Delta\theta - v_2 T)$$

Changing variables,

$$y_2^2(\epsilon_f - \epsilon_0) - 2y_2(y\epsilon_f - 1) + y^2\epsilon_f - 2x = 0$$

When $\epsilon_f = \epsilon_0$, we get Eq. (15). Otherwise,

$$y_2(\epsilon_f - \epsilon_0) = y\epsilon_f - 1 \pm \sqrt{y^2\epsilon_0\epsilon_f - 2y\epsilon_f + 2x(\epsilon_f - \epsilon_0) + 1} \quad (48)$$

which is the same as Eq. (16) except that the sign in front of the square root can be negative.

Since ϵ_0 can have at most 2 values, ϵ_f can have at most 2 values, and the sign in front of the square root can have at most 2 values, at worst one needs to solve Eq. (48) eight times to see if a valid value of y_2 can be obtained. In practice one does not need to try all eight possibilities. If $y > 0$, ϵ_0 and ϵ_f cannot both be negative. If $y < 0$, ϵ_0 and ϵ_f cannot both be positive. So only six cases remain.

It is tempting to simply write down the equations for the borders of each region and pick which solution is valid. That would determine ϵ_0 and ϵ_f . However, this method is not practical in general, as will be illustrated by trying it for $a_0 = -a_m$ and $a_f = a_m$. When a_1 and a_3 are both negative,

$$\epsilon_0 = -1 + \frac{2}{\pi^2} \text{ and } \epsilon_f = -2 + \frac{8}{\pi^2}$$

The minimum x is found by setting y_2 to y . From Eq. (48),

$$x = y - \frac{y^2\epsilon_0}{2}$$

Here, $-1 \leq y \leq 0$. When $-1 + a_f/2a_m = -1/2 \leq y \leq 0$, the maximum x is determined by setting $y_2 = 0$. Now Eq. (48) gives

$$x = \frac{y^2\epsilon_f}{2}$$

For $-1 \leq y < -1/2 = -1 + a_f/2a_m$, the maximum x is found by setting $y_2 = 1 + 2y$. Here Eq. (48) gives

$$x = y^2 + \frac{y}{2}(\epsilon_f + 6) + \frac{1}{2}(3\epsilon_0 + 4)$$

When a_1 and a_3 are both positive,

$$\epsilon_0 = 2 + \frac{8}{\pi^2} \text{ and } \epsilon_f = 1 + \frac{2}{\pi^2}$$

Now it takes three curves to describe the minimum x . For

$$0 \leq y \leq \frac{2}{\epsilon_0 + \epsilon_f}, \text{ then } y_2 = 0 \Rightarrow x = \frac{y^2}{2}\epsilon_f$$

$$\frac{2}{\epsilon_0 + \epsilon_f} \leq y \leq 1 + \frac{a_0}{2a_m}, \text{ then } y_2 = y \Rightarrow x = y - \frac{y^2}{2}\epsilon_0$$

$$1 + \frac{a_0}{2a_m} \leq y \leq 1, \text{ then } y_2 = 1 - y \Rightarrow x = y^2(2\epsilon_f - 3)y + \frac{1}{2}(4 - 3\epsilon_f)$$

The maximum x also requires three curves. When

$$0 \leq y \leq \frac{1}{\epsilon_0}, \text{ then } y_2 = y \Rightarrow x = y - \frac{y^2 \epsilon_0}{2}$$

$$\frac{1}{\epsilon_0} \leq y \leq \frac{1}{\epsilon_f}, \text{ then } y_2 = \frac{y \epsilon_f - 1}{\epsilon_f - \epsilon_0} \Rightarrow x = \frac{y^2 \epsilon_0 \epsilon_f - 2y \epsilon_f + 1}{2(\epsilon_0 - \epsilon_f)}$$

$$\frac{1}{\epsilon_f} \leq y \leq 1, \text{ then } y_2 = 0 \Rightarrow x = \frac{y^2 \epsilon_f}{2}$$

When a_1 is positive but a_3 is negative, the minimum and maximum x require three curves each.

$$\epsilon_o = 2 + \frac{8}{\pi^2} \text{ and } \epsilon_f = -2 + \frac{8}{\pi^2}$$

The minimum x is as follows. For

$$\frac{1}{2(\epsilon_0 - 1)} < y < 1 + \frac{a_0}{2a_m}, \text{ then } y_2 = \frac{2y + 1}{4} \Rightarrow x = \frac{1 - 2y \epsilon_f - 4y^2}{8}$$

$$0 < y < \frac{1}{2(\epsilon_0 - 1)}, \text{ then } y_2 = y \Rightarrow x = y - \frac{y^2 \epsilon_0}{2}$$

$$-1 + \frac{a_f}{2a_m} < y < 0, \text{ then } y_2 = 0 \Rightarrow x = \frac{y^2 \epsilon_f}{2}$$

The maximum x is as follows. For

$$\frac{1}{\epsilon_0} < y < 1 + \frac{a_0}{2a_m}, \text{ then } y_2 = y \Rightarrow x = y - \frac{y^2 \epsilon_0}{2}$$

$$0 < y < \frac{1}{\epsilon_0}, \text{ then } y_2 = \frac{1 - y \epsilon_f}{4} \Rightarrow x = \frac{1 - 2y \epsilon_f + \epsilon_f \epsilon_0 y^2}{8}$$

$$-1 + \frac{a_f}{2a_m} < y < 0, \text{ then } y_2 = \frac{2y + 1}{4} \Rightarrow x = \frac{1 - 2y \epsilon_f - 4y^2}{8}$$

When a_1 is negative but a_3 is positive, we obtain our final six curves.

$$\epsilon_0 = -1 + \frac{2}{\pi^2} \text{ and } \epsilon_f = 1 + \frac{2}{\pi^2}$$

The minimum x is as follows. For

$$\frac{1}{\epsilon_f} < y < 1, \text{ then } y_2 = 0 \Rightarrow x = \frac{y^2 \epsilon_f}{2}$$

$$0 < y < \frac{1}{\epsilon_f}, \text{ then } y_2 = \frac{y \epsilon_f - 1}{2} \Rightarrow x = \frac{-y^2 \epsilon_f \epsilon_0 + 2y \epsilon_f - 1}{4}$$

$$-1 < y < 0, \text{ then } y_2 = \frac{y - 1}{2} \Rightarrow x = \frac{y^2 + 2y \epsilon_f - 1}{4}$$

The maximum x is as follows. For

$$\frac{1}{2\epsilon_f - 1} < y < 1, \text{ then } y_2 = \frac{y - 1}{2} \Rightarrow x = \frac{y^2 + 2y \epsilon_f - 1}{4}$$

$$0 < y < \frac{1}{2\epsilon_f - 1}, \text{ then } y_2 = 0 \Rightarrow x = \frac{y^2 \epsilon_f}{2}$$

$$-1 < y < 0, \text{ then } y_2 = y \Rightarrow x = y - \frac{y^2 \epsilon_0}{2}$$

For other values of a_0 and a_f , different curves determine the boundaries of the regions. The difficulties in finding the internal borders of the area of validity are sufficiently great that were this algorithm to be implemented, one would simply try all six candidate solutions and pick the first one that worked.

Figure 11 shows the area of valid solutions for $a_0 = -a_m$ and $a_f = a_m$ superimposed on the one for $a_0 = a_f = 0$ shown in Fig. 5. Note the loss in phase space for valid solutions in the $a_f = -a_0 = a_m$ case.

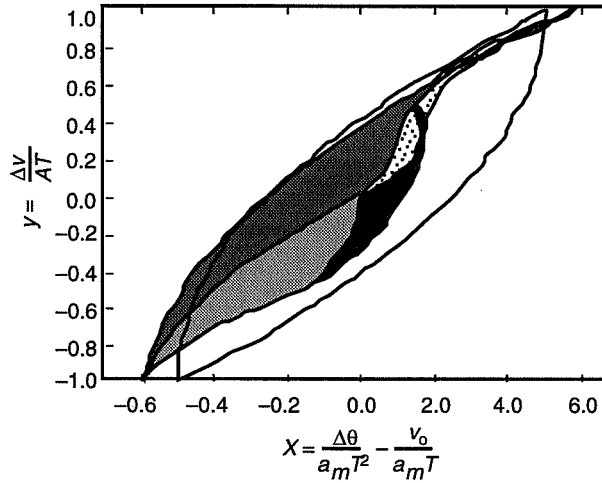


Fig. 11. Shrinkage of region of valid solutions for $a_f = -a_0 = a_m$

IV. Discussion and Conclusions

Acquisition scheme 4 is overly complex even if one does not calculate the internal borders of the area of validity. Such an algorithm would be very difficult to implement and maintain. Scheme 3 should

suffice for high-speed acquisitions and is recommended as an option on Deep Space Network antennas. The other schemes produce acceleration discontinuities which may cause undesirable excitations of the antenna structure.

The algorithm can be run with the entire set of commands output at once. However, in practice, it is not necessary to calculate all commands before implementing the first one. It is sufficient to find an acceptable acquisition time, T . The position and velocity commands can be calculated in real time as the antenna moves. If it is inconvenient to calculate the commands in real time, there may be enough processor time to calculate them in advance and store them.

Since the trajectory preprocessor cannot be used to supply commands until a satisfactory acquisition time is calculated, the question arises of how to find the acquisition time quickly. The problem is not trivial, as the target may have a trajectory that is very difficult to match. There are a number of possible strategies for picking a candidate acquisition time. A trade-off is involved. If the processor is so slow that it may take several tenths of a second to discover if a candidate acquisition time will work, one must be conservative in one's choice of candidate acquisition times. Only a few candidates can be tried. The candidate which is finally selected may not be optimal, but the time lost in finding a better solution may more than make up for the time saved by the improved answer. On the other hand, if thousands of candidate solutions can be tried in a second, one should expect to find an acquisition time that is within a fraction of a second of optimal. Mere processor speed does not guarantee success, as the processor may need to be shared with other tasks. Nor should it be forgotten that each target position may need to be translated in a relatively time-consuming manner to an equivalent antenna command. There may be coordinate conversions to apply, refraction must be taken into account, and subreflector squint must be corrected for, along with a host of other tabled or modeled systematic pointing errors. A trajectory preprocessor algorithm should not be developed for an antenna system unless one has a reasonable knowledge of the required and available processor time, both before and during the time period in which preprocessor commands are to be output.

When the trajectory preprocessor is used to match the trajectory of a sidereal object, the acquisition time is easy to estimate. There is usually no hurry to acquire the object, but even if there were, the preprocessor could handle the situation rather easily. A problem arises when the algorithm is used to match the trajectory of a fast-moving object that may be moving at 10 to 50 percent of the maximum antenna angular rate at acquisition.

It is understandable that one might wish to construct a simple, general algorithm to generate candidate acquisition times. One can guess a time of 1 sec, and should that be insufficient, continue with guesses of 2, 4, 8, 16, 32, 64, and 128 sec until a solution is found. If powers of two seem inappropriate, one can try powers of 3, 1.5, 1.2, or whatever. One can be satisfied with the first acceptable solution, or one can backtrack, looking for an even better one. Another idea is to start with the maximum $\Delta\theta/v_{max}$ and $2\Delta v/a_{max}$. Any of these ideas may be acceptable, but it seems far better to produce a carefully constructed table of candidate acquisition times for each given mode, especially for low-Earth-orbiting satellites. A simple default mode can be included as well.

This trajectory preprocessor algorithm depends greatly on the ability to predict exactly where the antenna will be when preprocessor commands are to begin. Any confusion resulting from misapplication of pointing corrections or differences between hoped for and actual position will result in a discontinuity in command position, which is precisely the problem that trajectory preprocessing is supposed to avoid. Choosing anticipated commands for the initial antenna position and velocity does no good if the antenna is pointed elsewhere. Using the actual antenna position does little good if the antenna is moving quickly and the preprocessor commands are due to start only a second or two later. Other initialization errors are possible that could render the preprocessor ineffective. For example, if incorrect or inappropriate velocity or acceleration limits are used, so that the antenna cannot respond properly to the preprocessor commands, antenna control will be back into the nonlinear region that the preprocessor was designed to

rescue it from. As long as care is taken to avoid mistakes of this sort, the preprocessor should serve a useful function.

There is no reason to demand that an antenna controller always be in a mode for which trajectory preprocessing is in use. The preprocessor can be an option used especially in cases for which very accurate tracking is required or for which control problems are anticipated. For this reason, an acquisition scheme that matches target acceleration may be favored over one that does not; the preprocessor may be used primarily when one wishes to avoid what sometimes seem like small acceleration discontinuities. However, use of a preprocessor as an option does not mean that it should be considered as an ad hoc feature rather than an integral part of a control system design. The issues of how and where to fit preprocessing into a system should be addressed even if it is not yet decided whether or not such an algorithm will be implemented. This would avoid problems that may arise when one attempts to add it after the rest of the system is complete.

As pointing requirements become more strict and tracking speeds increase, trajectory preprocessing will become a more and more valuable option to improve antenna control. The algorithm described in this article could be put to good use in the Deep Space Network.

Acknowledgments

The author thanks Jeff Mellstrom for pointing out the need for trajectory preprocessing, for his encouragement in numerous discussions about proposed solutions to the preprocessing problem, and for his help in reviewing and testing MATLAB versions of this preprocessor. Thanks also to Wodek Gawronski for supplying the model of DSS 13 and the PI controller, for reading the draft of this article, for his helpful suggestions, and for his enthusiasm about the results. Finally, thanks will to Jeff Schredder, Henry Valtier, and Hal Ahlstrom for their help in programming acquisition scheme 3, testing it, and evaluating it for use on DSS 27.

References

- [1] W. K. Gawronski, C. S. Racho, and J. A. Mellstrom, "Linear Quadratic Gaussian and Feedforward Controllers for the DSS-13 Antenna," *The Telecommunications and Data Acquisition Progress Report 42-118, vol. April-June*, Jet Propulsion Laboratory, Pasadena, California, pp. 37-55, August 15, 1994.
- [2] W. K. Gawronski and J. A. Mellstrom, "Elevation Control System Model for the DSS 13 Antenna," *The Telecommunications and Data Acquisition Progress Report 42-105, vol. January-March 1991*, Jet Propulsion Laboratory, Pasadena, California, pp. 83-108, May 15, 1991.

1995 108217
324476 9P

N95-14631

311-14
19789
P 9

The Network Operations Control Center Upgrade Task: Lessons Learned

J. S. Sherif
Software Product Assurance Section
and
California State University, Fullerton

T.-L. Tran and S. Lee
Software Product Assurance Section

This article synthesizes and describes the lessons learned from the Network Operations Control Center (NOCC) upgrade project, from the requirements phase through development and test and transfer. At the outset, the NOCC upgrade was being performed simultaneously with two other interfacing and dependent upgrades at the Signal Processing Center (SPC) and Ground Communications Facility (GCF), thereby adding a significant measure of complexity to the management and overall coordination of the development and transfer-to-operations (DTO) effort. Like other success stories, this project carried with it the traditional elements of top management support and exceptional dedication of cognizant personnel. Additionally, there were several NOCC-specific reasons for success, such as end-to-end system engineering, adoption of open-system architecture, thorough requirements management, and use of appropriate off-the-shelf technologies. On the other hand, there were several difficulties, such as ill-defined external interfaces, transition issues caused by new communications protocols, ambivalent use of two sets of policies and standards, and mistailoring of the new JPL management standard (due to the lack of practical guidelines). This article highlights the key lessons learned, as a means of constructive suggestions for the benefit of future projects.

I. NOCC Background

The Network Operations Control Center (NOCC) facility is one of three major components that comprise the Deep Space Network (DSN). The other two components are the Deep Space Communications Complexes (DSCCs), where the antennas and other front-end equipment are located, and the Ground Communications Facility (GCF), which provides communication links between the DSCCs, the NOCC, and flight project operations control centers (commonly referred to as POCCs). An example of such a POCC at JPL is the Space Flight Operations Control Center (SFOC) of the Multimission Operations Support Office (MOSO).

The NOCC is divided into two major subfacilities. One subfacility directly supports the DSN controllers and provides the day-to-day focal point for DSN operations-to-flight project interface. The other

produces operations support data for the Operations Engineering and Analysis (OEA) Group and the DSCCs and provides selected data products (e.g., tracking orbit data files) to its customers (i.e., flight projects and their respective organizational elements). The former is named NOCC-RT, since it deals mainly with real-time monitor-and-control operations. The latter is referred to as NOCC-NRT (nonreal time); this includes the NOCC support subsystem (NSS), the navigation subsystem (NAV), and the NOCC very long baseline interferometry processor subsystem (NVP).

The existing NOCC-RT is composed of old MODCOMP computers that can no longer be maintained at a reasonable cost. Moreover, their very limited memory capacity can no longer handle the increasing computing load. The existing software was written in MODCOMP assembly language and is not salvageable.

II. NOCC Upgrade Task

The scope of the NOCC upgrade task involved the redesign of the NOCC-RT and the replacement of the NOCC-RT hardware and software in its entirety. Installation of the hardware and software was divided into two main phases: Phase I and Phase II. Phase I hardware installation began in November 1990, and Phase II ended in July 1993. During this period, the existing MODCOMP real-time monitors (RTMs) continued to support old missions and whatever new missions were required.

The main thrust of the first phase involved the replacement of a subset of existing RTMs with Sun SPARC-1 workstations and new application software written in C language and utilizing a MOTIF-based graphical user interface (GUI). Phase II continued the transition to the high-performance Sun workstations and the replacement of the old MODCOMPs.

A. Elements of Successful Projects

Successful projects always exhibit an overall plan with shared purpose and goals and management's commitment to these goals. Also, and of equal importance, are the presence and support of dedicated and skilled process people. Tran summarizes the criteria for in-depth assessment of projects and gives attributes of projects that are considered successful.¹ These attributes include (1) consistent visibility of requirements, (2) well-enforced configuration control, (3) involvement of sponsors, users, and customers throughout the development life cycle, (4) support of a dedicated and skilled development team, (5) effective team communications, and (6) compliance to sound process policies or guidelines (for a disciplined and cost-effective development process).

Successful projects are those that meet valid functional (or design) requirements as well as user expectations; adhere to the spirit of process standards that promote rigor, discipline, and continuous improvement; and are accomplished on time and within budget.

B. NOCC-Specific Success Factors

Phase I of the NOCC upgrade task met 93 percent of the allocated functional requirements and was accomplished within budget and schedule. Additionally, the NOCC-RT system transfer agreement identified all known liens, and the delivered products met with user satisfaction, both upon initial transfer to operations and today. Details of the requirements traceability matrices for the NOCC-RT,² for frequency

¹ T.-L. Tran, "SSORCE In-Depth Assessment Worksheet," JPL Interoffice Memorandum LT:522-92 (internal document), Jet Propulsion Laboratory, Pasadena, California, p. 11, April 20, 1992.

² Ibid.

and timing,³ and for telemetry and monitor⁴ are contained in JPL internal documents. In summary, the NOCC upgrade task is considered a very successful project. NOCC-specific success factors include: (1) top management support, (2) focused ownership of requirements, (3) the team's can-do attitude, (4) use of enabling and extensible commercial technologies, and (5) a proactive software assurance function, supported and owned by program (i.e., TDA), project, and line management.

Top management support resulted in successful implementation of the project by assuring project visibility while minimizing organizational uncertainties. This support conveyed a perception of constancy in overall project purpose, and of mutual dependency—which united the entire team for a deeper commitment to the project plan and objectives.

Explicit and sustained ownership of requirements by system engineering throughout the product development cycle enabled a more systematic approach to requirements management, especially for better control of risk items, such as unexamined assumptions, neglected constraints, overspecification (or “gold plating”), misplaced or misassigned priorities, and excessive changes (or requirements-creeping syndrome). This focused ownership also facilitated the sharing of a single philosophy and a unified set of concepts, thereby contributing to easier identification of requirements-related problems and faster problem resolution or disposition. The real benefit of requirements management is a visible, common context of customer-driven needs and requirements, so that technical trade-offs between locally and globally optimized design alternatives can be made concurrently by different individuals or different subsets of the project team. Thus, the prescription of the overall architecture of the NOCC-RT, the layered approach to monitor-data presentation schemes, and spacecraft-and-link-oriented user interaction strategies were more openly debated, weighed, and ultimately more consistent with one another. (Refer to Ellman and Carlton [2] for more detail on NOCC-RT user interface design.)

Dedication of cognizant personnel and their enthusiasm during the two phases of the NOCC upgrade were major factors in the project success, but were even more significant to the first phase. The team's resilience in working with and around two sets of standards, namely the new JPL D-4000 and the old Telecommunications and Data Acquisition (TDA)/810-10 standard; its ability to upgrade the NOCC while keeping the old NOCC operational; and the can-do attitude, including toward incorporating unplanned, yet necessary, design changes, all contributed to a successful delivery of Phase I (and of Phase II).

The use of extensible technologies was and will remain a critical success factor for the NOCC-RT's overall flexibility and its access to different migration or evolutionary paths.

C. NOCC-Specific Difficulties

Yet, the road to “success” was not without hurdles. A few difficulties encountered by the NOCC upgrade task included the following: (1) ill-defined monitor-data interfaces with flight projects, (2) transition issues caused by new communications protocols, and (3) ambivalent use of two sets of policies and standards.⁵

Ill-defined data flow interfaces could be partially attributed to the fact that three DSN facilities (namely, the NOCC, SPC, and GCF) were being upgraded simultaneously. This complicated the devel-

³ B. Falin, *Network Operations Control Center Subsystem Functional Requirements Document, Frequency and Timing Subsystem (1990-1995)*, 822-021 (internal document), Jet Propulsion Laboratory, Pasadena, California, January 15, 1989.

⁴ D. L. Ross, *Network Operations Control Center Subsystem Functional Requirements Document, Telemetry and Monitor Subsystem (1991-1995)*, 822-25, JPL D-6101 (internal document), Jet Propulsion Laboratory, Pasadena, California, February 1, 1989.

⁵ T.-L. Tran, *Network Operations Control Center Subsystem Functional Requirements Document, Monitor and Control Subsystem (1990-1995)*, 822-23, JPL D-5783 (internal document), Jet Propulsion Laboratory, Pasadena, California, June 30, 1989.

opment and coordination of the interface specifications with the 26-m subnet projects and one primary DSN customer (i.e., Mars Observer).

The transition issues caused by the dual use of commercial off-the-shelf (COTS) protocols and DSN new communications protocols were extremely problematic and required extra effort and time to be resolved properly. This diverted project resources (equivalent to a full calendar month) into the dispositioning of this problem.

The ambivalent use of two sets of policies and standards, namely the new JPL D-4000 standard and the old TDA 810-10, caused some confusion. This is due to the fact that the JPL D-4000 is a rather high-level process model that lacks practical application guidelines. Also, the old TDA 810-10 standard calls for reviews and milestones that differ in rigor and scope from those of JPL D-4000.

Frequent unavailability of the old NOCC for testing is a somewhat uncontrollable problem, since the facility is required to be operational all the time. This problem may have delayed the project integration schedule. However, this delay was not significant.

III. Lessons Learned

The success of Phase I of the NOCC upgrade capped a major transition step for the DSN, going from an environment of memory-limited, single-sourced computing systems that are kept alive with cannibalized parts to a distributed environment of Unix-based, reduced instruction-set computer (RISC)-architecture workstations connected with one another via the transmission control protocol/user datagram protocol/internet protocol (tcp/udp/ip) protocol suite. In a period of budget constraints and rapid technological change, the upgraded NOCC continues its move toward an open-system support environment—while undergoing a few application-level adjustments. The decision to adopt the “open system” architecture, and to use commercially available communications protocols, has propelled the NOCC into the 1990’s and will have a profound impact on the way the futures of the NOCC and JPL ground data systems evolve. Additionally, there are some aspects of the product development process that deserve special analysis. In order to make the lessons-learned more relevant, this section proposes to present “findings” that reflect the local particularities of the NOCC upgrade and associated “recommendations” that generalize from the findings and make them portable to other project or application settings.

A. Findings and Recommendations on Requirements Management

The NOCC experience entails software development “in the many,” i.e., major modifications to 8 subsystems and 25 major interfaces and integrating these changes into the operational environment—and all of this without impacting real-time spacecraft support. (Refer to Fig. 1 for a context diagram of the NOCC-RT.) Against the background of high DSN-availability requirements for around-the-clock nominal and emergency spacecraft tracking, the DSN/NOCC functional requirements documents have shown that system-level and subsystem-level requirements can support, qualify, constrain, or presuppose one another. Furthermore, some requirements can be hidden assumptions. Others are design goals, and a few others are implementation or technology goals disguised as implementation constraints. Such requirements contamination prevails and represents one end of the spectrum, although the extent to which it occurs varies from one subsystem (or application) to another. This finding had also been confirmed by a field study, as discussed in [5,6]. It was found that the traditional way of requirements capture by prose-like, unstructured, obscure, and somewhat ambiguous statements is no longer effective. New techniques and tools for requirements engineering are advocated by Goguen and Linde [3], Smith [7], Ohnishi and Agusa [6], and Macaulay [5]. At the other end of the spectrum, requirements can be orthogonal to one another. This high level of rigor is sometimes worthwhile pursuing, sometimes not.

In the absence of formal techniques or without the advent of some expert tools, specifying valid or orthogonal requirements remains an elusive goal. Research in the knowledge-based systems and tools for formal specification is now undergoing a revival of great significance, as noted in [4].

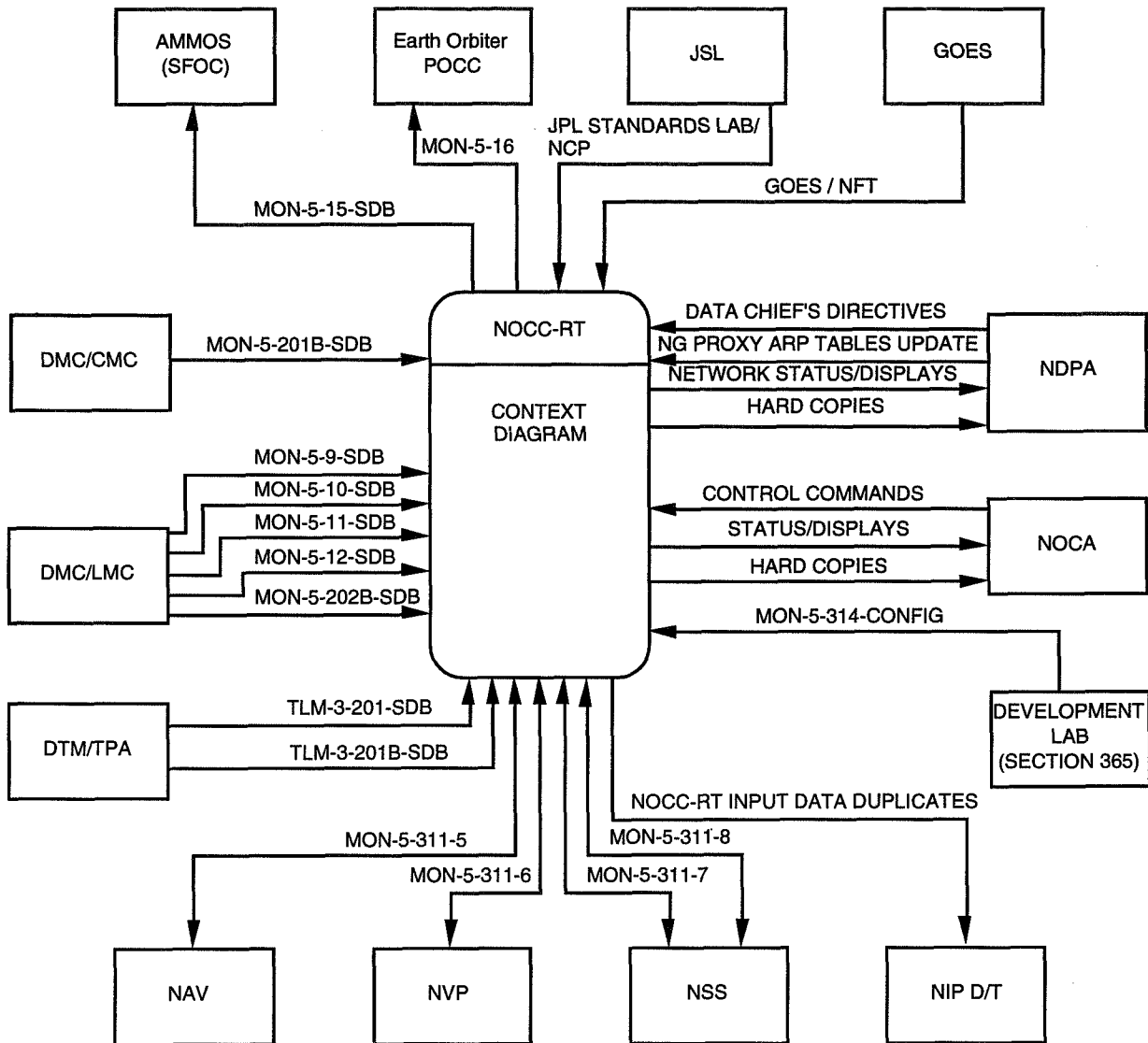


Fig. 1. NOCC-RT context diagram (Phase I).

The recommendations for requirements management include the following:

- (1) There must be an automated facility or tool to support and enforce the requirements management process, thereby making it more cost effective.
- (2) The customers, users, system engineers, developers, and test engineers should all work as a team in validating the requirements up front. Of equal importance is the thorough assignment (and reassignment, as appropriate) of requirements priorities. And, the system engineer (instead of a manager) must be the person in charge of sharing this information about requirements, up front and continuously, with all team members.
- (3) The requirements management process must be owned by a single individual, and preferably by the system engineer (or his or her delegate, such as a subsystem engineer or a process assurance analyst). This owner must also be responsible for requirements baselining and requirements-database configuration control to ensure a minimum number of hand overs.

- (4) Since the user representatives (e.g., DSN operations engineers) are key players in acceptance testing, they must be responsible for reviewing and concurring with the acceptance criteria specified for each and every high-level requirement (or “customer acceptance criteria”). This buy-in concept is a critical success factor for alignment between user expectations and planned capabilities.

B. Findings and Recommendations on Team Management

Many factors make team management of software projects different from other engineering fields. Software is generally more complex than other engineering projects. It requires a disciplined environment that enables creativity rather than a regimented environment where accountability and commitment to quality are lost. Quality is understood here in the context of total quality management, where the product meets user expectations at acceptable costs. As previously pointed out, effective team communications have always been an element of overall project success [1].

The recommendations on team management include the following:

- (1) At the outset, project management should establish a project-wide communications infrastructure. Such an infrastructure includes physical connectivity as well as a hundred-percent person-to-person connectivity. Central to this infrastructure is the existence of a common information repository that is accessible to each and every team member. This would encourage and enhance team building by enabling the sharing of information on requirements changes, design changes, etc., among the whole team, sponsors, customers, and users. It is essential to recognize that hard wiring team members is an alternative (e.g., via collocation), but should not be the only alternative. Soft wiring of all team members and project management via electronic mail is a must.
- (2) Also critical to effective communications is the establishment of an agreed-upon product-development process model. Such a model must have clear definitions of the control process (including any hand-over points), well-identified decision-making points, risk factors, cost constraints, and schedule agreement.
- (3) Built-in mechanisms must be in place to monitor the state of alignment between management’s understanding and that of the team members regarding the goals, objectives, and constraints of the project; these include (a) what is to be built, (b) who or which subteam is responsible for performing what piece of the to-be-delivered product, (c) who the collaborators are for each individual or subteam, (d) how the work is to be performed (i.e., in how many phases and with how many deliveries), (e) what the reporting and control requirements are, and (f) the providing of adequate training on the selected development techniques and tools (e.g., object-oriented analysis and design methodology and tools for source code control and requirements traceability).
- (4) Project management must optimize the team size in proportion to the effort required for each phase of the life cycle of the project. Baseline estimates compiled from industry show that it is more economical to invest in quality up front (e.g., in the preproject or requirements phase) than in the back end of the process (e.g., in the coding/full-scale production phase or integration-and-test phase). This is, indeed, consistent with the tenets of total quality management, which have reaffirmed that error prevention and process quality provide more value for the money than error correction, late error correction, and work arounds (via product inspections) [4].

C. Findings and Recommendations on Process Policies

Implementation should be consistent with the model and standards that are agreed upon by project management from the start of the project. For example, following the spiral model of software development is different from following the waterfall model [1]. The major difficulty with NOCC-RT process

policies was the dual use of standards that come from two different inheritances, as was pointed out earlier. The recommendations on process policies include the following:

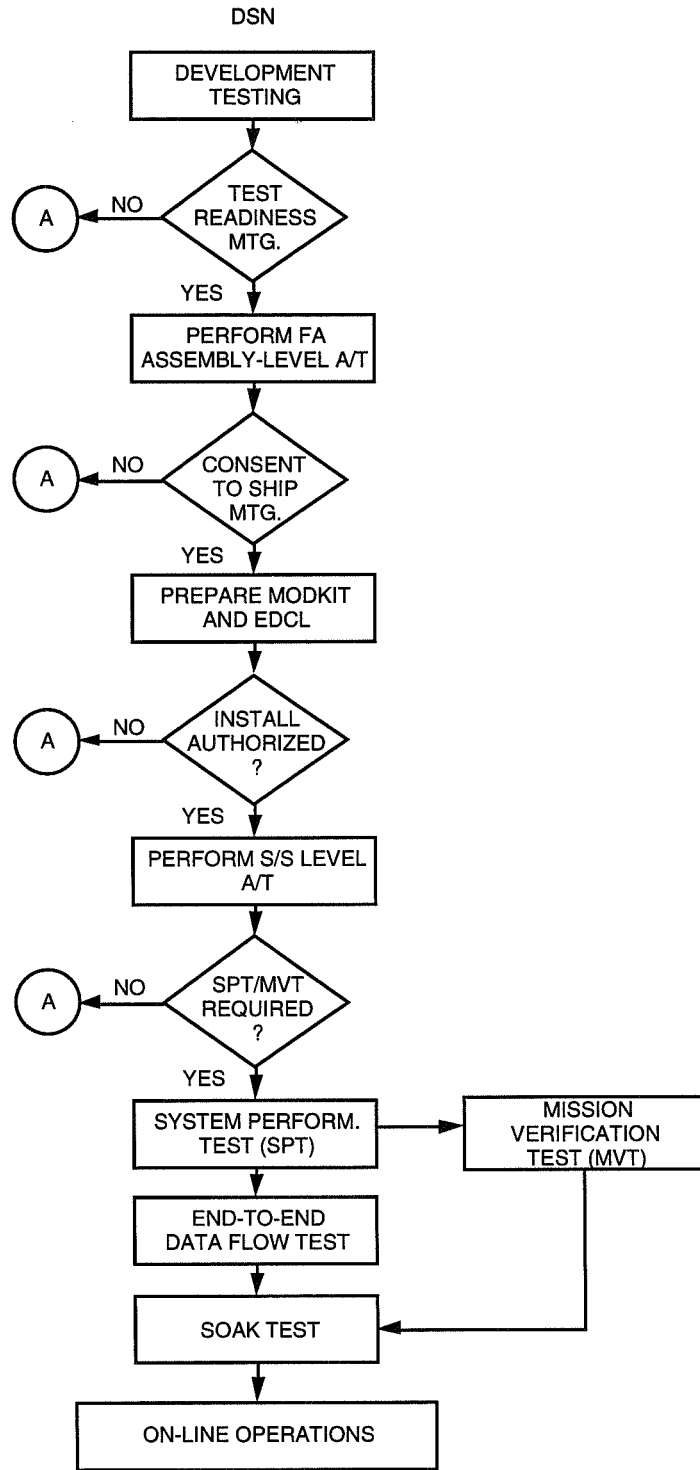
- (1) Do not select a standard that is too general, too difficult to tailor, or too difficult to interpret.
- (2) Use industry standards that conform to the task at hand and that can provide application guidelines with specific and concrete examples for various software activities (e.g., software requirements analysis or design), for various application families (e.g., general purpose versus embedded), and for various methodologies (e.g., structured analysis, object-oriented analysis and design, or data analysis and design).
- (3) The effort allocated to implementation should be based on concrete estimates and quantified uncertainties and be aligned with the effort estimates suggested by an industry baseline [1].
- (4) Every process policy must be supported and enforced by some automated tool. Otherwise, drop that policy. In other words, have as few laws as possible, but make them sensible and enforce them.

D. Findings and Recommendations on the Integration-and-Test Process

Integration and test (I&T) is a recognized critical aspect of product development. The DSN's I&T process has various levels of formality, which ultimately prepare it for mission-support readiness. These levels include unit (or module) test, assembly-level integration, preacceptance test, acceptance test, DSN data flow test, and mission verification test. An overview of this process is depicted in Fig. 2. In its current state, the DSN process is hampered by an excessive number of hand overs, a paperwork-intensive sign-off subprocess that is always out of synchronization with its objectives; also, its ownership is distributed over TDA's system engineering (responsible for defining functional requirements and associated acceptance criteria), TDA's implementation engineering (responsible for allocation of budget and approval of project implementation schedule and management), project management from the technical organization (responsible for overall project achievement, including development testing through acceptance testing), TDA Operations (responsible for system-level testing and assuring operational readiness of the DSN), and TDA Operations' main contractor (responsible for actually performing the system performance/mission verification, DSN end-to-end data flow, and soak testing). It is also worth noting that the current culture behind testing does not recognize the importance of ultimate customer acceptance and satisfaction as a driver. Accordingly, testing has been considered to be a "less critical" appendage of system engineering and has become a de facto back-end process focused on identifying problems and liens.

The recommendations on I&T include the following:

- (1) Test planning must start at the beginning of the project, concurrently with requirements analysis or capability planning, or as early as possible. Unless there is a specific test-plan sample to emulate, do not follow to the letter a standard or guideline that is too general or asks for too many test-design details too early (such as test-case detailed objectives). This recommendation is especially applicable to new implementations (as opposed to minor upgrade or sustaining projects, which have the convenient knowledge of an existing architecture and configuration).
- (2) Acquire or draw up the test process diagram that is imposed on the project (as a matter of policy), and share it with all team members. Ensure that system engineering, test engineering, and project management have a common understanding of the hand-over points and sign-off requirements along the I&T process. Do not assume that some "old-timers" know it all. If it is not in writing, the likelihood that their knowledge is not aligned with the de facto practice is extremely high (if not certain).
- (3) The effort allocated to I&T must reflect the major steps of the process diagram, the hand-over points, and the decision points for go/no go (or pass/no pass). Accordingly, the work breakdown structure and schedule for I&T must be consistent with these steps and points.



- (A) RETURN DEPENDENT UPON CIRCUMSTANCES/DIRECTION OF REVIEW BOARD, e.g.,
 (a) EXECUTE FURTHER TESTING AT SYSTEM OR SUBSYSTEM LEVEL
 (b) RETURN TO DEVELOPMENT FOR REDELIVERY
 (c) REMOVE OPEN LIENS

Fig. 2. Test process flow diagram.

IV. Conclusions

The NOCC upgrade task met all functional and design requirements as well as user expectations and adhered to the spirit of process standards that promote rigor, discipline, and continuous improvement; it also was accomplished on time and within budget.

Acknowledgments

The authors would like to express their sincere thanks to Dr. Joseph H. Yuen, Editor, *The Telecommunications and Data Acquisition Progress Report*; Dr. Li Tien-tien, Distributed Computers, Advanced Laboratory for Parallel High-Performance Applications; and Patricia A. Ehlers for comments and suggestions that greatly improved this article.

References

- [1] B. Boehm, *Software Engineering Economics*, Englewood Cliffs, New Jersey: Prentice Hall, 1981.
- [2] A. Ellman and M. Carlton, "Deep Space Network (DSN), Network Operations Control Center (NOCC) Computer-Human Interfaces," *Proceedings, Second Int. Symposium on Ground Systems for Space Mission Operations*, Pasadena, California, pp. 561-564, November 16-20, 1992.
- [3] J. A. Goguen and C. Linde, "Techniques for Requirements Elicitation," *Proceedings, IEEE Int. Symposium on Requirements Engineering*, San Diego, California, pp. 152-164, January 4-6, 1993.
- [4] K. Ishikawa, *What is Total Quality Control? The Japanese Way*, Englewood Cliffs, New Jersey: Prentice Hall, 1985.
- [5] L. Macaulay, "Requirements Capture as a Cooperative Activity," *Proceedings, IEEE Int. Symposium on Requirements Engineering*, San Diego, California, pp. 174-181, January 4-6, 1993.
- [6] A. Ohnishi and K. Agusa, "CARD, A Software Requirements Definition Environment," *Proceedings, IEEE Int. Symposium on Requirements Engineering*, San Diego, California, pp. 90-93, January 4-6, 1993.
- [7] T. J. Smith, "READS: A Requirements Engineering Tool," *Proceedings, IEEE Int. Symposium on Requirements Engineering*, San Diego, California, pp. 94-97, January 4-6, 1993.

1995/08218
324482

N95-14632

TDA Progress Report 42-118

12p

19770
August 15, 1994

P. 11

Low-Earth-Orbiter Resource Allocation and Capacity Planning for the DSN Using LEO4CAST

G. Fox and C. Borden
Systems Analysis Section

The Deep Space Network provides tracking and communication services for a number of U.S. and international low-Earth-orbiting (LEO) and near-Earth missions. This service is supplied by the 26-m subnet (located at each of the DSN complexes), the 9-m and the 34-m Antenna Research System antennas at Goldstone, and the 11-m antennas (following the orbital VLBI mission). An increasing number of LEO missions are planned for DSN support, which will result in increasingly complex ground resource allocation and mission support trades. To support TDA decision making on mission support and cost-effective ground system evolution for this 26-m subnet, LEO4CAST has been developed. LEO4CAST is a tool that uses statistical approaches to provide useful information for long-term ground system capacity planning and near-term resource allocation (prior to detailed time-of-day scheduling). LEO4CAST is currently beta-test software and is being exercised by both the Office of Telecommunications and Data Acquisition (TDA) and the JPL Systems Division.

I. Introduction

The DSN is responsible for planning, allocating, and operating the set of ground antennas that supports low-Earth-orbiting (LEO) and other near-Earth missions. Typically, the DSN accommodates user requirements through a combination of explicit resource allocation and negotiation of user requests. With the impending increase in mission requests for coverage on the near-Earth antenna set, negotiations become significantly more complex and costly.

Figure 1 provides an overall view of the LEO subnet capacity-planning and mission-support analysis process. LEO4CAST, a low-Earth-orbiter load-forecasting, resource-allocation, and capacity-planning simulation, is designed to support that analysis process. It is built on analysis capabilities already operational for the 34- and 70-m subnets, PC4CAST [1], which is used by TDA and the Multimission Operations Systems Office (MOSO) for resource allocation and capacity planning. Direct application of this tool, however, is inappropriate due to several complicating factors unique to low-Earth-orbiter missions and ground systems. Of primary importance is the uncertainty in low-Earth-orbiter mission trajectories (primarily due to atmospheric drag), which impacts mission view periods beyond several weeks. The new LEO4CAST software tool provides the capability to statistically determine antenna loading by missions with uncertain view periods. It uses the PC4CAST methodology to calculate deterministic mission loads, and when combined with the probabilistic mission loads, it generates mission accommodation, inter-mission conflict, and ground system loading statistics.

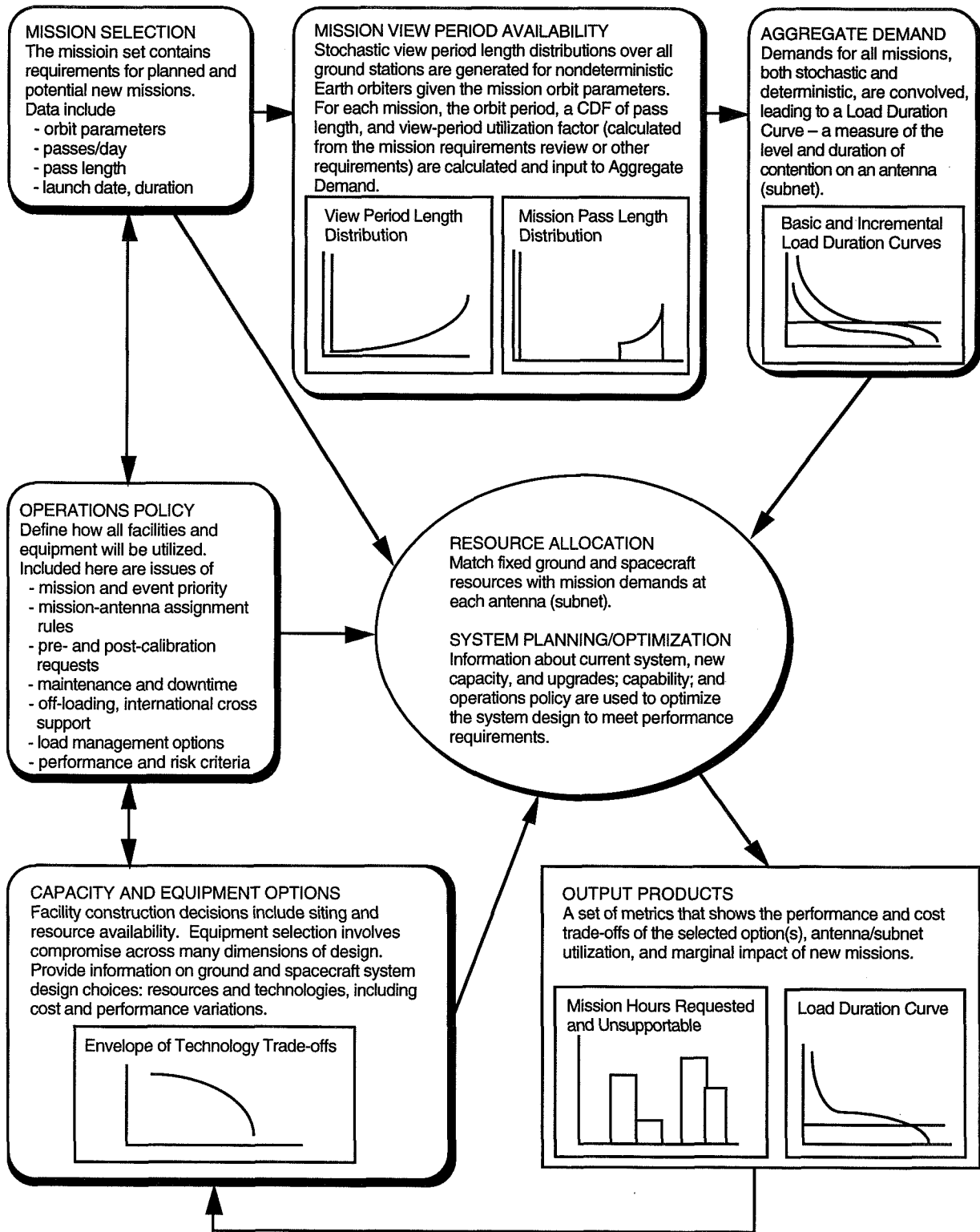


Fig. 1. LEO subnet capacity planning and mission support.

LEO4CAST provides the capability to assess numerous ground resource and flight system options using “what if” sensitivity analysis techniques. The scope of analysis spans mission parameter variation (e.g., mission sets, requests, and priorities) and ground system options (e.g., current and proposed antenna capacity, location, capability, and operations procedures). Analysis results reflect the uncertain nature of mission demands and provide an improved basis on which to base mission coverage commitments. Furthermore, impacts of improved operational processes (e.g., reduced pre- and post-calibration times), additional DSN or non-DSN antennas, or changes to mission priorities can be directly assessed.

In the following sections, LEO4CAST’s capabilities are described and sample output metrics are displayed. Anticipated future developments to support TDA decision making are also discussed. LEO4CAST is currently in beta test and has a *Preliminary User’s Guide*.¹ It is anticipated that additional system performance metrics to support TDA planning will be identified while undergoing beta test.

II. System Architecture

LEO4CAST is a Microsoft Windows application that has been developed for initial use on client-server architecture, Novell-networked IBM PCs. It consists of a set of relational databases, a probabilistic view period generator and load forecaster, and custom output forms (Fig. 2). For timely, cost-effective development, commercial off-the-shelf software and reusable software modules have been utilized wherever practical. This allows development activity to focus on design and implementation of algorithms specific to forecasting and capacity planning.

Operation of the tool requires network access to a Systems Division-maintained view period database for those missions having predictable known station rise and set times. Additional user inputs are entered and modified using Microsoft ACCESS, a standard relational database-interface tool, on Btrieve databases in the user’s home directory. The analytical engine uses both new and reused (from PC4CAST) code written in Borland C++ (Version 4.0) utilizing object-oriented design principles. Where possible, the code is ANSI standard C++, thus facilitating evolution to a multiplatform environment. Tabular outputs provide input to Microsoft Excel for graphical display. In Excel, users can use the existing graphical outputs or design their own to suit the needs of any particular study.

III. Method

LEO4CAST computes loading statistics for a set of antennas and a set of missions that require telecommunications services during a fixed forecast interval. Each mission is characterized by either explicit view periods or by orbit parameters: semimajor axis, eccentricity, inclination, and argument of perigee. These parameters are used to generate view-period-length probability distributions for each antenna. Mission view periods generated internally are referred to as probabilistic (or stochastic). In creating these distributions a lack of information about orbit timing drives the use of uniform random distributions for the ascending node and the crossing time for each mission.

Tracking requirements for each mission are aggregated to forecast the demand on each antenna. All deterministic missions are first combined together into a load duration curve (LDC), as is done in PC4CAST. This involves collecting all the statistics on mission contention derived from the input station rise and set times for each mission, modified by requirements information. The independence of the deterministic and stochastic mission sets allows them to be combined to yield the total antenna LDC. The information contained in the LDC provides a complete set of loading and contention statistics. Outputs for each antenna, which include summary metrics for marginal mission impacts and pairwise mission contention,

¹ *LEO4CAST Preliminary User’s Guide* (internal document), Jet Propulsion Laboratory, Pasadena, California, April 1994.

are generated and can be used in Excel to generate charts and tables. See Section V for a description of performance output metrics currently available.²

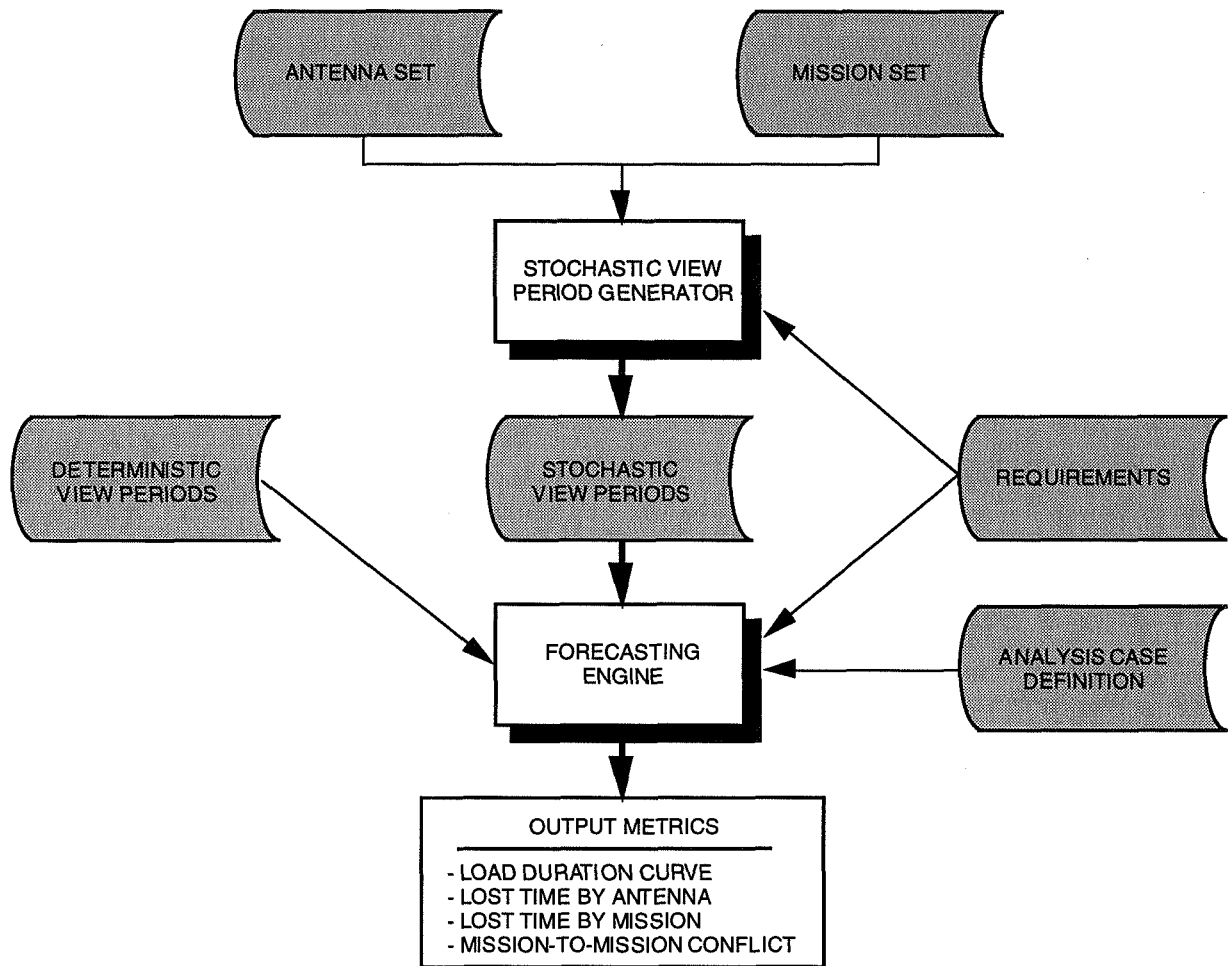


Fig. 2. LEO4CAST architecture.

IV. Inputs

User inputs to LEO4CAST are of four types: forecast interval, mission orbit parameters, antenna location, and mission-tracking requirements by antenna. For those missions with known view periods, view-period rise and set times are read directly from an external file. In addition, there is an initialization file (LEO4CAST.INI) for setting up run-time performance and accuracy parameters.

Nonspacecraft users of antenna time (e.g., such DSN services as antenna calibration and maintenance) should be included as “Missions,” in addition to the set of spacecraft missions. LEO missions are modeled probabilistically and require mission orbit parameters be specified. Deterministic missions must have their view periods entered into the “View Period” database on the server. The “Antenna” database contains information describing the antenna location (latitude and longitude). The “Requirements” database is

² For more information on the LEO4CAST analysis procedures and a real application of the methodology, see G. Fox, C. Borden, and S. Matousek, *Future DSN Support of Small Earth Orbiters*, Section 7, “Ground System Load Forecasting and Capacity Planning Analysis,” JPL D-10099 (internal document), Jet Propulsion Laboratory, Pasadena, California, October 14, 1993. A future paper will discuss the analytical approaches used.

where tracking requirements for missions are identified and assigned to the ground system resources (antennas). Mission requests for each antenna include tracks per day, minutes per track, and minimum acceptable view-period length. Requirements also include antenna pre- and post-calibration times.

V. Outputs and Graphics

LEO4CAST provides a number of output metrics useful for ground system planning and mission design analysis. The primary output is a load-duration curve (LDC) table that displays the combined demands of all missions on each antenna and subnet. Mission view periods, tracking requests, and ground-system operations requirements are included in the LDC. Figure 3 displays a sample LEO4CAST load-duration curve for the fourth quarter of 1995.³ The duration is the fraction of time at which load is greater than or equal to the selected load level. The area under the curve above 1.0 (subnets) reflects the amount of time that missions are unable to be supported by the subnet due to simultaneous contention (i.e., lost time). Figure 4 provides the mission data used in the study.

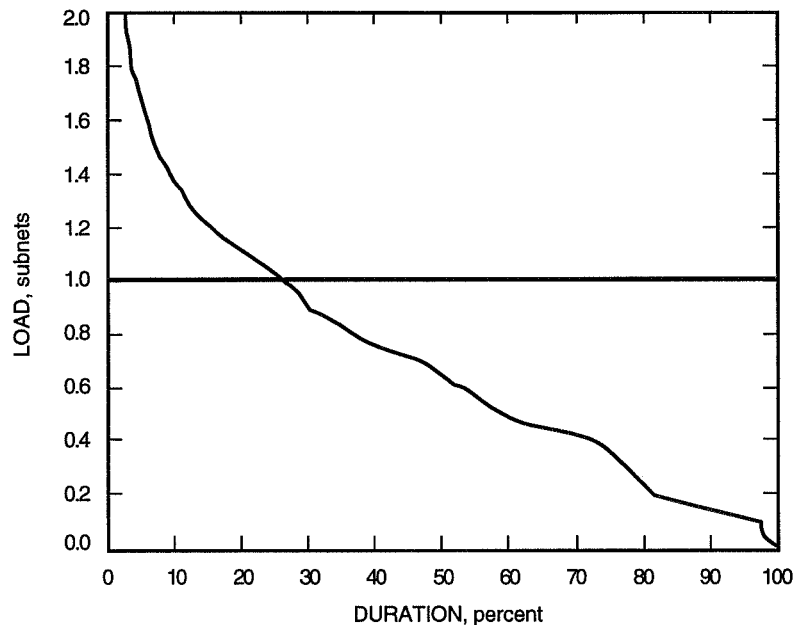


Fig. 3. Fourth quarter 1995 baseline 26-m subnet loading. Lost time = 14.75 percent.

For forecasting studies, mission lost time provides a view to the amount of mission conflict on the designated antenna set. Ground system and mission planners can use these lost time outputs for long-term “what if” studies of changes in ground system capacity, capability, or operations procedures, and for mission sensitivity studies. Figure 5 presents a 5-year display of lost time for 1995–1999.⁴ The multiyear aspect of the figure provides insight into the long-term nature of demand on the system. Of particular note is the reduction in lost time (as a percent of requested time) after the second quarter of 1995 due to reducing pre- and post-calibration time requirements from 25 to 12 min. Furthermore, the overall level of mission requests unsupported over the 5-year time horizon is significant. LEO4CAST provides a quantitative basis for evaluating lost time and the consequences of changes in mission requests and/or ground system capability.

³ Ibid.

⁴ Ibid.

Project	Launch Date	End Primary Mission	End Extended Mission	Requirements, passes/day	Perigree, km	Apogee, km	Inclination, deg	
NIMBUS-7	24-Oct-78	4-Jan-90	31-Dec-99	6 (15min/pass)	944	968	99	
ROSAT	1-Jun-90	31-Dec-95	31-Dec-95	2 (10min/pass)	580	580	53	No views at Canberra, Fairbanks, McMurdo
SAMPEX	12-Jun-92	30-Jul-95	31-Dec-99	3 (8min/pass)	514	692	82	
TOPEX/POSEIDON	10-Aug-92	10-Aug-95	10-Aug-97	6 (10min/pass)	1336	1336	66	
YOHKOH	26-Aug-91	25-Aug-94	26-Aug-99	4 (9min/pass)	515	770	31.1	No views at Fairbanks, McMurdo
ASTRO-D	20-Feb-93	10-Mar-96	1-Jan-00	4 (9.5min/pass)*	536	642	31.1	No views at Canberra, Fairbanks, McMurdo
FAST	23-Aug-94	30-Sep-95	31-Dec-99	4 (10min/pass)	350	4200	83	No views at Canberra, McMurdo
IRTS	1-Jan-95	2-Jul-95	2-Jul-95	4 (30min/pass)	400	500	97*	
NOAA-K	1-Mar-95	30-Apr-95	28-Feb-97	6 (5min/pass)*	833	833	99	
NOAA-L	1-Jul-96	30-Aug-96	1-Jul-98	6 (16min/pass)	870	870	99	
NOAA-M	1-Jan-97	2-Mar-97	1-Jan-99	6 (16min/pass)	833	833	99	
RADARSAT	1-Feb-95	2-May-95	1-Feb-00	3 (10min/pass)	792	792	98.5	Requirements at Canberra only
SWAS	1-Jun-95	30-Jun-98	31-Dec-99	3 (8min/pass)	600	600	65	
TOMS-EP	1-Jul-94	31-Jul-96	31-Jul-00	4 (15min/pass)	955	955	99.3	
GAMES	1-Jun-98	15-Dec-98	15-Jun-01	3 (10min/pass)*	480	480	86	
LTP5-1	1-Jun-99	31-Jul-99	30-Aug-99	6 (5min/pass)*	350	350	28.5	No views at Madrid, Fairbanks, McMurdo
STEP	1-Sep-99	13-May-00	13-May-00	1.875 (8min/pass)	550	550	97.84	
TIMED L	1-Dec-99	30-Nov-01	30-Nov-01	2.1425 (7min/pass)	400	400	49	No views at Fairbanks, McMurdo
GEOTAIL	24-Jul-92	2-Jul-95	31-Dec-99	24/week(1hr/pass)	512,000	1,400,000	5	Double lunar swingbys, night view
ACE	1-Aug-97	31-Dec-99	31-Dec-02	1/day (3hr/pass)	L1 Halo	L1 Halo	28.8	
AXAF I	1-Sep-98	9-Sep-03	9-Sep-03	1/day (8hr/pass)*	10,000	100,000	28.5	
Cluster	1-Dec-95	1-Mar-98	31-Dec-99	10/month (2hr/pass)	25,512	140,316	90	
ISO	10-Sep-95	1-Apr-97	30-Jun-97	1/day (8hr/pass)	1,000	70,000	5.2	
POLAR	1-May-94	2-Dec-95	31-Dec-99	4/day (45min/pass) & 1/day (216min/pass)	12,756	57,403	90	
SOHO	1-Jul-95	29-Nov-97	21-Jan-00	3/day (1.6hr/pass) & 1/day (8hr/pass)	6,554	1,213,350	28.8	Maintains 4-deg sun angle at L1 point (1,700,000 km)
STRV 1	12-Feb-94	12-Feb-95	12-Feb-95	1/day (2hr/pass)*	200	35,977	7	
WIND	12-Dec-93	12-Dec-95	12-Dec-96	1/day (2hr/pass)	510,215	1,594,535	5	Double lunar swingbys, day view

The first 18 missions are modeled as stochastic, the last 9 as deterministic.
Assumes 6-deg horizon mask.
Launch support, NSTS requirements, and backup support for other subnets/systems are not included.
*Best estimate.

Fig. 4. Mission set for 26-m subnet loading.

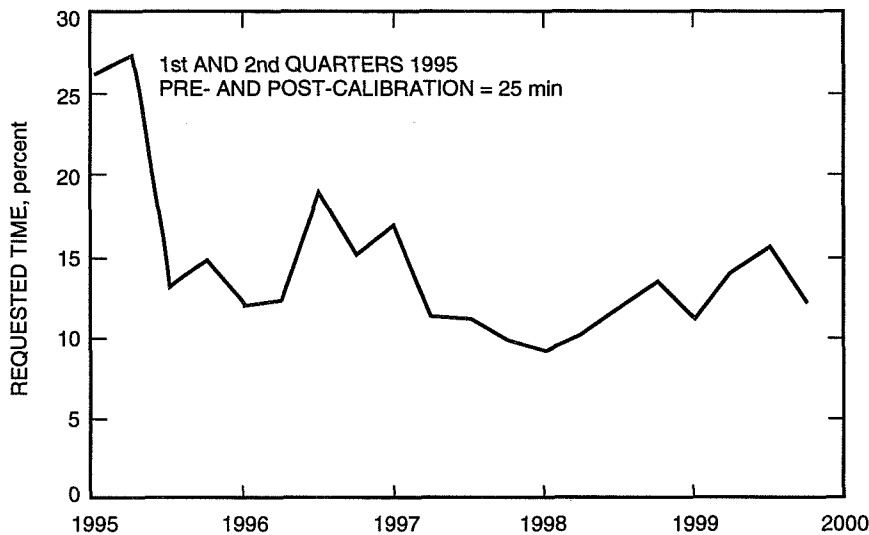


Fig. 5. Percent of lost time for the 26-m network for 1995–1999. Pre- and post-calibration = 12 min for all missions.

A sensitivity analysis on reduction of pre- and post-calibration time from 25 to 12 min is shown in Fig. 6. The percentage of mission lost time is shown to increase significantly (e.g., in the second quarter of 1996 there is a 56-percent increase in lost time, from 12.2 to 19.1 percent, due to an increase in pre- and post-calibration time from 12 to 25 min). To illustrate the importance of operations time dedicated to pre- and post-calibration, a second curve is added to the figure indicating the benefit of a second low-Earth-orbiter antenna added at Goldstone. To first order, the additional antenna provides only a small improvement over reduced pre- and post-calibration time reduction. Long-term planning of mission, antenna capacity, and operations policies are facilitated by these types of LEO4CAST “what if” analysis capabilities. Future capabilities will also include life-cycle cost-effectiveness measures.

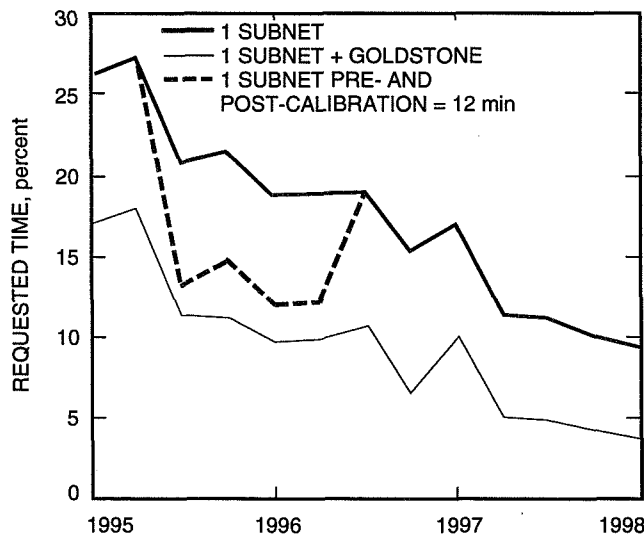


Fig. 6. Percent of lost time for the 26-m subnet for 1995–1997. Reduction of pre- and post-calibration from 25 to 12 min delayed from mid-1995 to mid-1996.

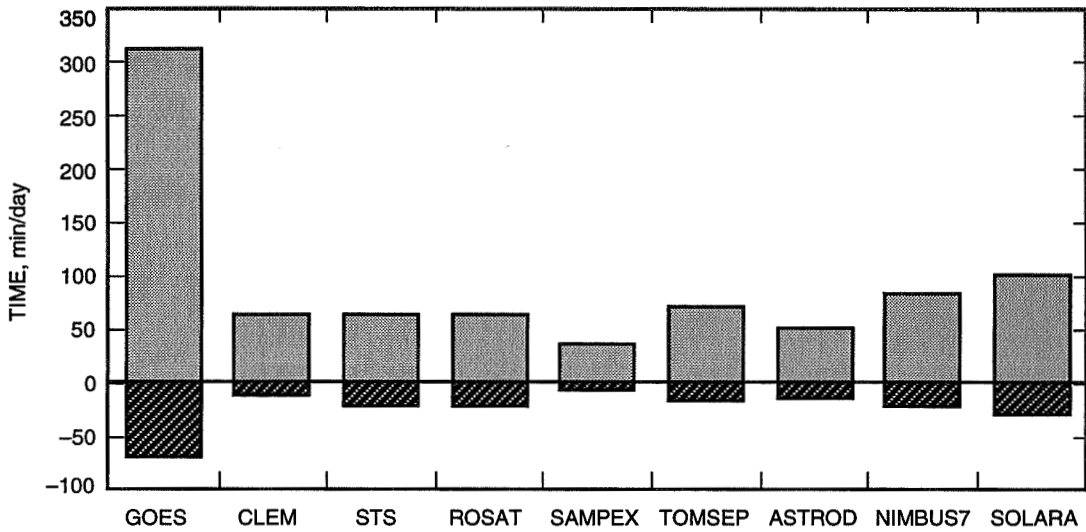


Fig. 7. Mission requirements at Goldstone. Marginal unscheduled time, including pre- and post-calibration.

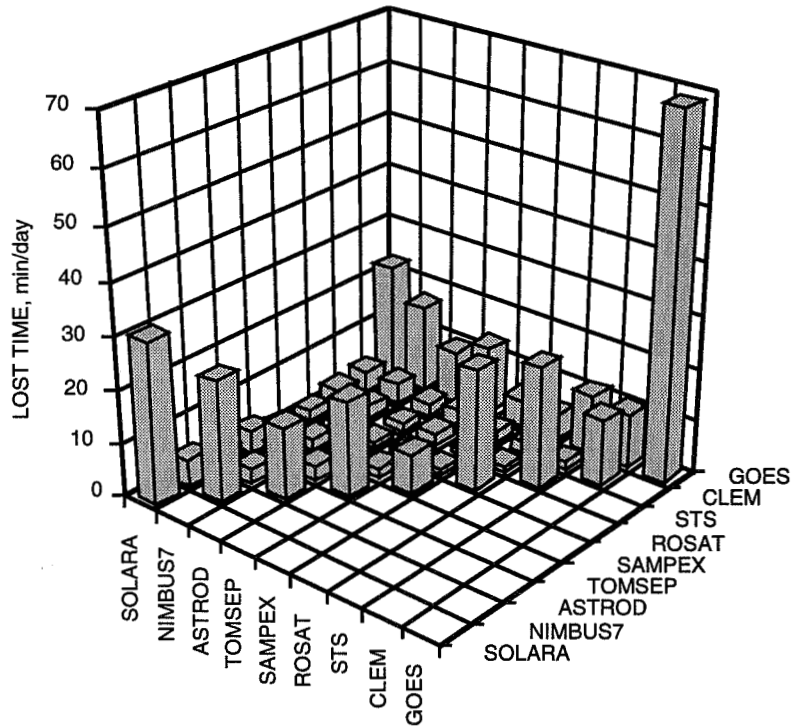


Fig. 8. Tall tent poles: mission bumps mission.

LEO4CAST also provides performance metrics to evaluate near-term resource allocation and mission request and/or priority options. To illustrate, mission-specific coverage and lost time on the 26-m subnet is shown in Fig. 7 for a recent analysis. The area above zero for each mission represents the expected mission coverage. Below zero indicates expected unsupportable requests (i.e., lost time due to contention with other missions).

A more detailed view as to which missions are simultaneously competing for antenna time is displayed in Figs. 8 and 9. Each mission's lost time matches the lost time shown in Fig. 7. Inter-mission conflicts

are shown with the assumption that each conflicting mission's lost-time contribution reflects that it is the marginal mission (i.e., the last one to be loaded). When mission priorities for the low-Earth-orbiter and near-Earth missions are implemented in LEO4CAST, prioritized lost time will be displayed. As LEO4CAST gets additional use, it is anticipated that new long-range planning and near-term resource allocation metrics will be provided to support management decision making.

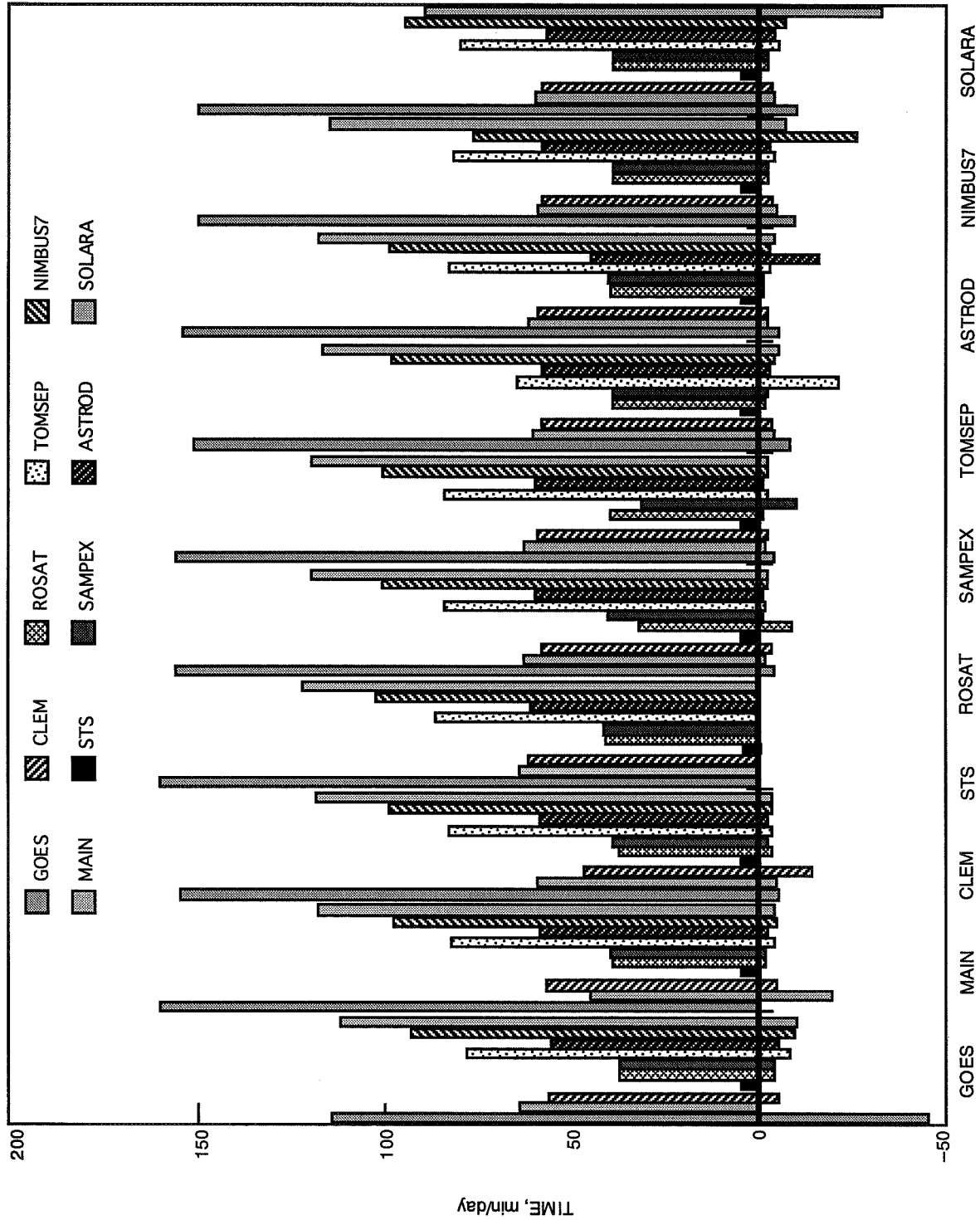


Fig. 9. Mission-on-mission lost time impact.

VI. Future Directions

LEO4CAST has been initially exercised on long-term mission and capacity planning studies and near-term resource allocation studies. As a result of these initial applications, recommendations for extensions and improvements in analysis capability, display of system performance metrics, and multiplatform access have been provided. It should be noted that extension of certain LEO4CAST capabilities will be closely coupled with PC4CAST developments.

In order to more realistically represent mission view periods and requirements, and to link missions whose orbits are serially correlated, a simulation capability is being investigated. Simulation would further enable more realistic assignment of missions to ground antennas, allow the determination of confidence levels in loading results, and provide a basis for the validation of the analytical model. It is anticipated that the simulation would supplement the analytical approach when more fidelity is desired.

Additional analysis extensions include automation of improved procedures for antenna allocation to missions. The current manual process is cumbersome and does not guarantee selection of a superior allocation. Specifically, realistic TDA rules and constraints must be incorporated within the optimization framework. Additional long-term analysis developments include capacity, capability, and siting evolution across subnets and a comprehensive end-to-end design trade-off analysis capability for ground and flight systems and processes. Trade-off studies between subsystems should consider not only performance variation but also system life-cycle cost minimization.

System performance metrics currently available, such as the LDC and the contention matrix, have been described above. Continuing application of LEO4CAST will result in the need for additional metrics to support mission and ground-system decision making. One potential area for further development is in support of a resource allocation process yet to be defined for the 26-m subnet. Such metrics are needed to provide timely insight into mission and antenna conflicts, which should assist in the resolution of contention and aid in providing a more efficient scheduling process.

The ability to access multiple databases and deploy cross-platform applications is becoming increasingly important. In the near term, MOSAIC is being evaluated for cost-effective, multiplatform data browsing. MOSAIC, or a future commercial follow-on, will be considered for multiplatform tool deployment in the future.

Acknowledgments

Grateful appreciation and thanks are expressed to J. R. Hall and (posthumously) Ed Posner for their support and encouragement in the development of these tools. Special thanks go to Fred McLaughlin and Steve Wolf for agreeing to be beta testers. Steve Loyola and Dave Werntz deserve congratulations for pushing the state of the art in resource load forecasting and scheduling under real-time resource availability constraints. Additional thanks are due to J. Kwok, Steve Matousek, and Mark Garcia for their contributions to analysis approaches and software testing. Finally, Sil Zendejas deserves recognition for his superb software design and implementation.

Reference

- [1] S. J. Loyola, "PC4CAST—A Tool for DSN Load Forecasting and Capacity Planning," *The Telecommunications and Data Acquisition Progress Report 42-114*, vol. April–June 1993, Jet Propulsion Laboratory, Pasadena, California, pp. 170–184, August 15, 1993.

Referees

The following people have refereed articles for *The Telecommunications and Data Acquisition Progress Report*. By attesting to the technical and archival value of the articles, they have helped to maintain the excellence of this publication during the past year.

Y. Bar-Sever	J. J. Bautista	D. Bayard	L. Bright
M. Calhoun	K.-M. Cheung	M. Costa	R. G. Covington
L. Deutsch	S. Dolinar, Jr.	M. Esquivel	V. A. Feria
M. Gatti	W. Gawronski	J. Gevargiz	N. Ho
W. J. Hurd	S. Kayalar	A. Kiely	A. Konopliv
A. Lee	S. Lichten	S. T. Lowe	G. Lutes
R. J. McEliece	A. Mileant	D. D. Morabito	F. Pollara
D. J. Rochblatt	C. Ruggier	R. Sadr	M. M. Shihabi
H. Smith	S. Soares	P. H. Stanton	S. Stephens
M. Sue	L. Swanson	M. Thorburn	S. W. Thurman
L. Tientien	S. Townes	B. G. Williams	P. A. Willis
K. E. Wilson	S. Wolf	S. C. Wu	X. S. Yao
L. E. Young	G. Zimmerman		